DOCTOR OF PHILOSOPHY

Assessing the Performance and Economics of Advanced Burnable Absorbers

Bolukbasi, Mustafa

Award date:
2024

Awarding institution:
Bangor University

Assessing the Performance and Economics of Advanced Burnable Absorbers

Mustafa Bolukbasi

PRIFYSGOL
BANGOR
UNIVERSITY

School of Computer Science and Electronic Engineering
College of Environmental Sciences and Engineering

Submitted in partial satisfaction of the requirements for the
Degree of Doctor of Philosophy in Nuclear Engineering and Science.

Supervisors Prof. Simon C. Middleburgh *and* Prof. Bill Lee

April, 2024

Declaration

I hereby declare that this thesis is the results of my own investigations, except where otherwise stated. All other sources are acknowledged by bibliographic references. This work has not previously been accepted in substance for any degree and is not being concurrently submitted in candidature for any degree unless, as agreed by the University, for approved dual awards.

Yr wyf drwy hyn yn datgan mai canlyniad fy ymchwil fy hun yw'r thesis hwn, ac eithrio lle nodir yn wahanol. Caiff ffynonellau eraill eu cydnabod gan droednodiadau yn rhoi cyfeiriadau eglur. Nid yw sylwedd y gwaith hwn wedi cael ei dderbyn o'r blaen ar gyfer unrhyw radd, ac nid yw'n cael ei gyflwyno ar yr un pryd mewn ymgeisiaeth am unrhyw radd oni bai ei fod, fel y cytunwyd gan y Brifysgol, am gymwysterau deuol cymeradwy.

Mustafa Bolukbasi

Abstract

In the pursuit of sustainable and low-carbon energy sources, nuclear energy has emerged as a viable and reliable option. However, the economic aspect of nuclear energy remains concerning. Efforts in research and technological innovation are currently being made to address these economic issues while ensuring the highest safety standards. The focus lies on two primary areas with the utilization of new fuel designs: to reduce costs while maintaining the same power output, or the extension of fuel cycles to increase capacity factors.

A fuel design utilizing a novel approach is employed to generate comparable or greater energy output, necessitating fewer natural resources and enhancing waste management, all while maintaining safety. Among the commonly employed burnable absorbers in light water reactors, gadolinium oxide is recognized for its functionality. Nevertheless, its drawbacks impede fuel efficiency. In light of this, a novel fuel design, achieved by enriching gadolinium oxide with the most effective absorber isotopes of gadolinium, offers a solution to eliminate these drawbacks and yield economic advantages without compromising safety.

Moreover, the nuclear power industry has identified the capacity factor of nuclear power plants as an aspect that can be enhanced. This factor gauges the actual output of a plant within a specific timeframe in relation to its hypothetical maximum output if it could continuously function at full capacity. A method to increase the capacity factor is through longer fuel cycles. Nevertheless, extending the duration of these cycles necessitates the inclusion of more fissile material, which presents difficulties in maintaining reactivity control. Consequently, the development of a new design for burnable absorbers becomes imperative to address this challenge.

In this study, an examination is undertaken to explore the potential consequences of incorporating enriched gadolinium oxide, specifically enriched with gadolinium-157, into fuel compositions. Initially, a 2D neutronic analysis is conducted employing the Monte Carlo particle transport method to compare the reactivity properties of natural gadolinium oxide and the enriched variant. The depletion behaviour of the primary neutron-absorbing isotopes and the breeding behaviour of plutonium-239 are also investigated. Subsequently, the study expands to encompass a comprehensive 3D fuel cycle analysis spanning an 18-month cycle. During this phase, the impact of transitioning from utilizing natural gadolinium oxide to employing enriched gadolinium oxide on various factors such as peaking factors, reactivity feedback parameters, shutdown margin, and power profile is thoroughly analysed. Furthermore, the study delves into the economic implications associated with this transition.

Adopting an unconventional approach, this research also explores an innovative solution to overcome the reactivity control challenge that arises from the adoption of high-assay low-enriched uranium in 36-month fuel cycles. The study focuses on the introduction of new designs, namely the Discrete Burnable Absorber Pin and Moderated Discrete Burnable Absorber Pin designs, utilizing zirconium diboride or uranium diboride as burnable absorbers. To evaluate the reactivity characteristics of these novel designs, as well as investigate the depletion behaviour of neutron-absorbing isotopes and the breeding behaviour of plutonium-239, a 2D neutronic analysis is conducted employing the Monte Carlo particle transport method. Additionally, a comprehensive 3D fuel cycle analysis is carried out to examine the transition from an 18-month cycle to a 36-month cycle using high-assay low-enriched uranium. This analysis encompasses an assessment of peaking factors, reactivity feedback parameters, shutdown margin, power profile, and the potential economic advantages that these designs may offer. The study also discusses future research directions to be pursued, thus paving the way for further research in this field.

Acknowledgements

I would like to express my sincere gratitude to the Turkish Ministry of National Education for their sponsorship, which has made this journey possible. I am immensely thankful for their support as it has been a constant source of inspiration and motivation.

I am indebted to my first supervisor Prof. Simon Middleburgh, for his invaluable guidance, insightful comments, patience, and unwavering support. I am profoundly grateful for his tireless commitment to my academic journey.

Likewise, I extend my sincere thanks to my second supervisor, Prof. Bill Lee, whose significant contributions have greatly enhanced this research. His extensive knowledge and objective perspectives have enriched my work.

I would also like to express my appreciation to Dr. Marcus Dahlfors and Scott Vrtiska for their valuable contributions to my work. Their expertise and insights have been instrumental in this research, and I am truly grateful for their time and efforts.

Furthermore, I want to acknowledge the entire academic and technical team at the Nuclear Futures Institute, as well as my fellow students. The collaborative and supportive environment they have fostered has made my experience enjoyable.

I want to give special thanks to my parents, who has always been there for me, providing unwavering support in all aspects of my life.

Lastly, and most importantly, my heartfelt thanks go to my dear wife Gulsum, whose endless support throughout my PhD journey has been a source of strength. Her encouragement, patience, and constant presence and endless love in my life have made a significant difference.

Once upon a time, I was merely a spark and…

Contents

List of Figures

List of Tables

Abbreviations

AO	Axial Offset
ARI	All Rods In
BA	Burnable Absorber
BC	Boron Coefficient
BOC	Beginning of the Cycle
BWR	Boiling Water Reactor
CBC	Critical Boron Concentration
e-Gd_2O_3	Enriched Gadolinium Oxide
EFPD	Effective Full Power Days
EOC	End of the Cycle
HFP	Hot Full Power
HZP	Hot Zero Power
ITC	Isothermal Temperature Coefficient
LCOE	Levelized Cost of Electricity
LWR	Light Water Reactor
MTC	Moderator Temperature Coefficient
MWe	Megawatt Electrical
MWh	Megawatt Hour
MWt	Megawatt Thermal
n-Gd_2O_3	Natural Gadolinium Oxide
NPP	Nuclear Power Plant

PWR	Pressurized Water Reactor
RPF	Relative Power Fraction
SMR	Small Modular Reactor
SWU	Separative Work Units
UDC	Uniform Doppler Coefficient

Chapter 1

Introduction and Literature Review

Nuclear energy will play a crucial role in the goal of achieving net zero emissions by 2050 [1]. Consequently, numerous research initiatives are underway to enhance the economic viability of Light Water Reactors (LWRs), which represent the majority of active reactors worldwide, while ensuring safety. Nuclear Power Plants (NPPs) incur high construction costs, which can be offset by increasing power generation through a high capacity factor, increasing the number of effective full power days (EFPDs) [2].

On the other hand, extending the duration of the fuel cycle often necessitates higher fuel enrichment [3]. In the commercial nuclear industry, concerns regarding nuclear weapon proliferation have historically imposed limitations on enrichment levels beyond 5% uranium-235 (^{235}U) [4]. While these restrictions are crucial for security, they also limit the ability of nuclear energy to achieve higher burnups and improve fuel cycle economics. As energy demand escalates and the requirement for efficient and sustainable energy sources intensifies, there is a growing demand in producing fuels with higher levels of enrichment.

Maintaining control over reactivity becomes challenging when enrichment levels exceed 5% by weight of ^{235}U. Critical design elements encompass reactivity control, the ability to safely shut down during extended cycle durations and fulfilling high burnup requirements in terms of thermomechanical behaviour. To address these challenges, the novel approaches of burnable absorber (BA) designs that selectively absorb neutrons in high-power regions becomes necessary, enabling effective control of power peaks and providing smoother burnup. Therefore, maximizing their effectiveness in minimizing power peaking effects and ensuring safe and stable reactor operation is of utmost importance.

Extending the fuel cycle length in nuclear power generation undoubtedly poses significant challenges that require extensive research and development. It involves exploring innovative approaches to maximize nuclear fuel utilisation, and enhance reactor performance, without compromising the safety. Thorough investigation is indispensable to obtain a comprehensive understanding of the intricate dynamics associated with prolonging the fuel cycle. This knowledge will facilitate the development of novel solutions to enhance the efficiency, safety, and sustainability of nuclear power generation.

In situations where extending the nuclear power cycle is not feasible or preferable, an alternative approach is available that can still provide economic advantages while decreasing the amount of fissile material required to operate the nuclear power plant within the same cycle length. This approach involves the characterization and optimization of BAs. By implementing this approach, the economic efficiency of nuclear power generation can also be improved without the need to extend the fuel cycle.

1.1 Light Water Reactors

Light Water Reactors have been the cornerstone of electricity generation in over 20 countries for more than fifty years. The primary focus of LWR performance has been on its steady-state operation. Maximizing efficiency becomes a crucial consideration because LWRs typically operate continuously at full power except for scheduled maintenance outages [5].

LWRs dominate the global nuclear reactor fleet, accounting for more than 80 percent [6]. The two main types of LWRs that utilise light water as both the moderator and coolant are Pressurized Water Reactors (PWRs) and Boiling Water Reactors (BWRs). As of May 2023, PWRs constitute 74 percent of operational nuclear reactors, while BWRs make up 10 percent [7], as depicted in Figure 1. These reactors have been widely adopted due to their established technology and proven track record.

On the other hand, there is currently significant interest in Small Modular Reactors (SMRs) that offer the flexibility to respond to regional energy demands, improved safety and reduced initial investment costs compared to large NPPs [8]. SMRs are designed to be smaller in size and can be deployed in various locations, providing a more tailored approach to energy supply [9]. This adaptability makes them an attractive option for meeting the evolving energy needs of specific regions.

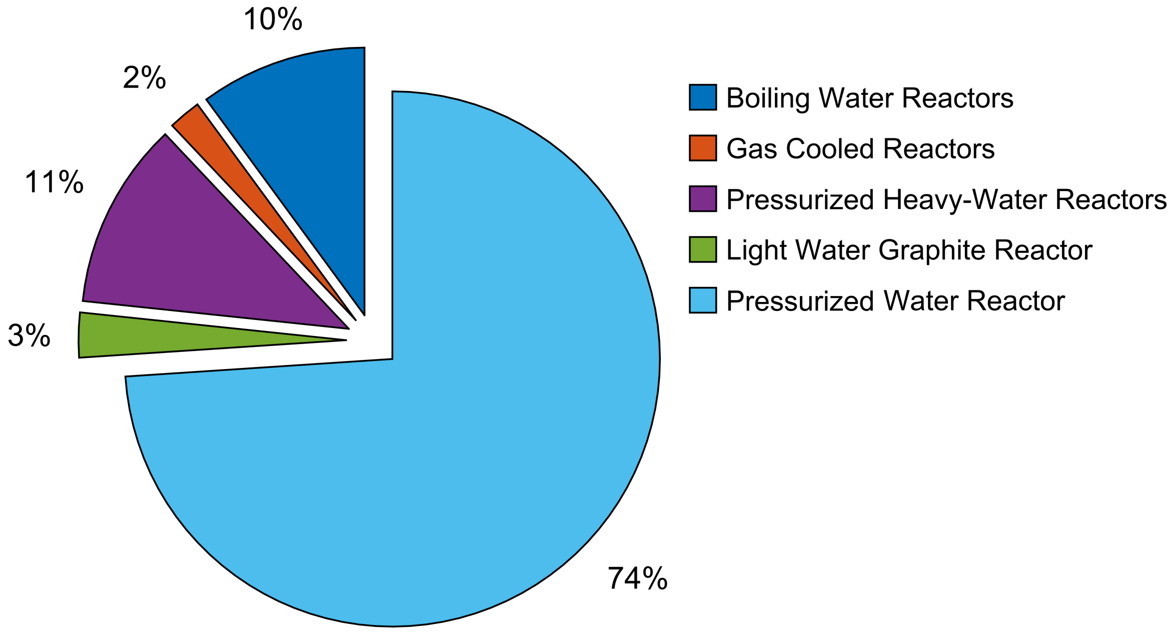

Figure 1 – Percentage of operational nuclear reactors. Adapted from [7].

1.1.1 Pressurized Water Reactors

PWRs are widely used globally and are considered a prominent nuclear reactor technology [10]. The concept and development of the PWR originated during the mid-20^{th} century, primarily driven by the desire to create a compact, high-energy reactor capable of powering naval vessels, particularly submarines [11].

As a type of nuclear power reactor, PWRs are designed to utilise uranium fuel [10]. Approximately 100 tonnes of uranium are contained within a commercial PWR, distributed across approximately 50,000 fuel rods and 18 million fuel pellets, depending on the specific design. The heat produced by the reactor is then employed to convert water into steam, which subsequently drives the turbine connected to an electricity generator. The crucial aspect of the PWR design is maintaining water at high-pressure used for cooling the reactor core, preventing it from reaching its boiling point [10].

The operational mechanism of a PWR features a two-loop system, as depicted in Figure 2 [12]. In the primary loop, the water is kept under high pressure (150 bar) and is heated by the reactor core to approximately 300°C, providing an efficiency of about 32% [12], [13]. Despite this high temperature, the water remains in a liquid state as it does not reach its boiling point. The thermal energy of the heated water is subsequently transferred to a secondary loop through a steam generator, which functions as a heat exchanger. Within this secondary loop, the water undergoes a transformation into steam, enabling its utilisation to drive the turbine and generate electricity [12].

In comparison to BWRs, PWRs possess a significant advantage: the water circulating within the reactor core is kept separate from the turbine system, which substantially reduces the risk of radioactive substances reaching the turbine and the surrounding environment [10].

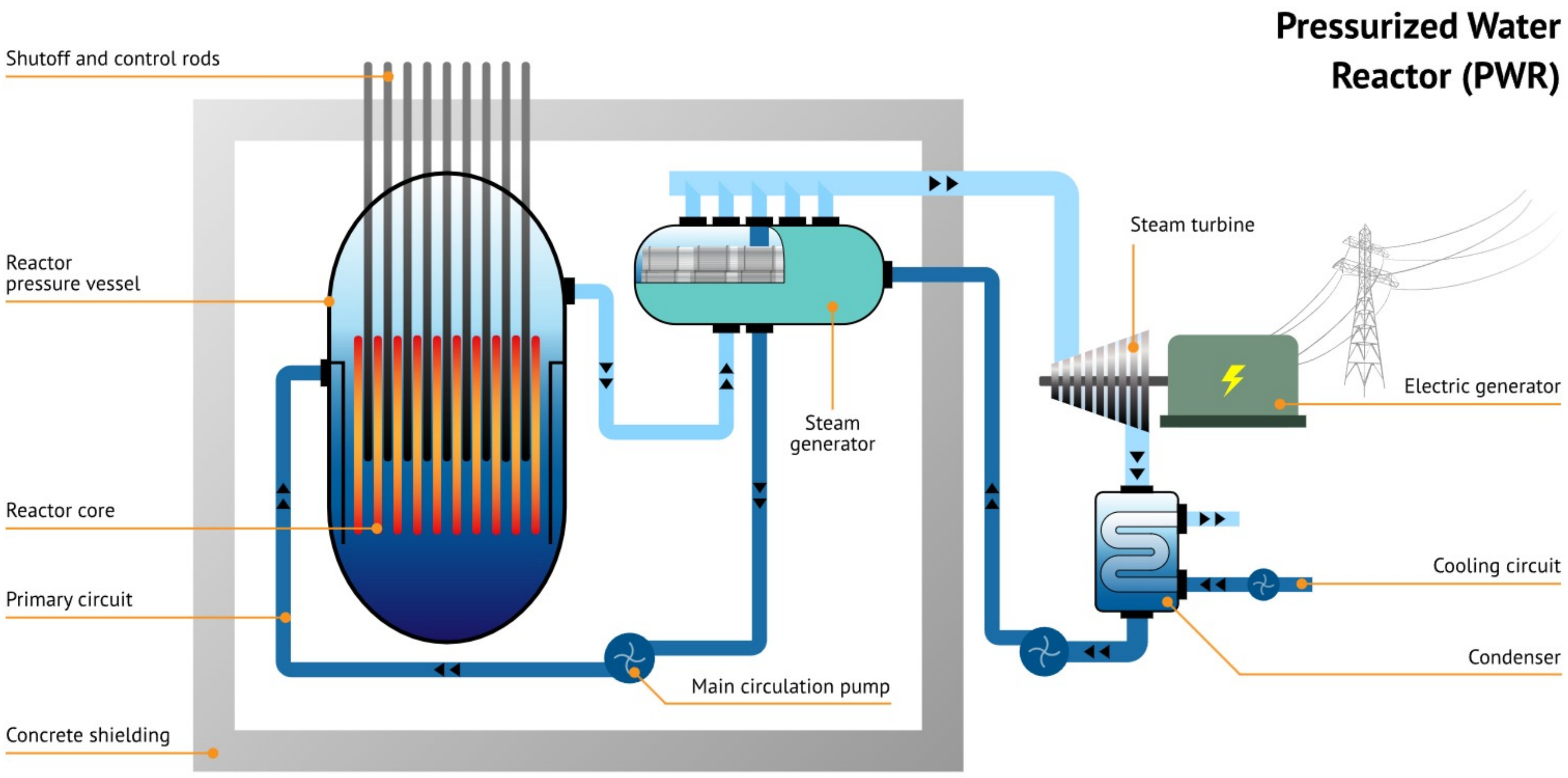

Figure 2 – PWR schematic [14].

1.1.2 Boiling Water Reactors

With a utilisation rate of 12% among all commercial LWRs, BWRs hold the second position after PWRs [7]. The development of BWRs took place in the late 1950s through collaboration between the Nuclear Energy Division of General Electric Company and Argonne National Laboratory [15].

BWRs offer a less complex yet equally powerful alternative to PWRs. Their operation involves steam formation within the core and direct steam transfer to the turbines [16], [17]. After passing through the turbines, the steam is cooled by the water in the second circuit and redirected back to the reactor core, maintaining a vapor pressure that is half of what PWRs operate at [18].

The schematic diagram of a typical BWR is presented in Figure 3. What sets BWRs apart is the core, where bulk boiling occurs, leading to a complex two-phase flow that may exhibit instability under specific conditions [15]. Ordinary water, isotopically un-enriched and known as light water, serves as both a coolant and a moderator in these reactors. Within the core, water is permitted to reach its boiling point at a pressure of 75 atmospheres, which raises the boiling point to 285°C. The resulting steam is then utilised directly to power a steam turbine. Afterward, the steam is condensed and reintroduced into the reactor core, completing the recycling process [16].

In BWRs, reactivity adjustments can be achieved through two methods: control rods and manipulation of the recirculation flow rate. Increasing the recirculation flow rate results in a higher proportion of liquid water to steam in the core, which enhances reactivity, reactor power, and steam production [19].

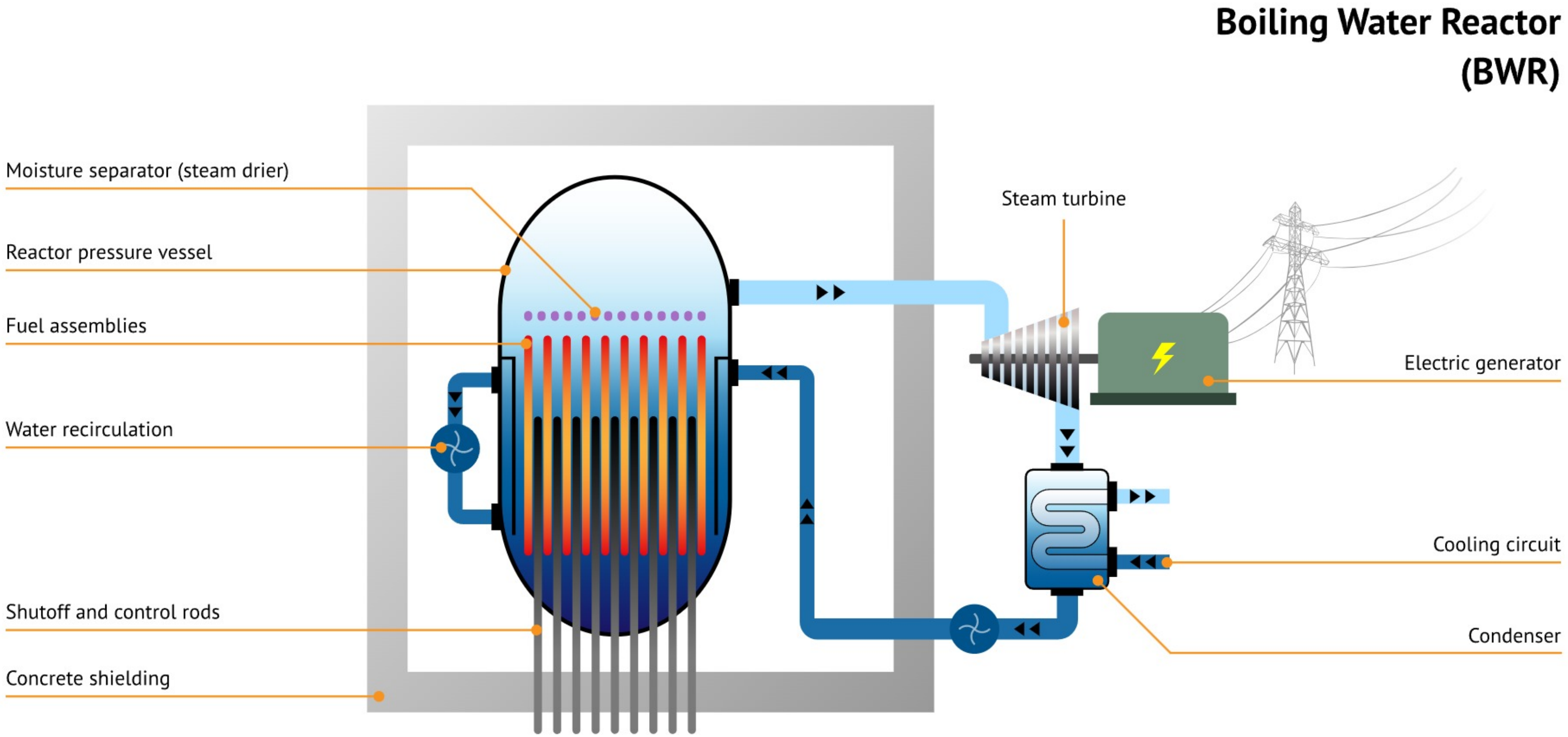

Figure 3 – BWR schematic [14].

Despite their simple design, BWRs possess intricate internal systems, offering an efficiency rate of approximately 33% [16]. In addition, BWRs typically have a lower power density, necessitating larger constructions for high power output [20].

1.1.3 Small Modular Reactors

The unique design and inherent benefits of Small Modular Reactors have contributed to their increasing popularity. SMRs are typically characterized as nuclear reactors with an output power not exceeding 300 MWe [21]. Their smaller power level, physical size, modular architecture, and improved safety and security features differentiate SMRs from conventional reactors [22]. A key feature of SMRs is their construction approach, involving prefabrication in a controlled factory environment, module by module, resulting in improved quality and efficiency [8].

Due to their smaller size, SMRs can be commissioned in locations that are not suitable for larger NPPs. This is primarily due to their smaller footprint, which allows for more flexibility in terms of siting options [23]. The compact design of SMRs enables the installation of multiple units on the same site, expanding their applicability to remote areas and specific purposes like mining or desalination. The option of locating the reactor unit underground or underwater further enhances their resilience against natural or human-induced hazards [21].

Enhanced safety is another significant advantage of SMRs [21], [23]. Utilising inherent safety features including low power and operating pressure, as well as passive safety systems, decreases the need for external force, human intervention, or external power for system shutdown. This minimizes the potential for hazardous releases of radioactivity, ensuring a safer environment for the general public [23].

The International Atomic Energy Agency (IAEA) promotes international collaboration in the design, development, and commissioning of SMRs. The potential of this technology is evident in the ongoing development of advanced projects such as NuScale, SMART, ACP100, and IRIS, which are examples of PWRs [24].

1.2 Nuclear Fuel Cycle

The entirety of the nuclear fuel cycle encompasses all the necessary steps and procedures that nuclear fuel must undergo before and after its utilisation in a nuclear power plant, with the ultimate goal of generating electricity [25]. A schematic of the nuclear fuel cycle can be seen in Figure 4. The "front end", which is a series of process that the fuel undergoes before being used in a NPP, includes the mining process as well as recovery, conversion, enrichment, and fabrication [26]. Following its use in a reactor, uranium is classified as "spent fuel" and may undergo additional phases such as temporary storage, reprocessing, and recycling, culminating in its eventual disposal as waste, thus constituting the "back end" of the fuel cycle [26].

Two distinct strategies are employed in this context, including the open (once-through) fuel cycle and the closed fuel cycle, which are determined by each country's political and economic approach to nuclear energy [27]. These strategies differ based upon the methods used to handle spent nuclear fuel, which is nuclear fuel that has been irradiated within a nuclear reactor. An open fuel cycle describes a method in which nuclear fuel is used only once and then discarded without recycling. A closed nuclear fuel cycle, on the other hand, features reprocessing spent fuel to recover valuable elements such as uranium and plutonium, which may then be recycled to create new fuel [27].

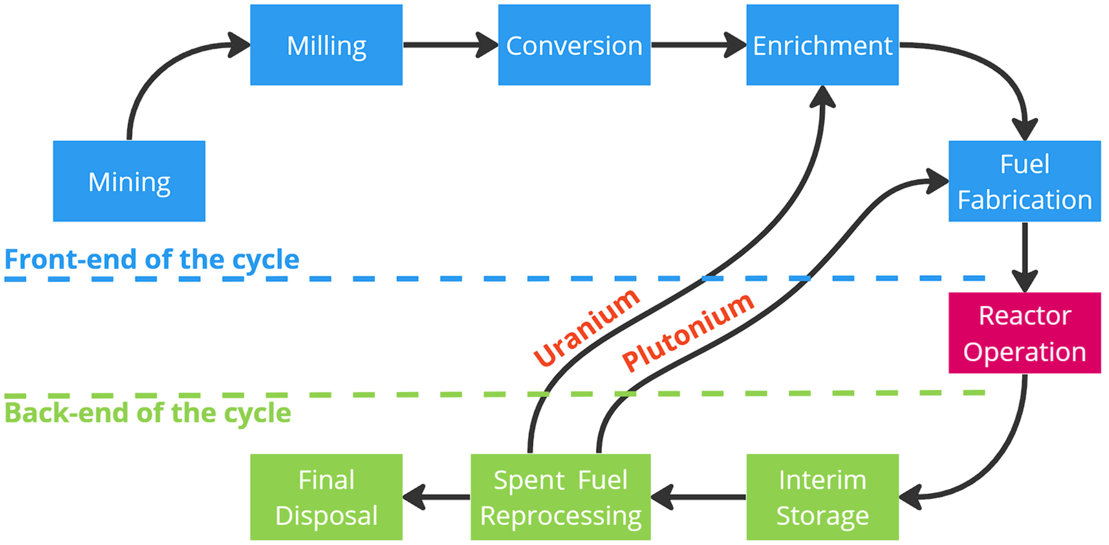

Figure 4 – Stages of the nuclear fuel cycle. Adapted from [28].

1.2.1 Front-end of the Nuclear Fuel Cycle

1.2.1.1 Mining and Milling

The nuclear fuel cycle comprises uranium mining and milling, which are intricate processes employing various techniques tailored to the specific characteristics of the ore deposit and economic considerations [29], [30]. Different extraction methods are employed, ranging from conventional approaches like open pit and underground mining to non-conventional techniques such as in-situ recovery, which depend heavily on the concentration of the ore body and geological factors [29]. The choice between surface (open pit) and underground mining is determined by the depth of the deposit, with the former typically used for shallow deposits and the latter for deeper ones [30].

Once the uranium ore is extracted, it undergoes refining at a nearby uranium mill, where it is transformed into uranium concentrate, commonly referred to as "yellowcake" [30]. The milling process involves crushing and grinding the ore into a fine powder, followed by the addition of chemicals that induce a reaction separating uranium from other minerals [31]. While this process yields a relatively small quantity of uranium concentrate compared to the amount of waste material generated, known as tailings, the tailings contain a higher concentration of radioactive and potentially toxic elements [29]. However, the radioactivity of the tailings diminishes more quickly compared to the original ore [30].

To ensure the safety of these processes, specific precautions are taken, such as implementing enhanced ventilation in underground mines to mitigate airborne radiation exposure [30]. Processed water from solution mining operations is returned to the groundwater reservoir, enabling the mining process to be repeated [31].

1.2.1.2 Conversion

The yellowcake cannot be directly used as fuel for a nuclear reactor, which necessitates further processing [30]. In order to accomplish this, the yellowcake is transported to a conversion facility where it undergoes transformation into uranium hexafluoride (UF_6) [26]. The conversion primarily caters to power plants that require enriched uranium as fuel, which constitutes the majority [32].

The conversion of yellowcake to UF_6 takes place due to the requirement of the uranium being in a gaseous state [30], [32]. UF_6 has the capability to become gaseous at relatively low temperatures. Within the conversion facility, the liquid UF_6 is poured into 14-ton cylinders while still in its liquid state. After approximately five days of cooling, these containers hold solidified UF_6, which is then ready to be transported to an enrichment plant for the subsequent phase in the nuclear fuel cycle [26], [30].

The UF_6 gas consists of three naturally occurring uranium isotopes: ^{234}U, ^{235}U, and ^{238}U. However, for the efficient operation of nuclear reactor designs, the concentration of the ^{235}U isotope needs to be increased. Consequently, the unaltered UF_6 gas, with its original isotopic concentration, is commonly referred to as natural UF_6 [31]. Once this stage is completed, the UF_6 product is enriched and then reconverted to produce enriched uranium oxide, which represents a crucial step in the nuclear fuel cycle [30].

1.2.1.3 Enrichment

Natural uranium is primarily composed of two isotopes, with ^{238}U accounting for 99.3% and ^{235}U making up only 0.7% [32]. Most reactor types require a higher concentration of ^{235}U, ranging from 3% to 5%, in order to facilitate the fission process and generate heat energy [31]. Thus, the enrichment process plays a crucial role in increasing the ratio of the fissile isotope ^{235}U in uranium, ultimately yielding suitable fuel for nuclear reactors.

Previously, uranium enrichment relied on gas diffusion technology; however, in recent years, this method has been replaced by gas centrifuge technology, which requires less energy [30]. During gas centrifugation, the feed, which is a UF_6 gas, is introduced into a rotating centrifuge. As a result of the centrifugal force induced by the high-speed rotation, the heavier ^{238}U atoms accumulate towards the outer edge of the centrifuge, while the lighter ^{235}U atoms gather toward the centre [26], [29]. This process is repeated multiple times which increases the isotopic composition of ^{235}U from 0.71% to the desired level [29].

The enrichment process yields enriched UF_6 as its final product [30]. The energy requirements of the process increase with greater disparity between the isotopic compositions of ^{235}U in the product and the tails. The necessary energy to enrich a specific quantity of feed to a specific ratio is measured in terms of separative work units (SWUs) [29].

In addition to these conventional methods, novel enrichment technologies, including atomic vapor laser isotope separation and molecular laser isotope separation, are currently being developed. These laser-based enrichment processes have the potential to achieve higher initial enrichment factors and offer a faster alternative to conventional methods [31]. Regardless of the chosen technology, the end product of the enrichment process remains enriched uranium hexafluoride, which is subsequently converted into enriched uranium oxide [30].

1.2.1.4 Fabrication

Fuel fabrication entails the conversion of enriched uranium hexafluoride into fuel suitable for nuclear reactors, employing a series of processes. Enriched UF_6 is chemically treated, resulting in the formation of uranium dioxide (UO_2) powder [26]. The UO_2 powder is then shaped into small cylinders and exposed to high temperatures through a sintering procedure [32].

After the sintering processes, fuel pellets are placed into long metal tubes known as fuel cladding, typically composed of zirconium alloys [32]. The fuel cladding serves a dual purpose: it securely encloses the fuel pellets and acts as a barrier against any potential release of radioactive gases. The fuel assembly is then constructed by combining the fuel rods, which are formed by inserting numerous uranium fuel pellets into the fuel cladding. This carefully engineered fuel assembly facilitates effective heat transfer to the circulating cooling water during reactor operation [32].

1.2.2 Back-end of the Nuclear Fuel Cycle

1.2.2.1 Interim Storage

Interim storage plays a vital role in ensuring the secure storage and continuous monitoring of spent fuel within the nuclear fuel cycle [25]. To gradually reduce the activity and heat of the spent fuel, preparing it for final disposal, this step is crucial [26]. The location of interim storage facilities can either be on the reactor site or in a centralized facility situated away from the reactor site. While central facilities offer the advantage of consolidating containers, facilitating easy monitoring, the transportation of spent fuel to such a facility necessitates a separate procedure [25].

Two distinct methods exist for interim storage: dry and wet storage [25]. Dry storage has passive cooling systems and has reduced operating and maintenance costs. This method gained significant attention following the Fukushima Daiichi accident, which underscored the risks associated with coolant loss from pools [25]. In dry storage systems, spent fuel is placed within containers or barrels filled with inert gas. These containers can be positioned on a concrete pad that serves both as a storage platform and provides radiation shielding [33].

In wet storage, on the other hand, the fuel is immersed in a pool to enable cooling and provide radiation protection. This method is employed immediately after the fuel is extracted from the reactor due to its high temperature and radioactivity levels [26]. However, while water efficiently dissipates heat and shields against radiation, it also acts as a moderator, potentially leading to criticality [25].

1.2.2.2 Spent Fuel Reprocessing

The efficient utilisation of resources and the minimization of waste are achieved through the process known as reprocessing. Recyclable materials make up approximately 97% of spent fuel, making it a prime candidate for reprocessing. To harness its energy potential, a series of chemical processes are employed during the reprocessing of spent fuel [25]. These processes involve the stripping of fuel bundles, the breakdown of fuel pellets, and the subsequent separation of uranium, plutonium, and fission products [26]. Following the separation of uranium and plutonium, they undergo a series of processes and are reintegrated into the fuel cycle, resulting in a reduction of waste [30].

Plutonium, when combined with uranium, can be used to produce mixed oxide fuel (MOX) for nuclear reactors [32]. On the other hand, uranium recovered through reprocessing undergoes conversion into UF_6 and undergoes enrichment before being reintegrated into the fuel cycle. This process helps decrease the need for additional enrichment and the production of depleted uranium [32].

Originally focused on military applications in the 1940s, reprocessing technology witnessed significant advancements with the development of the Plutonium Uranium Extraction (PUREX) process [25]. The commercial importance of reprocessing grew in the 1960s due to escalating uranium prices and the necessity to reduce reliance on natural uranium. Currently, several countries possess their own reprocessing plants, including France, the United Kingdom, India, and Russia [25].

It is also important to note that spent fuel policy is determined depending on military policies, geological conditions, political culture and civil society, and technological culture [34]. For the management of nuclear waste, Canada, Finland, Hungary, Spain, USA, and UK have chosen the direct disposal and retrievability method, while China, France, India, Japan and Russia apply reprocessing. Additionally, Belgium and the Netherlands export their nuclear waste to France, while Bulgaria exports its waste to Russia [34].

1.2.2.3 Final Disposal

The final stage of the nuclear fuel cycle involves the ultimate disposal of both spent fuel and high-level waste (HLW) generated from reprocessing, regardless of the volume, quality, and reduction of radiotoxicity [25]. Deep geological repositories (DGR), for example, have gained international recognition as a suitable solution for the storage of nuclear waste [25].

Currently, the prevailing approach for managing most radioactive waste is deep geological disposal, which incorporates a "multi-barrier" concept combining natural and engineered barriers to prevent the migration of radionuclides to the environment and human exposure. This consensus has been embraced by numerous countries worldwide, including the USA, UK, France, and Finland [30].

1.3 Burnable Absorbers

The importance of burnable absorbers (BAs) is significant since they play an essential role in controlling reactivity across extended fuel cycles, especially at the beginning of the fuel's life. By controlling excessive reactivity during reactor operation, BAs promote a more gradual depletion of fuel, minimising the need for frequent control rod adjustments [35]. Furthermore, it has been demonstrated that some types of BAs have the capacity to modify the neutron spectrum, resulting in less ^{235}U depletion and, as a result, enhanced breeding of fissile ^{239}Pu during reactor operation [36]. As the fuel nears the end of its life, the existence of more fissile ^{239}Pu atoms results in less rapidly decreasing reactivity [37].

The transmutation of isotopes with lower neutron cross-sections is facilitated effectively through the capturing of neutrons, leading to a more efficient use of fuel subsequently. The ideal burnable absorbers are characterized by leaving no residual absorption in the system after their depletion [38]. As neutrons are absorbed by burnable absorbers, they mitigate excessive initial reactivity at the beginning life of the fuel [38]. This absorption is considered crucial in reactor operations, particularly when new fuel assemblies replace old ones, guaranteeing that the reactor core's heat production is re-balanced [39].

Factors such as economics, thermal hydraulics, operating cycle duration, manufacturing, radiation damage response, and reprocessing/disposal all have an impact on the selection and optimisation of BAs [35], [40]. In modern LWRs, the implementation of burnable absorbers encompasses three distinct types: Integral Burnable Absorbers (IBAs), Integral Fuel Burnable Absorbers (IFBAs), and external burnable absorbers (WABA and Pyrex). The IBAs approach involves the mixing of neutron absorber material with UO_2 fuel during the fuel fabrication stage, with the specific percentage determined by the operational requirements of the reactor [41]. IFBAs, on the other hand, are obtained by coating a thin layer of neutron-absorbing material around the uranium fuel pellet [42]. Lastly, external burnable absorbers find their typical usage during the initial cycle of the reactor and are generally removed from the assemblies before the next cycle [43].

Certain materials, including boron, gadolinium, dysprosium, hafnium, and erbium, are either utilised or possess the potential to be utilised in the composition of burnable absorber materials, attributed to their superior neutron absorption capabilities [40].

1.3.1 Gadolinium Oxide and Enriched Gadolinium Oxide

Gadolinium oxide (Gd_2O_3) is frequently utilised as a burnable absorber due to the substantial neutron capture cross-section exhibited by gadolinium isotopes [36]. To extend suppression and exploit self-shielding effects, it is typically incorporated into the fuel composition of a limited number of fuel rods, with a percentage ranging from 0.10 wt.% to 14.00 wt.% [39], [41], [44].

The presence of Gd isotopes in the outer layers of the fuel pellet enables the capture of neutrons that are moderated by the cooling water. Consequently, the burnable absorber isotopes in the inner layers are depleted at a later stage, thereby ensuring a longer lifespan within the fuel composition [44]. Gd_2O_3 serves as a means to control the power peak in the assembly and in a PWR reduces the required boric acid concentration. Additionally, it does not have negative impact on fuel reprocessing [45], [46].

As the Gd isotopes are gradually depleted, the reactivity increases and ultimately reaches the level of reactivity observed in fuel without the presence of Gd isotopes when they are nearly completely depleted [47]. Following this, the reactivity follows a similar trend to fuel without burnable absorbers. However, the isotopes with low thermal neutron capture cross-sections contribute to reactivity suppression during the later stages of fuel life, known as residual reactivity penalty [48].

Natural Gd consists of seven stable isotopes, with ^{155}Gd (14.80 wt.%) and ^{157}Gd (15.65 wt.%) possessing the highest neutron absorption cross-sections, measuring 61,000 ± 500 barn and 254,000 ± 2000 barn (at 2200 m/s), respectively [48]. When ^{157}Gd captures a neutron that might have otherwise initiated a fission event, it transmutes into ^{158}Gd, which exhibits a significantly lower neutron cross-section and is effectively "burned" away. However, when ^{156}Gd (comprising approximately 20 wt.% of the natural abundance of Gd and resulting from the neutron capture of ^{155}Gd) absorbs a neutron, it produces ^{157}Gd, which acts as an efficient absorber. This production of neutron-absorbing isotopes reduces the burnout efficiency of the burnable absorber, leading to residual reactivity suppression at the end life of the fuel [49].

The presence of Gd_2O_3 in the fuel composition results in a reactivity trend similar to fuel without burnable absorbers. However, the isotopes with low thermal neutron capture cross-sections contribute to reduced reactivity at the later stages of fuel life and an increase in Gd_2O_3 content in the fuel composition leads to an increase in residual reactivity penalty. Moreover, the thermal conductivity of the fuel gradually decreases as the gadolinium content in the fuel composition increases [50], thus reducing the thermo-mechanical performance.

The negative effect described above can be mitigated by enriching Gd_2O_3 with ^{157}Gd, the most efficient neutron-absorbing Gd isotope [38]. This enrichment process allows for a reduction in the amount of Gd_2O_3 required in the fuel pellets, thereby minimizing the negative impact on pellet thermal conductivity [51], [52] and potentially eliminating the penalties traditionally imposed on the thermo-mechanical operating limit for Gd fuel rods. Moreover, it reduces the displacement of uranium oxide (UO_2) in the fuel matrix, resulting in higher UO_2 loading in the assembly [53].

While Santala et al. (1997) proposed that enrichment with ^{157}Gd could be achieved using conventional techniques [38], Renier and Grossbeck (2001) argued that the high cost of these techniques, amounting to up to $1000 per gram of ^{157}Gd, would surpass the cost of the fuel itself [54]. However, they suggested that this cost could be reduced by utilising new techniques such as the plasma separation process (PSP). Subsequently, Yilmaz (2005) concluded that the cost of enriching ^{157}Gd using PSP was less than $10 per gram/^{157}Gd [53].

Bejmer and Seveborn (2004) conducted an in-reactor performance evaluation utilising Gd_2O_3 enriched with 70 wt.% ^{157}Gd in the fuel composition. They argued that enriched Gd_2O_3 in the reactor core functions as a more effective burnable absorber compared to natural Gd_2O_3. By keeping the uranium enrichment constant, more fissile isotopes can be loaded, leading to the prolongation of EFPDs through the elimination of residual reactivity, as well as improvements in thermal conductivity [55].

The neutronic performance of the PWR Angra-2 reactor fuel assembly was examined by Campolina et al. (2018). The low BA loading provided by enriched Gd_2O_3 was found to bestow fuel cycle cost benefits, enabling prolonged cycle operation. It was estimated that the economic advantage of generating additional energy during an extended cycle amounted to \$4 million, suggesting potential savings with a Gd enrichment cost below \$371/g [56].

The effective utilisation of enriched Gd_2O_3 in AP-1000 fuel assemblies was studied by Khoshahval (2022). The various neutronic parameters of the AP-1000 fuel assembly, such as k_{inf}, peak pin power, and reactivity swing were examined at different burnups. It was observed by the author that the reactivity change in cases involving enriched ^{155}Gd was smoother compared to those involving enriched ^{157}Gd. Based on the findings, it was concluded that enriched Gd_2O_3, containing enriched ^{155}Gd and/or ^{157}Gd, surpassed natural gadolinium as a burnable poison in terms of reactivity swing and residual binding, without negatively affecting power peaking [57].

Dalle et al. (2013) investigated the effects of different burnable absorber levels using Gd_2O_3 enriched with ^{155}Gd. They stated that enriched Gd_2O_3 enriched with ^{155}Gd enables the attainment of more stable reactivity in long cycles compared to natural Gd_2O_3. Furthermore, positive improvements in thermal conductivity can be achieved by reducing the percentage of Gd_2O_3 in the fuel composition [51].

Yilmaz et al. (2006) examined the effects of using enriched Gd_2O_3 on fuel performance. They observed that the utilisation of enriched Gd_2O_3 reduces the burnable absorber concentration in the fuel composition, consequently reducing the displacement of UO_2. This approach allows for the achievement of reactivity behaviour similar to that of fuel containing natural Gd_2O_3, but with lower uranium enrichment than when natural Gd_2O_3 is employed as the burnable absorber [58].

1.3.2 Zirconium Diboride and Uranium Diboride

Boron is another widely used neutron absorber material in nuclear reactors. The composition of natural boron consists of two isotopes, namely ^{10}B (19.9 wt.%) and ^{11}B (80.1 wt.%) [59]. When a reactor operates, neutrons are captured by the ^{10}B isotope . As a consequence of this neutron capture, a transformation occurs in which ^{10}B converts into a combination of ^{7}Li and ^{4}He [60], as illustrated in Equation 1.

$$ {}^{10}_{5}\mathrm{B} + {}^{1}_{0}\mathrm{n} \rightarrow {}^{7}_{3}\mathrm{Li} + {}^{4}_{2}\mathrm{He} + \gamma \tag{1} $$

Zirconium diboride (ZrB_2) is extensively utilised as a BA in NPPs with its high melting point, favourable neutron absorption properties, and excellent thermal conductivity [61] [62]. Not causing a residual reactivity penalty makes it practically an ideal burnable absorber [63]. ZrB_2 is commonly employed as the form of IFBA, a thin coating on the surface of pellets [42]. The loading of IFBAs within a fuel assembly can be arranged in various patterns based on the specific operational requirements [64].

However, in IFBA usage scenarios, the thickness of the ZrB_2 coating can only be increased within certain limitations, and even at the maximum BA ratio in the reactor core, the self-shielding effect remains limited due to relatively rapid depletion of ^{10}B isotopes [54]. As a result, the outer layer of the pellet undergoes substantially earlier burnup than the centre leading to rather rapid consumption of the IFBA coating. Additionally, a peak in reactivity occurs quite early in the fuel's lifetime, limiting the fuel's maximum ^{235}U enrichment [65]. These drawbacks that IFBAs have make them unsuitable for cycles longer than 24-months [64], [66], [67].

On the other hand, the feasibility of UB_2 as a candidate for a burnable absorber has been under intensive scrutiny, considering its characteristics encompassing a high thermal conductivity and a superior melting point due to its intermetallic structure, which sets it apart from UO_2 [68]. The density of UB_2 exceeds that of UO_2, enabling a higher loading of fissile isotopes into the reactor core. The peculiarity of UB_2 was observed to suppress the reactivity at the beginning of the fuel's life and promote increased reactivity towards the end of fuel's life. Furthermore, compared to uranium dioxide, UB_2 exhibits a higher uranium density, with values of 9.67 g/cm^3 and 11.68 g/cm^3, respectively [65]. Fuel-cycle economics can be enhanced through the utilisation of UB_2 as it enables the attainment of extended fuel cycles due to the prolonged survival of ^{10}B atoms [69].

The presence of uranium in UB_2 leads to an increased uranium concentration within the pellet after reactivity suppression, thereby amplifying the fuel's performance during the later stages of the fuel cycle, when UB_2 is employed as BA [65]. During the consumption of boron or uranium from UB_2 through neutron absorption and fission, uranium serves as a shielding agent for boron, and vice versa. Furthermore, the generation of fission products resulting from reactions involving both uranium and boron has the potential to contribute to the stability of the structure [65]. Therefore, UB_2's distinctive features establish it as a potential burnable absorber for achieving high burnup.

1.4 Economic Considerations

Across the globe, there is an observed increase in energy demand as each day goes by [70]. This surge is influenced by a multitude of factors, ranging from the expansion of industries and growing populations to the escalating use of digital technologies. As the planet becomes more populated, industries continue to grow, and digitalization permeates every aspect of society, the hunger for energy consistently grows.

In view of this, the significance of energy production costs is increasingly emphasized. It is widely acknowledged that high production costs can result in escalated prices for both consumers and businesses. Consequently, this could impede economic growth and potentially exacerbate social disparities. As a result, efforts are frequently made to seek measures aimed at reducing the cost of energy production, with the goal of maintaining equilibrium in the global economy.

Among the array of energy sources available, nuclear power assumes a unique role. While historically regarded as an expensive option due to substantial upfront costs and stringent regulatory requirements, it is also acknowledged for its efficient large-scale energy production capabilities [71]. This efficiency has the potential to offset long-term operational expenses.

Figure 5 depicts the cost structure of nuclear power generation, highlighting many different factors that impact overall expenditures. The cost structure of nuclear power generating is influenced by factors such as the front-end and back-end of the fuel cycle stages, operation and maintenance operations, decommissioning procedures, and total investment.

Fuel costs account for 16% of total costs at both the front and rear ends of the cycle. Front-end fuel expenses, that constitute for 12% of total expenditures, reflect the procedures involved in preparing fuel, such as uranium mining, milling, conversion, enrichment, and fuel fabrication [72]. Back-end fuel expenses, which account for 4% of total expenditures, include spent fuel management, such as interim storage, reprocessing, depending on the fuel cycle strategy of the specific country, and final disposal [73]. In addition, the operation and maintenance costs represent a quarter of the total cost, signifying the ongoing expenses required to run and maintain the nuclear facility. These costs include everything from the salaries of staff and replacement of equipment, routine maintenance, and emergency repairs [71].

The majority of the cost, 59%, is included in the total investment cost. This cost covers the initial capital expenditure, including the planning, design, and construction of the plant, in addition to licensing and regulating costs [71]. On the other hand, the decommissioning of the facility is given a negligible part of the entire cost, constituting 0.3% of total expenditures. The cost includes the process of safely completing and conducting the necessary decommissioning and decontamination activities of a nuclear power facility after its operational lifespan has expired [74].

Figure 6 displays a graph depicting the monthly electricity production by fuel data from OECD countries between December 2021 and December 2022. Upon examining the graph, valuable insights into the energy demand patterns throughout the year can be gleaned. It is evident that energy production, which aligns with the energy demand, is significantly higher during the mid-winter and mid-summer seasons compared to other months. Furthermore, the proportion of nuclear energy in relation to the total energy generated fluctuates between approximately 14% and 16% during the year.

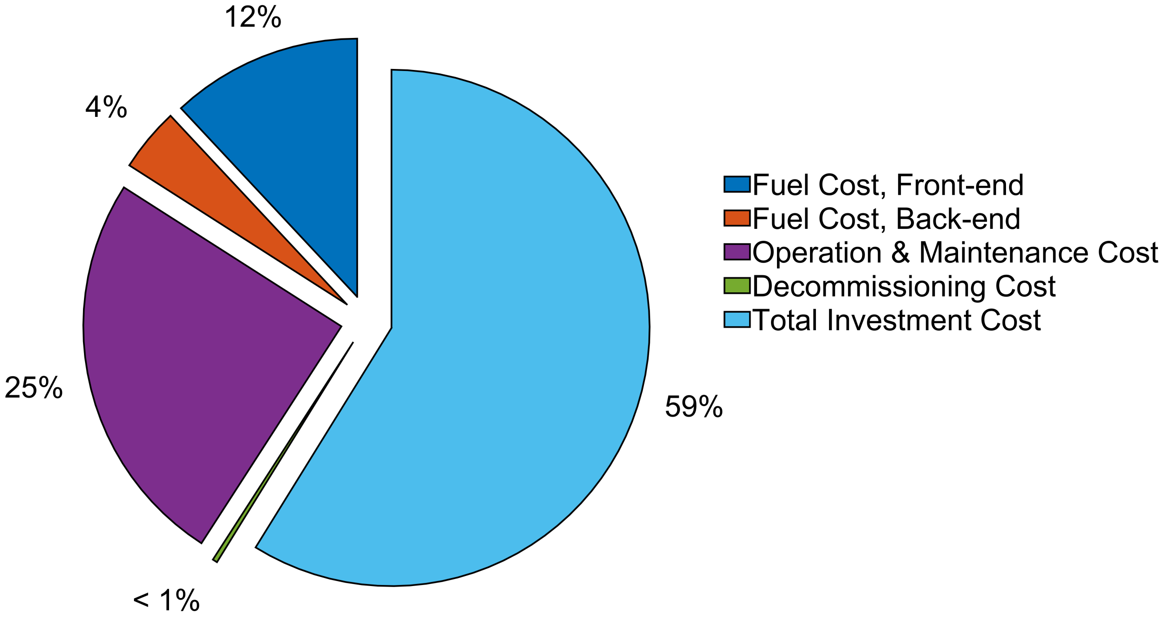

Figure 5 – The breakdown of costs in nuclear power generation. Adapted from [73].

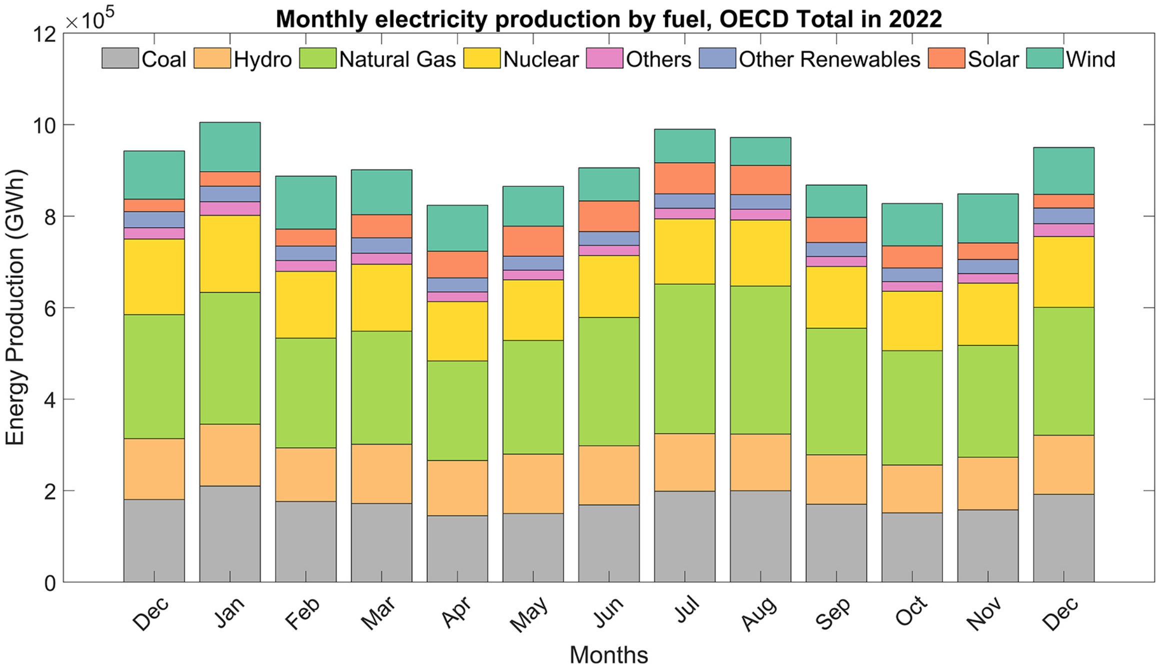

Figure 6 – Monthly electricity production by fuel, OECD total in 2022. Adapted from [70].

The capacity factor, on the other hand, is an important metric that influences the economics of nuclear power generation. It is defined as the ratio of the amount of generated electricity to the highest potential electricity production that a power plant can produce within a time period at full power [75]. Rothwell et al. (1995) demonstrated the impact of refueling frequency on a nuclear power plant's capacity factor and overall electricity production. In their study, it was observed that with annual refuelings lasting for 2 months, the maximum capacity factor of the plant, assuming no forced outages, reached 83.5%. However, by extending the refueling interval to 24 months, the maximum capacity factor improved to 91.8% [76]. As evident from the findings, reducing the number of refuelings increases the total amount of electricity generated by the reactor over its lifespan. This outcome brings substantial economic benefits to the province, as highlighted.

According to Kovac (2016), the refueling time of a nuclear power plant is approximately 45 days, regardless of whether the fuel cycle length is 12-months or 18-months. The duration of the fuel cycle directly affects the total number of days the plant remains closed, with a longer fuel cycle resulting in an extended operation time for the power plant. Over a period of three years, a nuclear power plant with a 12-month fuel cycle undergoes two refueling outages, leading to an average closure period of 90 days. In contrast, a power plant with an 18-month fuel cycle length requires refueling only once, resulting in an average closure period of 45 days during the same period. Additionally, the 18-month fuel cycle offers advantages such as increased energy production and lower maintenance costs, while also presenting disadvantages such as higher fuel and interim storage costs. However, the economic benefits brought about by the 18-month fuel cycle far exceed those extra costs [77]. It should also be noted that the US Energy Information Administration (2022) reported that the average duration of refueling outages in 2021 was 32 days as of October 2021 in USA [78].

Extending outages beyond their planned duration is considered undesirable. A solid balance exists between security and cost in the planning of nuclear power plants. While regular and extensive maintenance and refueling operations improve safety, they also increase total expenses. This circumstance results in increased costs due to the disruption, greater need for personnel, and increased production of radioactive waste [79]. For example, in a 1,000-megawatt reactor, each additional day can cost around $1 million [79], [80].

Secker et al. (2017) investigated the economic implications of different fuel cycle lengths using the PHOENIX-P code for a PWR plant. The study considered a fixed refueling time of 15 days and investigated fuel cycles lasting 12, 18, and 24-months. During a six-year period, it was found that the cost of fuel for the 18-month cycle was $24.2 million higher compared to the cost of the 12-month fuel cycle. However, the 18-month cycle was projected to generate 1.5 percent more electricity than the 12-month cycle. Furthermore, the 24-month fuel cycle incurred an additional cost of $30.6 million compared to the 18-month cycle, while producing 0.7 percent more electricity than the 18-month cycle. The researchers emphasized that the optimal length of the fuel cycle depends on the profitability of the additional energy to be generated [81].

Youinou and Sen (2014) conducted a study to increase the fuel cycle length from 18-months to 24-months. In their research, they concluded that extending the fuel cycle duration from 18-months to 24-months would yield an additional profit of $5 million per year [82].

Handwerk (1998) conducted a study on a PWR reload core, with the objective of achieving a cycle length of 38.8 and 44.6 calendar months. The study assumed an operating capacity factor of 87% with a single-batch configuration. It was concluded that compliance with both physics and fuel performance design limits could be ensured by enriching the fuel to 7.00 wt.% ^{235}U. However, they indicated that the design necessitates control rods with higher worth in order to meet the shutdown safety requirements [75].

An investigation into the economic feasibility of prolonging the duration of the cycle in currently operating PWRs was conducted by Delgado et al. (1999). They presented a core design for reloading that successfully met the essential physics and fuel performance criteria for a 36-month cycle with 6.50 wt.% ^{235}U enriched fuel, incorporating Gd_2O_3 as the BA. They concluded that depending on operational and economic conditions, the 36-month core demonstrated potential as a competitive alternative to the 18-month reference core in the future [83].

1.5 High-Assay Low-Enriched Uranium

The use of an enriched fuel beyond the 5.00 wt.% ^{235}U enrichment level is the key to meeting the overall demand for long fuel cycles [84]. By increasing the enrichment level to the range of 6-7 wt.%, the energy delivery time of the fuel in the reactor can be significantly improved, thereby extending the cycle time. Additionally, this expansion of enrichment limits allows for a more flexible core design and a more efficient utilisation of resources [85].

The High Assay Low Enriched Uranium (HALEU) application is the enrichment approach under consideration. HALEU is characterized by having a fuel mass in which the fissile isotope ^{235}U constitutes 5 to 20 percent. Through the use of HALEU fuels, a reactor can achieve higher burnup levels and generate a greater amount of energy from a given fuel quantity [2].

In the pursuit of developing new fuel designs, HALEU has emerged as a pivotal resource [86]. This derivative of uranium can serve as a starting material for the creation of various innovative fuel designs, including uranium alloys, ceramic pellets, and even liquid fuels. Each of these fuels, when deployed, holds the potential to facilitate demonstrations of advanced reactor and microreactor operations. Furthermore, the inherent properties of HALEU suggest the possibility of transitioning the currently operating light-water reactors to HALEU-based uranium oxide fuels. Such a transition could lead to longer operating cycles and improved economic viability for power plants, directly addressing the utilities sector's demand for efficiency and power [86].

1.6 Aims and Objectives

The aims and objectives of the thesis are outlined as follows.

- Analyse impacts on reactivity of the use of enriched gadolinium oxide (e-Gd_2O_3) in comparison to natural gadolinium oxide (n-Gd_2O_3).
- Analyse the effect of e-Gd_2O_3 on peak factor parameters, reactivity feedback parameters and shutdown margin.
- Compare the economic implications of transition from n-Gd_2O_3 to e-Gd_2O_3.
- Assess the impact of ZrB_2 and UB_2 Discrete Burnable Absorber Pins (DBAPs) and Moderated Discrete Burnable Absorber Pins (MDBAPs) on the reactivity.
- Investigate the transition from an 18-month fuel cycle utilising IFBA to a 36-month fuel cycle using HALEU fuel and ZrB_2 and UB_2 MDBAPs.
- Analyse the effect of HALEU with MDBAPs on peak factor parameters, reactivity feedback parameters and shutdown margin.

- Assess the possible economic benefits of extending the cycle length from 18-months to 36-months.

1.7 Thesis Structure

- Chapter 2 provides an overview of the Fundamental Measures of Performance, including peak factor parameters and reactivity feedback parameters, and introduces the reactor performance codes Serpent and CASMO/SIMULATE, which are used in the study.
- Chapter 3 explores the potential of e-Gd_2O_3 in nuclear fuel compositions through 2D neutronic analysis, comparing reactivity properties with n-Gd_2O_3 and examining depletion and ^{239}Pu breeding behaviour, ultimately paving the way for 3D fuel cycle analysis.
- Chapter 4 focuses on fuel cycle analysis of e-Gd_2O_3 and n-Gd_2O_3 over an 18-month cycle, examining their impact on peaking factors, reactivity feedback parameters, relative power distribution, and fuel loading cost, in the context of transitioning from n-Gd_2O_3 to e-Gd_2O_3.
- Chapter 5 investigates promising BA designs such as DBAPs and MDBAPs with ZrB_2 or UB_2 through a neutronic analysis to evaluate their reactivity behaviours, ^{239}Pu breeding, and ^{10}B depletion.
- Chapter 6 focuses on the possibility of transitioning from an 18-month fuel cycle using IFBA as BA to a 36-month fuel cycle with HALEU fuel, testing ZrB_2 and UB_2 DBAPs and MDBAPs as BA, investigating changes in peaking factors, reactivity feedback parameters, and analysing power distribution.
- Chapter 7 presents a summary and conclusions of the research findings, as well as suggestions for future work.

Chapter 2

Methodology: Reactor Performance Codes and Fundamental Measures of Performance

2.1 Reactor Performance Codes

2.1.1 Serpent 2: Monte Carlo Reactor Physics Code

The Serpent code has been developed to simulate the continuous transmission of neutrons and photons in three dimensions [87]. Since 2004, the VTT Technical Research Centre in Finland has been working on its development, catering to various applications involving particle management. Over time, Serpent has undergone significant improvements from its initial focus on reactor physics, expanding its capabilities to encompass a wider range of simulations. By employing a comprehensive physics model, the code enables the simulation of interactions between neutrons, photons, and their combined effects [87].

One major challenge in Serpent lies in the computationally intensive nature of the Monte Carlo approach [87]. Consequently, the code highlights the significance of parallel computing in solving this predicament. Within Serpent, the behaviour of neutrons during interactions is controlled by classical collision kinematics and Evaluated Nuclear Data File (ENDF) reaction rules [88].

An exceptional feature of Serpent involves the utilisation of continuous energy interaction data derived from analysed nuclear data files which minimizes the need for guesswork by ensuring that models incorporate the most precise neutron interaction data available [87]. Moreover, Serpent can be utilised without restrictions imposed by application-specific reactor technologies, as it imposes no limitations.

Furthermore, the algorithm possesses an inherent capability for conducting burnup calculations, enabling the tracking of how radioactive decay influences the concentrations of nuclides and neutron interactions [88]. This approach to burnup computations is applicable to both nuclear fuel and activated materials.

To enhance user convenience, Serpent automates processes that require minimal user input, such as dividing the depletion zone and creating transformation and decay routes. This simplified method streamlines the simulation process, making the Serpent a flexible and user-friendly tool [87].

2.1.2 Studsvik's CASMO-4/SIMULATE-3 Advanced Nuclear Design Code Package

CASMO-4 was created by Studsvik Scandpower Inc with the aim of carrying out burnup calculations for assemblies, primarily focusing on BWRs and PWRs, as well as pin cells [89]. The code has been designed to employ two-dimensional transport theory and handle diverse geometric layouts. These layouts encompass cylindrical fuel rods with varying compositions, organized in a square pitch array. CASMO-4 has integrated specific functionalities to accommodate a wide range of fuel rod configurations, which include gadolinium, erbium, IFBA, and other elements. Additionally, despite not having a sensitivity analysis feature, the program's capabilities extend to conducting computations for reflectors/baffles and performing fundamental calculations for fuel storage racks [89].

The distinct characteristics and capabilities of CASMO-4 are evident in its ability to deliver precise and efficient calculations [89]. The program employs the Method of Characteristics to provide a solution for two-dimensional transport, accommodating various energy group structures. In addition, the university release of the CASMO-4 houses the ENDF/B-VI nuclear data library without individual capture and scattering reactions which are instead combined into total scattering and capture reactions [90].

Notably, CASMO-4 possesses the capability to manage non-symmetric fuel bundles while leveraging the symmetry of most bundles to streamline computations. It takes into account thermal expansion and calculates effective resonance cross-sections individually for each fuel pin. A unique aspect of CASMO-4 lies in its approach to depletion calculation, utilising a predictor-corrector method that minimizes the number of burnup steps, particularly advantageous when burnable poison rods are present. Moreover, CASMO-4 generates two-group cross-section data crucial for 3D fuel cycle analysis in SIMULATE-3 [89].

On the other hand, SIMULATE-3 is an advanced 3D two-group reactor analysis code extensively utilised for conducting transient analyses in PWRs and BWRs [91]. Relying on the QPANDA neutronics model, it applies fourth-order polynomial representations to characterise the intranodal flux patterns. Although not having the capability for sensitivity analysis, its exceptional precision enables critical calculations pertaining to neutronic and thermal-hydraulic analyses, ensuring accuracy that meets licensing standards. The code is specifically designed to solve transient three-dimensional, two-group neutron diffusion equations. Moreover, it incorporates a six-group model to account for delayed neutron precursors. SIMULATE-3 encompasses a wide array of features, including reload shuffling, which involves reintroducing previously discharged fuel, the computation of reactivity coefficients and rod worths [91].

2.2 Fundamental Measures of Performance

The critical aspect of reactor performance and safety in nuclear power is influenced by the behaviour of nuclear fuels. Through the analysis of nuclear fuel performance, the strengths and limitations of the fuels are identified, leading to the development of advanced fuel designs and reactor concepts. In order to comprehensively evaluate the performance of nuclear power plants, various crucial indicators have been established as fundamental measures. These measures, such as neutron multiplication factor, nuclear enthalpy rise hot channel factor, the heat flux hot channel factor, critical boron concentration, moderator temperature coefficient etc., provide valuable insights into different aspects of fuel behaviour and reactor operation, allowing for a comprehensive assessment of nuclear power plants.

The neutron multiplication factor (k) is defined as the average quantity of neutrons resulting from one fission event that lead to subsequent fission events [92]. Since a self-sustained fission chain reaction in a nuclear reactor requires the system to be critical, each fission event must precisely trigger another fission event. In this context, K-infinity (k_{inf}) is specifically described as the ratio between the number of neutrons generated through fission in the present generation and the number that got absorbed in the preceding generation, considering an infinite system where no loss is caused by leakage [93]. Conversely, K-effective (k_{eff}) represents the ratio of neutrons generated through fission in the present generation to the total number that was lost in the previous generation as a result of absorption and leakage [92].

Moving on to operational parameters in the thermal-hydraulic analysis of nuclear reactors, the nuclear enthalpy rise hot channel factor ($F_{\Delta H}$) plays a crucial role. It is the ratio of the average rod power throughout the core to the maximum axially integrated power of a single fuel rod [94]. Maintaining $F_{\Delta H}$ within its designated boundaries is important to prevent the possibility of a departure from nucleate boiling (DNB), which can be triggered by accidents such as a loss of reactor coolant flow, a loss of normal feed water flow, or an unintentional opening of a pressurizer relief valve [95].

Similarly, the heat flux hot channel factor (F_Q) is another significant parameter that ensures the integrity and safety of the nuclear power plant under normal operating conditions and potential accident scenarios [96]. It is defined as the ratio of the maximum local fuel rod linear power density to the average fuel rod linear power density of the core [95].

Next, the boron coefficient (BC) depicts the impact of alterations in the boron concentration on the reactivity of the reactor [97]. A related concept is the critical boron concentration (CBC), which represents the amount of boron required to reach a critical state within a nuclear reactor. CBC implies that it is the specific boron concentration which attains an ideal equilibrium in fission processes [95]. The presence of boron in the primary coolant efficiently controls long-term reactivity fluctuations because of its homogeneous distribution in the core [98].

Another important coefficient is the moderator temperature coefficient (MTC), which refers to the change in reactivity caused by a one-degree change in moderator temperature [99]. The MTC is desired to remain within the design parameters since it might become undesirable in circumstances including reactor shutdown and anticipated drops in coolant temperature transients. These situations can result in steam generator tube failure because the core can become more reactive as the temperature decreases, caused by an increase in the density of the coolant [95].

In addition, the uniform Doppler coefficient (UDC) represents the reactivity change resulting from a uniform alteration in the fuel temperatures, divided by the corresponding change in the average fuel temperature [94]. Another coefficient, the isothermal temperature coefficient (ITC), refers to the alteration in reactivity caused by a one-degree change in both fuel and moderator temperatures [95].

Lastly, the shutdown margin is the amount of reactivity that enables the reactor to be subcritical or to turn subcritical from its present state. It ensures the subcritical condition and safeguards against variations or uncertainties related to the reactor's reactivity caused by parameters including temperature, pressure, or fuel composition [100]. The shutdown margin calculation can be executed by utilising Equation 2 [94].

$$SDM = \Delta k_1 + 0.9(\Delta k_2 - \Delta k_3) \tag{2}$$

In this equation, the symbol Δk_1 represents the differences in reactivity values between hot full power (HFP) and hot zero power (HZP). Similarly, Δk_2 denotes the difference in reactivity values between HFP and the condition where all control rods are inserted (ARI). Lastly, Δk_3 represents the differences in reactivity values between ARI and the hypothetical case where the most efficient control rod is non-operational.

Chapter 3

Neutronic Analysis of Enriched Gadolinium Oxide

A research paper titled "Performance and economic assessment of enriched gadolinia burnable absorbers" was published in Progress in Nuclear Energy using the methodology and a portion of the data presented in this chapter [101].

3.1 Chapter Overview

Nuclear energy production is a crucial part of the world's energy mix, and the development of more efficient and effective fuel compositions is essential for the continued growth of this industry. One promising area of research is the use of e-Gd_2O_3 (Gd_2O_3 with enriched with 100.00 wt.% gadolinium-157) in nuclear fuel compositions. This chapter highlights the potential implications of the use of e-Gd_2O_3 in fuel compositions, explains the method of 2D neutronic analysis using the Monte Carlo particle transport method and discusses the results, which pave the way for 3D fuel cycle analysis by revealing the potential of e-Gd_2O_3.

The reactivity properties of n-Gd_2O_3 and e-Gd_2O_3 were compared. Following this, the depletion behaviour of main neutron absorbing isotopes as well as the breeding behaviour of ^{239}Pu in the case of e-Gd_2O_3 were examined and compared to the n-Gd_2O_3case.

3.2 Method

For the 2D neutronic analysis of n-Gd_2O_3 and e-Gd_2O_3, an AP-1000 PWR reactor designed by the Westinghouse Electric Company was selected as the reference reactor to evaluate the reactivity behaviour of e-Gd_2O_3 and compare it with n-Gd_2O_3.

Neutronic analyses were performed using the Serpent 2 Monte Carlo reactor physics code using the JEFF-3.1 nuclear data library. In the simulations, 300 active and 20 inactive cycles were used with 30,000 neutrons in each cycle. The important parameters used in modelling the reference reactor, as listed in Table 1, were taken into consideration. The average fuel temperature was set at 900 K [102], [103], while the average temperature of the Zircaloy-4 cladding was set at 583 K. Considering the average boron concentration a standard PWR would have within a cycle, the boric acid concentration in the coolant was assumed to be 650 ppm ($1\text{ppm} = 10^{-6}$).

For the purpose of maximizing the impact of using e-Gd_2O_3 compared to n-Gd_2O_3, it was assumed that e-Gd_2O_3 contains 100.00 wt.% ^{157}Gd atoms after enrichment, although it is acknowledged that any enrichment process is likely to result in impurities. Fuel densities with Gd_2O_3 content were calculated using Equation 3 [104], taking into account a 95% theoretical density due to porosity that may occur during fuel production.

The enrichment of ^{235}U, considered throughout the study, ranges from 4.00 wt.% to 6.00 wt.%, allowing for an examination of the potential effects of extending commercially available enrichment for light water reactors beyond 5.00 wt.% and revealing possible trends. Based on the findings, the reactivity behaviours of fuel models that contain e-Gd_2O_3 were analysed and compared to those of the fuel models that contain n-Gd_2O_3 to determine the average quantity of e-Gd_2O_3 that could potentially be utilised as a substitute for the n-Gd_2O_3 in the fuel model. This investigation aimed to identify the feasibility of e-Gd_2O_3 as an alternative material and to assess its efficiency in terms of reactivity. Comparisons were carried out between two separate sets. The first comparison was based on the highest peak point reactivity match, with the maximum difference being limited to 350 pcm. The second comparison focused on the matches in which the peak point reactivity occurred at the same burnup step.

$$\rho = 10.962 - 0.0348x \tag{3}$$

where ρ is the density of the UO_2/Gd_2O_3 and x is the weight percentage of the Gd_2O_3 in fuel composition.

Table 1 – Fuel design parameters for the AP-1000 PWR used in simulations [105].

Parameter	Value
Rod array	17 × 17
Number of control rods	25
Fuel rod pitch (cm)	1.26
Pellet diameter (cm)	0.4095
Rod diameter (cm)	0.475
Cladding material	Zircaloy-4
Cladding thickness (cm)	0.057
Average fuel temperature (K)	900
Average Cladding temperature (K)	583
Fuel density (%T.D.)	95
Soluble boric acid concentration (ppm)	650

It is widely known that, due to self-shielding effects, the Gd atoms in the outer layers of the fuel pellet will transmute more rapidly than those in the inner layers. This is because they absorb neutrons moderated by the coolant water, which shields the Gd atoms in the inner portions of the pellet [106]. In order to observe the depletion behaviour of the Gd isotopes in the fuel pellets as a function of radius, the fuel pellets were divided into 11 radial layers of equal volume, as seen in Figure 7. This method was also used to observe changes in ^{239}Pu breeding. The study found that the reactivity error margins varied up to 21 pcm (1 pcm = 10^{-5}), which was considered too small to impact the results and presenting in the graphs.

The design of the fuel assembly was based on two reference assemblies as in Figures 8 (A1) and 9 (A2), both of which contained 24 burnable absorber rods and 25 control rods. However, the distribution of the burnable absorber rods differed between the assemblies. The rods had the same design, with regular rods made of UO_2 and burnable absorber rods containing different proportions of Gd_2O_3 in addition to UO_2. Despite these differences, it was found that there was no noteworthy change in the reactivity profiles of the two BA placement designs, as will be explained in the next section. For this reason, the design seen in Figure 8 was chosen as a BA rod layout for subsequent simulations.

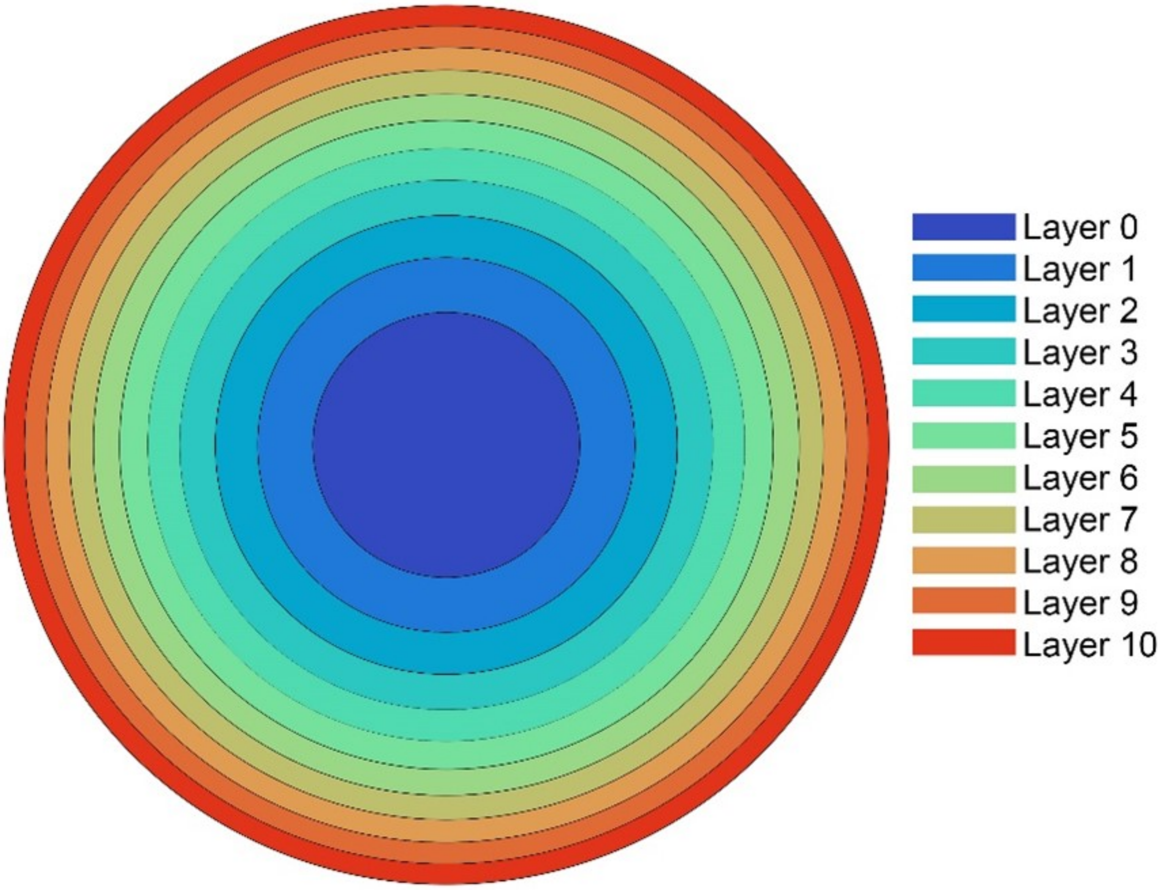

Figure 7 – Radial layers of the fuel pellet.

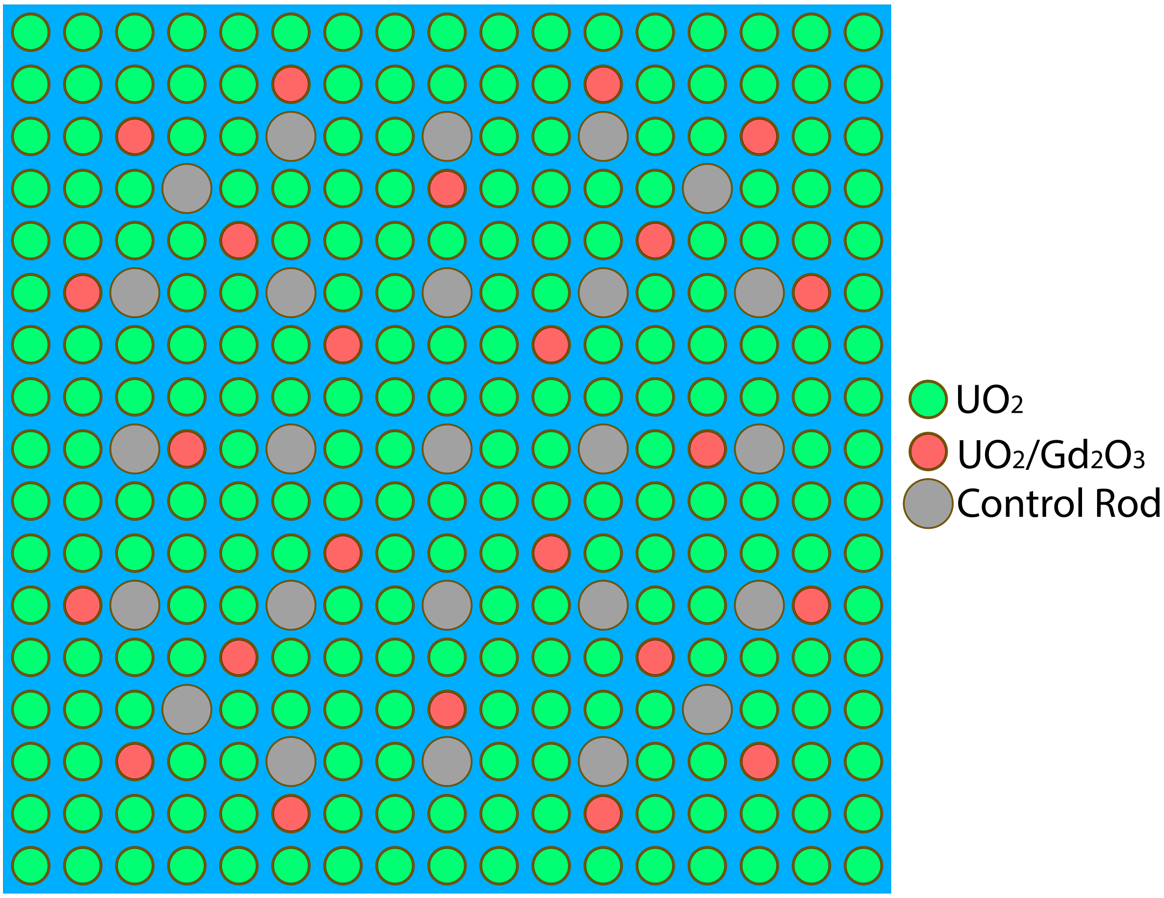

Figure 8 – Fuel assembly design A1 with 24 BA rods. Adapted from [107].

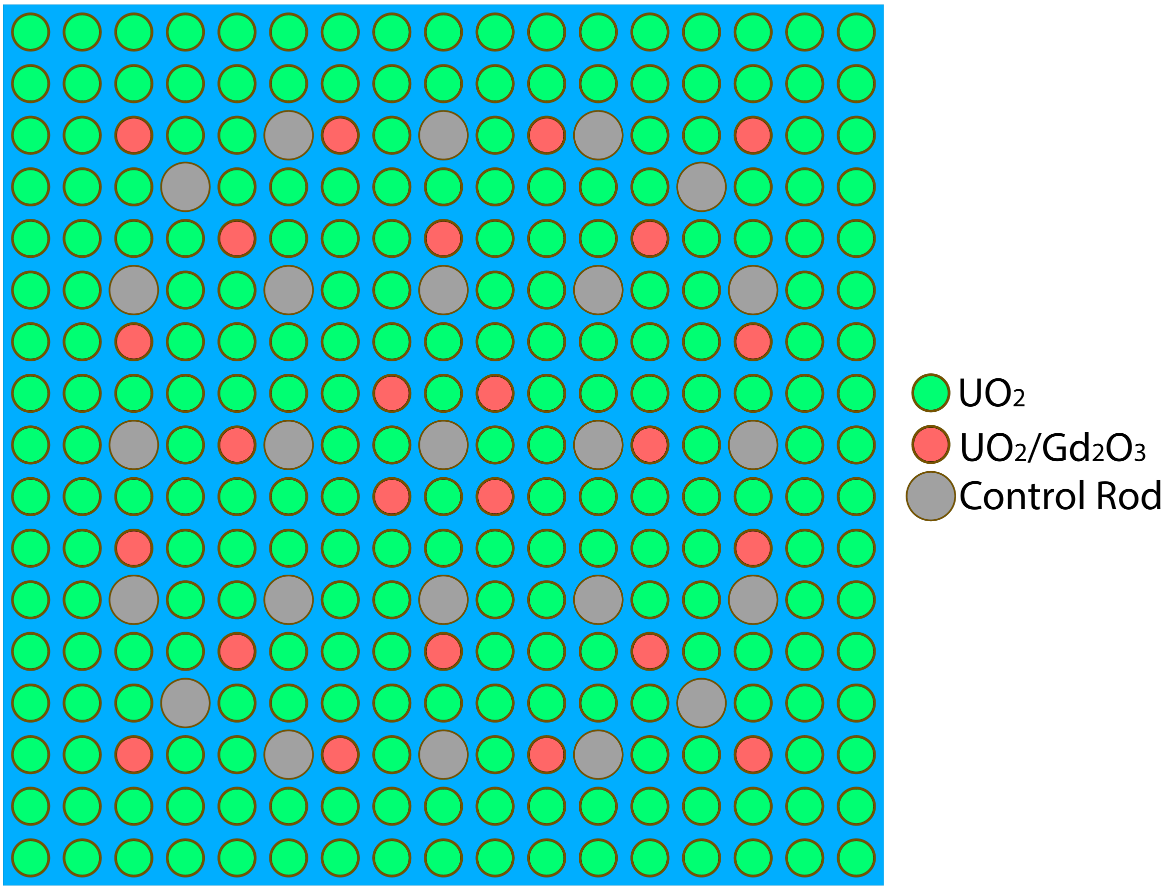

Figure 9 – Fuel assembly design A2 with 24 BA rods. Adapted from [36].

3.3 Results and Discussion

3.3.1 Reactivity Behaviour of n-Gd_2O_3

Figure 10 shows the infinite multiplication factor (k_{inf}) of different n-Gd_2O_3 additions to the two assembly designs, A1 and A2. The figure highlights that keeping the number of BA rods but changing their locations within the assembly does not cause a significant effect on the overall reactivity behaviour. As expected, the larger addition of n-Gd_2O_3 causes a larger suppression in reactivity and also shifts the peak point reactivity towards higher burnups. As a result of these behavioural trends, all subsequent simulations were performed using the A1 assembly layout, seen in Figure 8.

Figure 11 illustrates the infinite multiplication factor of fuels that contain different percentages of n-Gd_2O_3, such as 1.00 wt.%, 2.00 wt.%, 4.00 wt.%, and 6.00 wt.% in 5.00 wt.% ^{235}U enriched fuels. It can be observed that there is a rapid decrease in the k_{inf} values at the beginning of the fuels' lives. This phenomenon is attributed to the rapid rise of xenon-135 and samarium-149 fission products, both of which possess high thermal neutron absorption cross-sections, in the fuel composition before they reach the equilibrium [108].

Following this, the reactivity in the assembly without BA decreases steadily; however, in assemblies that have BA, the reactivity initially rises to a maximum level before BA is nearly depleted, hereafter called the "peak reactivity". After the peak reactivity point, reactivity decreases steadily along with the assembly without BA, agreeing with [109]. It can also be observed that assemblies with more burnable absorber content result in a lower infinite multiplication factor at the end of the fuel's life, due to the residual reactivity penalty.

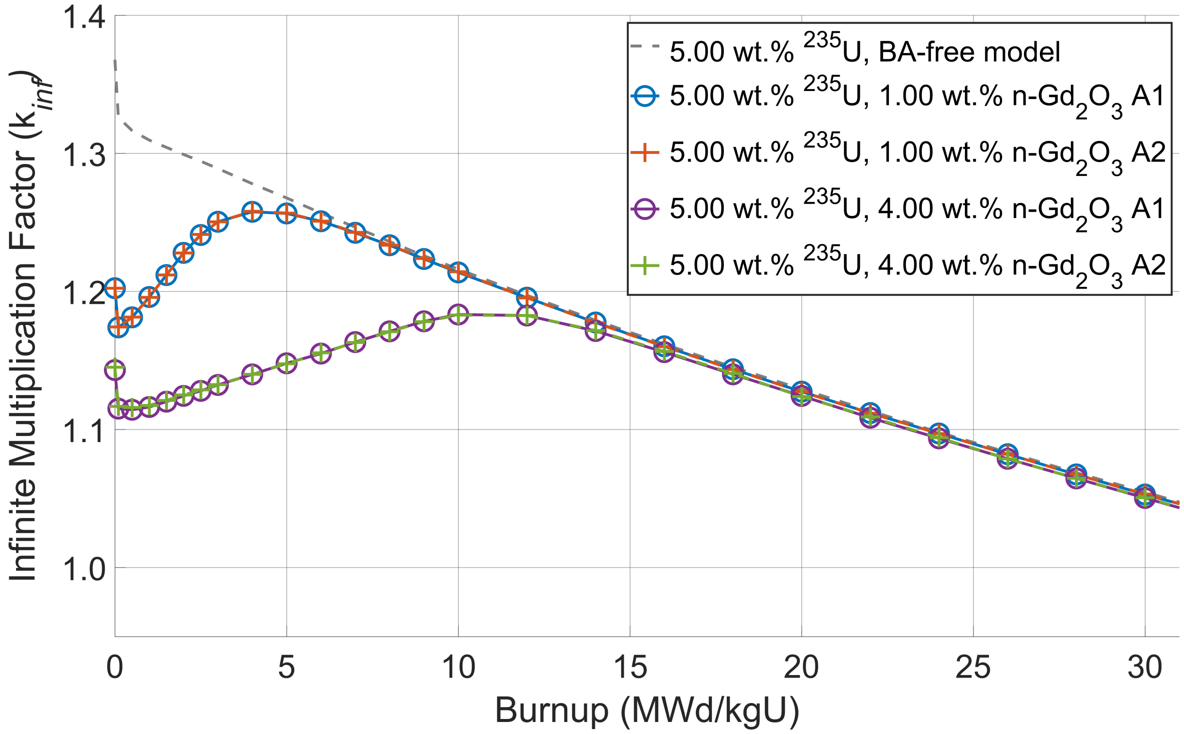

Figure 10 – Infinite multiplication factors (k_{inf}) of the fuel models with 5.00 wt.% ^{235}U with no BA, 1.00 wt.% and 4.00 wt.% n-Gd_2O_3 in two different assembly layouts (A1 and A2).

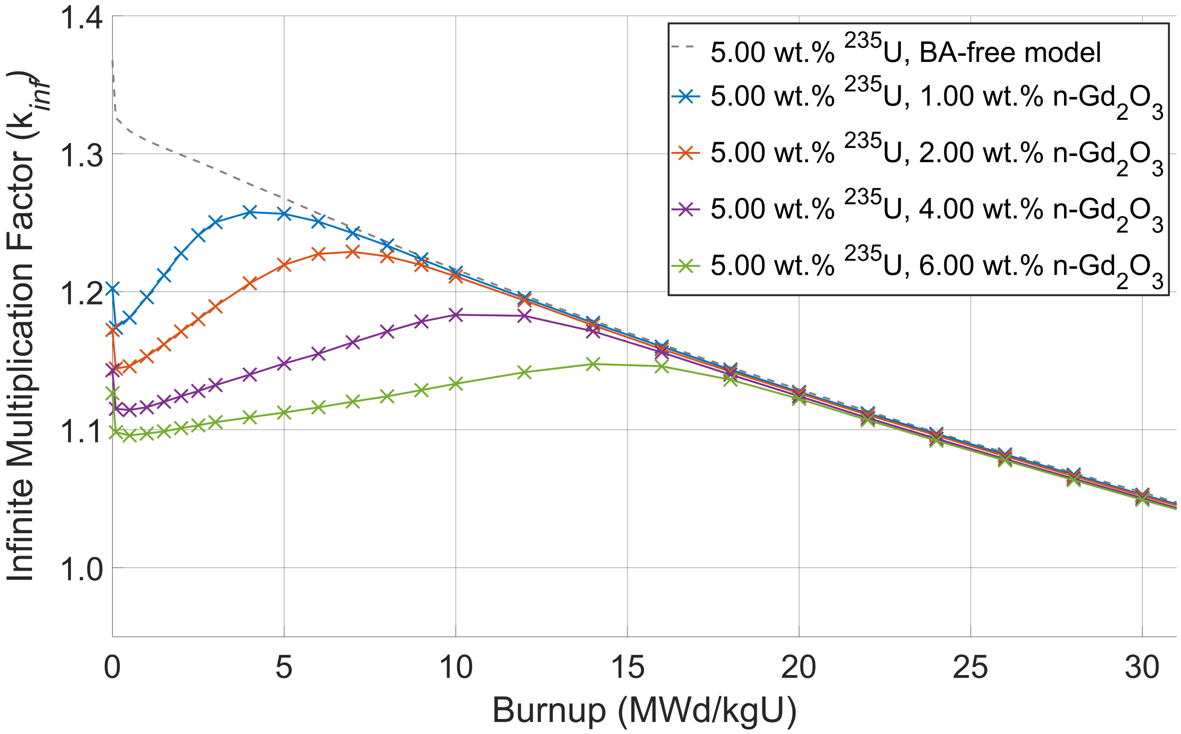

Figure 11 – Infinite multiplication factors for fuel models with 5.00 wt.% ^{235}U enrichment level and containing 1.00 wt.%, 2.00 wt.%, 4.00 wt.% and 6.00 wt.% n-Gd_2O_3.

Figure 12 illustrates the trends in the infinite multiplication factor of model fuels with varying ^{235}U enrichment levels in assembly A1, which contains 4.00 wt.% n-Gd_2O_3 burnable absorber rods while Figure 13 shows the ^{155}Gd and ^{157}Gd depletion behaviours in these fuel models. It can be seen in Figure 12, the total reactivity increases with increasing ^{235}U content, as expected. For each enrichment level, models with BA rods have lower multiplication factors at the beginning of the fuel's life compared to BA-free models with the same ^{235}U enrichment. As burnup progresses, the multiplication factor increases until the ^{155}Gd and ^{157}Gd isotopes are mostly depleted, as in Figure 13. With the depletion of these isotopes, the full fissile content of the assembly becomes exposed and the infinite multiplication factor begins to decline again, approaching the reactivity curve of the reference model without BA additions.

Additionally, comparing the main thermal neutron absorbing isotopes of the Gd, ^{157}Gd is depleted at a faster rate than ^{155}Gd when a selected ^{235}U enrichment level is considered. This is because of the difference in thermal neutron absorption cross-section between the two isotopes. ^{157}Gd has a higher thermal neutron absorption cross-section compared to ^{155}Gd as discussed earlier in Chapter 1.3.1, which explains its faster depletion rate.

It is also noticeable that, after the depletion of the Gd isotopes, there is a slight decrease in the reactivity of the fuel models with BA content, compared to BA-free models. Furthermore, since ^{235}U is a neutron absorber, with the increase in the concentration of ^{235}U in the fuel composition, the depletion of the Gd isotopes is delayed and the rate of residual reactivity increases as in Figure 13, as consistent with [51].

Figure 14 shows a comparison of the reactivity behaviour of model fuels, 5.00 wt.% ^{235}U enriched, with 2.00 wt.% n-Gd_2O_3 and 2.00 wt.% e-Gd_2O_3 to demonstrate the variations in reactivity that occur when the same amount of n-Gd_2O_3 and e-Gd_2O_3 are added in fuel composition. It can be seen that the reactivity is suppressed more and flattened in the fuel model with e-Gd_2O_3 compared to the fuel model with n-Gd_2O_3. The reason for this behaviour is the higher presence of ^{157}Gd in the e-Gd_2O_3 assembly. The reactivity suppression in the fuel model with e-Gd_2O_3 is higher and lasts longer than the fuel model with n-Gd_2O_3 which is in line with the findings of [54].

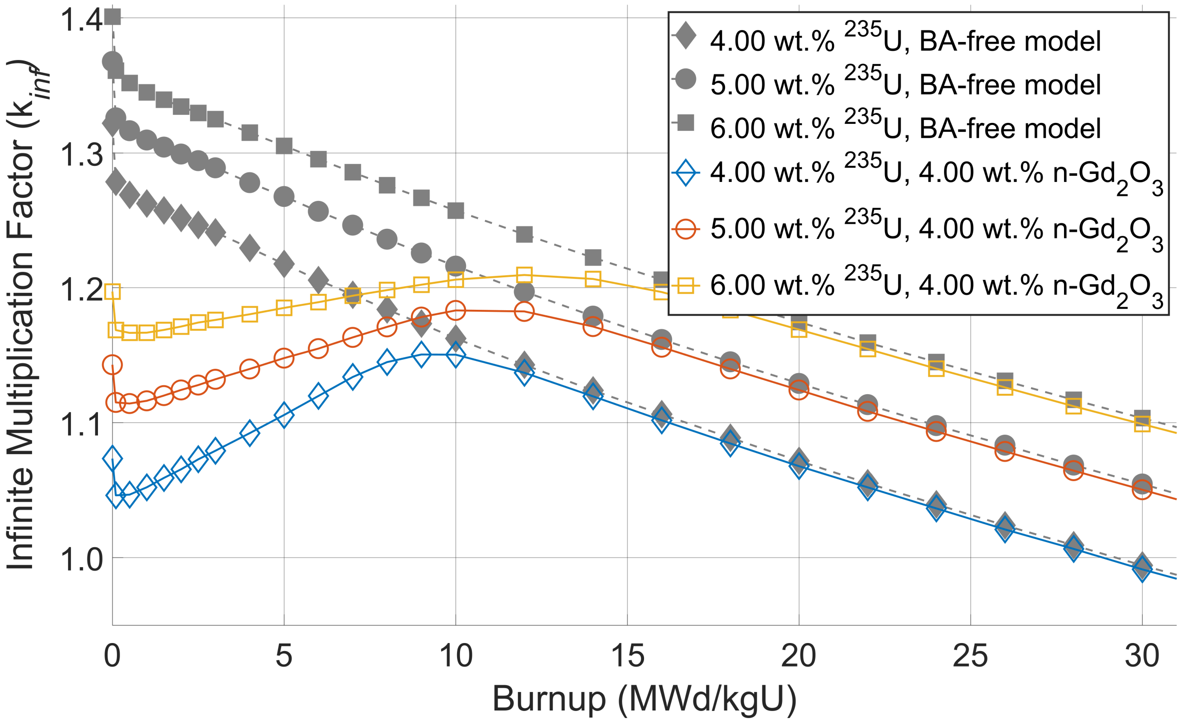

Figure 12 – Infinite multiplication factors of model fuels with 4.00 wt.%, 5.00 wt.% and 6.00 wt.% ^{235}U and 4.00 wt.% n-Gd_2O_3 and their reference models without BA.

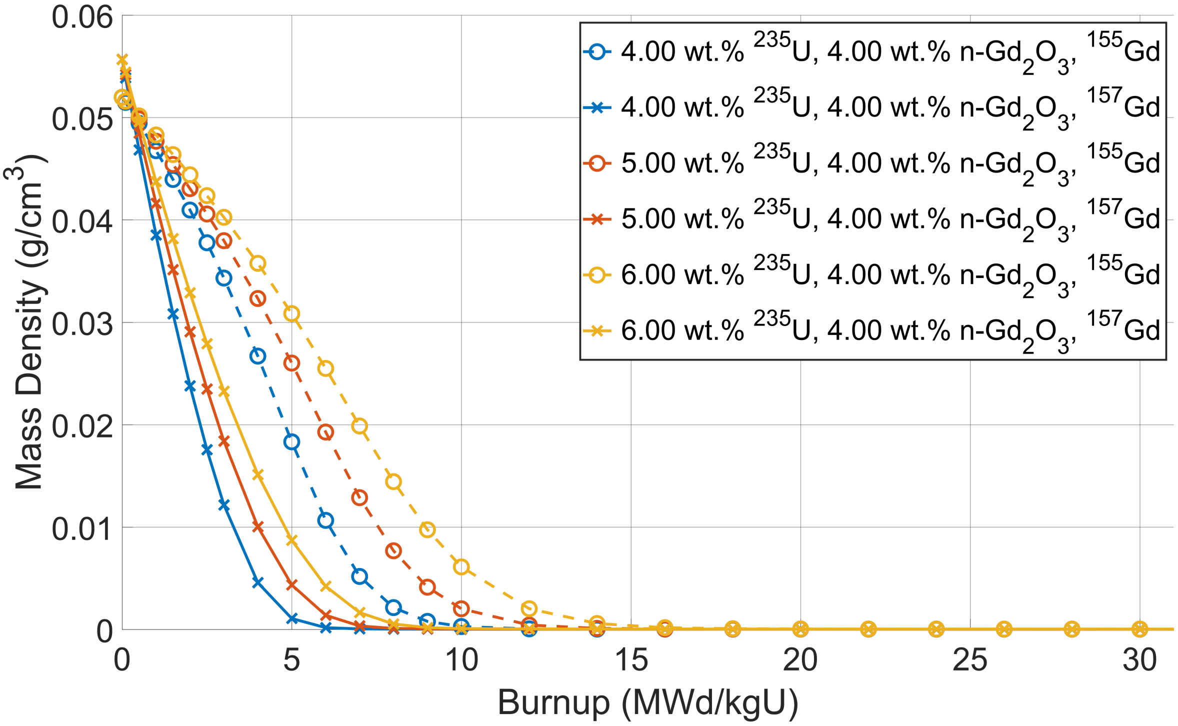

Figure 13 – ^{157}Gd and ^{155}Gd depletion behaviours of model fuels with 4.00 wt.%, 5.00 wt.% and 6.00 wt.% ^{235}U and 4.00 wt.% n-Gd$_2$O$_3$.

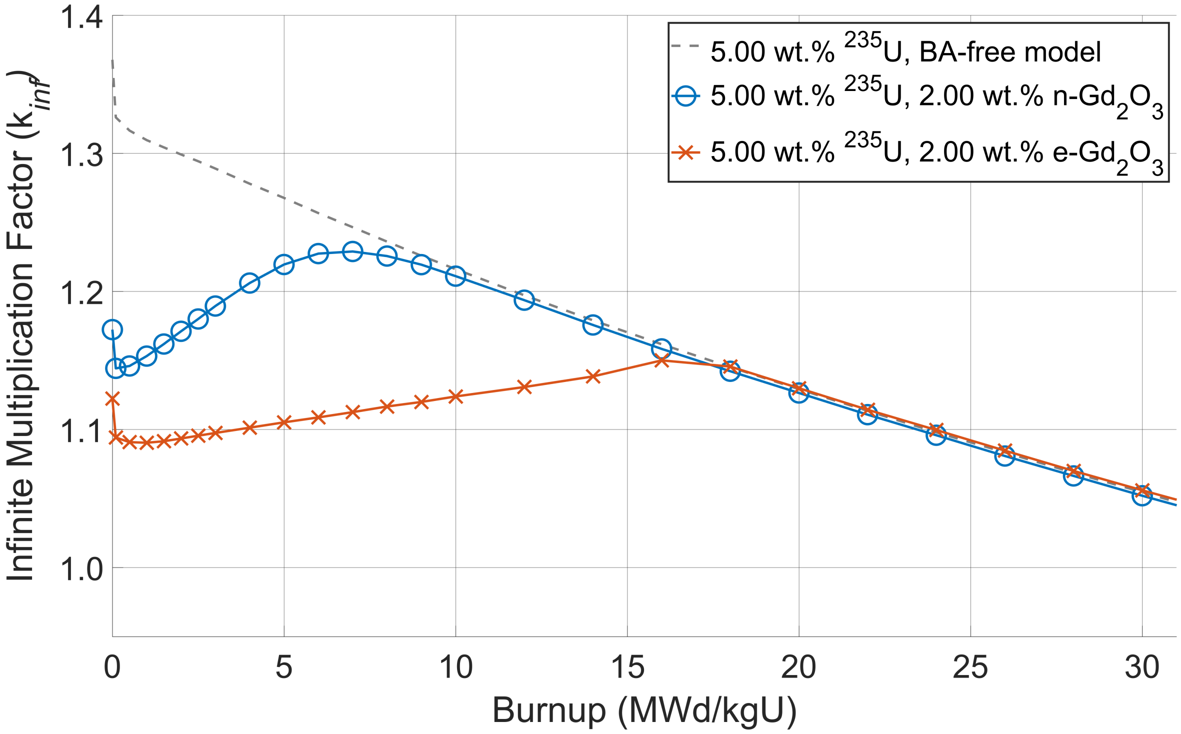

Figure 14 – Infinite multiplication factors of model fuels with 5.00 wt.% ^{235}U and 2.00 wt.% n-Gd_2O_3, 5.00 wt.% ^{235}U and 2.00 wt.% e-Gd_2O_3, and 5.00 wt.% ^{235}U and without BA.

3.3.2 Matching Similar Peak Point Reactivity Behaviours

Figure 15 shows the infinite multiplication factor comparison and reactivity differences (Δk_{inf}) of various fuel models that are all enriched with 5.00 wt.% ^{235}U. Figures 15a, 15b, and 15c respectively demonstrate the matches of fuel models that have peak point reactivity at the same burnup step such as 2.00 wt.% n-Gd_2O_3 and 0.65 wt.% e-Gd_2O_3, 4.00 wt.% n-Gd_2O_3 and 1.10 wt.% e-Gd_2O_3, and 6.00 wt.% n-Gd_2O_3 and 1.55 wt.% e-Gd_2O_3; Figures 15d, 15e, and 15f illustrate the reactivity differences of these matches, respectively.

Observing Figures 15a and 15d, it can be seen that the fuel model using 0.65 wt.% of e-Gd_2O_3 has a 1,267 pcm lower infinite multiplication factor compared to the fuel model using 2.00 wt.% of n-Gd_2O_3 at the beginning of their lives. The Δk_{inf} curve in Figure 15d shows that the fuel model using e-Gd_2O_3 demonstrates a lower infinite multiplication factor compared to the fuel model using n-Gd_2O_3 until 5.00 MWd/kgU. From 5.00 MWd/kgU, the fuel model using e-Gd_2O_3 begins to display a higher infinite multiplication factor than the fuel model using n-Gd_2O_3. This difference reaches its maximum value of 1,480 pcm at the peak reactivity point, 7.00 MWd/kgU, after the depletion of the Gd, as seen in Figure 17a. Then, the infinite multiplication factors of both fuel models start to decline in parallel with the infinite multiplication factor of the BA-free fuel model. However, the multiplication factor of the fuel model using e-Gd_2O_3 is higher than n-Gd_2O_3's and almost identical to that of the BA-free fuel model. For instance, at 20.00 MWd/kgU, the fuel model with e-Gd_2O_3 has a 29 pcm lower infinite multiplication factor compared to the BA-free fuel model, whereas the fuel model using n-Gd_2O_3 has a 277 pcm lower multiplication factor compared to the BA-free fuel model.

Alternatively, as seen in Figures 15b and 15e, the fuel model using 1.10 wt.% of e-Gd_2O_3 demonstrates a 158 pcm lower multiplication factor compared to the fuel model using 4.00 wt.% of n-Gd_2O_3 at the beginning of their lives. The Δk_{inf} curve in Figure 15e shows that the fuel model using e-Gd_2O_3 continues to exhibit a lower multiplication factor compared to the fuel model using n-Gd_2O_3 until around 2.50 MWd/kgU. Beyond this point, the fuel model using e-Gd_2O_3 begins to display a higher multiplication factor than the fuel model using n-Gd_2O_3. This difference reaches its maximum value of 2,680 pcm at 10.00 MWd/kgU, where both fuel models reach the peak point reactivity, following the depletion of most Gd isotopes as seen in Figure 17b. Then, the multiplication factors of both fuel models start to decline, and their decrease parallels the decline in the multiplication factor of the BA-free fuel model. The multiplication factor of the fuel model using e-Gd_2O_3 is greater than n-Gd_2O_3's and nearly equal to the multiplication factor of the BA-free fuel model. For instance, at 20.00 MWd/kgU, the fuel model containing e-Gd_2O_3 has a 23 pcm lower infinite multiplication factor compared to the BA-free fuel model, whereas the fuel model using n-Gd_2O_3 has a 490 pcm lower multiplication factor compared to the BA-free fuel model. However, at 30.00 MWd/kgU, while the fuel model containing e-Gd_2O_3 has a 49 pcm higher infinite multiplication factor compared to the BA-free fuel model, the fuel model using n-Gd_2O_3 has a 426 pcm lower multiplication factor compared to the BA-free fuel model.

In contrast, as seen in Figures 15c and 15f, the fuel model using 1.55 wt.% e-Gd_2O_3 has an infinite multiplication factor that is 429 pcm higher than the fuel model using 6.00 wt.% n-Gd_2O_3 at the beginning of their lives. This difference increases during the burnup and at 14.00 MWd/kgU, both fuel models reach their peak point reactivity, with the difference in infinite multiplication factor reaching up to 2,941 pcm. Afterwards, the infinite multiplication factor of both fuel models shows a decreasing trend parallel to the BA-free fuel model. However, contrary to the other fuel models using e-Gd_2O_3 that were previously mentioned, this fuel model using e-Gd_2O_3 has an infinite multiplication factor that is 18 pcm higher than the BA-free fuel model at 20.00 MWd/kgU, while the fuel model using n-Gd_2O_3 has a 687 pcm lower infinite multiplication factor than the BA-free fuel model. Additionally, at 30.00 MWd/kgU, the fuel model using e-Gd_2O_3 has a higher infinite multiplication factor by 56 pcm when compared to the BA-free fuel model, whereas the fuel model using n-Gd_2O_3 has a 548 pcm lower multiplication factor compared to the BA-free fuel model.

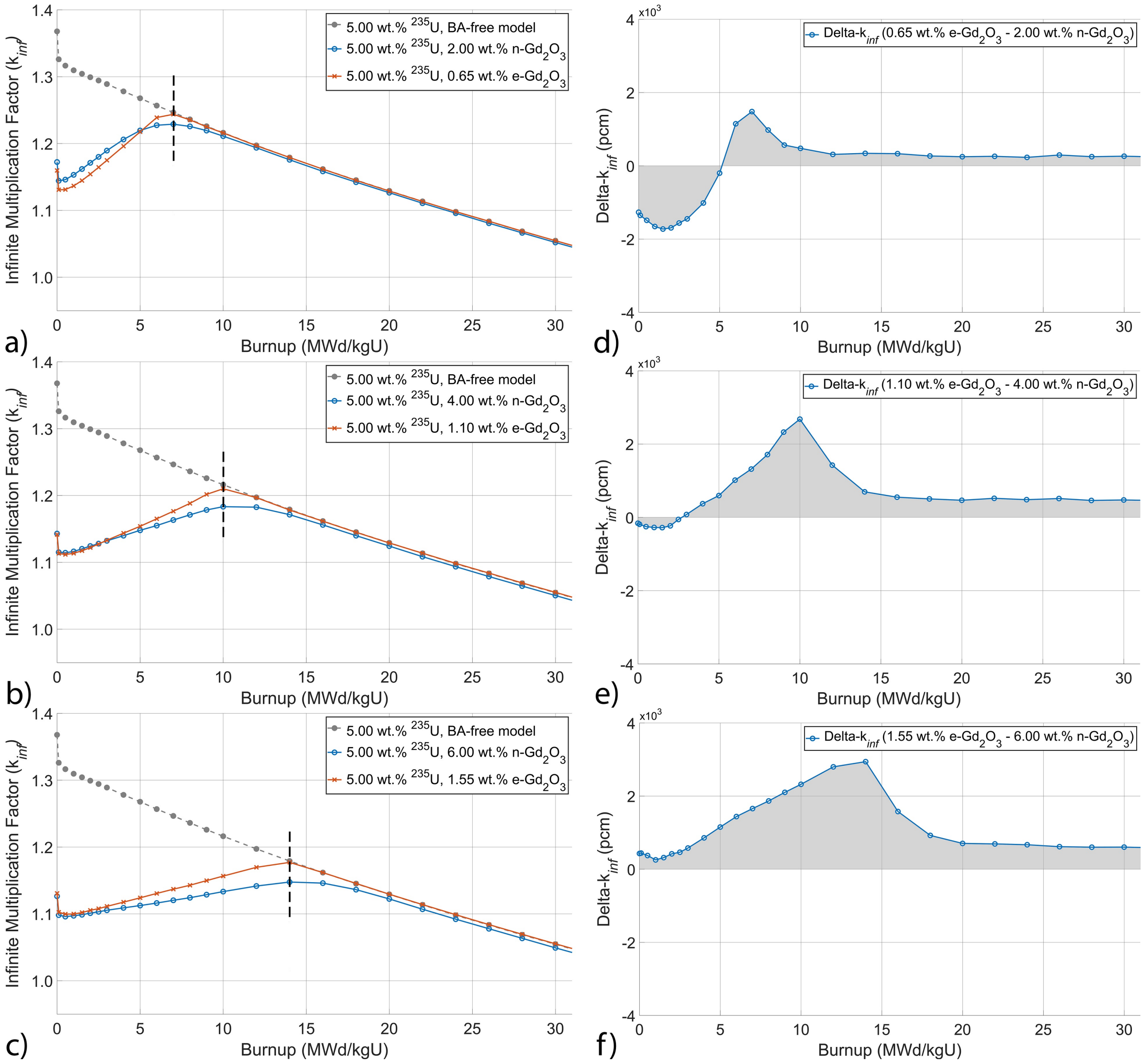

Figure 15 – Infinite multiplication factors (a, b, c) and Delta-k$_{inf}$ curves (d, e, f) for fuel models with matched similar peak point reactivity behaviours.

3.3.3 Matching Equal Peak Point Reactivity

Figure 16 shows the infinite multiplication factor comparison and reactivity differences of various fuel models that are all enriched with 5.00 wt.% ^{235}U. Figures 16a, 16b, and 16c respectively demonstrate the matches of fuel models that have equal peak point reactivity such as 2.00 wt.% n-Gd_2O_3 and 0.85 wt.% e-Gd_2O_3, 4.00 wt.% n-Gd_2O_3 and 1.45 wt.% e-Gd_2O_3, and 6.00 wt.% n-Gd_2O_3 and 2.00 wt.% e-Gd_2O_3. Figures 16d, 16e, and 16f illustrate the reactivity differences of these matches, respectively.

By examining Figures 16a and 16d, it can be seen that the fuel model using 0.85 wt.% e-Gd_2O_3 has a lower infinite multiplication factor by 2,240 pcm compared to the fuel model using 2.00 wt.% n-Gd_2O_3 at the beginning of their lives. The Δk_{inf} curve in Figure 16d indicates that the fuel model that uses e-Gd_2O_3 exhibits a reduced infinite multiplication factor in comparison to the fuel model that uses n-Gd_2O_3 until the Gd isotopes are almost completely depleted (as seen in Figure 17a). The fuel model using n-Gd_2O_3 reaches its peak reactivity at 7.00 MWd/kgU, while the fuel model using e-Gd_2O_3 reaches it at 8.00 MWd/kgU. After this point, the infinite multiplication factors of both fuel models decline in parallel with the infinite multiplication factor of the BA-free fuel model. However, the fuel model that uses e-Gd_2O_3 has a higher multiplication factor than the n-Gd_2O_3 fuel model and is almost the same as the BA-free fuel model. For example, at 20.00 MWd/kgU, the fuel model that uses e-Gd_2O_3 has a lower infinite multiplication factor by 7 pcm, which is within the error margin, compared to the BA-free fuel model, while the fuel model that uses n-Gd_2O_3 has a lower infinite multiplication factor by 277 pcm compared to the BA-free fuel model.

It can be observed from Figures 16b and 16e that the utilisation of 1.45 wt.% of e-Gd_2O_3 in the fuel model results in a lower multiplication factor by 1,102 pcm compared to the fuel model using 4.00 wt.% n-Gd_2O_3, at the beginning of their lives. The Δk_{inf} curve in Figure 16e reveals that this difference remains throughout the depletion of Gd isotopes (as seen in Figure 17b). However, once both fuel models reach their peak reactivity, the multiplication factor of both fuel models starts to decline, following a similar pattern to the multiplication factor of the BA-free fuel model. Moreover, the infinite multiplication factor of the fuel model using e-Gd_2O_3 is higher than that of the fuel model using n-Gd_2O_3 and the BA-free fuel model for the rest of the fuels' life. For example, at 20.00 MWd/kgU, the fuel model with e-Gd_2O_3 has a 13 pcm higher infinite multiplication factor compared to the BA-free fuel model, whereas the fuel model using n-Gd_2O_3 exhibits a 490 pcm lower infinite multiplication factor in comparison to the BA-free fuel model. Additionally, at 30.00 MWd/kgU, while the fuel model with e-Gd_2O_3 has a 68 pcm higher infinite multiplication factor compared to the BA-free fuel model, the fuel model utilising n-Gd_2O_3 displays a 426 pcm lower infinite multiplication factor in comparison to the BA-free fuel model.

On the other hand, it can be observed in Figures 16c and 16f that the fuel model using 2.00 wt.% e-Gd_2O_3 exhibits an infinite multiplication factor that is 406 pcm lower than the fuel model using 6.00 wt.% n-Gd_2O_3 at the beginning of their lives. As both fuel models reach their peak reactivity, the infinite multiplication factors tend to a parallel decline with the infinite multiplication factor of the fuel model without BA. The infinite multiplication factor of the fuel model using e-Gd_2O_3 is higher than that of the fuel model using n-Gd_2O_3 and the BA-free fuel model throughout the rest of the fuel's life. For instance, at 20.00 MWd/kgU, the infinite multiplication factor of the fuel model using e-Gd_2O_3 is 70 pcm greater than that of the BA-free fuel model, while the fuel model using n-Gd_2O_3 has a 687 pcm lower infinite multiplication factor in comparison to the BA-free fuel model. Moreover, at 30.00 MWd/kgU, the fuel model using e-Gd_2O_3 displays a 130 pcm higher infinite multiplication factor compared to the BA-free fuel model, whereas the fuel model using n-Gd_2O_3 has a 548 pcm lower infinite multiplication factor in comparison to the BA-free fuel model.

The use of BA delays the consumption of ^{235}U and hardens the neutron spectrum, resulting in a higher fissile generation of ^{239}Pu [110]. As demonstrated by Figures 15 and 16, the infinite multiplication factors of the models using n-Gd_2O_3 show a decrease that parallels the BA-free model and approaches to the model without BA during the burnup. However, this approach is not at a level to compensate for the residual reactivity penalty caused by the Gd isotopes other than the main neutron-absorbing ones, considering the average life of the fuel. On the other hand, with the use of e-Gd_2O_3, although the BA addition displaces the uranium from the fuel composition, a relatively higher reactivity is obtained, close to the BA-free fuel model and higher than it in some cases. The reason for this increase is that e-Gd_2O_3 delays the consumption of ^{235}U more than n-Gd_2O_3 and hardens the neutron spectrum more, causing more fissile ^{239}Pu atoms to be bred as seen in Figure 19.

In the consideration of using e-Gd_2O_3 instead of n-Gd_2O_3, two methods were examined to determine the amount to be used: matching similar peak point reactivity behaviours and matching equal peak point reactivity. From the trends observed in both (Figures 15 and 16), it can be seen that when the similar peak point reactivity behaviours were matched, a higher reactivity was obtained in all fuel model pairs compared to when matching equal peak point reactivity. Although gains could be achieved at the end of the cycle in matches where a high proportion of BA was used in the fuel composition when matching the equal peak point reactivity, these gains were not as high as when the similar peak point reactivity behaviours are matched. Thus, matching the similar peak point reactivity behaviours might be preferred to determine the proportion of e-Gd_2O_3 needed when substituting n-Gd_2O_3 with e-Gd_2O_3.

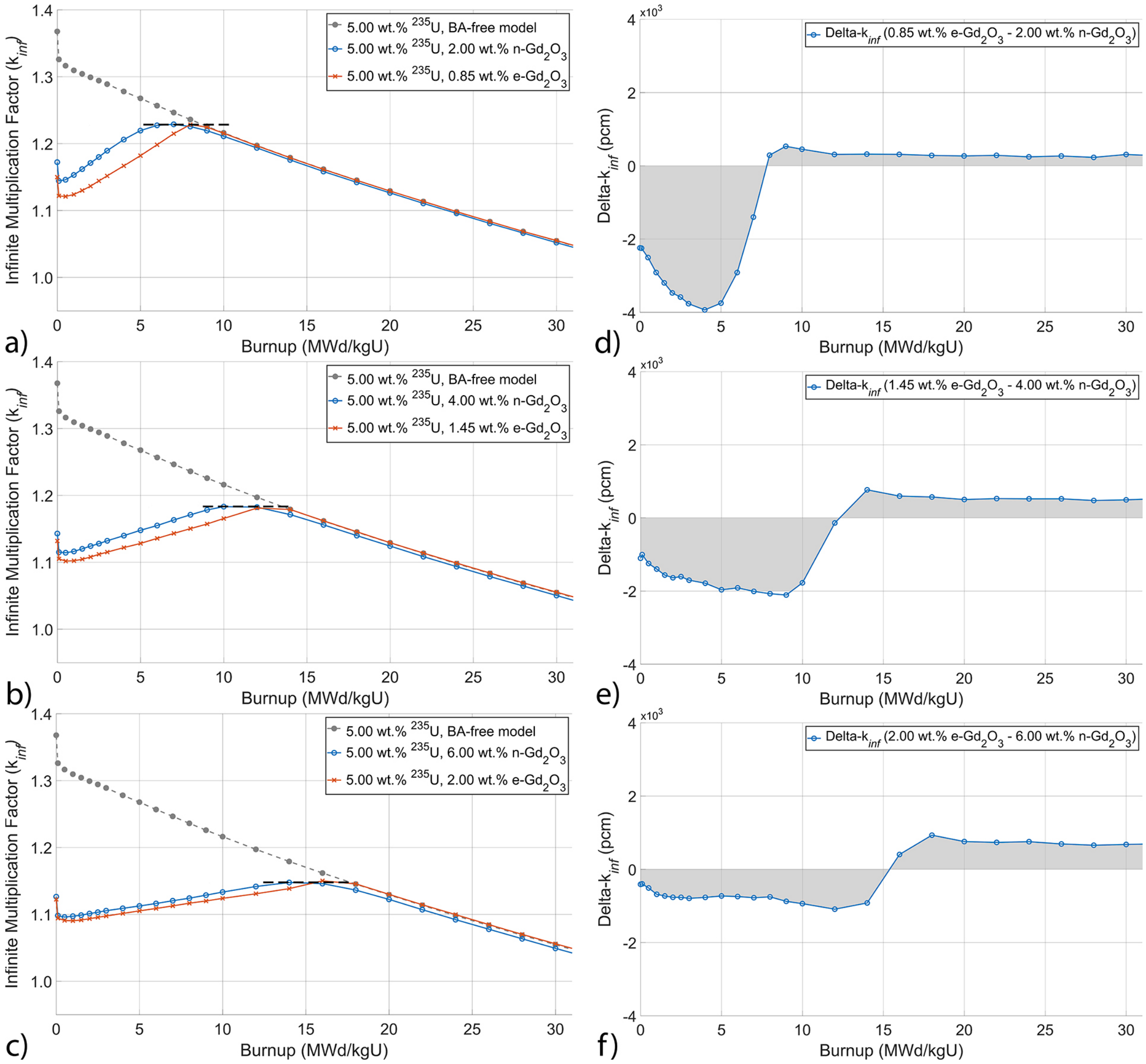

Figure 16 – Infinite multiplication factors (a, b, c) and Delta-k_{inf} curves (d, e, f) of fuel models with matched equal peak point reactivity

3.3.4 Depletion Behaviour of Gadolinium Isotopes

Figure 17 represents the depletion behaviour of the ^{155}Gd and ^{157}Gd isotopes in fuel models using n-Gd_2O_3 and e-Gd_2O_3, reported in Figures 15 and 16, as a function of burnup. Figure 17a shows the matches of the fuel model using 2.00 wt.% n-Gd_2O_3 with 0.65 wt.% e-Gd_2O_3 which have their peak point reactivity at same burnup step, as well as 0.85 wt.% e-Gd_2O_3 which has equal peak point reactivity. Figure 17b presents the matches of the fuel model using 4.00 wt.% n-Gd_2O_3 with 1.10 wt.% e-Gd_2O_3 which have their peak point reactivity at same burnup step, along with 1.45 wt.% e-Gd_2O_3 which has equal peak point reactivity. Figure 17c shows the matches of the fuel model using 6.00 wt.% n-Gd_2O_3 with 1.55 wt.% e-Gd_2O_3 which have their peak point reactivity at same burnup step as well as 2.00 wt.% e-Gd_2O_3 which has equal peak point reactivity.

When examining Figure 17, it can be observed that although the fuel models using e-Gd_2O_3 have a higher mass density of ^{157}Gd atoms than those using n-Gd_2O_3 in matches where the peak point reactivity occurs at the same burnup step, they are mostly depleted at almost the same burnup step as the fuel models using n-Gd_2O_3. The depletion of most of the ^{157}Gd atoms in all matches showing the same peak point reactivity, on the other hand, occurs later in fuel models using e-Gd_2O_3. This delay progresses in parallel with the increase in the BA ratio in the fuel composition, as expected. For instance, when comparing the ^{157}Gd depletions of the 2.00 wt.% n-Gd_2O_3 and 0.85 wt.% e-Gd_2O_3 fuel models shown in Figure 17a, the ^{157}Gd atoms in e-Gd_2O_3 persist for about 1.00 MWd/kgU longer than n-Gd_2O_3. Moreover, when comparing the 6.00 wt.% n-Gd_2O_3 and 2.00 wt.% e-Gd_2O_3 fuel models shown in Figure 17c, the ^{157}Gd atoms of the e-Gd_2O_3 fuel model persist for around 6.00 MWd/kgU longer. Moreover, the ^{155}Gd atoms of all fuel models are depleted later than the ^{157}Gd atoms due to their lower thermal neutron absorption cross-section, as expected. It is noteworthy that the depletion of Gd isotopes mentioned earlier refers to near-complete depletion since certain Gd atoms persist in the centre of the fuel pellets for a certain period. This can be observed in the examination of the radial depletion behaviour of Gd isotopes (see Figure 18).

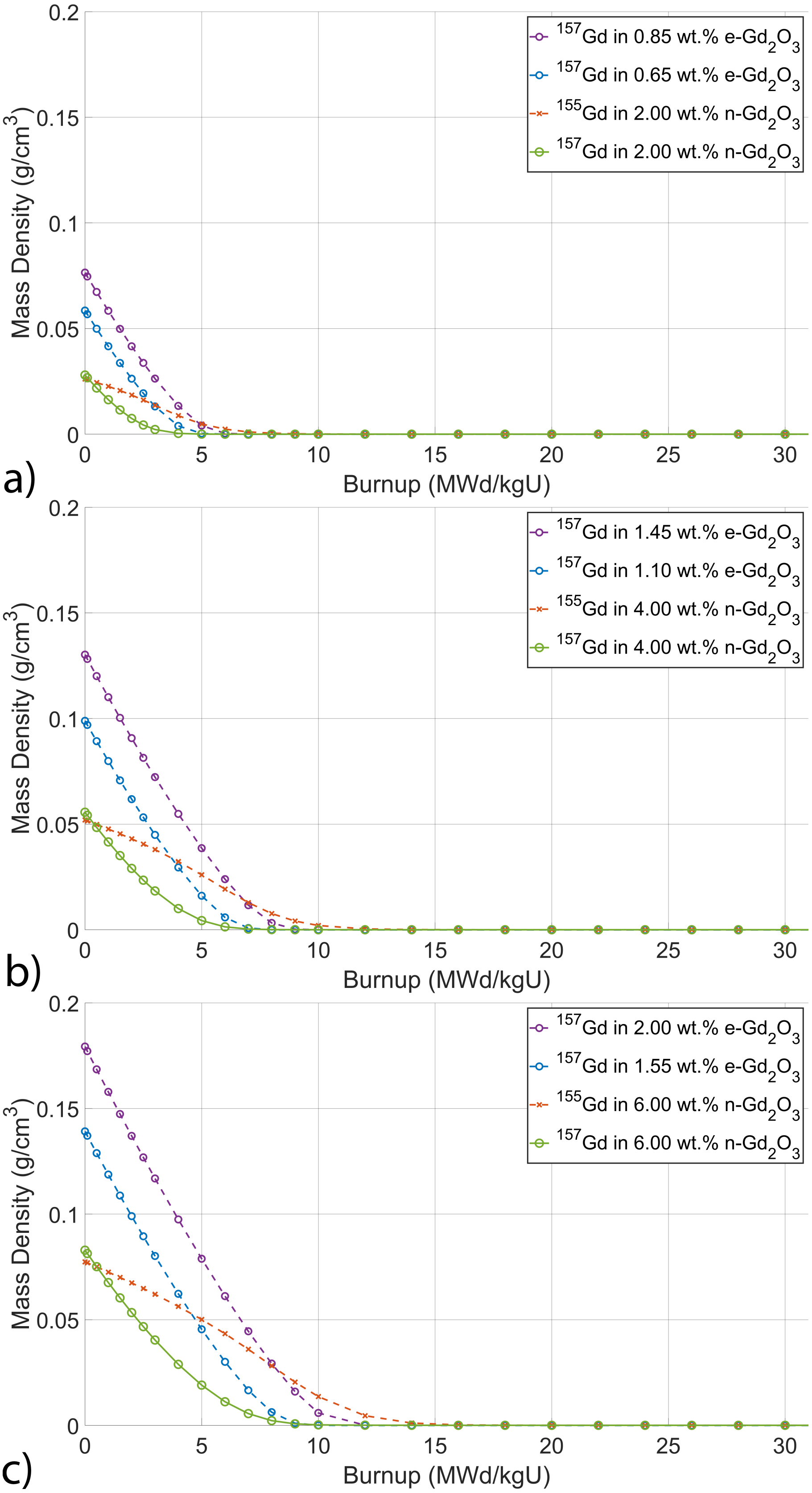

Figure 17 – ^{157}Gd and ^{155}Gd depletion behaviours of 2.00 wt.% n-Gd$_2$O$_3$, 0.65 wt.% and 0.85 wt.% e-Gd$_2$O$_3$ (a), 4.00 wt.% n-Gd$_2$O$_3$, 1.10 wt.% and 1.45 wt.% e-Gd$_2$O$_3$ (b), and 6.00 wt.% n-Gd$_2$O$_3$, 1.55 wt.% and 2.00 wt.% e-Gd$_2$O$_3$ (c).

Figure 18 illustrates the average radial Gd depletion behaviour of fuel rods containing BA of the 6.00 wt.% n-Gd_2O_3 and 1.55 wt.% e-Gd_2O_3 fuel models, that show the peak point reactivities at the same burnup step. Specifically, Figure 18a and Figure 18b show the depletion behaviour of the ^{155}Gd and ^{157}Gd isotopes of the fuel model using 6.00 wt.% n-Gd_2O_3, respectively, while Figure 18c shows the depletion behaviour of the ^{157}Gd isotope of the fuel model using 1.55 wt.% e-Gd_2O_3. It should also be noted that since the ^{157}Gd and ^{155}Gd atoms within the fuel composition are depleted before 15.00 MWd/kgU, there is no need to examine beyond this point. In addition, since the depletion rate slows down from the pellet surface to its centre, due to the self-shielding effect, and shows a similar trend in all fuel models containing BA, it was deemed unnecessary to present the results of all fuel models.

Examining the Figure 18, it is seen that the depletion of Gd isotopes occurs more rapidly on the surface of the fuel pellet. This is due to the self-shielding effect, which causes the neutrons that penetrate the fuel pellet to be absorbed by the Gd isotopes in the outer layers and prevents them from penetrating the inner layers of the pellet. As burnup progresses, the neutrons that enter the fuel pellet continue to be captured by the Gd isotopes in the outer layers, leading to a cycle that persists until they reach the centre of the pellet. Despite the fact that the mass density of ^{157}Gd atoms is greater in the fuel model using e-Gd_2O_3, it exhibits a nearly parallel depletion pattern to the fuel model using n-Gd_2O_3, when considering the matches where the peak reactivity occurs at same burnup step (as in Figure 17). However, ^{155}Gd atoms, which have a lower thermal neutron absorption cross-section in n-Gd_2O_3, can persist for a longer time. For instance, when observing the behaviour of ^{157}Gd atoms in the 1.55 wt.% e-Gd_2O_3 fuel model, it can be observed that the ^{157}Gd atoms on the fuel pellet's surface are depleted almost entirely at around 3.00 MWd/kgU, while some ^{157}Gd atoms in the pellet centre persist in the fuel composition for up to roughly 14.00 MWd/kgU.

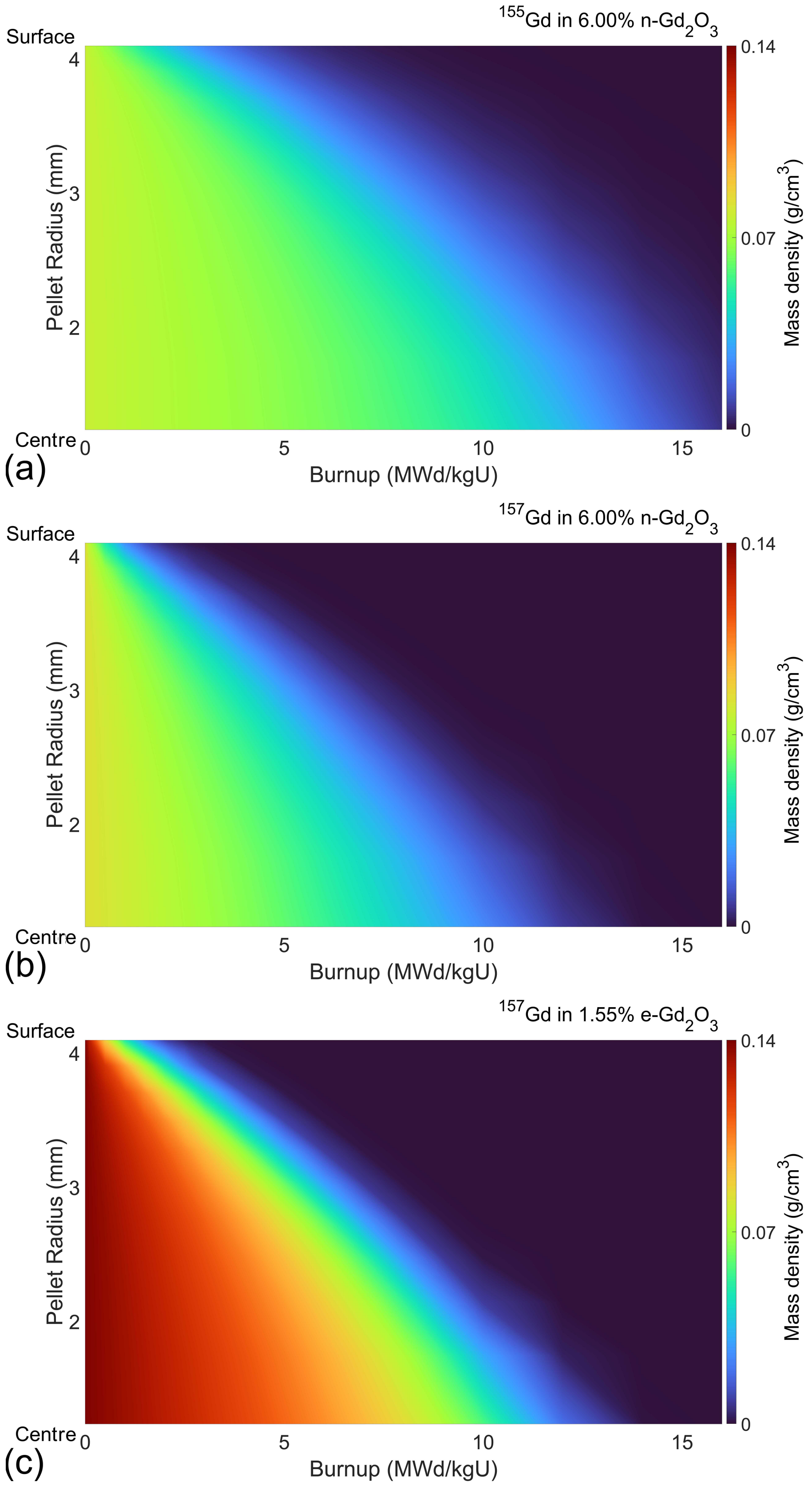

Figure 18 – Radial depletion behaviour of (a) ^{155}Gd in 6.00 wt.% n-Gd_2O_3, (b) ^{157}Gd in 6.00 wt.% n-Gd_2O_3 and (c) ^{157}Gd in 1.55 wt.% e-Gd_2O_3.

3.3.5 Plutonium-239 Breeding Behaviour

Figure 19 shows the breeding behaviour of ^{239}Pu, where a comparison is made between the BA-free fuel model and fuel models using n-Gd_2O_3 and e-Gd_2O_3, delta-^{239}Pu. Figure 19a compares the fuel models that were previously reported in Figure 15, matching fuel models that have peak point reactivity at the same burnup step. On the other hand, Figure 19b compares matching fuel models that have equal peak point reactivity, which were reported in Figure 16. From Figure 19, it can be observed that the mass density of ^{239}Pu increases as the Gd isotopes are depleted in all fuel models using n-Gd_2O_3, compared to the BA-free fuel model. Additionally, the delta-^{239}Pu peaks when almost all of the Gd isotopes are depleted. The degree of increase in mass density depends on the n-Gd_2O_3 ratio in the fuel composition. Subsequently, the mass density of ^{239}Pu decreases and approaches the mass density of ^{239}Pu in the BA-free fuel model. However, at 50.00 MWd/kgU, which can be considered as the end of the fuel assemblies' life, the ^{239}Pu content is higher and directly proportional to the BA concentration.

Comparing the ^{239}Pu breeding in fuel models that use e-Gd_2O_3 with those using n-Gd_2O_3, it is evident that the fuel models using e-Gd_2O_3 result in higher ^{239}Pu breeding than the fuel models using n-Gd_2O_3 in all matches. Furthermore, it should be noted that fuel models using e-Gd_2O_3 in equal peak-point reactivity pairings produce more ^{239}Pu breeding, as they have higher BA concentrations. For instance, when comparing 2.00 wt.% e-Gd_2O_3 in Figure 19b with 1.55 wt.% e-Gd_2O_3 in Figure 19a, the former results in more ^{239}Pu breeding.

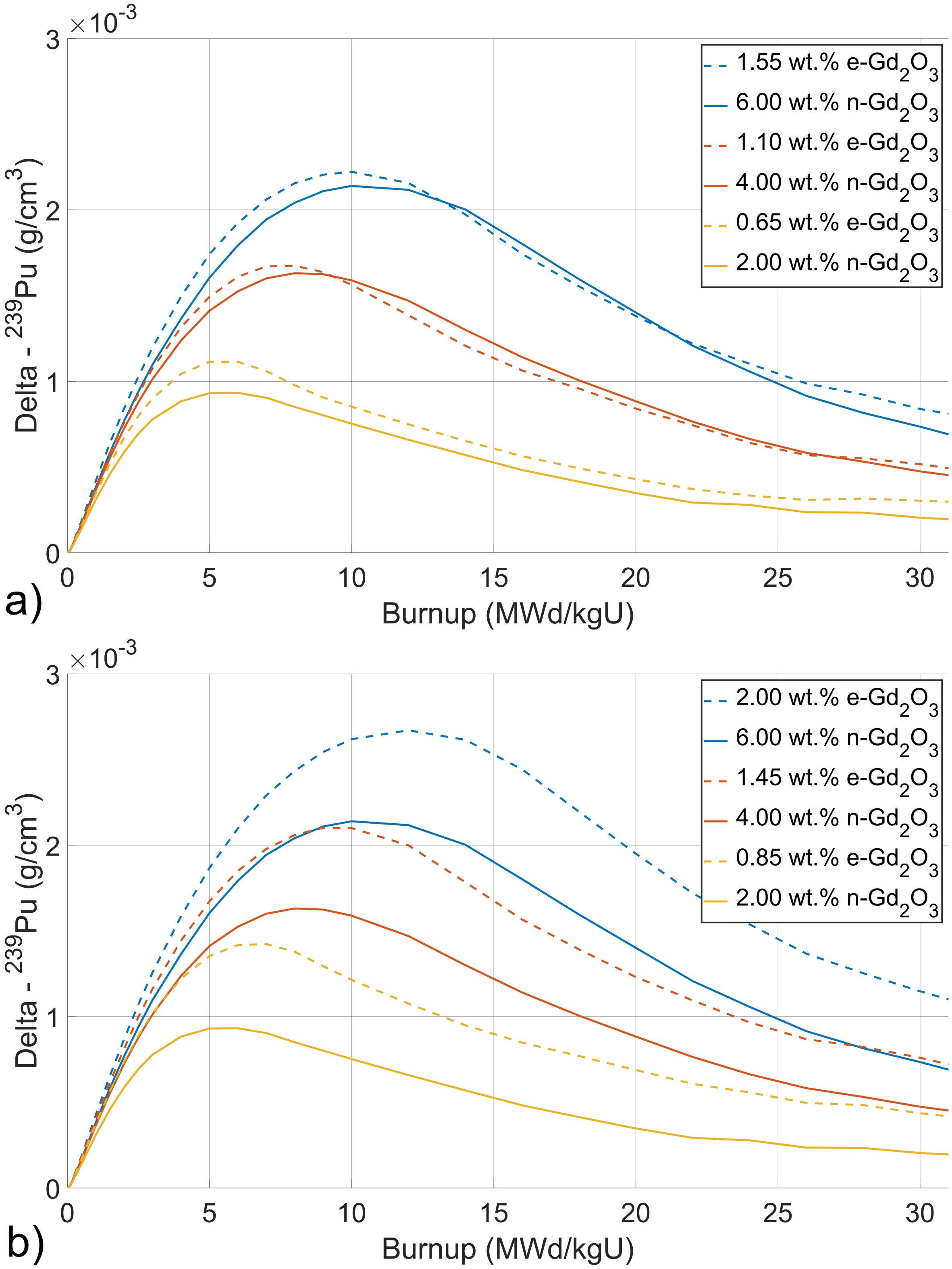

Figure 19 – ^{239}Pu breeding behaviour of fuel models using n-Gd_2O_3 and e-Gd_2O_3 (a) matches where peak point reactivity occurs at the same burnup step, and (b) matches with equal highest reactivity values, as compared with BA-free fuel model.

Figure 20, shows the breeding of ^{239}Pu in BA-containing rods of fuel models using 6.00 wt.% n-Gd_2O_3, and 1.55 wt.% e-Gd_2O_3, fuel models that have the peak point reactivity at the same burnup step. The trend of breeding ^{239}Pu is consistent across all other fuel models, making it unnecessary to elaborate on all of them.

Upon closer examination of Figure 20, it can be observed that the use of e-Gd_2O_3 had no noteworthy impact on the distribution of ^{239}Pu mass density across the pellet. In both fuel models, the mass density of ^{239}Pu rises from the centre of the pellet to the surface, peaking at the surface of the pellet. In comparison to the pellet centre, the mass density of ^{239}Pu at the surface is up to twice as high. This is due to the self-shielding effect, that ^{238}U atoms on the surface can capture more neutrons compared to those in the centre. Moreover, as reported earlier in Figure 18, the use of e-Gd_2O_3 as a fuel model leads to an increase in the production of ^{239}Pu.

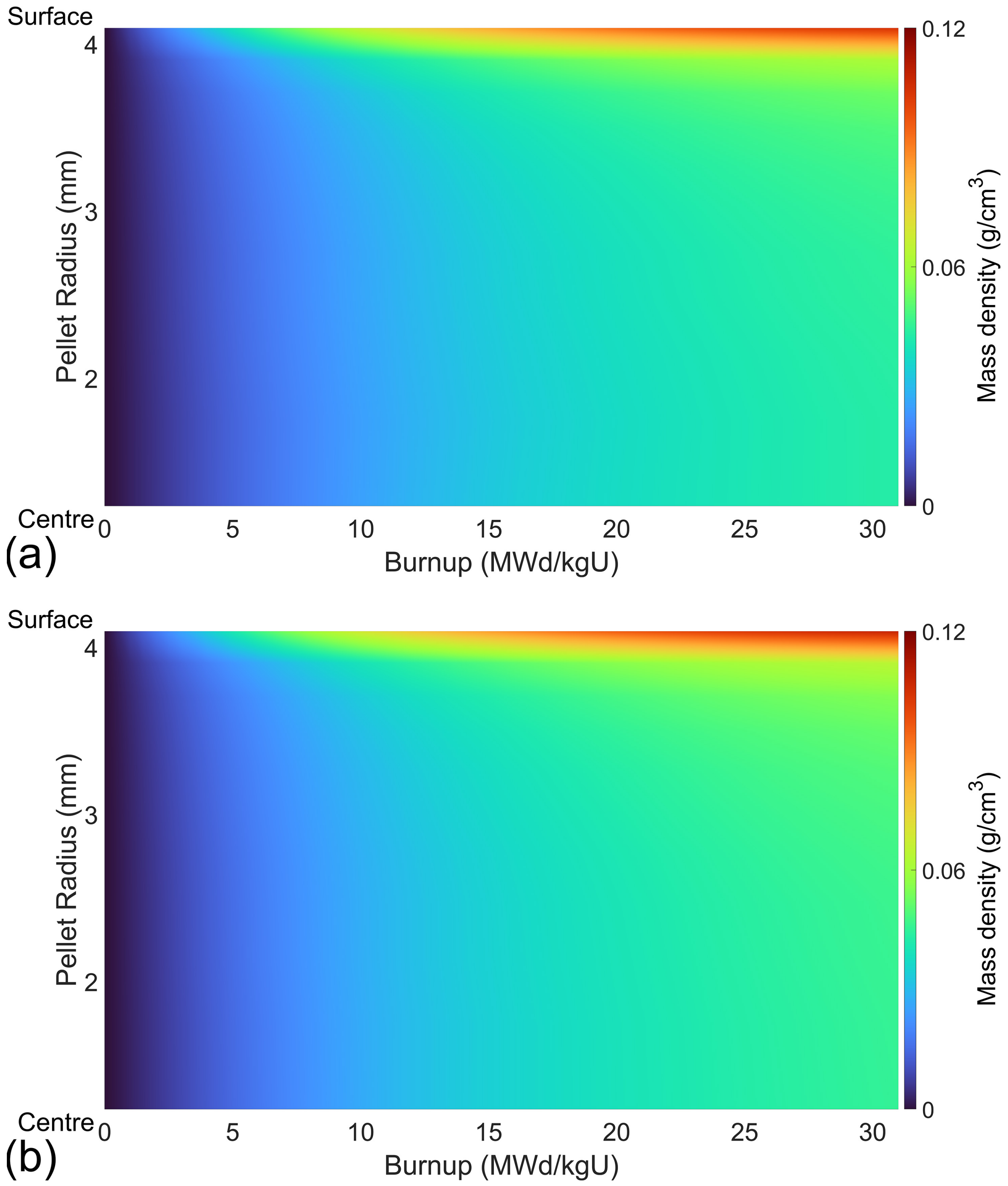

Figure 20 – Radial ^{239}Pu breeding in BA rods of fuel models using (a) 6.00 wt.% n-Gd_2O_3 and (b) 1.55 wt.% e-Gd_2O_3.

3.3.6 Serpent and CASMO-4 Comparison for Reactivity Determination

As mentioned previously in Section 3.2, the neutronic analyses in this chapter were conducted with the Serpent 2 Monte Carlo reactor physics code using the JEFF-3.1 nuclear data library. Monte Carlo simulations involve probabilistic modeling using random numbers to simulate the behaviour of particles in a nuclear system. In contrast, deterministic computational methods rely on solving partial differential equations to describe the behaviour of particles in the system. Monte Carlo simulations tend to be more resource-intensive, requiring significant computational power and time for convergence. Therefore, considering the numerous variables involved, conducting fuel cycle analyses using Monte Carlo method codes such as Serpent is not a practical approach. Consequently, as will be discussed in Chapter 4, fuel cycle analyses in this study were performed using Studsvik's CASMO-4/SIMULATE-3 advanced nuclear design code system.

However, the university release of the CASMO-4/SIMULATE-3 code system utilises the ENDF/B-VI neutron data library. Therefore, calculations performed with these two codes may differ due to the use of different libraries and the meshing options. To highlight these differences, fuel assemblies were modeled using the same dimensions and parameters for CASMO-4. Figures 21a and b show the infinite multiplication factor curves of the fuel models with n-$Gd_2O_3$and Δk_{inf}, respectively, obtained using Serpent and CASMO-4.

Upon examining Figure 21, it is observed that higher infinite multiplication factor values are obtained with Serpent. Additionally, as the burnups of the fuels approach 30.00 MWd/kgU, the disparity between the values obtained with the two codes decreases. Specifically, for fuel models containing 2.0 wt.%, 4.0 wt.%, and 6.0 wt.% n-Gd_2O_3, the differences between the two codes peak at 895 pcm, 749 pcm, and 691 pcm, and reduce to 257 pcm, 229 pcm and 218 pcm, respectively, at 30.00 MWd/kgU. In addition, at the beginning of the life of the BA-free fuel model this difference is 1066 pcm, which is the highest difference, while at 30.00 MWd/kgU it is 164 pcm.

In conclusion, when comparing the results obtained with Serpent and CASMO-4, it is evident that the infinite multiplication factor values differ between the two codes. Due to the inability to change the neutron data libraries of the codes used in the project, it was not possible to conduct a comprehensive benchmark test to identify the cause of these differences.

However, considering the trends of the curves obtained with both codes, it is observed that the discrepancy diminishes with the progress of the burnup. Therefore, it can be assumed that 3D full core analyses conducted with either code will yield results that are parallel.

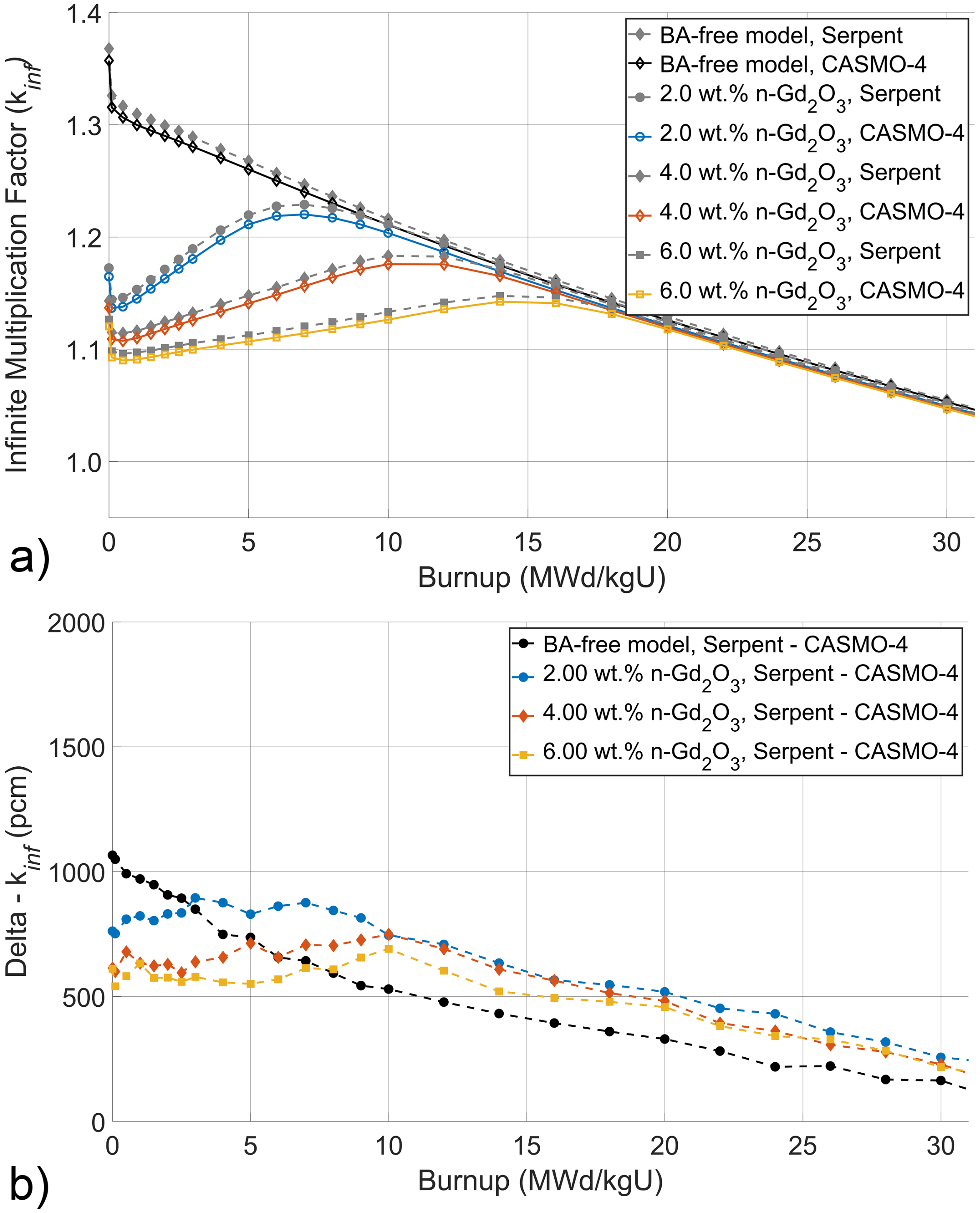

Figure 21 – Infinite multiplication factor of fuel models enriched with 5.00 wt.% ^{235}U obtained with Serpent and CASMO-4.

3.4 Chapter Summary

The impact of enriched Gd_2O_3 has been examined. The reactivity and depletion behaviour of BA and ^{239}Pu breeding were evaluated by comparing e-Gd_2O_3 to n-Gd_2O_3.

The results have shown that increasing the concentration of n-Gd_2O_3 in the fuel composition delays the time to reach peak reactivity due to the longer consumption of Gd isotopes. However, increasing the amount of n-Gd_2O_3 in the fuel composition also leads to an increase in the main non-neutron absorbing isotopes of Gd in the system, causing the residual reactivity penalty.

On the other hand, using e-Gd_2O_3 in the fuel composition can provide a similar reactivity behaviour to n-Gd_2O_3 while using a smaller volume of BA because a lower proportion of Gd_2O_3 is added to the fuel composition, resulting in a lower proportion of UO_2 being displaced from the fuel and providing higher reactivity. The use of e-Gd_2O_3 also reduces the amount of Gd isotopes that cause residual reactivity from the fuel matrix, resulting in a cleaner burn of the BA in the fuel.

Matching the n-Gd_2O_3 and e-Gd_2O_3 by arranging that peak point reactivity occurs at the same burnup point, the use of e-Gd_2O_3 allows higher reactivity to be obtained than n-Gd_2O_3. The amount of gained-reactivity rises significantly with the increase in n-Gd_2O_3/e-Gd_2O_3 ratio. On the other hand, matching the n-Gd_2O_3 and e-Gd_2O_3 by making equal the peak point reactivity, e-Gd_2O_3 can provide total gained-reactivity compared to n-Gd_2O_3 if there is high BA addition to the fuel composition.

The self-shielding effect prevents the depletion of BA isotopes in the fuel, which is exacerbated by the increase of ^{235}U in the fuel composition as a result of using e-Gd_2O_3. Furthermore, the rate of ^{239}Pu breeding reaches its highest concentration where BA isotopes are depleted, and the use of e-Gd_2O_3 provides a slightly higher ^{239}Pu production than the n-Gd_2O_3 usage. Thus, an increase in reactivity occurs with the use of fuel containing e-Gd_2O_3.

Overall, the study highlights the potential benefits of using e-Gd_2O_3 in fuel compositions, such as a reduction in the volume of BA needed, a cleaner burn of the BA in fuel, and the possibility of increasing ^{239}Pu content.

Chapter 4

Fuel Cycle Analysis of Enriched Gadolinium Oxide

A research paper titled “In-reactor behaviour and economic assessment of enriched gadolinia burnable absorbers” was published in Progress in Nuclear Energy using the methodology and a portion of the data presented in this chapter [111].

4.1 Chapter Overview

In this chapter, the fuel cycle analysis of e-Gd_2O_3, a potential burnable absorber candidate, is compared with n-Gd_2O_3, based on the neutronic analysis conducted in Chapter 3. A standard 3-loop PWR, designed by Westinghouse Electric Company, was used as the reference for the study. The impact of replacing n-Gd_2O_3 with e-Gd_2O_3 on peaking factors, such as nuclear enthalpy rise hot channel factor and heat flux hot channel factor, was explored. Furthermore, the alteration in the critical boron concentration, which is a vital element in the reactivity control, was investigated.

Reactivity feedback parameters, including moderator temperature coefficient, isothermal temperature coefficient, uniform Doppler coefficient, and boron coefficient, were examined for both e-Gd_2O_3 and n-Gd_2O_3, as these factors are crucial to ensuring reactor safety and stability. A comparison of the average axial relative power distribution and the assembly-wise 2D relative power fraction was conducted between e-Gd_2O_3 and n-Gd_2O_3. Lastly, the changes in fuel loading cost and the levelized cost of electricity (LCOE) resulting from the transition from n-Gd_2O_3 to e-Gd_2O_3 in the fuel cycle were assessed and compared.

4.2 Method

Simulations were conducted with Studsvik’s CASMO-4/SIMULATE-3 advanced nuclear design code system, utilising the ENDF/B-VI neutron data library. A standard Westinghouse Electric Company designed 3-loop PWR reactor was selected as the reference Nuclear

Power Plant for these simulations, with some NPP features, as provided in Studsvik's PWR equilibrium model [112], and simulation parameters provided in Table 2 [96], [113].

Although impurities may persist after the enrichment processes, this study assumed a complete enrichment of Gd_2O_3 with ^{157}Gd to explore the full potential of e-Gd_2O_3. The densities of UO_2/Gd_2O_3 fuels in the research were determined by utilising a method from the literature (see Equation 3) [104] and considering the fuel's density to be 95% of the theoretical value, taking into account the possible occurrence of porosity during the manufacturing process. Furthermore, instead of using axial blankets in the fuel rods, a 15.24 cm BA-free zone was chosen at both the upper and lower sections of the fuel assembly to achieve a more uniform axial power distribution.

Table 2 – Fuel design parameters and operation limits of a standard Westinghouse 3-loop PWR [96], [112], [113].

Parameter	Value
Reactor type	3-loop PWR
Coolant inlet temperature at full power (°C)	286
Power output (MWt/MWe)	2,900/964
System pressure (MPa)	15.5
Control rod material	Ag - In - Cd
Number of fuel assemblies	157
Rod array	17 × 17
Assembly pin pitch (cm)	1.26
Fuel pellet radius (cm)	0.410
Number of control rods/guide tube	24/1
Number of BA rods	24
Fuel assembly pitch (cm)	21.50
Fuel assembly height (cm)	365.76
Cladding material	Zircaloy-4
UO_2 fuel density (% of TD)	95
Nuclear Enthalpy Rise Hot Channel Factor ($F_{\Delta H}$)	≤ 1.66
Heat Flux Hot Channel Factor (F_Q)	≤ 2.41
Moderator temperature coefficient (pcm/°F)	$-50 \leq \text{MTC} < 0$
Shutdown margin (pcm)	≤ -1770
Cycle length (months)	18
Effective full power days	508
Refueling outages (days)	40

The two-group cross-section data for approximately 1,500 fuel designs were generated using CASMO-4, applying default azimuthal subdivision. These designs included a range of ^{235}U enrichment levels, from 4.40 to 4.95 wt.%, varying amounts of n-Gd_2O_3 in the fuel composition, ranging from 2.00 to 10.00 wt.%, alongside the corresponding levels of e-Gd_2O_3, which could demonstrate similar reactivity behaviour to n-Gd_2O_3. Following that, the required library for SIMULATE-3 was created utilising the CMS-Link software package.

In the operation of nuclear reactors, maintaining a balance between the reactor capacity factor and maximum discharge burnup is a critical aspect. A strategy with a lower batch number typically enhances the reactor's capacity factor. This method decreases the frequency of refueling outages, although it brings complexities in controlling excess reactivity, consequently improving the reactor's operational availability [114]. However, this approach often requires a compromise in terms of the discharge burnup level.

On the other hand, operation with a larger batch number leads to increased discharge burnup. The idea behind this that, with a greater number of batches, each fuel assembly remains in the reactor for a longer duration, resulting in higher burnup levels [114]. This extended use of fuel assemblies results in efficient utilisation of nuclear material. Nevertheless, this method demands more frequent refueling outages, which will adversely affect the reactor's capacity factor.

Therefore, in designing the reactor core, it is essential to consider the balance between the reactor capacity factor and discharge burnup which directly affect the economics. However, the primary focus of this study is not to achieve an optimized core design but to directly compare the use of e-Gd_2O_3 with n-Gd_2O_3. Consequently, it is important to note that the fuel loading pattern used in the simulations is not optimized.

For the simulations, it was assumed that the reactor was running 508 EFPDs in an 18-month fuel cycle with 64 fresh fuel assemblies (each having 24 BA rods as in Figure 8) for the transition from n-Gd_2O_3 to e-Gd_2O_3 and each refueling outage resulted in the discharge of 29 twice-burned and 35 once-burned fuel assemblies. this fuel core design, a 3-batch model, was adopted from existing literature. In addition, to prevent power peaks, fresh fuels were divided into four different groups. Figure 22 shows the distribution of the fresh, once-burned and twice-burned fuel assemblies in the reactor core as well as their previous locations.

Around 30,000 distinct combinations were examined in SIMULATE-3, considering the assumption that the fuel model featuring the highest ^{235}U enrichment would be employed in the group with the least amount of new fuel. This extensive testing enabled the determination of the optimal uranium enrichment and n-Gd_2O_3 levels necessary to achieve the targeted EFPDs in that specific fuel loading pattern. Following that, e-Gd_2O_3 was loaded as BA for the subsequent cycles.

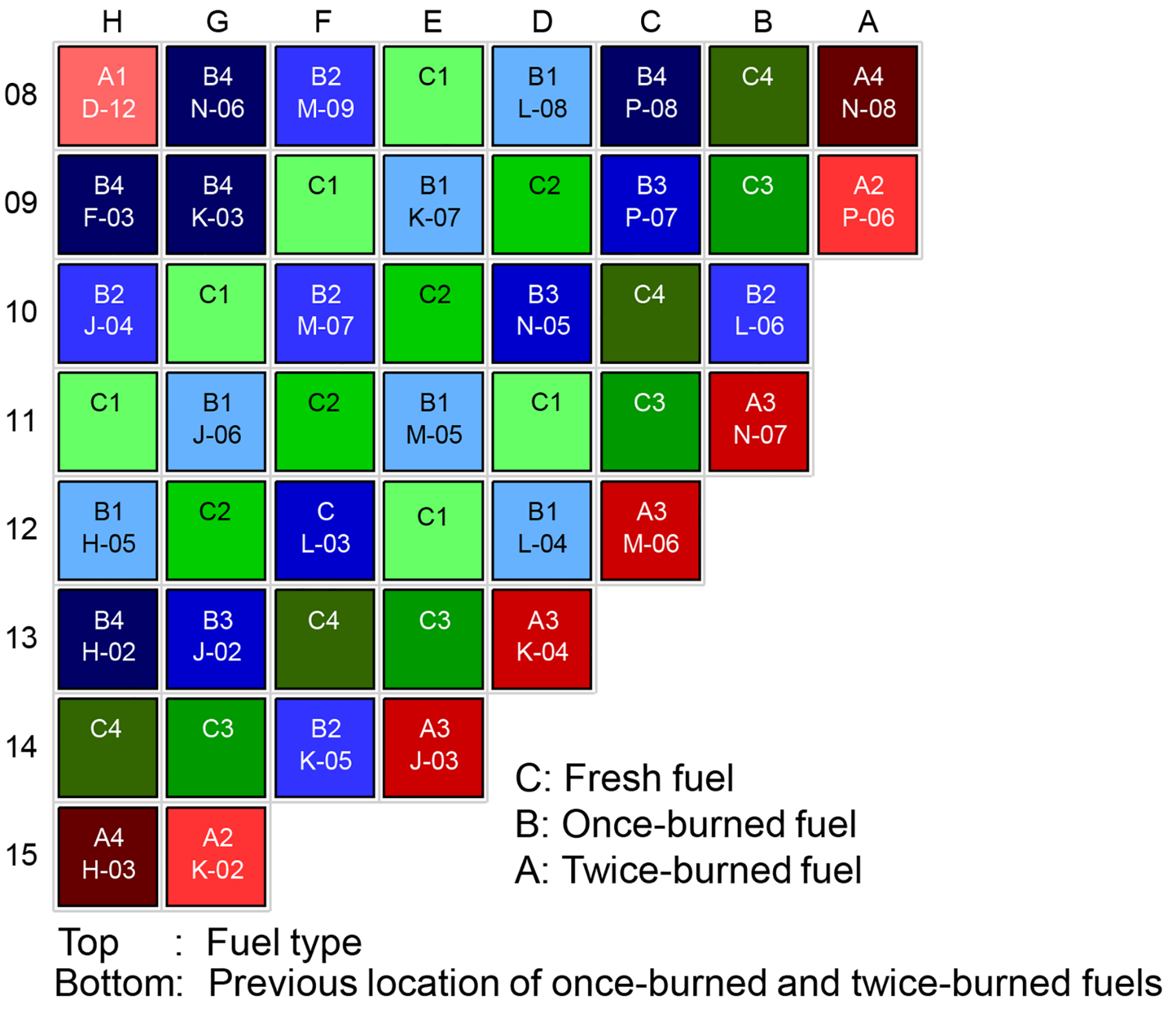

	H	G	F	E	D	C	B	A
08	A1 D-12	B4 N-06	B2 M-09	C1	B1 L-08	B4 P-08	C4	A4 N-08
09	B4 F-03	B4 K-03	C1	B1 K-07	C2	B3 P-07	C3	A2 P-06
10	B2 J-04	C1	B2 M-07	C2	B3 N-05	C4	B2 L-06	
11	C1	B1 J-06	C2	B1 M-05	C1	C3	A3 N-07	
12	B1 H-05	C2	C L-03	C1	B1 L-04	A3 M-06		
13	B4 H-02	B3 J-02	C4	C3	A3 K-04			
14	C4	C3	B2 K-05	A3 J-03				
15	A4 H-03	A2 K-02						

C: Fresh fuel
B: Once-burned fuel
A: Twice-burned fuel

Top : Fuel type
Bottom: Previous location of once-burned and twice-burned fuels

Figure 22 – Fuel loading layout. Adapted from [115].

Analysis of several fuel parameters was conducted including nuclear enthalpy rise hot channel factor, heat flux hot channel factor, critical boron concentration, moderator temperature coefficient, isothermal temperature coefficient, uniform Doppler coefficient and boron coefficient as well as shutdown margin. The effect of utilising e-Gd_2O_3 on average axial relative power distribution and assembly-wise 2D relative power fraction was examined. Additionally, the average axial 2D relative power fraction profile of the core was analysed across 12 axial nodes.

Taking into account the unit costs of all components of the front-end of the cycle, both the total fuel cost and the fuel cost per MWh were calculated. Alongside the expenses related to uranium purchase, conversion, enrichment, and fabrication, the cost associated with the enrichment process of e-Gd_2O_3 was also incorporated into the relevant scenario. Unit prices were set as low, medium, and high to accommodate unforeseen changes in unit costs that could occur in the future.

The calculation of component costs followed the methodology outlined by OECD/NEA [72]. In addition, component costs, parameter notation and fuel cycle data for the cost calculations are given in the Appendix. However, an illustration of the formulas employed in the computation of component costs is provided in Equation 4, in which X_i represents the quantity of the processed product, f_i denotes the operation's loss factor, P_i signifies the cost per unit, S_i indicates the rate of escalation, and t represents time, while t_i signifies the reference date for the monetary unit.

$$F_i = X_i \times F_i \times P_i \times (1 + S_i)^{t-t_i} \tag{4}$$

4.3 Results and Discussion

4.3.1 Fuel Cycle Analysis

In the n-Gd_2O_3 usage scenario, to reach 508 EFPDs within design and operation limits, various combinations were tested by separately modifying the ^{235}U enrichment levels by 0.50 wt.% and BA percentages by 1.00 wt.% at each step, using the fuel loading scheme previously shown in Figure 22. Among these, the combination with the lowest initial CBC value was chosen as the reference for examination in the study.

Table 3 shows the ^{235}U enrichment levels, the percentage of burnable absorbers and the labels of the core positions of the fuels required to achieve 508 EFPDs within the operational and safety limits for the n-Gd_2O_3 usage scenario.

Table 3 – Fuel configuration parameters for achieving 508 EFPDs for n-Gd_2O_3 and e-Gd_2O_3.

Number of fresh FAs	Uranium enrichment (wt.%)	BA level (wt.%)	In-core position
20	4.75	10.00	C1
16	4.80	10.00	C2
16	4.95	6.00	C3
12	4.95	4.00	C4

Results of the simulations showed that a cycle with n-Gd_2O_3 necessitates 20 fuel assemblies at 4.75 wt.% ^{235}U enrichment and 10.00 wt.% BA loading, 16 fuel assemblies at 4.80 wt.% ^{235}U enrichment and 10.00 wt.% BA loading, 16 fuel assemblies at 4.95 wt.% ^{235}U enrichment and 6.00 wt.% BA loading, and 12 fuel assemblies at 4.95 wt.% ^{235}U enrichment and 4.00 wt.% BA loading.

As demonstrated earlier in Section 3.3.4, the ratio of e-Gd_2O_3 exhibiting the same reactivity behaviour as n-Gd_2O_3, referred to as the n-Gd_2O_3/e-Gd_2O_3 ratio, approaches 1/4 with an increasing amount of n-Gd_2O_3. For ease in simulations, this ratio was assumed to be 1/4 for all fuel models. In fuel models with 4.75 wt.% and 4.80 wt.% ^{235}U enrichment levels, instead of 10.00 wt.% n-Gd_2O_3 as BA, 2.50 wt.% e-Gd_2O_3 was used. In the fuel model with a 4.95 wt.% ^{235}U enrichment level and 6.00 wt.% n-Gd_2O_3 BA level, 1.50 wt.% e-Gd_2O_3 was employed. Finally, in the fuel model with a 4.95 wt.% ^{235}U enrichment level and 4.00 wt.% n-Gd_2O_3 fuel level, 1.00 wt.% e-Gd_2O_3 was utilised.

When comparing e-Gd_2O_3 and n-Gd_2O_3 in transition and equilibrium cycles, it is important to analyse several key factors, such as critical boron concentration, nuclear enthalpy rise hot channel factor, heat flux hot channel factor, moderator temperature coefficient, isothermal temperature coefficient, uniform Doppler coefficient, and boron coefficient. By evaluating these parameters, the differences between fuels in the context of transition and equilibrium cycles can be better understood.

Table 4 displays the results of the transition and equilibrium cycles' critical boron concentration, effective multiplication factor at beginning of the cycle, maximum nuclear enthalpy rise hot channel factor, and maximum heat flux hot channel factor, burnup, and cycle EFPDs for both the scenarios reported in Table 3, where 508 EFPDs is achieved using n-Gd_2O_3, and the scenario where the BA ratio is reduced to 1/4 of n-Gd_2O_3 for each fuel group without changing the ^{235}U enrichment level, and e-Gd_2O_3 is used as BA. The cycle labelled as cycle "0" in the table is considered the final cycle where n-Gd_2O_3 was employed as a burnable absorber. From cycle 1 onwards, as BA e-Gd_2O_3 is employed.

Table 4 – Comparison of cycle parameters for n-Gd_2O_3 and e-Gd_2O_3

Cycle Number	Cycle Definition	CBC - BOC (ppm)	CBC at 10 MWd/kgU (ppm)	k_{eff} - BOC	Maximum $F_{\Delta H}$	Maximum F_Q	Cycle Burnup (MWd/kgU)	Cycle EFPDs
-1	n-Gd_2O_3 equilibrium cycle	1,267.7	745.7	1.07886	1.608	1.887	20.187	507.6
0	n-Gd_2O_3 equilibrium cycle	1,267.8	745.7	1.07886	1.608	1.888	20.188	507.6
1	e-Gd_2O_3 transition cycle first feed	1,380.2	1020.7	1.08570	1.629	1.918	20.816	524.8
2	e-Gd_2O_3 transition cycle second feed	1,398.1	1022.0	1.08692	1.639	1.929	20.886	528.0
3	e-Gd_2O_3 transition cycle third feed	1,390.2	1015.6	1.08646	1.636	1.928	20.821	526.9
4*	e-Gd_2O_3 equilibrium cycle	1,392.0	1016.8	1.08656	1.638	1.927	20.830	527.1
5	e-Gd_2O_3 equilibrium cycle	1,391.6	1016.6	1.08654	1.637	1.928	20.828	527.1
6	e-Gd_2O_3 equilibrium cycle	1,391.7	1016.6	1.08655	1.638	1.927	20.828	527.1

As shown in Table 4, following the third feed, the cycle parameters stabilized, and the equilibrium cycle is achieved starting from the fourth cycle.

As previously mentioned in Chapter 3, using e-Gd_2O_3, 100 wt.% enriched with the main neutron-absorbing isotope ^{157}Gd and free of isotopes causing residual reactivity penalty, enables a reduction in the BA levels. This leads to an increased amount of uranium of the fuel which means more uranium fuel can be loaded into the reactor. When using e-Gd_2O_3 without altering the ^{235}U uranium enrichment level, it becomes feasible to load an extra ~150 kg of UO_2 fuel into the reactor by loading one-quarter of the e-Gd_2O_3 compared to n-Gd_2O_3 in each cycle.

Considering these facts, an examination of the n-Gd_2O_3 and e-Gd_2O_3 equilibrium cycles in Table 4 reveals that using n-Gd_2O_3 results in a burnup of approximately 20.188 MWd/kgU, while using e-Gd_2O_3 leads to a 3.2% increase, achieving 20.83 MWd/kgU. Additionally, the n-Gd_2O_3 equilibrium cycle has ~508 EFPDs, whereas the e-Gd_2O_3 equilibrium cycle has ~527 EFPDs, corresponding to a 3.7% increase (about 19 EFPDs).

Upon examining the critical boron concentrations of the n-Gd_2O_3 and e-Gd_2O_3 equilibrium cycles, it is observed that the critical boron concentration required for reactor operation increases due to the elevated amount of uranium, and consequently, the fissile isotope content, resulting from the use of e-Gd_2O_3. In the n-Gd_2O_3 equilibrium cycle, the critical boron concentration is 1,267.8 ppm at the beginning of the cycle, which increases by approximately 9.8% (~124 ppm) in the e-Gd_2O_3 equilibrium cycle, reaching 1,392.0 ppm. Conversely, the critical boron concentration at 10.00 MWd/kgU shows an approximate 36.4% (~271 ppm) increase, and necessitates 1,016.8 ppm in the e-Gd_2O_3 equilibrium cycle while it is 745.7 ppm in the n-Gd_2O_3 equilibrium cycle. Moreover, the BOC k_{eff} value is 1.07886 in the n-Gd_2O_3 equilibrium cycle while it increases by ~770 pcm to 1.08656 in the e-Gd_2O_3 equilibrium cycle.

On the other hand, when examining the maximum nuclear enthalpy rise hot channel factor and maximum heat flux hot channel factor values for the n-Gd_2O_3 and e-Gd_2O_3 equilibrium cycles, it can be observed that the maximum nuclear enthalpy rise hot channel factor, which is 1.606 in the n-Gd_2O_3 equilibrium cycle, increases by approximately 2% to 1.639 in the e-Gd_2O_3 equilibrium cycle. Additionally, the maximum heat flux hot channel factor value increases by around 2.0% from 1.888 to 1.927. The increases in the maximum nuclear enthalpy rise hot channel factor and maximum heat flux hot channel factor in the equilibrium cycles are within the safety and operational limits. Additionally, it can be observed that these values do not exceed the safety and operational limits in the n-Gd_2O_3 to e-Gd_2O_3 transition cycles.

As the EFPDs rise with the use of e-Gd_2O_3, there is an accompanying increase in the overall fuel loading costs for each cycle due to the additional expenses associated with the increase in uranium to be loaded into the reactor and the process of enriching Gd_2O_3 with ^{157}Gd. Despite these increased costs, the 19-day extension in EFPDs might result in a lower fuel cost per kWe. Certainly, it should not be noted that sensitivity analyses are necessary to support this assumption.

A crucial aspect to consider is that the refueling outage will stay constant at 40 days and each cycle will be 18 months and 19 days. Consequently, the lack of a standard may result in some refueling outages aligning with periods of peak electricity demand, as demonstrated in Chapter 1.4. For this reason, maintaining a consistent 18-month cycle with 508 EFPDs proves to be a more effective scheduling approach when e-Gd_2O_3 is used as BA.

In this context, the required ^{235}U enrichment for the e-Gd_2O_3 usage scenario has been determined by keeping constant the e-Gd_2O_3 ratios of the fuel groups, decreasing the ^{235}U enrichment levels by 0.01% for all fuel groups in each step. Table 5 illustrates the required ^{235}U enrichment levels to reach 508 EFPDs for both n-Gd_2O_3 and e-Gd_2O_3 usage scenarios along with BA levels, and the core position labels for all fuel groups.

When examining Table 5, it can be seen that to reach 508 EFPDs by using e-Gd_2O_3 at a quarter of the proportion of n-Gd_2O_3, the necessary ^{235}U enrichment levels are as follows: 4.59 wt.% instead of 4.75 wt.% in fuel group C1, 4.64 wt.% instead of 4.80 wt.% in fuel group C2, 4.79 wt.% instead of 4.95 wt.% in fuel group C3, and 4.79 wt.% instead of 4.95 wt.% in fuel group C4.

Table 6 shows the critical boron concentration, effective multiplication factor at BOC, maximum nuclear enthalpy rise hot channel factor and heat flux hot channel factor, burnup, and cycle EFPDs for the transition and equilibrium cycles of both the n-Gd_2O_3 and e-Gd_2O_3 usage scenarios for 508 EFPDs.

Table 5 – Fuel configuration parameters for n-Gd_2O_3 and e-Gd_2O_3 usage scenarios, achieving 508 EFPDs.

Number of fresh FAs	Fuels with n-Gd_2O_3		Fuels with e-Gd_2O_3		In-core position
	^{235}U enrichment (wt.%)	BA level (wt%.)	^{235}U enrichment (wt.%)	BA level (wt.%)	
20	4.75	10.00	4.59	2.50	C1
16	4.80	10.00	4.64	2.50	C2
16	4.95	6.00	4.79	1.50	C3
12	4.95	4.00	4.79	1.00	C4

Table 6 – Comparison of cycle parameters for n-Gd_2O_3 and e-Gd_2O_3

Cycle Number	Cycle Definition	CBC - BOC (ppm)	CBC at 10 MWd/kgU (ppm)	k_{eff} - BOC	Maximum $F_{\Delta H}$	Maximum F_Q	Cycle Burnup (MWd/kgU)	Cycle EFPDs
-1	n-Gd_2O_3 equilibrium cycle	1,267.7	745.7	1.07886	1.608	1.887	20.187	507.6
0	n-Gd_2O_3 equilibrium cycle	1,267.8	745.7	1.07886	1.608	1.888	20.188	507.6
1	e-Gd_2O_3 transition cycle first feed	1,300.4	968.8	1.08160	1.627	1.910	20.261	510.8
2	e-Gd_2O_3 transition cycle second feed	1,285.7	947.9	1.08179	1.634	1.931	20.099	508.1
3	e-Gd_2O_3 transition cycle third feed	1,286.5	947.3	1.08191	1.635	1.926	20.077	508.1
4*	e-Gd_2O_3 equilibrium cycle	1,285.8	947.1	1.08187	1.635	1.927	20.074	508.0
5	e-Gd_2O_3 equilibrium cycle	1,286.0	947.0	1.08188	1.635	1.927	20.074	508.0
6	e-Gd_2O_3 equilibrium cycle	1,286.0	947.0	1.08188	1.635	1.927	20.074	508.0

When the critical boron concentrations of the n-Gd_2O_3 and e-Gd_2O_3 equilibrium cycles are compared, it is seen that the critical boron concentration needed for reactor operation increases due to the elevated uranium content, and thus the fissile isotope content, brought by the use of e-Gd_2O_3. The critical boron concentration in the n-Gd_2O_3 equilibrium cycle is 1,267.8 ppm at the beginning of the cycle while it is 1,285.8 pcm in the e-Gd_2O_3 equilibrium cycle, corresponding to an increase by roughly 1.4% (18 ppm). Meanwhile, at 10.00 MWd/kgU, the critical boron concentration increases by approximately 27% (201 ppm) to 947.1 ppm in the e-Gd_2O_3 equilibrium cycle whereas it is 745.7 ppm in the n-Gd_2O_3 equilibrium cycle. Additionally, while the BOC k_{eff} value is 1.07886 in n-Gd_2O_3 equilibrium cycle, it increases by $\sim$300 pcm in e-Gd_2O_3 equilibrium cycle.

On the other hand, when comparing the maximum values for the maximum heat flux hot channel factor and the maximum nuclear enthalpy rise hot channel factor for the n-Gd_2O_3 and e-Gd_2O_3 equilibrium cycles, it can be seen that the maximum nuclear enthalpy rise hot channel factor, which is 1.608 in the n-Gd_2O_3 equilibrium cycle, increases by about 1.7% to 1.635 in the e-Gd_2O_3 equilibrium cycle. Additionally, the maximum heat flux hot channel factor value rises from 1.888 to 1.927 by around 2.0%. Furthermore, these values remain within the safety and operational limits in the n-Gd_2O_3 to e-Gd_2O_3 transition cycles.

4.3.2 Reactivity Feedback Parameters and Shutdown Margin

An examination of reactivity feedback parameters was conducted, as these factors are essential in maintaining safety and stability of the reactor. Figure 23 shows the curves for the moderator temperature coefficient, isothermal temperature coefficient, uniform Doppler coefficient, and boron coefficient of both n-Gd_2O_3 and e-Gd_2O_3 equilibrium cycles. Specifically, Figure 23a presents the curves for n-Gd_2O_3, while Figure 23b illustrates the curves for e-Gd_2O_3.

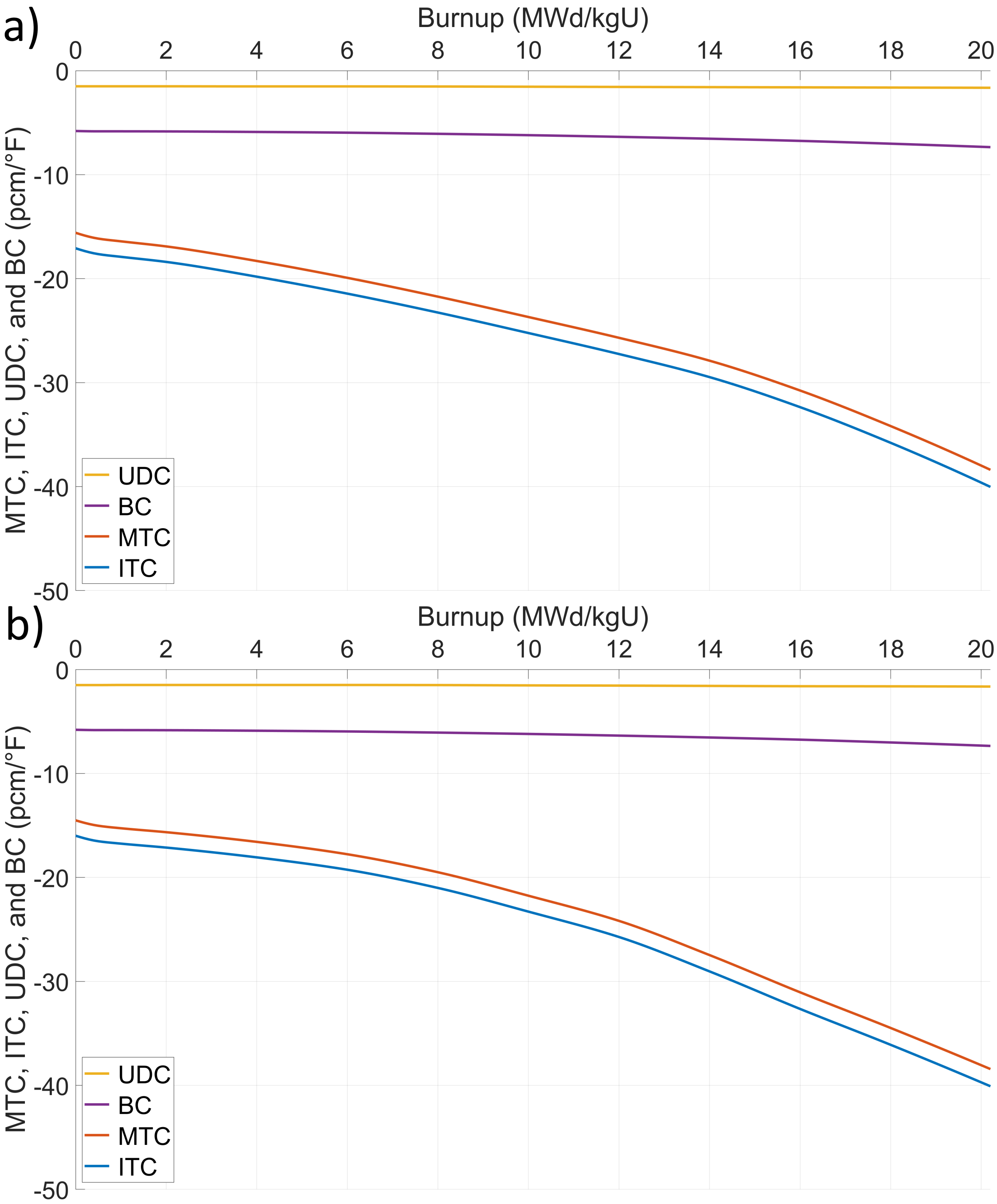

Figure 23 – Moderator temperature coefficient (MTC), isothermal temperature coefficient (ITC), uniform Doppler coefficient (UDC), and boron coefficient (BC) curves of (a) n-Gd_2O_3 equilibrium cycle and (b) e-Gd_2O_3 equilibrium cycle.

Upon analysing Figure 23, no noteworthy differences are detected in the uniform Doppler coefficient and boron coefficient between the n-Gd_2O_3 and e-Gd_2O_3 equilibrium cycles, at a first glance. However, changes up to 2 pcm/°F were observed in the moderator temperature coefficient and isothermal temperature coefficient values when the e-Gd_2O_3 equilibrium cycle was compared to the n-Gd_2O_3 equilibrium cycle.

For instance, examining the table, it is evident that the moderator temperature coefficient is -15.61 pcm/°F at the beginning of the n-Gd_2O_3 equilibrium cycle, while it is -14.53 pcm/°F at the beginning of e-Gd_2O_3 equilibrium cycle. At 10.00 MWd/kgU, the for n-Gd_2O_3 and e-Gd_2O_3 equilibrium cycles, the moderator temperature coefficients are -23.69 pcm/°F and -21.79 pcm/°F, respectively. Additionally, at the end of the cycles, they are -37.96 pcm/°F and -38.06 pcm/°F, respectively. The difference between n-Gd_2O_3 and e-Gd_2O_3 reaches the highest value in the middle of the cycle and reaches the lowest value at the end of the cycle.

Conversely, the isothermal temperature coefficient for the n-Gd_2O_3 equilibrium cycle is -17.11 pcm/°F, whereas it measures -16.01 pcm/°F for the e-Gd_2O_3 equilibrium cycle. At 10.00 MWd/kgU, the equilibrium cycles of n-Gd_2O_3 and e-Gd_2O_3 have values of -25.24 pcm/°F and -23.31 pcm/°F, respectively, while they are -39.61 pcm/°F and -39.71 pcm/°F at the end of the cycles, respectively. Similarly, as with the moderator temperature coefficient, the difference in isothermal temperature coefficient values between the n-Gd_2O_3 and e-Gd_2O_3 equilibrium cycles reaches its peak value at the middle of the cycle and attains its lowest value by the end of the cycle. Taking these findings into account, it can be concluded that the use of e-Gd_2O_3 instead of n-Gd_2O_3 does not negatively impact reactivity feedback parameters.

On the other hand, the shutdown margin, a crucial aspect of reactor safety, was calculated for both the e-Gd_2O_3 and n-Gd_2O_3 equilibrium cycles. Table 7 displays the shutdown margins at the beginning and end of the equilibrium cycles for both n-Gd_2O_3 and e-Gd_2O_3. Upon initial observation, there is no significant difference in the shutdown margins between the n-Gd_2O_3 and e-Gd_2O_3 equilibrium cycles. However, higher shutdown margins are noted at the beginning of the cycle compared to the end of the cycle in both equilibrium cycles. This is attributed to the presence of BA in the reactor core. However, BA is almost entirely depleted during the cycle and does not persist at the end of the cycle, as explained in Section 3.3.4.

Specifically, the shutdown margin of the n-Gd_2O_3 equilibrium cycle is -3,734 pcm while it is -3,737 pcm for the e-Gd_2O_3 equilibrium cycle, at the beginning of both cycles. Conversely, when examining the results at the end of the cycle, the shutdown margin of the n-Gd_2O_3 equilibrium cycle is -2,324 pcm, whereas it is -2,364 pcm for the e-Gd_2O_3 equilibrium cycle. The relatively high shutdown margin of e-Gd_2O_3 in the equilibrium cycle is associated with its lower ^{235}U enrichment loading level.

Table 7 – Shutdown margins of n-Gd_2O_3 and e-Gd_2O_3 equilibrium cycles

Fuel Type	BOC (pcm)	EOC (pcm)
n-Gd_2O_3	-3,734	-2,324
e-Gd_2O_3	-3,737	-2,264

4.3.3 Axial and Assembly-wise Relative Power Fractions

The average axial relative power distribution was investigated to assess the changes brought about by the utilisation of e-Gd_2O_3 on the axial power profile. Figure 24 presents the average axial 2D relative power distribution graphs for the n-Gd_2O_3 and e-Gd_2O_3 equilibrium cycles at the beginning and end of each cycle. Upon examining Figure 24, it becomes apparent that the use of e-Gd_2O_3 does not lead to significant impact on the average axial relative power profile.

When comparing the results, a deviation of ±2% is observed over the fuel assemblies at the beginning of the cycles. However, at the end of the cycle, the average axial relative power fraction in the lower half of the fuel assemblies experiences reductions of up to 5% at about 90cm above the bottom of the reactor core, while the upper half of the fuel assemblies sees increases of up to 7% at about 335 cm above the bottom of reactor core.

An analysis of the assembly-wise 2D relative power fraction changes resulting from the use of e-Gd_2O_3 was conducted. Figure 25 illustrates the 2D relative power fraction comparisons for the equilibrium cycles of both n-Gd_2O_3 and e-Gd_2O_3 at beginning and end of the cycles.

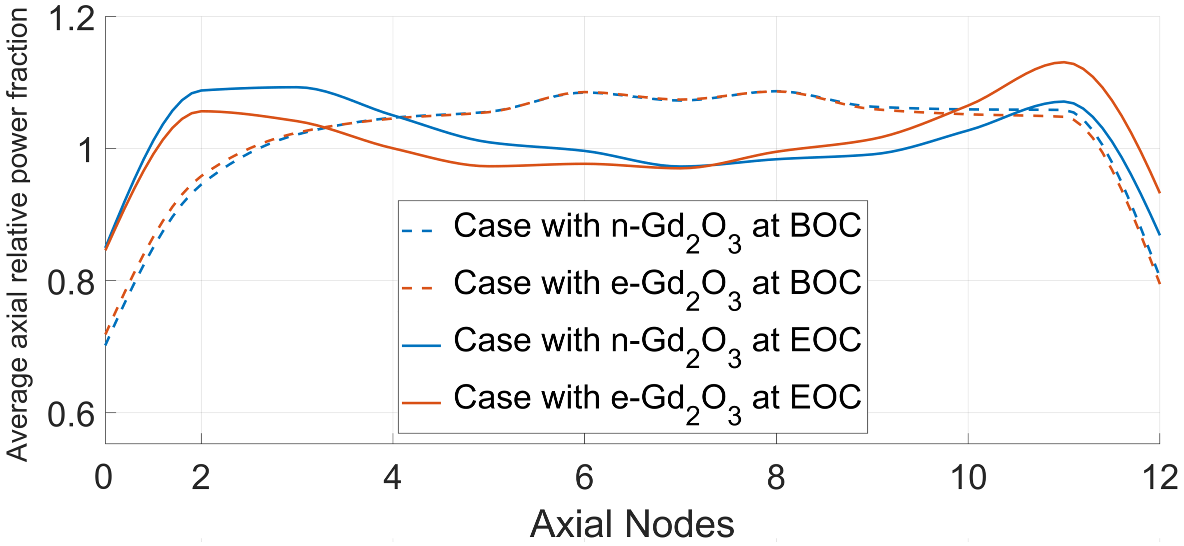

Figure 24 – n-Gd_2O_3 and e-Gd_2O_3 equilibrium cycles' average axial relative power profiles.

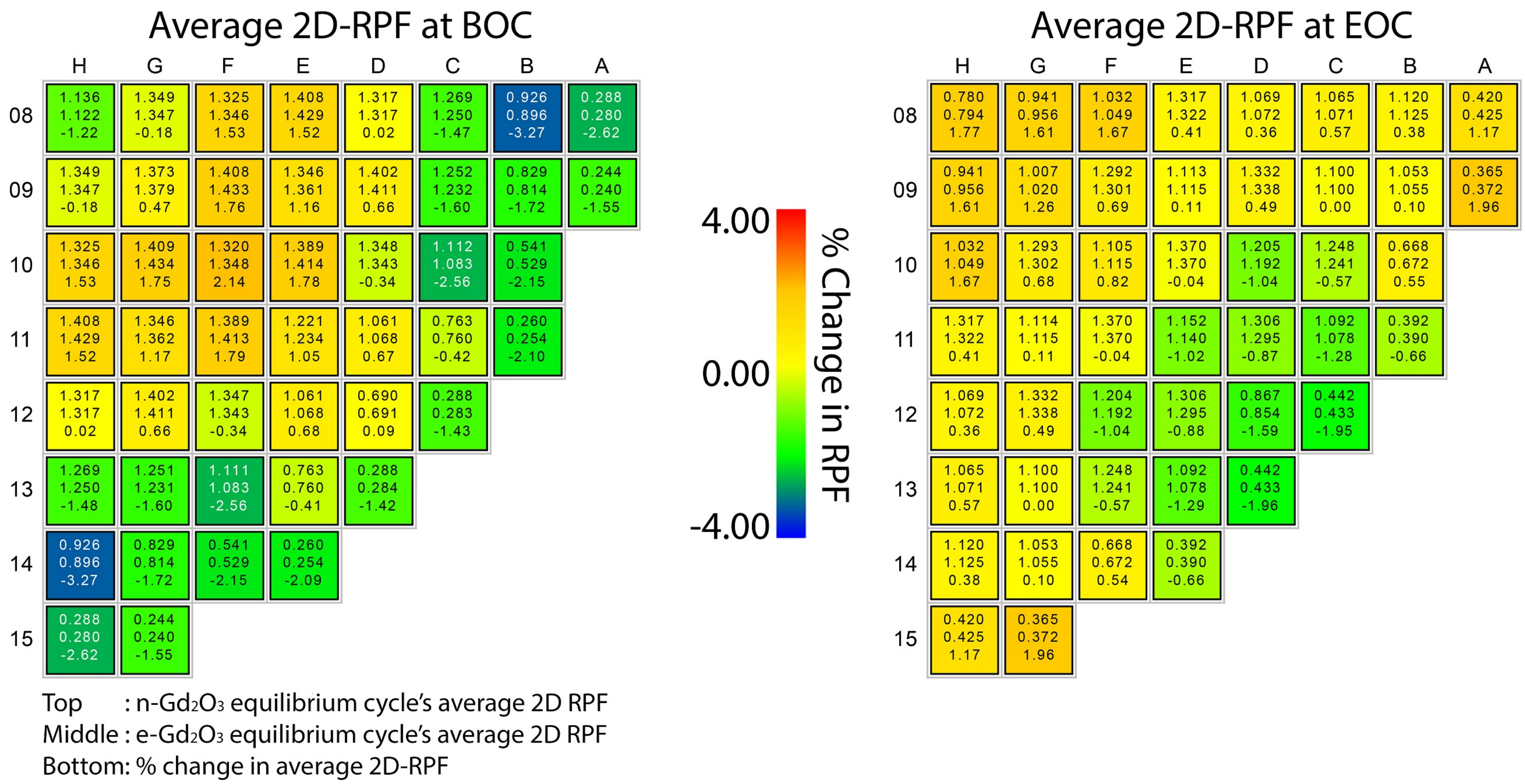

Average 2D-RPF at BOC

	H	G	F	E	D	C	B	A
08	1.136 1.122 -1.22	1.349 1.347 -0.18	1.325 1.346 1.53	1.408 1.429 1.52	1.317 1.317 0.02	1.269 1.250 -1.47	0.926 0.896 -3.27	0.288 0.280 -2.62
09	1.349 1.347 -0.18	1.373 1.379 0.47	1.408 1.433 1.76	1.346 1.361 1.16	1.402 1.411 0.66	1.252 1.232 -1.60	0.829 0.814 -1.72	0.244 0.240 -1.55
10	1.325 1.346 1.53	1.409 1.434 1.75	1.320 1.348 2.14	1.389 1.414 1.78	1.348 1.343 -0.34	1.112 1.083 -2.56	0.541 0.529 -2.15	
11	1.408 1.429 1.52	1.346 1.362 1.17	1.389 1.413 1.79	1.221 1.234 1.05	1.061 1.068 0.67	0.763 0.760 -0.42	0.260 0.254 -2.10	
12	1.317 1.317 0.02	1.402 1.411 0.66	1.347 1.343 -0.34	1.061 1.068 0.68	0.690 0.691 0.09	0.288 0.283 -1.43		
13	1.269 1.250 -1.48	1.251 1.231 -1.60	1.111 1.083 -2.56	0.763 0.760 -0.41	0.288 0.284 -1.42			
14	0.926 0.896 -3.27	0.829 0.814 -1.72	0.541 0.529 -2.15	0.260 0.254 -2.09				
15	0.288 0.280 -2.62	0.244 0.240 -1.55						

Average 2D-RPF at EOC

	H	G	F	E	D	C	B	A
08	0.780 0.794 1.77	0.941 0.956 1.61	1.032 1.049 1.67	1.317 1.322 0.41	1.069 1.072 0.36	1.065 1.071 0.57	1.120 1.125 0.38	0.420 0.425 1.17
09	0.941 0.956 1.61	1.007 1.020 1.26	1.292 1.301 0.69	1.113 1.115 0.11	1.332 1.338 0.49	1.100 1.100 0.00	1.053 1.055 0.10	0.365 0.372 1.96
10	1.032 1.049 1.67	1.293 1.302 0.68	1.105 1.115 0.82	1.370 1.370 -0.04	1.205 1.192 -1.04	1.248 1.241 -0.57	0.668 0.672 0.55	
11	1.317 1.322 0.41	1.114 1.115 0.11	1.370 1.370 -0.04	1.152 1.140 -1.02	1.306 1.295 -0.87	1.092 1.078 -1.28	0.392 0.390 -0.66	
12	1.069 1.072 0.36	1.332 1.338 0.49	1.204 1.192 -1.04	1.306 1.295 -0.88	0.867 0.854 -1.59	0.442 0.433 -1.95		
13	1.065 1.071 0.57	1.100 1.100 0.00	1.248 1.241 -0.57	1.092 1.078 -1.29	0.442 0.433 -1.96			
14	1.120 1.125 0.38	1.053 1.055 0.10	0.668 0.672 0.54	0.392 0.390 -0.66				
15	0.420 0.425 1.17	0.365 0.372 1.96						

Top : n-Gd_2O_3 equilibrium cycle's average 2D RPF
Middle : e-Gd_2O_3 equilibrium cycle's average 2D RPF
Bottom: % change in average 2D-RPF

Figure 25 – n-Gd_2O_3 and e-Gd_2O_3 equilibrium cycles' assembly-wise average 2D relative power fraction profiles.

When examining Figure 25a for the beginning of the cycles, the most significant decrease of 3.27% occurs at locations B-08 and H-14, which contain fresh fuel. The fuels at these locations have a 4.95 wt.% ^{235}U enrichment and 4.00 wt.% n-Gd_2O_3 for the n-Gd_2O_3 equilibrium cycle, while the e-Gd_2O_3 equilibrium cycle has fuels with 4.79 wt.% ^{235}U enrichment and 1.00 wt.% e-Gd_2O_3. Simultaneously, the largest increase of 2.14% is observed at the F-10 location, where the fuel has been burned once. At this location, the fuels for the n-Gd_2O_3 and e-Gd_2O_3 equilibrium cycles have ^{235}U enrichment of 4.80 wt.% and 4.64 wt.%, respectively, along with 10.00 wt.% n-Gd_2O_3 and 2.50 wt.% e-Gd_2O_3.

When examining Figure 25b for the end of the cycles, the most substantial decrease, approximately 1.95%, takes place at locations C-12 and D-13, where fuels have been burned twice and are slated for discharge in the next cycle. The fuels at these locations for the n-Gd_2O_3 equilibrium cycle have a 4.95 wt.% ^{235}U enrichment level and a 6.00 wt% n-Gd_2O_3 level, while those for the e-Gd_2O_3 equilibrium cycle have a 4.79 wt.% ^{235}U enrichment level and a 1.50 wt.% e-Gd_2O_3 level. Additionally, the largest increase of 1.96% is detected at locations A-09 and G-15, which contain fuels that have been burned twice and are set for discharge in the next cycle. For the n-Gd_2O_3 and e-Gd_2O_3 equilibrium cycles, the fuels at these locations have ^{235}U enrichment levels of 4.80 wt.% and 4.64 wt.%, respectively, while containing 10.00 wt.% n-Gd_2O_3 and 2.50 wt.% e-Gd_2O_3.

In general, using e-Gd_2O_3 instead of n-Gd_2O_3 does not result in any adverse effects on reactivity feedback parameters, such as moderator temperature coefficient, isothermal temperature coefficient, uniform Doppler coefficient, and boron coefficient. Furthermore, when assessing the average axial relative power distribution and assembly-wise 2D relative power fraction, no significant negative impact is observed. On the contrary, although it is not significant, it positively affects the shutdown margin as it requires a lower ^{235}U enrichment level. The absence of negative characteristics of e-Gd_2O_3 compared to n-Gd_2O_3 makes it a promising burnable absorber candidate.

4.3.4 Economic Assessment

The economic aspects of the two equilibrium cycles involving the use of n-Gd_2O_3 and e-Gd_2O_3, both having 508 EFPDs, were assessed. As previously described in the method section, the evaluation took into account both the fuel loading expenses for each cycle and the $LCOE_{front-end}$ for the equilibrium cycles.

Detailed information on the cost calculations for the low, nominal, and high price scenarios in the context of both n-Gd_2O_3 and e-Gd_2O_3 usage were calculated considering the change in the cost of each component. Table 8 presents the individual component costs categorized as low, nominal, and high.

Table 8 – Component costs for n-Gd_2O_3 and e-Gd_2O_3 equilibrium cycles

	Fuel loading cost of n-Gd_2O_3			Fuel loading cost of e-Gd_2O_3		
	Low	Nominal	High	Low	Nominal	High
Cost of uranium ($M)	12.394	31.316	107.856	12.039	30.419	104.768
Cost of conversion ($M)	2.394	4.788	6.998	2.326	4.651	6.798
Cost of enrichment ($M)	27.516	36.310	43.686	26.464	34.921	42.014
Cost of fabrication ($M)	8.665	15.069	21.661	8.72	15.165	21.799
Cost of ^{157}Gd enrichment ($M)	0	0	0	0.36	0.55	0.84

Upon examining the data in Table 8, it becomes evident that, in the equilibrium cycle where n-Gd_2O_3 is the preferred BA, the costs for uranium, conversion, enrichment, and fabrication are approximately \$31.316 million, \$4.788 million, \$36.310 million, and \$15.069 million, respectively. Conversely, in the equilibrium cycle where e-Gd_2O_3 is the preferred BA, these costs are nominally \$30.419 million, \$4.651 million, \$34.921 million, and \$15.165 million, respectively. In addition to these costs, using e-Gd_2O_3 incurs a nominal additional expense of \$0.55 million (ranging from \$0.36 million to \$0.84 million depending on the fluctuation in prices) associated with the enrichment process of Gd_2O_3 with ^{157}Gd.

When comparing the cost components in both equilibrium cycles, a decrease in all costs except fabrication is observed. Specifically, taking the nominal cost into consideration, using e-Gd_2O_3 results in savings of around \$0.90 million from uranium costs, approximately \$0.14 million from conversion costs, and nearly \$1.39 million from enrichment costs. However, fabrication cost is about nominally \$0.1 million higher where e-Gd_2O_3 is preferred. This difference is reasonable considering the formulas used for cost calculations. In order to apply the process of ^{235}U enrichment, a significantly larger amount of natural uranium is required than the fuel to be loaded into the reactor, as seen in Equation 11. As a result of using e-Gd_2O_3, transferring a smaller amount of ^{235}U isotope to the fuel to be charged into the reactor leads to a reduction in enrichment process costs, which, in turn, lowers the amount of natural uranium to be purchased and processed, thus reducing conversion and uranium costs. On the other hand, the fabrication cost is directly related to the amount of uranium to be loaded into the reactor, as can be seen in Equation 16. Therefore, although e-Gd_2O_3 requires a lower enrichment level of ^{235}U, reducing other cost items, the need to charge approximately 150 kg of additional uranium into the reactor leads to an increase in the fabrication cost.

Table 9 presents a detailed summary of the financial gains achieved by opting for e-Gd_2O_3 over n-Gd_2O_3. Upon closer examination of the table, it becomes evident that when n-Gd_2O_3 is used, the cost of fuel to be loaded into the reactor for each cycle amounts to approximately \$87.48 million (with a range of $\sim$\$50.97 million to $\sim$\$180.20 million, depending on price fluctuations). Conversely, when e-Gd_2O_3 is utilised, the fuel cost for each cycle is around \$85.71 million (fluctuating between $\sim$\$49.90 million and $\sim$\$176.22 million, based on price variations).

This implies that the use of e-Gd_2O_3 as BA leads to a substantial saving of around \$1.77 million when taking into account the nominal prices. It is important to note that these savings are subject to fluctuations depending on the variations in prices considered. In the given study, the potential savings range from \$1.06 million to \$3.98 million, demonstrating the economic benefits of opting for e-Gd_2O_3 in the equilibrium cycle.

On the other hand, the $LCOE_{front-end}$ was assessed for equilibrium cycles in both n-Gd_2O_3 and e-Gd_2O_3 usage scenarios. Table 10 displays the $LCOE_{front-end}$ (cost per MWh) for n-Gd_2O_3 and e-Gd_2O_3 equilibrium cycles. Upon examining the data in Table 10, the fuel cost per MWh for using n-Gd_2O_3 is approximately \$7.44, while the fuel cost for e-Gd_2O_3 is about \$7.29 (subject to fluctuations in prices). As can be clearly seen, e-Gd_2O_3 provides savings of roughly \$0.15, and this value varies between ~\$0.09 and ~\$0.34, depending on price fluctuations.

Table 9 – Fuel loading costs of n-Gd_2O_3 and e-Gd_2O_3 in each fuel cycle

	Low ($M)	Nominal ($M)	High ($M)
n-Gd_2O_3	∼50.97	∼87.48	∼180.20
e-Gd_2O_3	∼49.90	∼85.71	∼176.22
Difference	∼1.06	∼1.77	∼3.98

Table 10 – $LCOE_{front-end}$ costs of n-Gd_2O_3 and e-Gd_2O_3 in each fuel cycle

	Low ($/MWh)	Nominal ($/MWh)	High ($/MWh)
n-Gd_2O_3	∼4.34	∼7.44	∼15.33
e-Gd_2O_3	∼4.24	∼7.29	∼14.99
Difference	∼0.09	∼0.15	∼0.34

The cost analyses clearly demonstrate that using e-Gd_2O_3 significantly contributes to reducing the total cost and fuel cost per MWh, even with the additional ^{157}Gd enrichment expense it incurs. For a nuclear power plant halfway through its 60-year lifespan, it can be assumed that it will nominally yield savings of more than $28 million in the latter half of its service life, depending on future prices.

4.4 Chapter Summary

In this chapter, the potential in-core behaviour of e-Gd_2O_3, enriched with 100 wt.% ^{157}Gd atoms, was assessed. A comparison was made between the required uranium enrichment levels for n-Gd_2O_3 and e-Gd_2O_3 by targeting 508 EFPDs within a 18-month cycle. Various peaking factors and reactivity feedback parameters were evaluated for both n-Gd_2O_3 and e-Gd_2O_3 usage scenarios. Additionally, average axial and 2D assembly-wise relative power distributions were examined and compared for the two scenarios. The shutdown margin and the economic benefits of e-Gd_2O_3 usage on fuel loading cost and fuel cost per MWh electricity production within the fuel cycle were also evaluated.

The results show that the use of e-Gd_2O_3, due to the discharged Gd isotopes with a low thermal neutron cross-section in the fuel composition, eliminates the residual reactivity penalty of n-Gd_2O_3 has and allows for increased uranium fuel loading. This results in achieving the targeted EFPDs with less ^{235}U enrichment than required with the use of n-Gd_2O_3. Furthermore, e-Gd_2O_3 does not have any negative effects on peak factor parameters such as heat flux hot channel factor and nuclear enthalpy rise hot channel factor.

Similarly, e-Gd_2O_3 does not cause any negative effects on reactivity feedback parameters such as moderator temperature coefficient, isothermal temperature coefficient, uniform Doppler coefficient, and boron coefficient, ensuring safe and reliable operation. No detectable negative effect on the shutdown margin was observed with the use of e-Gd_2O_3. Additionally, e-Gd_2O_3 usage had no significant positive or negative effect on the assembly-wise average 2D relative power fraction and average axial relative power distribution.

Lastly, the use of e-Gd_2O_3 provided a considerable economic advantage compared to n-Gd_2O_3, despite the ^{157}Gd enrichment cost. Depending on future prices, the potential savings range from $1.06 million to $3.98 million, demonstrating the economic benefits of opting for e-Gd_2O_3 in the equilibrium cycle.

Chapter 5

Neutronic Analysis of Discrete Burnable Absorber Pins

A research paper titled “Effect of ZrB_2 and UB_2 Discrete Burnable Absorber Pins on fuel reactivity” was published in Progress in Nuclear Energy using the methodology and a portion of the data presented in this chapter [116].

5.1 Chapter Overview

The exploration of alternative burnable absorber designs is essential for optimizing nuclear fuel performance, improving fuel efficiency, and maximizing economic advantages. One area of focus is the development of BA designs suitable for extended fuel cycles, which offer benefits such as reduced fuel handling, minimized number of refueling outages, and enhanced operational flexibility.

In this chapter, an investigation is conducted for promising BA designs: the Discrete Burnable Absorber Pin (DBAP) with zirconium diboride or uranium diboride as BA, and the Moderated Discrete Burnable Absorber Pin, that features a moderator at DBAP’s centre, which are particularly advantageous for fuel cycles longer than 24-months, addressing the limitations of IFBAs that suffer from the rapid depletion of ^{10}B atoms [67].

Initially, an overview of the Discrete Burnable Absorber Pin design is provided, highlighting its potential benefits. Subsequently, the Moderated Discrete Burnable Absorber Pin is introduced as an enhanced version of the Discrete Burnable Absorber Pin. A neutronic analysis is performed on these alternative BA designs to evaluate their reactivity behaviours and key aspects such as ^{239}Pu breeding and ^{10}B depletion are examined to assess their overall effectiveness in maintaining reactivity control and fuel utilisation.

5.2 Designed Model

Enica et al., in collaboration with Westinghouse Electric Company, have developed a novel design for a BA/pellet system, which aims to eliminate some of the drawbacks, negative impacts, and limitations of existing BAs used in modern nuclear reactors [117]. This new design entails placing the BA as a discrete pin at the centre of the annular fuel pellet, as illustrated in Figure 26. Unlike generic designs, the absorbing material is not homogeneously mixed with the fuel as with the common Gd_2O_3 additions to UO_2 nor coated on the outer surface of the fuel pellet as with IFBAs. Instead, the BA-containing material (ZrB_2 or UB_2) is separated from the fuel, which allows for greater control over reactivity and an extended fuel cycle beyond 24-months with the slow depletion of the BA in the pellet centre.

In this new Discrete Burnable Absorber Pin design, the boron absorber is kept separate from the majority of the fissile material, making it discrete despite the UB_2 containing fissile uranium itself. Furthermore, this design increases the relatively low thermal conductivity of the UO_2 fuel pellet, which tends to have a higher central temperature than surface temperature during normal reactor operation.

As will be detailed in Section 6.3.1, the development studies of this design have revealed that adding beryllium oxide (BeO) moderator, due to its superior chemical stability, tensile strength and Young's modulus [118], to the Moderated Discrete Burnable Absorber Pins could potentially increase the effective full power days (EFPDs) of the fuel. The MDBAP design consists of an annular fuel pellet with a moderator pin at the centre, as shown in Figure 27. By incorporating a moderator at the central location, the MDBAP design is expected to decrease the velocity of neutrons, which in turn enhances their ability to be absorbed. This mechanism allows for more neutrons to be captured by the fissile isotopes in the reactor core, thereby promoting a greater number of fission reactions and leading to efficient fuel utilisation and increased burnup.

5.3 Method

The AP-1000 PWR reactor, designed by Westinghouse Electric Company, was chosen as the reference reactor to evaluate the reactivity behaviour for the 2D neutronic analysis of DBAPs and MDBAPs. The Serpent 2 Monte Carlo reactor physics code was used to conduct the neutronic analyses, utilising the JEFF-3.1 nuclear data library. The simulations were performed using 300 active and 20 inactive cycles consisting of 30,000 neutrons. Various important parameters, as presented in Table 11, were considered while modelling the reference reactor. The fuel temperature was set at an average of 900 K [102], [103], and the Zircaloy-4 cladding temperature was set at an average of 583 K. Considering the average boron concentration a standard PWR would have within a cycle, the boric acid concentration in the coolant was assumed to be 650 ppm.

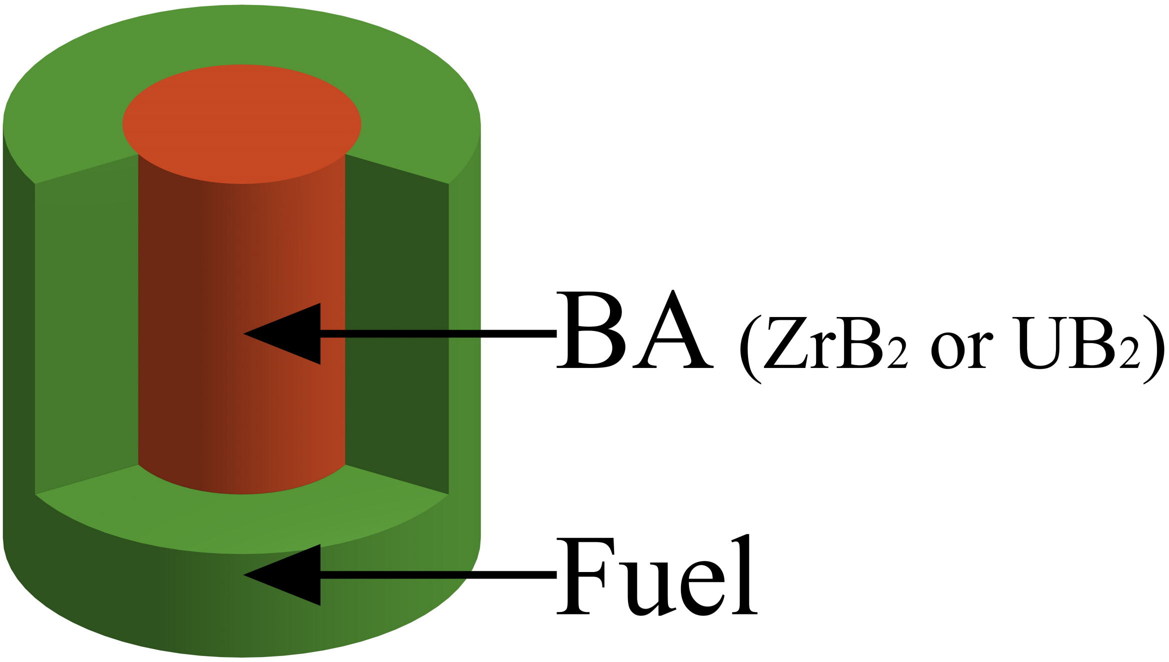

Figure 26 – DBAP design.

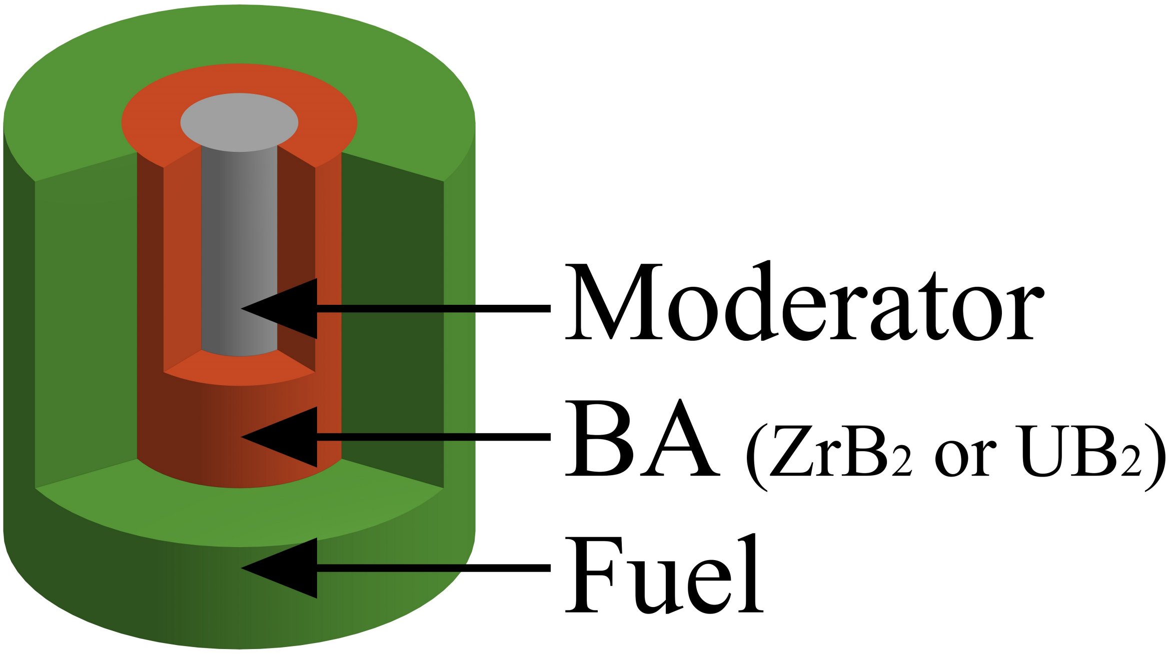

Figure 27 – MDBAP design.

Table 11 – Fuel design parameters for the AP-1000 PWR used in simulations [105], [119].

Parameter	Value
Rod array	17 × 17
Number of control rods	25
Fuel rod pitch (cm)	1.26
Pellet diameter (cm)	0.4095
Rod diameter (cm)	0.475
Cladding material	Zircaloy-4
Cladding thickness (cm)	0.057
Average fuel temperature (K)	900
Average cladding temperature (K)	583
Fuel density (%TD)	95.5
IFBA coating thickness (cm)	0.00256
Soluble boric acid concentration (ppm)	650

As absorber materials, ZrB_2 and UB_2 were used in DBAPs and MDBAPs designs, and BeO and graphite used as the moderator in MDBAPs. The primary purpose behind the development of DBAPs and MDBAPs is to use them as burnable absorbers for cycles longer than 24-months, with uranium enrichment levels above 5.00 wt.%. However, for a fair comparison with IFBA, the uranium enrichment level was set at 4.45 wt.%. It is essential to note that the trend would remain the same for different uranium enrichment levels. In addition, for all simulations where UB_2 was used, the ^{235}U enrichment level of UB_2 was set equal to that of the equivalent fuel pellets, 4.45 wt.%.

To observe the ^{239}Pu breeding behaviour in fuel pellets as a function of radius, fuel pellets containing DBAPs were analysed in five separate equal-volume radial layers, as seen in Figure 28a. Similarly, the DBAPs were divided into five separate equal-volume radial layers to study the depletion behaviour of ^{10}B in ZrB_2 and UB_2 as seen in Figure 28b. Moreover, since the error margins of the simulations were below 22 pcm, they were not included in the results. The number BA rods in each assembly design, on the other hand, was based on five distinct reference assemblies as in Figure 29. These designs are composed of 28, 44, 72, 88, and 112 BA (IFBAs, DBAPs or MDBAPs) rods, respectively [119].

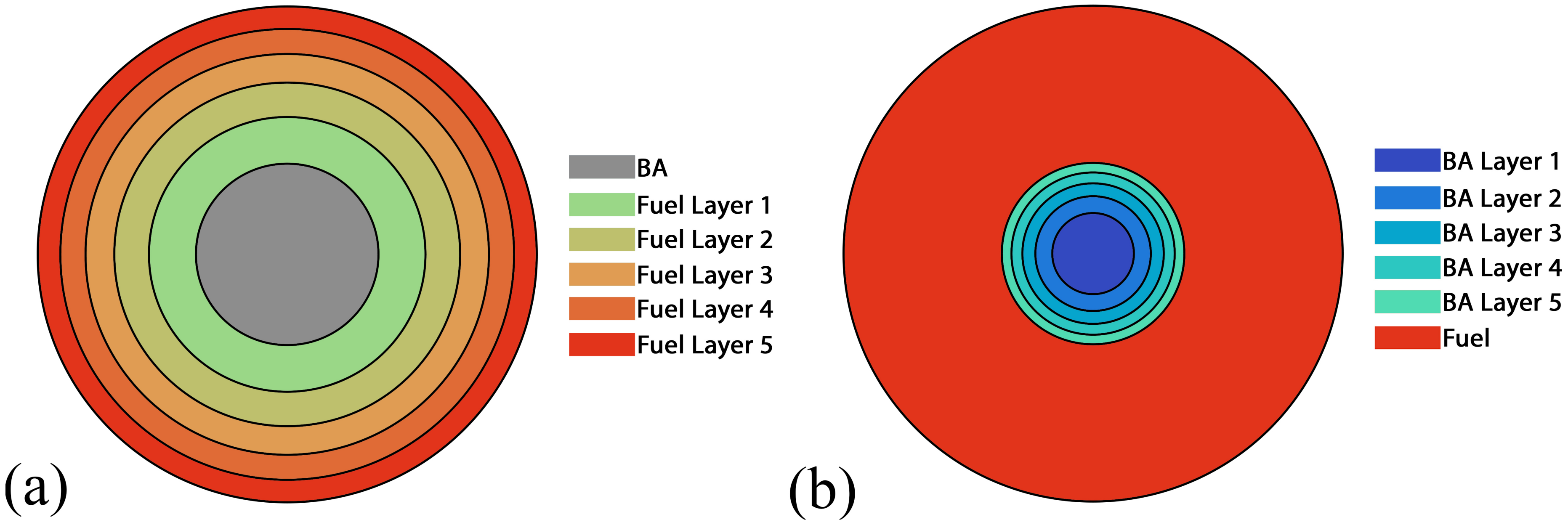

Figure 28 – Radial layers of the fuel pellet and DBAP.

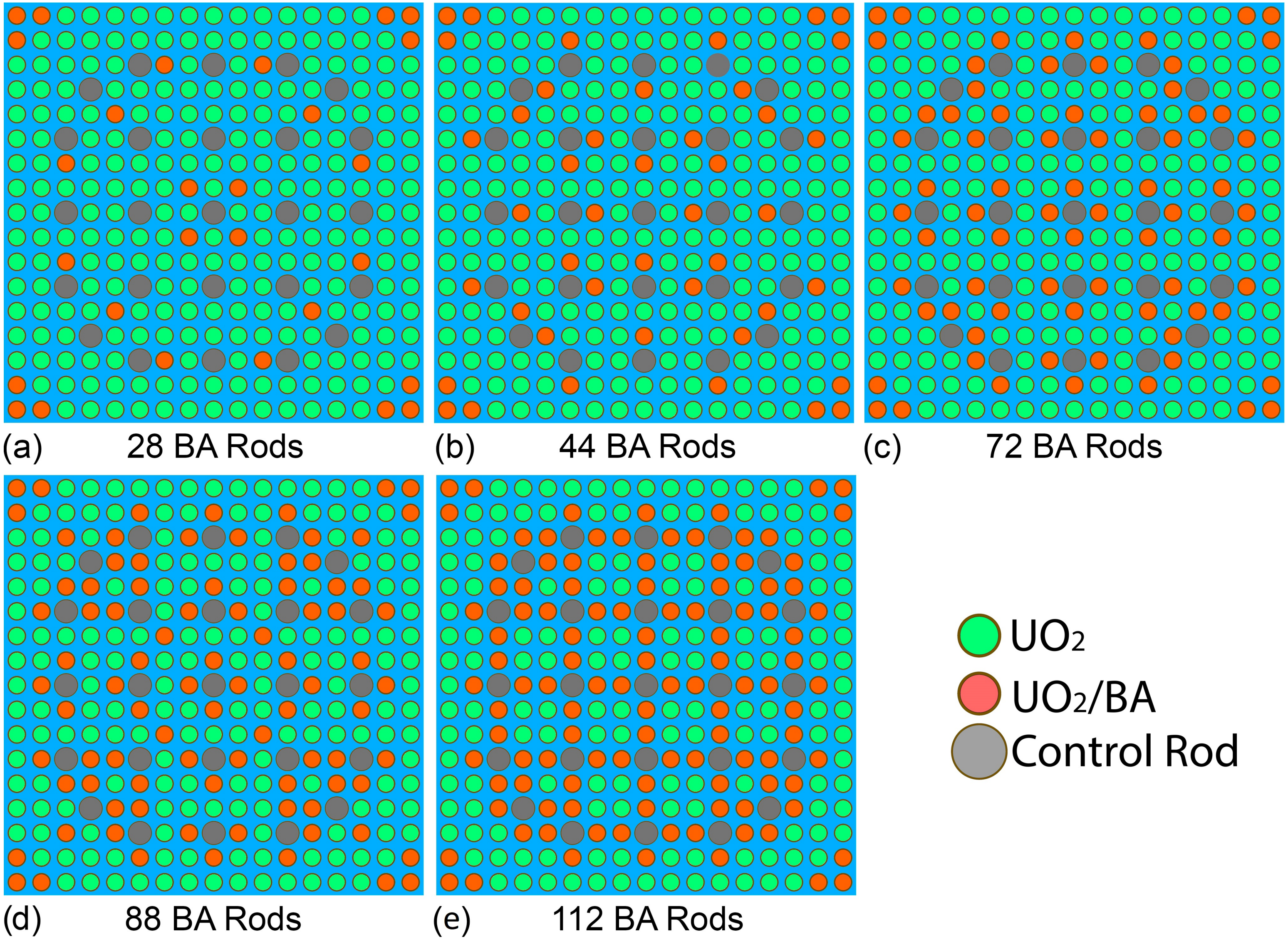

Figure 29 – Fuel assembly designs with (a) 28, (b) 44, (c) 72, (d) 88 and (e) 112 BA rods (for IFBAs, DBAPs or MDBAPs) used in simulations. Adapted from [119].

5.4 Results and Discussion

5.4.1 Reactivity Behaviour of Integral Fuel Burnable Absorbers

In Figure 30, the infinite multiplication factor curves are presented for fuel models with IFBA on 28, 44, 72, 88, and 112 fuel rods. Upon examining Figure 30, it is seen that the suppression of reactivity at the beginning of the fuel model's life rises as the number of IFBA rods in the fuel assembly increases. For instance, when compared to the BA-free fuel model, the fuel model with 28 IFBA rods in the fuel assembly has a suppression of reactivity by 7,921 pcm at the beginning of the cycle while the fuel model with 112 IFBA rods has a reactivity suppression of 29,313 pcm.

As burnup progresses, the k_{inf} values in all fuel models start to align with those of the BA-free fuel model. Notably, in fuel models containing 72, 88, and 112 IFBA rods, reactivity increases during burnup. Once reactivity reaches its peak, the peak point varies depending on the number of IFBA rods as a function of burnup, reactivity begins to decrease, displaying a parallel decline in relation to the BA-free fuel model.

As the ^{10}B atoms in the fuel models become almost completely depleted, the k_{inf} curve of all fuel models move closer to the BA-free fuel model's. However, unlike Gd_2O_3 (as in Section 3.3.1), ZrB_2 does not cause any residual reactivity penalty on the fuel. During burnup progression, the addition of the neutron absorber material, ^{10}B in this case, delays the consumption of ^{235}U atoms and hardens the neutron spectrum, promoting the production of higher amounts of fissile ^{239}Pu [109] compared to the BA-free fuel model. This results in greater fuel reactivity. Furthermore, as shown in Figure 30, an increase in the number of IFBA rods leads to higher reactivity at the end of the fuel's life. For instance, at 60.00 MWd/kgU, the fuel model with 28 IFBA rods has a higher k_{inf} value by 102 pcm compared to the BA-free fuel model, while the fuel model with 112 IFBA rods displays a higher k_{inf} value by 368 pcm.

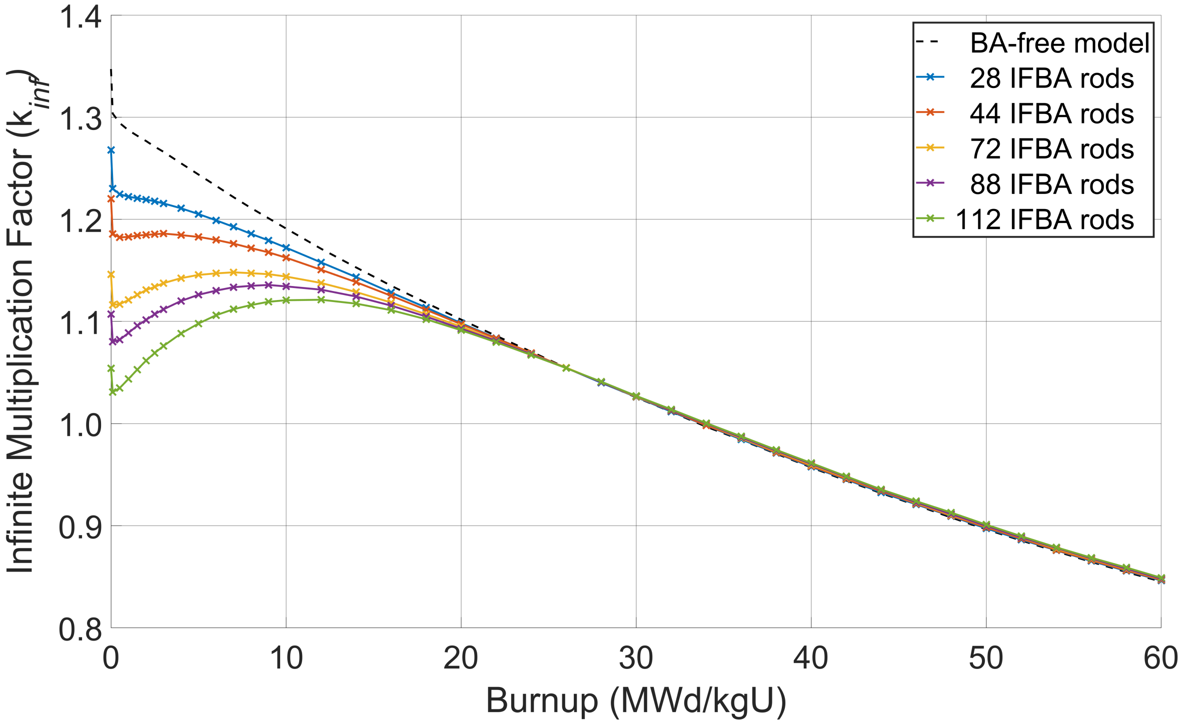

Figure 30 – Infinite multiplication factor (k_{inf}) of fuel models with IFBA coating in different numbers of rods.

5.4.2 Reactivity Behaviour of Discrete Burnable Absorber Pins

Figure 31 presents the infinite multiplication factor curves for fuel models with ZrB_2 DBAPs of varying radii (Figure 31a), along with the Δk_{inf} curves for fuel models with UB_2 DBAPs (Figure 31b) compared to those with ZrB_2 DBAPs . Upon detailed examination of Figures 31a and 31b, it can be seen that the suppression of reactivity increases with the increase in DBAP radius. For instance, in Figure 31a, compared to the BA-free fuel model, the fuel models with a 0.50 mm and 2.50 mm ZrB_2 DBAP have a 4,383 pcm and 28,728 pcm lower k_{inf} value at the beginning of the fuel life, respectively. Similarly, the fuel models with a 0.50 mm and 2.50 mm UB_2 DBAP have a 4,111 pcm and 27,409 pcm lower k_{inf} value at the beginning of the fuel life compared to the BA-free fuel model, respectively. In addition, when comparing the fuel models with 0.50 mm and 2.50 mm ZrB_2 DBAPs with the 0.50 mm and 2.50 mm UB_2 DBAPs, the ZrB_2 DBAPs have 272 pcm and 1,319 pcm lower k_{inf} values at the beginning of fuel life, respectively.

On the one hand, fuel models with both ZrB_2 and UB_2 DBAPs tend to show reactivity behaviour parallel to that of the BA-free fuel model's at the end of the fuels' lives, and their k_{inf} curves show a higher k_{inf} value than the BA-free fuel model depending on the DBAP radius at the end of the fuels' lives. The tendency for DBAP-used fuel models to reach the same reactivity as the BA-free fuel model is shifted with an increasing DBAP radius, which is due to the depletion of ^{10}B atoms within the fuel assembly being shifted by the self-shielding effect (as can be seen in Figure 36). For example, fuel models with 0.50 mm ZrB_2 and UB_2 DBAP show the same k_{inf} value as the BA-free fuel model at 37.00 MWd/kgU. The fuel model with 1.50 mm ZrB_2 DBAP shows the same k_{inf} value as the BA-free fuel model at 53.00 MWd/kgU, while the fuel model with 1.50 mm UB_2 DBAP shows the same k_{inf} value as the BA-free fuel model at 51.00 MWd/kgU.

On the other hand, in fuel models with both ZrB_2 and UB_2 DBAPs with radii of 2.00 mm and 2.50 mm, almost all of the ^{10}B atoms are depleted beyond 60.00 MWd/kgU (see Figure 36). Therefore, when considering the trend, these fuel models will show the same reactivity as the BA-free fuel models beyond 60.00 MWd/kgU.

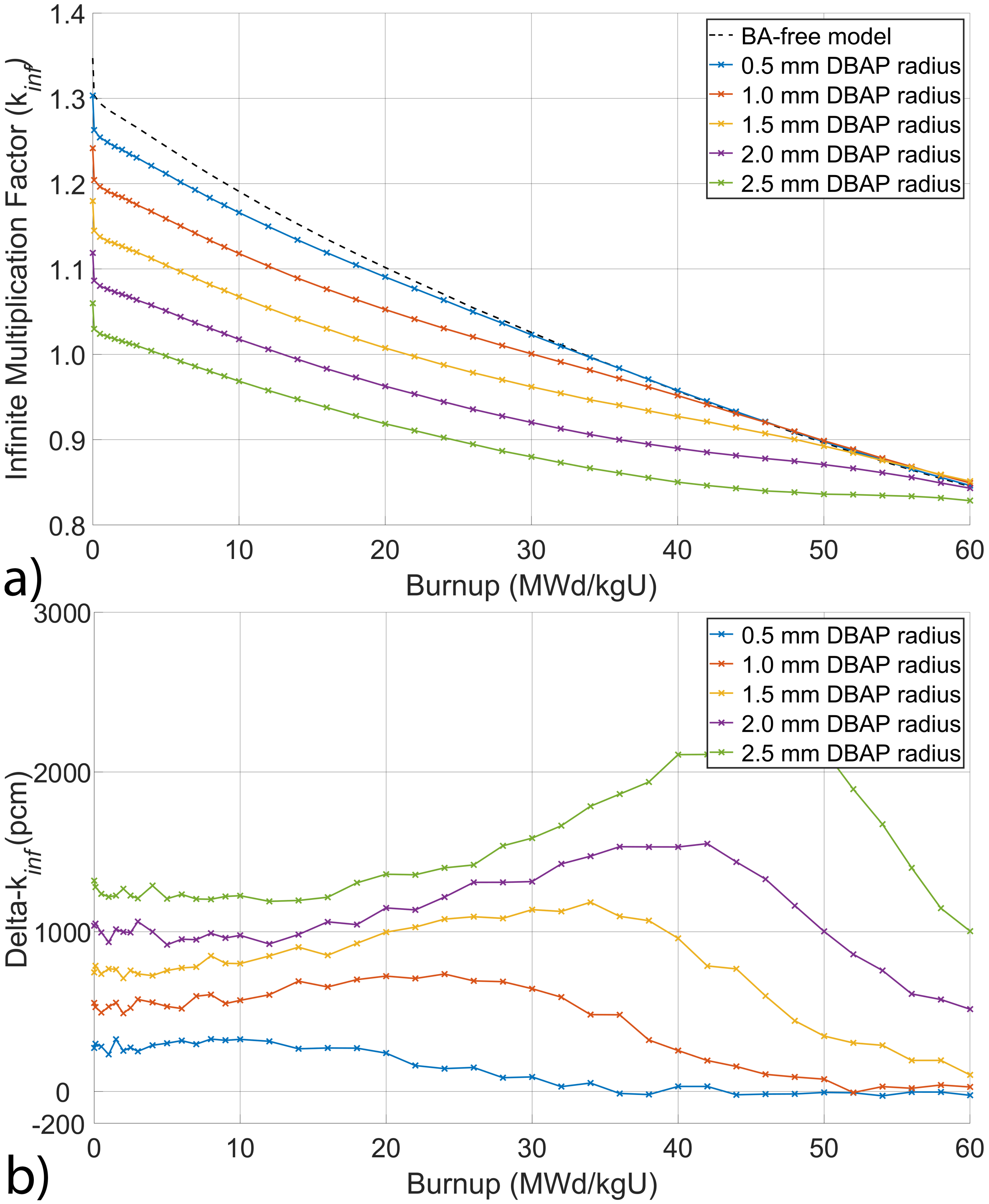

Figure 31 – Infinite multiplication factors (k_{inf}) of fuel models with ZrB_2 in 28 BA rods (a) and Δk_{inf} curves for fuel models with UB_2 DBAPs compared to ZrB_2 DBAPs UB_2 (b).

Another important point is that at the end of the fuel life, approximately 60.00 MWd/kgU, fuel models with 0.50 mm, 1.00 mm and 1.50 mm ZrB_2 DBAP are 101 pcm, 392 pcm, and 610 pcm higher in k_{inf} value than the BA-free fuel model, while fuel models with 0.50 mm, 1.00 mm and 1.50 mm UB_2 DBAP are 76 pcm, 149 pcm, and 714 pcm higher in k_{inf} value, respectively. It should not be forgotten that UB_2 has 4.45 wt.% ^{235}U enrichment and thus contributes to fission reactions.

Figure 32a illustrates the infinite multiplication factor curves of fuel models containing ZrB_2 with a radius of 1.00 mm, utilising them in different numbers of fuel rods, while Figure 32b presents the Δk_{inf} curves for fuel models with UB_2 DBAPs compared to those with ZrB_2 DBAPs. Upon examining Figure 32, it is evident that the reactivity suppression increases at the beginning of the fuel's life, and as the number of DBAP rods rises, a flattened behaviour is observed. Comparing the fuel models with ZrB_2 DBAPs containing 28, 72, and 112 rods to the BA-free fuel model, they suppress the reactivity by about 10,559 pcm, 26,351 pcm, and 37,761 pcm, respectively. Similarly, when comparing the fuel models with UB_2 DBAPs containing 28, 72, and 112 rods to the BA-free fuel model, they suppressed the reactivity by about 10,005 pcm, 25,003 pcm, and 35,907 pcm, respectively. It is worth noting that, at the late stage of the fuel's life, a higher reactivity is observed in all fuel models after the depletion of most of the ^{10}B atoms when compared to the BA-free fuel model.

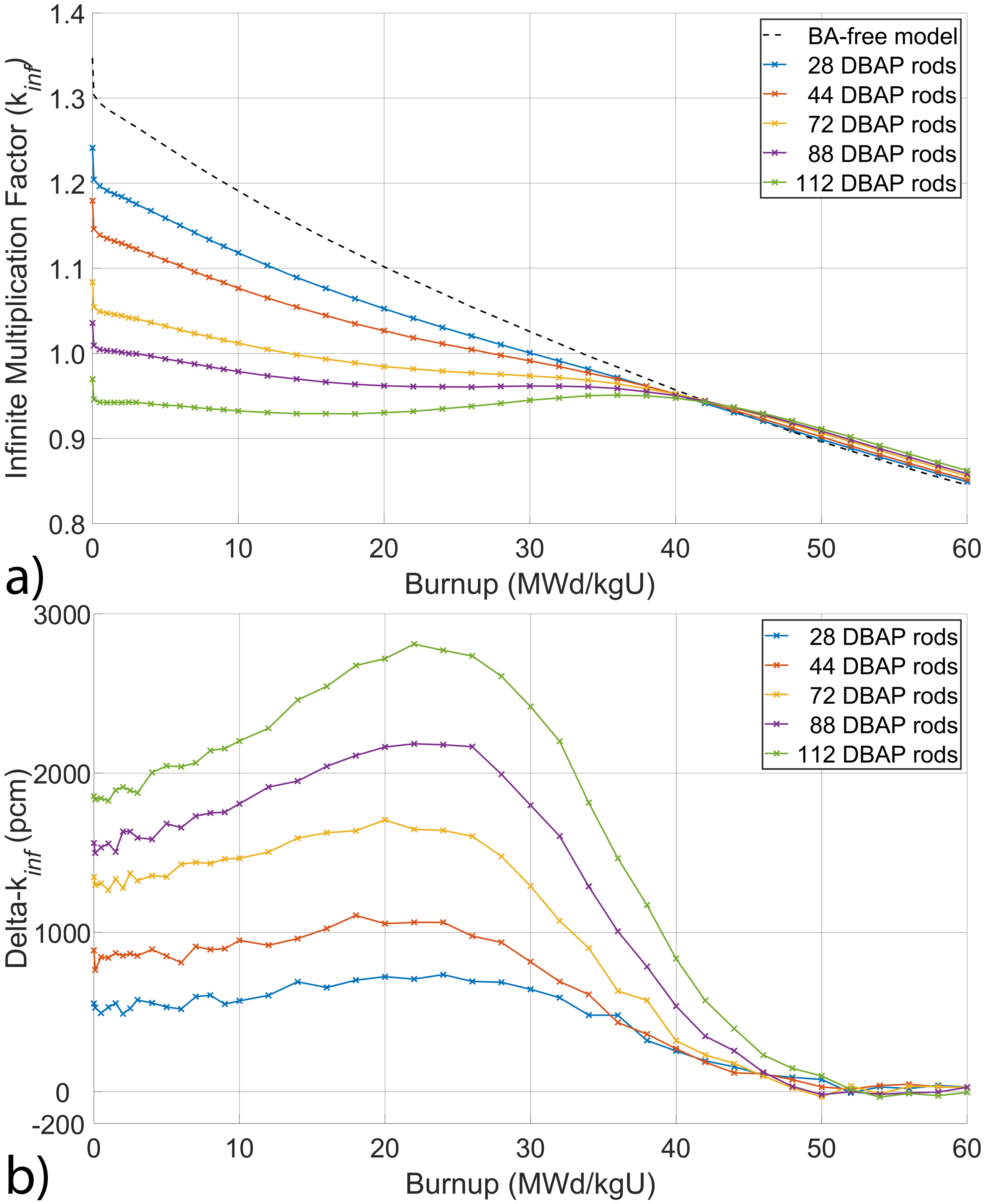

Figure 32 – Infinite multiplication factors (k_{inf}) of fuel models with 1.00 mm ZrB_2 (a) and Δk_{inf} curves for fuel models with UB_2 DBAPs compared to ZrB_2 DBAPs (b).

The fuel model with ZrB_2 DBAPs in 112 BA rods starts in a subcritical state at the beginning of the fuel's life ($k_{inf} = 0.998$). However, it decreases by approximately 2,700 pcm and reaches its lowest level before the complete depletion of ^{10}B atoms at 18.00 MWd/kgU. Afterward, it increases by about 2,200 pcm until the burnup point of 36.00 MWd/kgU, and then begins to decline in parallel with the BA-free fuel model after the depletion of most of the ^{10}B atoms in the fuel assembly. As with the other fuel models, it achieves higher reactivity than the reference BA-free fuel model for the remainder of the fuel's life. Additionally, it is evident that an increase in the number of BA rods results in up to 1,692 pcm higher reactivity, depending on the number of rods, at the end of the fuel's life.

In the case where UB_2 DBAPs are used in 112 BA rods, the behaviour is similar to that of the fuel model with ZrB_2 DBAPs. The reactivity decreases at the beginning of the fuel's life but then starts increasing until the burnup point of 36.00 MWd/kgU. Then it starts to decrease in parallel with the BA-free fuel model, after the depletion of most of the ^{10}B atoms. Following this, higher reactivity is achieved for the remainder of the fuel's life when compared to the BA-free fuel model. As with the fuel models containing ZrB_2 DBAPs, an increase in the number of BA rods containing UB_2 DBAPs results in up to 1,688 pcm higher reactivity, depending on the number of rods. Additionally, when comparing the fuel models with ZrB_2 and UB_2 DBAPs, all fuel models show similar k_{inf} values at the end of the fuel's life, with a difference in the error margin of ±22 pcm, which appears to be counter-intuitive at first, until fissile isotope breeding is considered.

To observe the changes in reactivity resulting from the redistribution of BA to a greater number of fuel rods within the fuel assembly while keeping the total BA amount unchanged, a series of simulations were conducted using two reference fuel models reported in Figures 31a and 31b, both with 1.50 mm DBAPs in 28 BA rods for both ZrB_2 and UB_2. The BA/total-fuel ratio of these two reference fuel models were distributed to DBAPs in 44, 72, 88, and 112 BA rods by reducing the DBAPs radii. Figure 33a shows the infinite multiplication factor curves of fuel models with 1.50 mm ZrB_2 DBAPs distributed, while Figure 33b shows fuel models with 1.50 mm UB_2 DBAPs distributed.

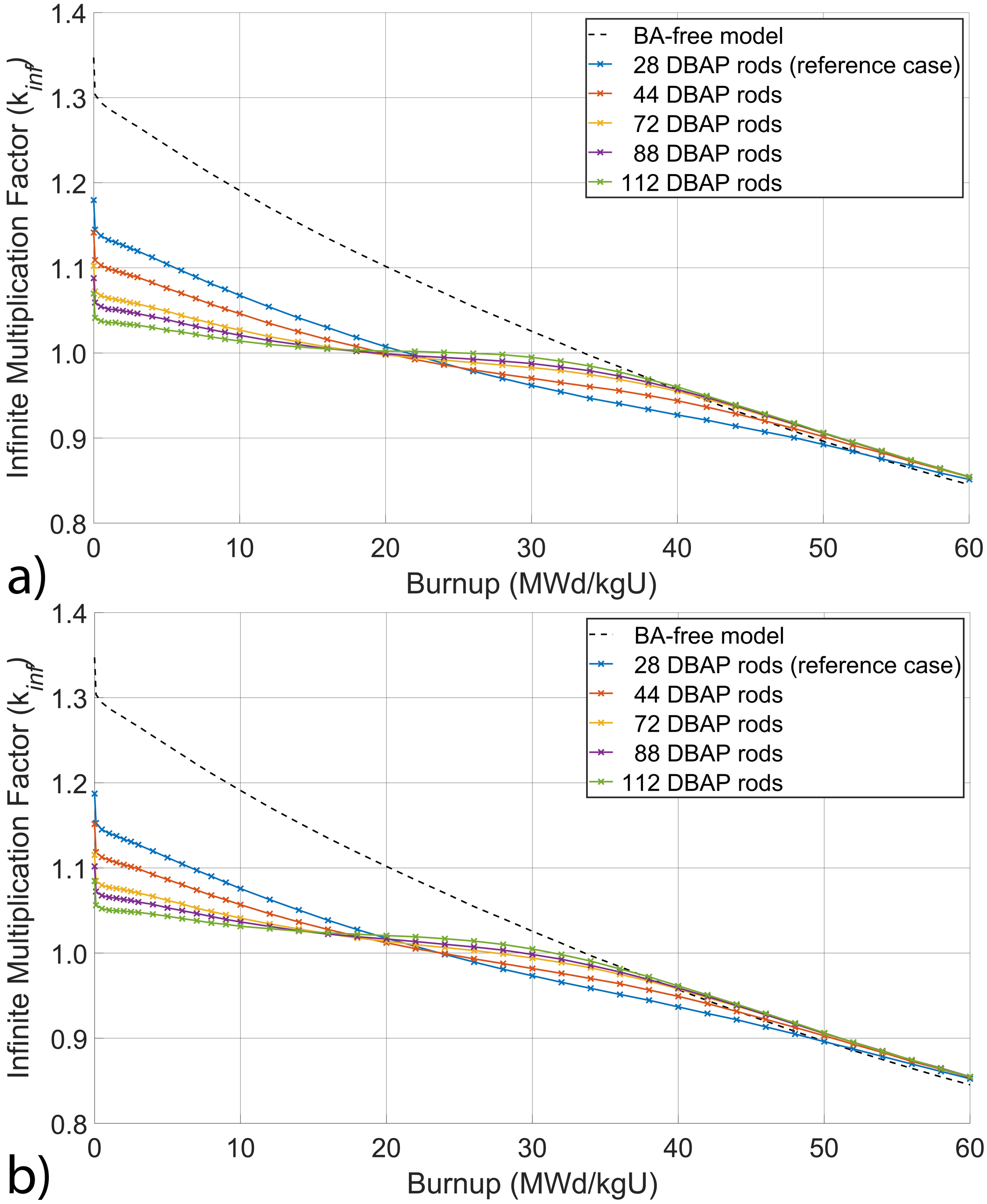

Figure 33 – Infinite multiplication factors (k_{inf}) of fuel models with fixed ZrB_2/total-fuel ratio in different numbers of BA rods (a) ZrB_2 and (b) UB_2 DBAPs.

As depicted in Figure 33a, the distribution of ZrB_2 BA in more rods, due to the increase in surface area, allows BAs to absorb neutrons at a higher rate at the beginning of the fuel's life, causing more suppression of the reactivity. When examining the cases with ZrB_2 DBAPs in detail, it is observed that reducing the radius of DBAPs and distributing them in the assembly leads to a slower decrease of reactivity towards the subcritical level in the fuel's life. For example, when the fuel model with 28 ZrB_2 DBAPs and a constant BA/total-fuel ratio is modified to include ZrB_2 DBAPs in 72 and 112 fuel rods, the k_{inf} value is respectively suppressed by 7,746 pcm and 11,002 pcm more at the beginning of the fuel's life, promoting a flatter k_{inf} curve. Additionally, higher reactivity is observed at the end of the fuel's life in all fuel models compared to the BA-free fuel model.

Similarly, when examining the fuel models with UB_2 DBAPs in detail, it is observed that the distribution of BA on more rods creates a slightly sharper reduction compared to the BA-free fuel model, which shows up towards the end of the assembly's life. For instance, when the fuel model with 28 UB_2 DBAPs and a constant BA/total-fuel ratio is modified to include UB_2 DBAPs in 72 and 112 fuel rods, the k_{inf} value is suppressed by 7,192 pcm and 10,264 pcm more, respectively, at the beginning of the fuel's life, promoting a flatter k_{inf} curve. Additionally, higher reactivity is observed at the end of the fuel's life in all fuel models compared to the BA-free fuel model.

This investigation demonstrates that distributing DBAPs in fuel assemblies with a constant BA/total-fuel ratio can result in not only a flatter reactivity profile but also higher reactivity in the mid-life of the fuel. For instance, distributing BA to 72 and 112 fuel rods in the fuel model with 28 ZrB_2 DBAPs and a constant BA/total-fuel ratio results in obtaining 2,793 pcm and 3,796 pcm higher k_{inf} values at 34.00 MWd/kgU, respectively. Similarly, distributing BA to 72 and 112 fuel rods in the fuel model with 28 UB_2 DBAPs and a constant BA/total-fuel ratio results in obtaining 2,414 pcm and 3,200 pcm higher k_{inf} values at 34.00 MWd/kgU, respectively. Therefore, using DBAPs in more fuel rods can lead to more efficient fuel utilisation.

5.4.3 Plutonium-239 Breeding Behaviour in BA Rods with Discrete Burnable Absorber Pins

In Figure 34a, the ^{239}Pu breeding behaviour of the fuel models with ZrB_2 DBAPs is illustrated. On the other hand, Figure 34b shows the Δ-^{239}Pu curves for fuel models with UB_2 DBAPs compared to ZrB_2 DBAPs. Upon closer inspection of the data in Figure 34, it is seen that the ^{239}Pu density in the fuel composition is closely linked to the radius of the DBAPs. The larger the radius, the harder the neutron spectrum, leading to an increase in ^{239}Pu density in cm^3. In all fuel models, the density of ^{239}Pu reaches its maximum value between 40.00 and 50.00 MWd/kgU. Furthermore, the fuel model with 2.50 mm ZrB_2 DBAPs has a ^{239}Pu density that is approximately 65% higher at the end of the fuel life than the fuel model with 0.50 mm ZrB_2 DBAPs.

A similar pattern is observed in the breeding behaviour of ^{239}Pu in UB_2 DBAP-containing fuel models. As the radius of the DBAPs increases, the production of ^{239}Pu also increases compared to the BA-free fuel model. In all fuel models, the density of ^{239}Pu reaches its peak value between 40.00 and 50.00 MWd/kgU. Furthermore, the density of ^{239}Pu in the fuel model with 2.50 mm UB_2 DBAPs is approximately 56% higher at the end of the fuel life than the fuel model with 0.50 mm UB_2 DBAPs. In addition, the fuel models with ZrB_2 DBAPs have a higher density of ^{239}Pu compared to those with UB_2 DBAPs of the same radius, as seen in Figure 34a.

Overall, Figure 34 indicates that the breeding behaviour of ^{239}Pu in fuel models is highly dependent on the radius of the DBAPs. Increasing the radius of the DBAPs leads to a harder neutron spectrum, which results in an increase in the production of ^{239}Pu. Additionally, it has been observed that, in all fuel models, the fraction of ^{240}Pu in the fuel assembly exceeds 7% within the total plutonium content after reaching 6.00 MWd/kgU.

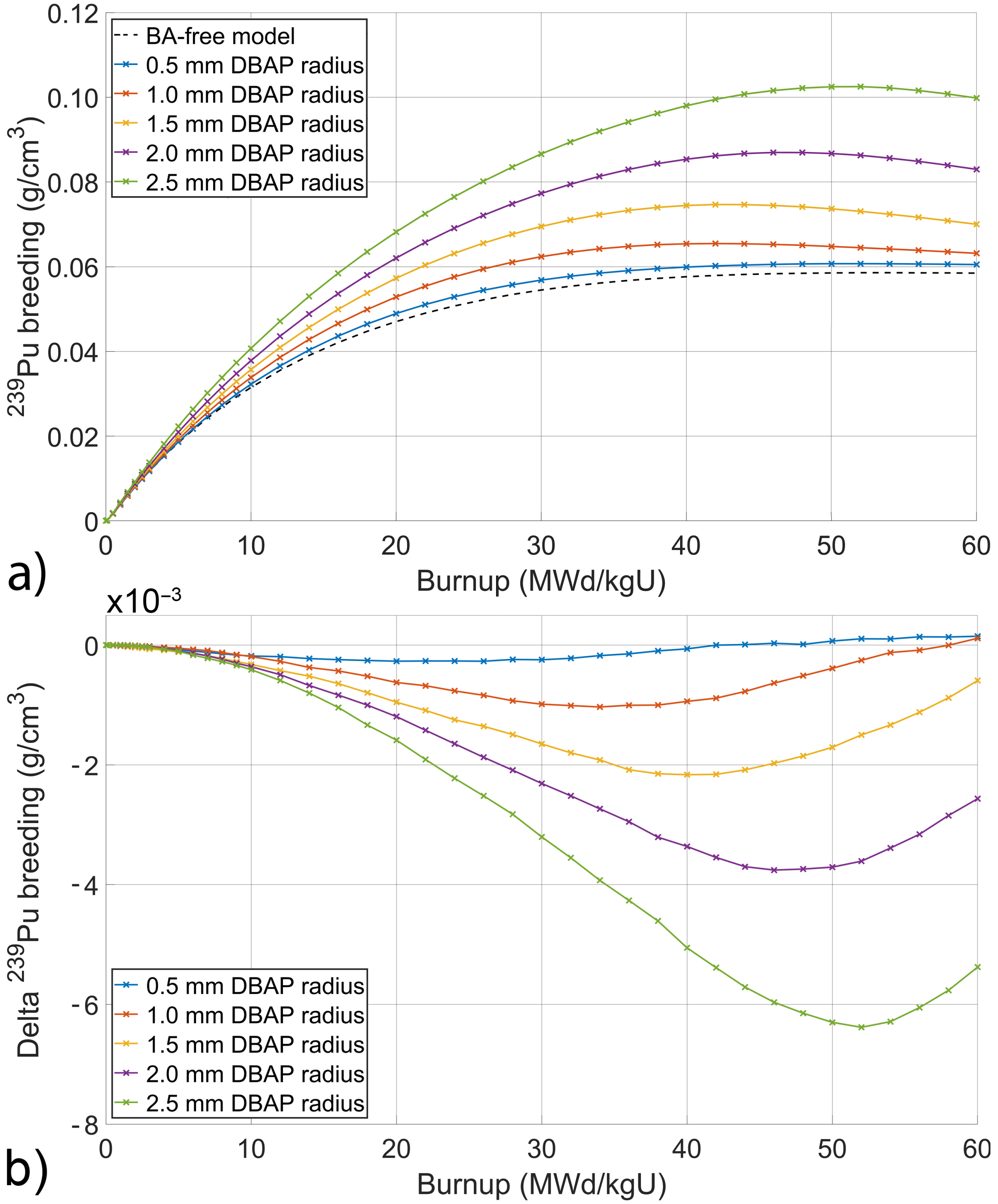

Figure 34 – ^{239}Pu breeding behaviours in BA rods of fuel models with ZrB_2 (a), and Δ-^{239}Pu curves for fuel models with UB_2 DBAPs compared to ZrB_2 DBAPs (b).

Figure 35 displays graphs of the ^{239}Pu breeding behaviour of fuel pellets in BA rods for the BA-free fuel model (Figure 35a) and fuel models with 1.50 mm ZrB_2 and UB_2 DBAPs (Figure 35b and c respectively) in 28 BA rods. The graphs indicate that in all layers, the mass density of ^{239}Pu increases faster in cases with DBAPs compared to cases without BA. Moreover, cases with ZrB_2 DBAPs show a faster increase in ^{239}Pu mass density compared to those with UB_2 DBAPs. Similar to the cases without BA, the mass density of ^{239}Pu is higher on the surface of the fuel pellets compared to the centre, as noted in previous studies [120].

This difference becomes particularly noticeable at around 26.00 MWd/kgU and is closely related to the amount of ^{10}B present in the system and the duration of depletion. The self-shielding effect is responsible for this behaviour, as the ^{239}Pu atoms on the surface can capture more neutrons than those in the centre. The presence of DBAPs results in a harder neutron spectrum and thus increases the production of ^{239}Pu. It is also worth mentioning that the mass density of ^{239}Pu is higher in the cases with ZrB_2 DBAPs compared to the cases with UB_2 DBAPs, as observed in Figure 35.

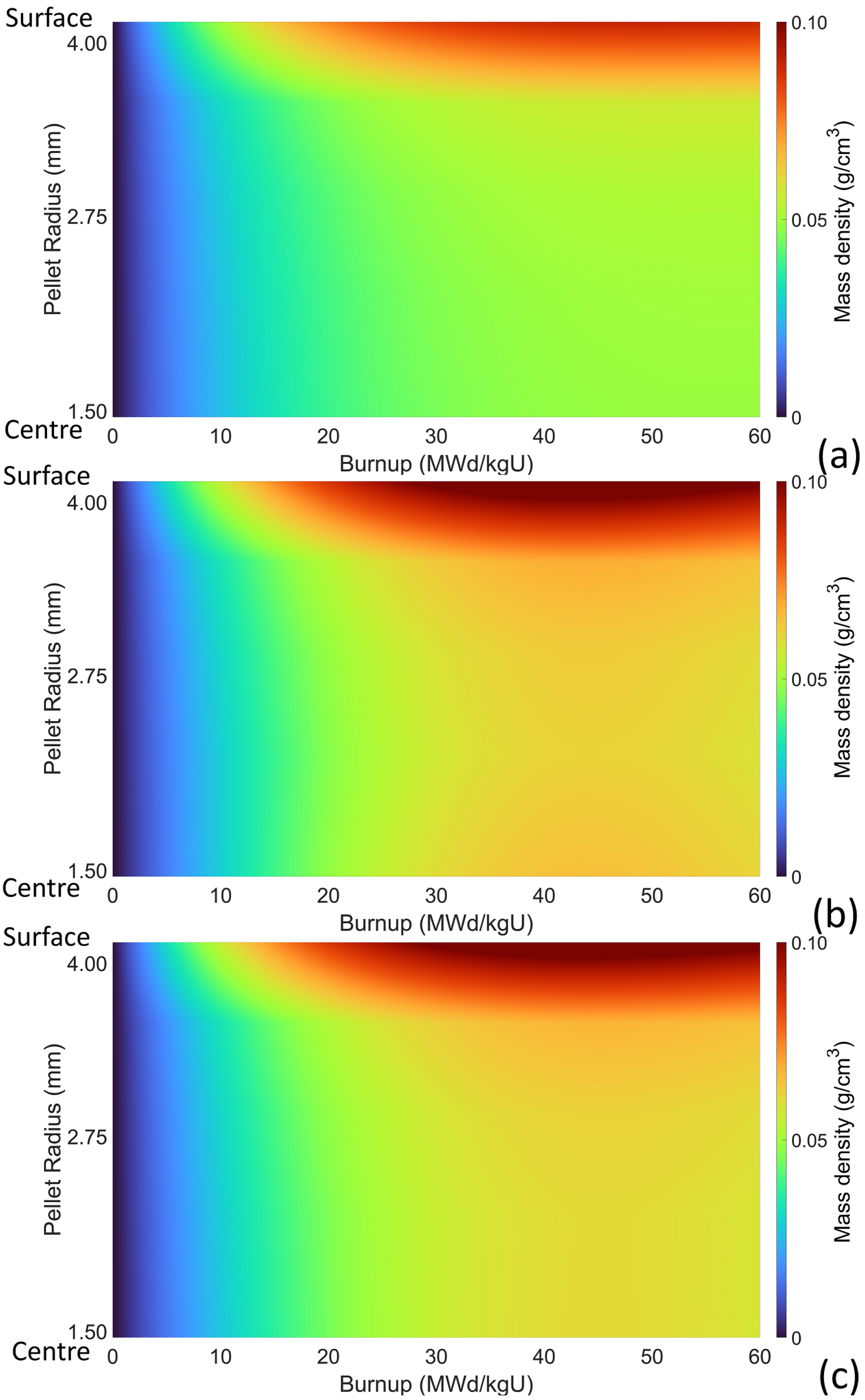

Figure 35 – Radial ^{239}Pu breeding on BA rods of BA-free fuel model (a), and fuel models with ZrB_2 (b) and UB_2 (c) DBAPs in 28 BA rods.

5.4.4 Boron-10 Depletion Behaviour in Discrete Burnable Absorber Pins

Figure 36 shows the behaviour of ^{10}B atoms depletion concerning the mass density (g/cm^3) of ^{10}B atoms in ZrB_2 and UB_2 DBAPs compositions with different radii. Upon examining Figure 36 in detail, it is seen that the fuel models with higher radius DBAPs have a larger number of ^{10}B atoms, despite having the same quantity of ^{10}B atoms per unit volume. This results in a more efficient self-shielding effect with the aid of the increased surface area caused by the larger radius, promoting the presence of ^{10}B atoms in the fuel assembly for an extended period. The fuel models with 2.00 mm and 2.50 mm ZrB_2 and UB_2 DBAPs still exhibit a substantial ^{10}B concentration at the end of the fuels' life.

In Figure 37, the radial depletion behaviour of ^{10}B atoms in the DBAPs of 28 BA rods with 1.50 mm radii ZrB_2 DBAPs (Figure 37a) and UB_2 DBAPs (Figure 37b) is illustrated. As seen in Figure 37a, the ^{10}B atoms within the ZrB_2 DBAPs experience faster depletion on the outer surface and slower depletion towards the centre. At 34.00 MWd/kgU, the ^{10}B atoms are almost entirely depleted on the outer surface of the DBAPs, whereas at the centre of the pellets, this occurs at 50.00 MWd/kgU due to the thermal neutron flux being reduced in the centre of the pellet.

When observing Figure 37b, it can be seen that the ^{10}B atoms in the UB_2 DBAPs are also depleted faster on the surfaces than in the centre. At 32.00 MWd/kgU, the ^{10}B atoms are nearly depleted on the outer surface of the DBAPs, while this occurs at 46.00 MWd/kgU at the centre of the pellets. It is worth noting that the annular uranium fuel also acts as a shield for the ^{10}B atoms, which in turn act as a shield for the uranium fuel since the ^{235}U will also absorb neutrons.

As one would expect, neutron absorbing atoms positioned within the centre of the fuel pellet will have an influence on the neutron flux. Therefore, radial thermal neutron flux profiles were examined. For this analysis, the fuel pellet was divided into equal volumes, as demonstrated previously in Figure 28.

Figure 38 depicts normalized radial thermal neutron flux profiles for a BA-free fuel pellet, a fuel pellet with 1.50 mm ZrB_2 DBAP, and a fuel pellet with 1.50 mm UB_2 DBAP, achieved through feature scaling (transforming the values to a range between 0 and 1). As can be seen, the use of DBAPs noticeably affects the neutron flux profile of the pellet, as expected, with a sharp change occurring between the outermost layer of the DBAP and the innermost layer of the annular UO_2 pellet. However, when comparing models using ZrB_2 DBAP and UB_2 DBAP, the neutron flux profiles in both types of DBAP models are similar.

On the other hand, in both types of DBAPs, after capturing neutrons ^{10}B atoms produce ^{4}He and ^{7}Li atoms. Thus, the breeding rates of ^{7}Li and ^{4}He atoms follow the depletion behaviour of ^{10}B atoms, and there is no need to consider them separately.

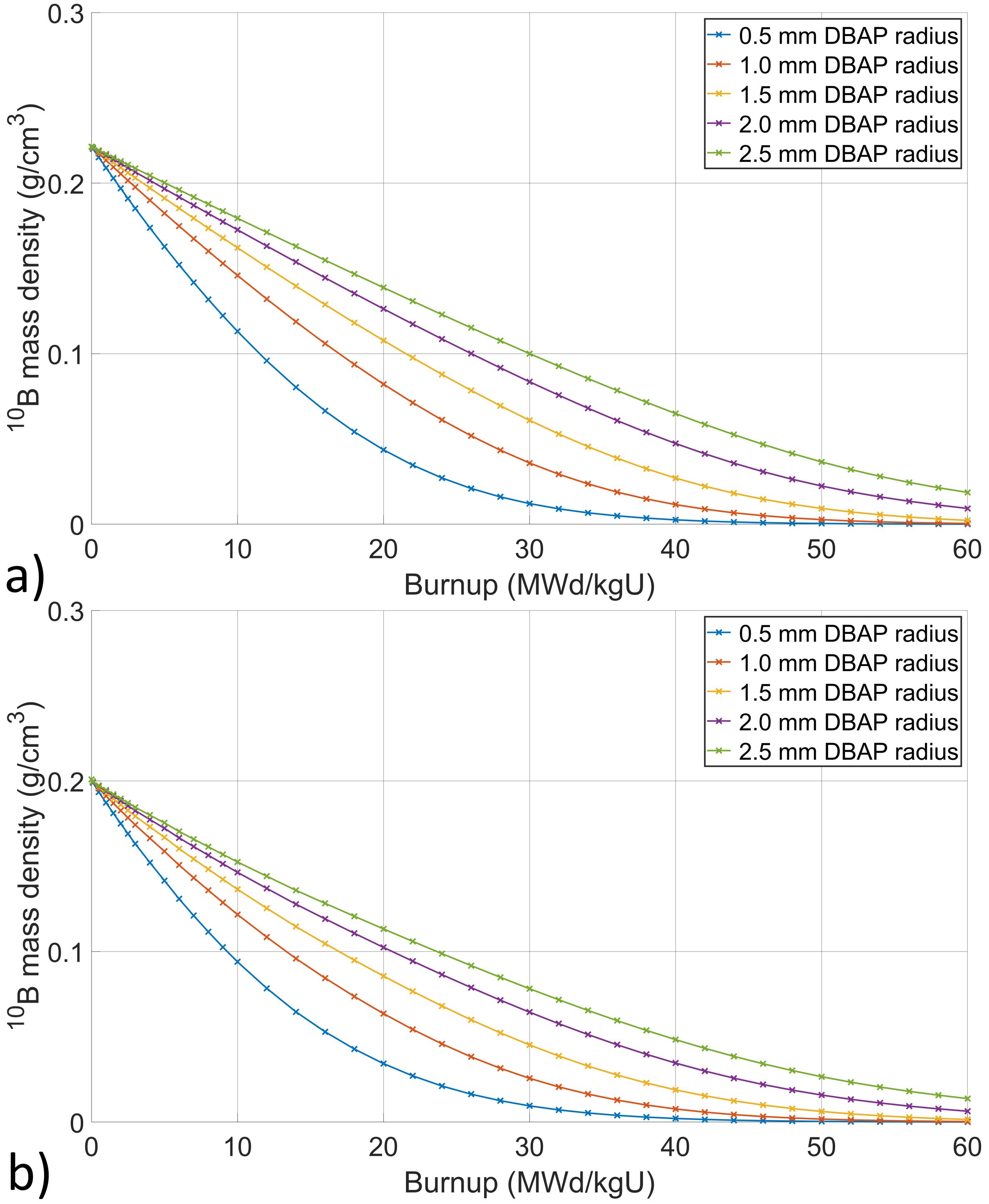

Figure 36 – ^{10}B depletion behaviour of fuel models with ZrB_2 (a) and UB_2 (b) DBAPs in 28 BA rods.

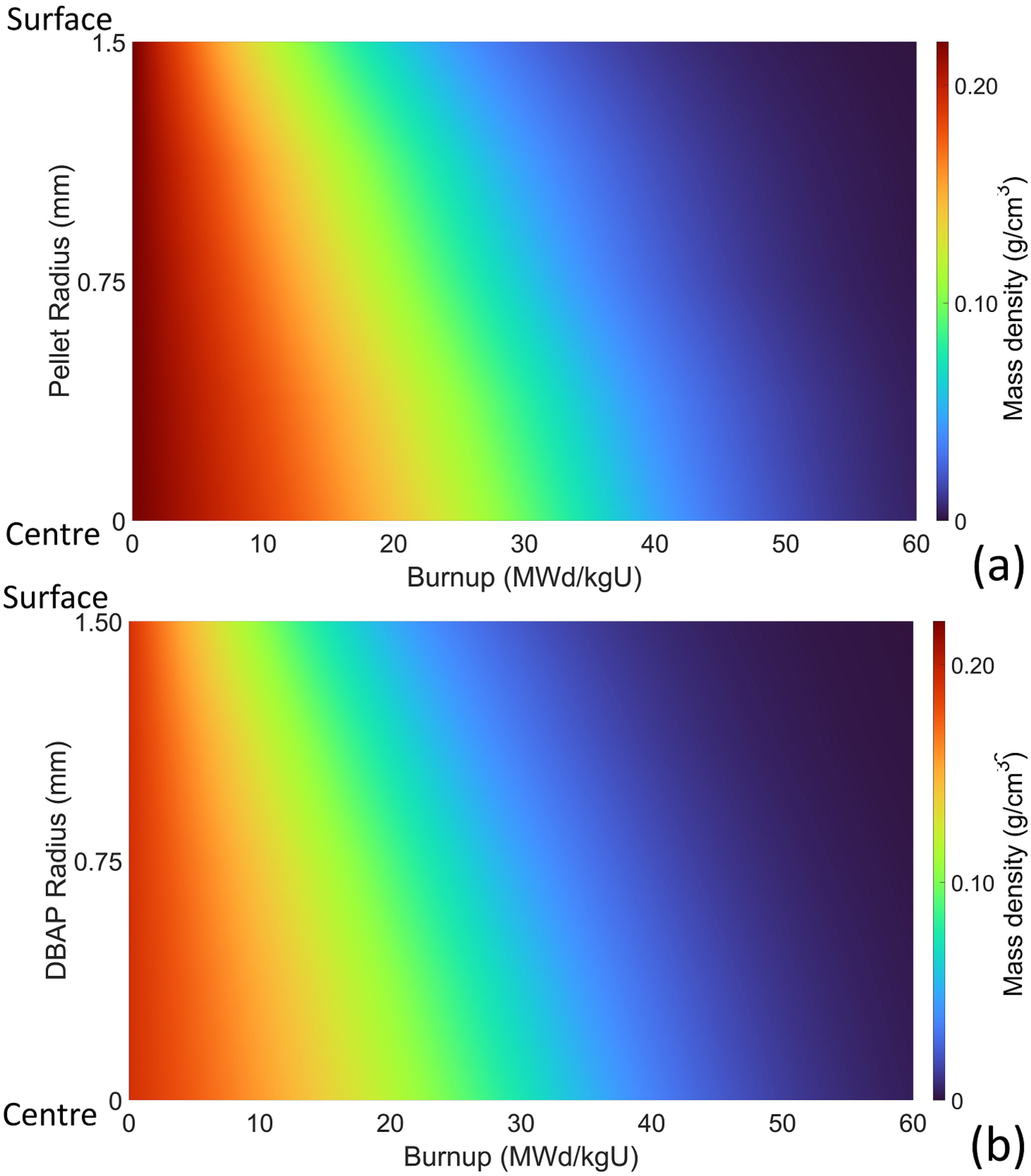

Figure 37 – ^{10}B radial depletion behaviour of fuel models with ZrB_2 (a) and UB_2 (b) 1.50 mm radii DBAPs in 28 BA rods.

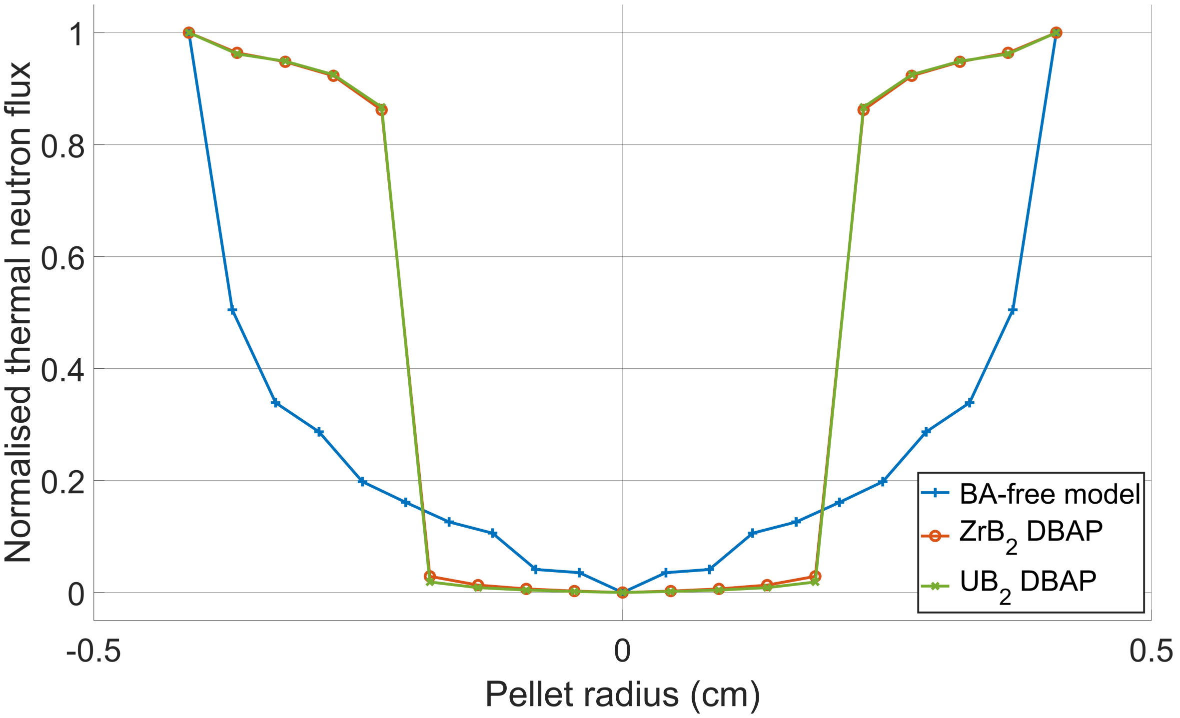

Figure 38 – Thermal neutron flux profile comparison of a BA-free fuel pellet, a fuel pellet with 1.50 mm ZrB_2 DBAP and a fuel pellet with 1.50 mm UB_2.

5.4.5 Moderated Discrete Burnable Absorber Pins

As will be explained in detail in Section 6.3.1, adding a moderator to DBAPs could potentially extend the EFPDs that fuel can provide. By implementing the design of MDBAPs, moderator is placed at the central location of the DBAP to slow down the velocity of neutrons. This mechanism facilitates the capture of more neutrons by the fissile isotopes in the reactor core, leading to an increase in the number of fission reactions and, therefore, more efficient fuel utilisation and an overall increase in power output.

Figure 39 shows the infinite multiplication factor curves for fuel models containing ZrB_2 MDBAPs (Figure 39a) and UB_2 MDBAPs (Figure 39b), utilising two moderator candidates, BeO and graphite, in 28 fuel rods. Upon detailed examination of Figure 39, it can be observed that the use of 1.00 mm BeO or 1.00 mm graphite as a moderator in 2.50 mm and 1.50 mm ZrB_2 and UB_2 MDBAPs did not cause any significant difference in the infinite multiplication factor. Therefore, BeO has been preferred as a moderator for use in the analysis of MDBAPs for the rest of the study.

Figure 40 shows the infinite multiplication factor curves of the fuel model with 2.50 mm radius DBAP in 28 fuel rods and fuel models using 2.50 mm MDBAP with 0.50 mm, 1.00 mm, 1.50 mm and 2.00 mm BeO moderator radius. Figure 40a shows infinite multiplication factor curves for fuel models with ZrB_2 DBAP and MDBAP, while Figure 40b shows the Δk_{inf} curves for fuel models with UB_2 MDBAPs compared to those with ZrB_2 MDBAPs.

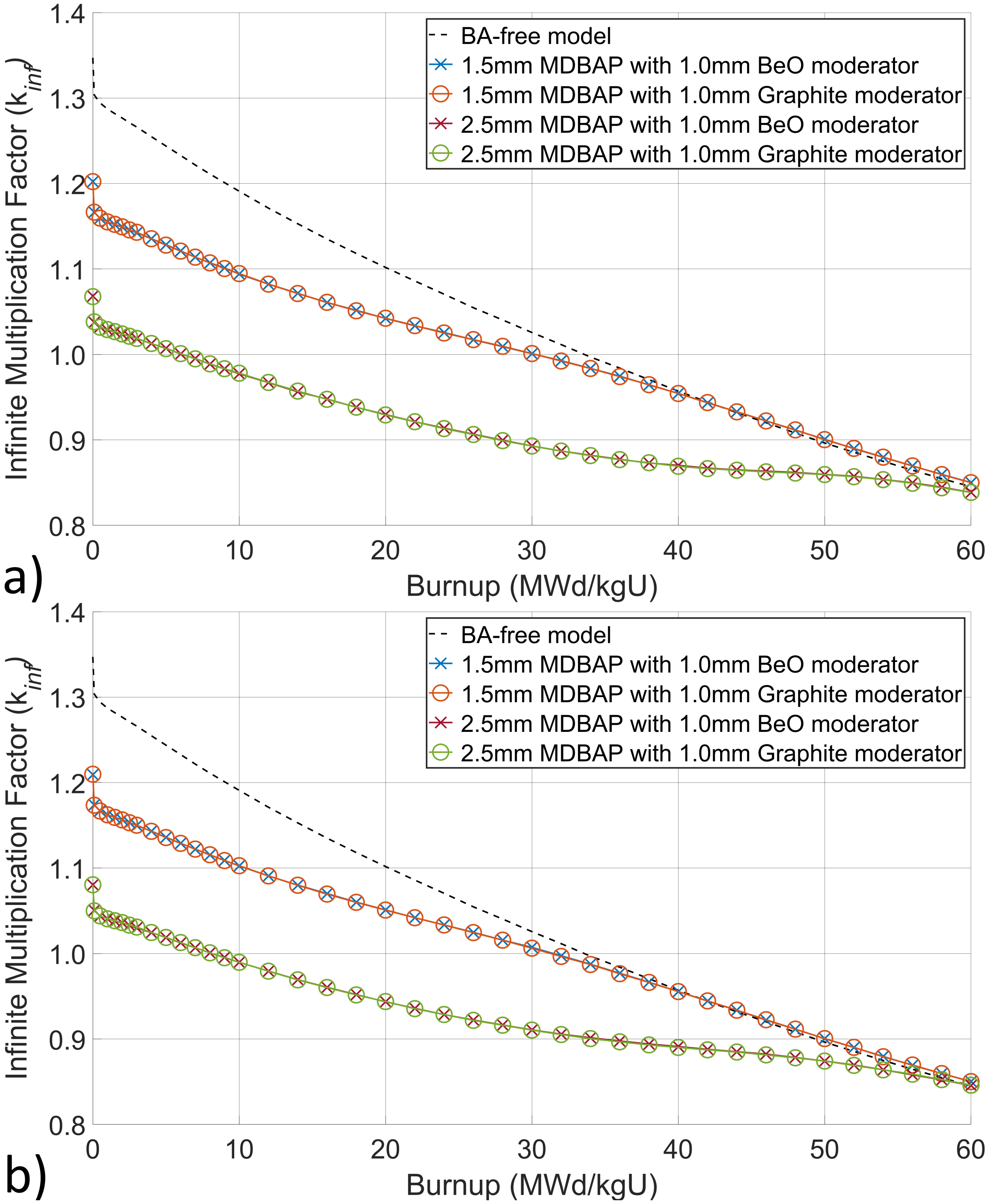

Figure 39 – Comparison of BeO and graphite moderator in different fuel models with ZrB_2 (a) and UB_2 (b) MDBAPs.

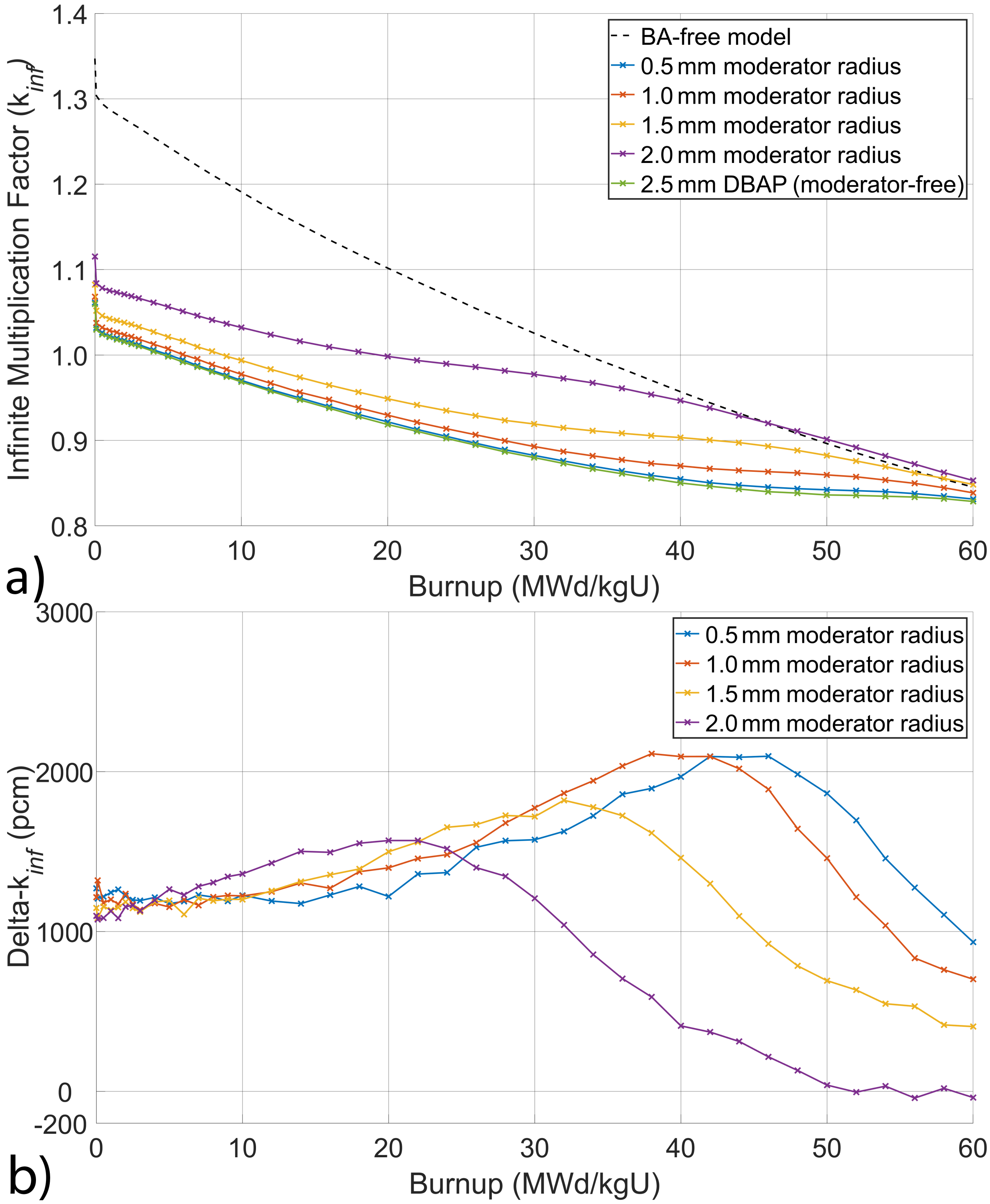

Figure 40 – Infinite multiplication factor (k_{inf}) curves for fuel models with ZrB_2 DBAPs and MDBAPs (a), and Δk_{inf} curves for fuel models with UB_2 MDBAPs compared to ZrB_2 MDBAPs (b).

Upon detailed examination of Figure 40, it becomes evident that the reactivity suppression in fuel models with ZrB_2 and UB_2 MDBAPs is lower at the beginning of the fuel's life. However, fuel models with MDBAPs provide a relatively higher k_{inf} value at the end of the life of the fuels compared to the fuel model using DBAPs. Moreover, the use of the moderator at a high radius yields higher k_{inf} values than the BA-free fuel model at an earlier stage.

When comparing the infinite multiplication factor curves of fuel models using ZrB_2 DBAPs with a radius of 2.50 mm and fuel models using 2.50 mm MDBAPs with moderator radii of 1.50 mm and 2.00 mm, as shown in Figure 40a, it is evident that the fuel model with 2.50 mm MDBAPs and a moderator radius of 1.50 mm suppresses 2,252 pcm less reactivity than the fuel model using DBAPs at the beginning of its life. On the other hand, the fuel model with a moderator radius of 2.00 mm suppresses 5,543 pcm less reactivity at the beginning of its life compared to DBAPs.

Examining the differences at the end of fuel life, the fuel model with a moderator radius of 1.50 mm provides a higher k_{inf} value by 1,984 pcm compared to the fuel model with DBAPs, while the fuel model with a moderator radius of 2.00 mm provides a higher k_{inf} value by 2,452 pcm. Additionally, both of these fuel models provide higher k_{inf} values by 306 pcm and 774 pcm at 60.00 MWd/kgU compared to the BA-free fuel model, respectively.

Another important point is that the fuel model with a moderator radius of 2.00 mm begins to provide higher k_{inf} values than the BA-free fuel model at around 46.00 MWd/kgU, while the fuel model with a moderator radius of 1.50 mm begins to provide higher k_{inf} values than the BA-free fuel model after 58.00 MWd/kgU.

When UB_2 and ZrB_2 MDBAPs are compared, it is observed that UB_2 MDBAPs suppress less reactivity than their ZrB_2 equivalents, despite having the same size. Specifically, at the beginning of the fuel's life, depending on the moderator radius, an increase of up to 1,300 pcm is noted. However, when examining fuel models with a 2.00 mm moderator radius, the UB_2 MDBAPs yield a reactivity that is 1,568 pcm higher at 22.00 MWd/kgU. Over the lifespan of the fuel, this difference gradually lessens and comes to a final difference of -30 pcm at the end of the cycle.

Additionally, as the moderator radius decreases, there is an observed rise in the peak values of Δk_{inf}, and the point at which these peak values are reached moves towards the later stages of the fuel's life. Moreover, a decrease in moderator radius also leads to an increase in the Δk_{inf} values at 60.00 MWd/kgU.

In general, considering Figure 40, it can be said that as the moderator radius in the MDBAPs fuel model approaches the radius of MDBAPs, and hence the amount of BA in the MDBAPs decreases, the gain in reactivity compared to the BA-free fuel model is achieved earlier in the fuel's life, which will pave the way to reach higher burnup.

Figure 41a shows the infinite multiplication factor curves of fuel models with 1.00 mm ZrB_2 MDBAPs with a moderator radius of 0.50 mm, in different numbers of fuel rods, while Figure 41b shows the Δk_{inf} curves for fuel models with UB_2 MDBAPs compared to those with ZrB_2 MDBAPs.

Upon examining Figures 41a and 41b, it can be seen that, similar to fuel models using DBAPs, the reactivity suppression at the beginning of the fuel life rises with the increase in the number of fuel rods containing MDBAPs in the fuel assembly. Similarly, after the depletion of almost all ^{10}B atoms, higher k_{inf} values are obtained at the end of the fuel's life, compared to the BA-free fuel model. For instance, at 60.00 MWd/kgU, the k_{inf} values of fuel models with ZrB_2 MDBAPs in 28, 44, 72, 88, and 112 fuel rods are 250 pcm, 457 pcm, 753 pcm, 943 pcm, and 1,208 pcm higher than the BA-free fuel model, respectively.

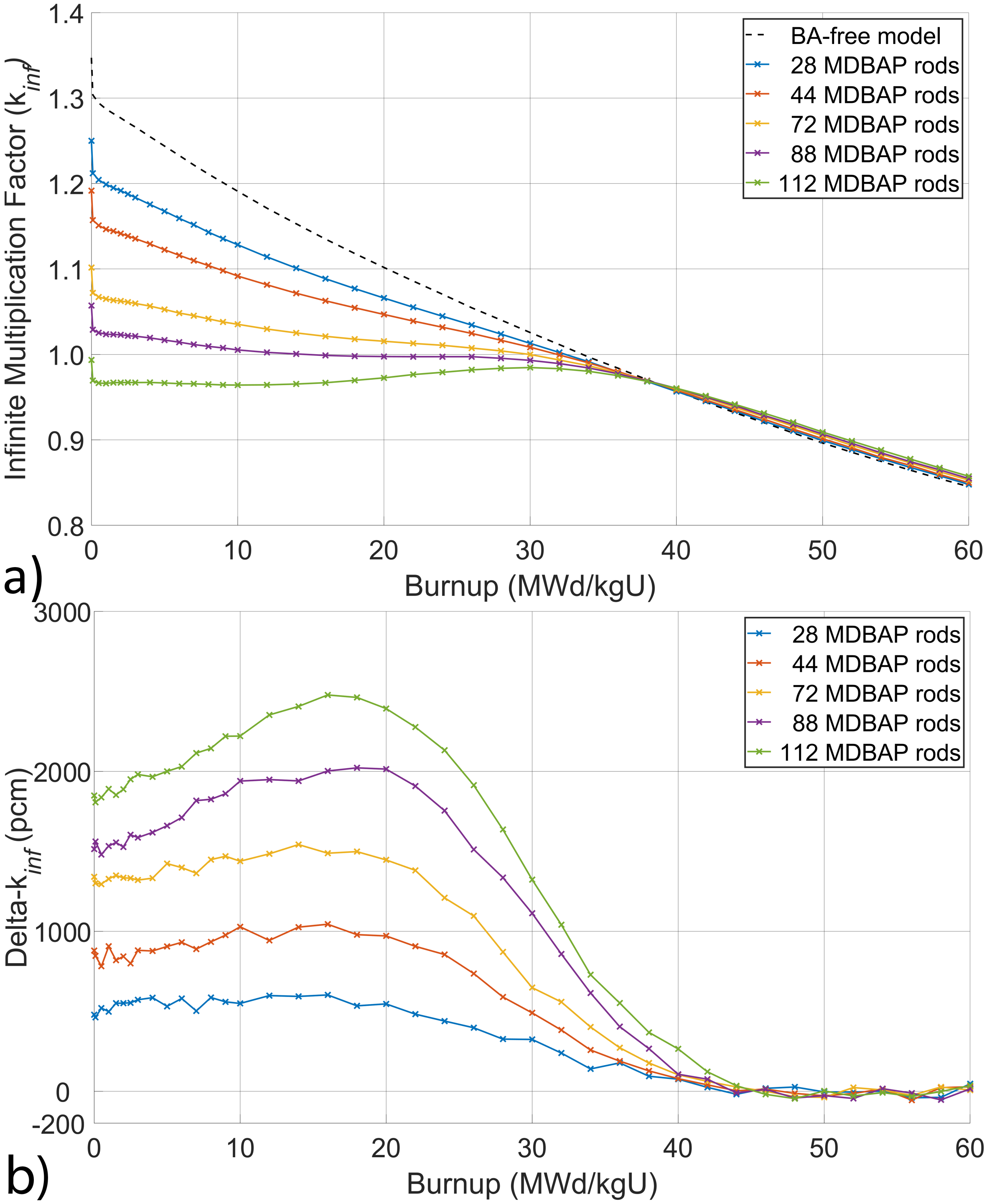

Figure 41 – Infinite multiplication factor (k_{inf}) curves for fuel models with 1.50 mm ZrB_2 MDBAPs with 1.00 mm moderator radius (a), and Δk_{inf} curves for fuel models with UB_2 MDBAPs compared to ZrB_2 MDBAPs (b).

On the other hand, at 60.00 MWd/kgU, the k_{inf} values of fuel models with UB_2 MDBAPs in 28, 44, 72, 88, and 112 fuel rods are 297 pcm, 485 pcm, 760 pcm, 958 pcm, and 1,244 pcm higher than the BA-free fuel model, respectively. It should be noted that, depending on the number of fuel rods containing BA in the fuel assembly, fuel models with ZrB_2 MDBAPs begin to provide higher k_{inf} values than the BA-free fuel model between 40.00 MWd/kgU and 43.00 MWd/kgU. Furthermore, it is found that UB_2 MDBAPs provide a higher reactivity compared to ZrB_2 MDBAPs. For instance, at the beginning of the fuel's life, a fuel assembly containing UB_2 MDBAPs in 112 fuel rods exhibits a reactivity value approximately 1,850 pcm higher. This difference climbs to about 2,470 pcm at 16.00 MWd/kgU, before it starts to lessen. Although, in the range between 45.00 and 60.00 MWd/kgU, there are instances where fuel models with ZrB_2 MDBAPs show up to 46 pcm higher reactivity, at 60.00 MWd/kgU, the fuel model with UB_2 MDBAPs manifests a 36 pcm higher reactivity value. Nevertheless, the overall implication is that, with an increase in the number of fuel rods containing MDBAPs, the reactivity obtained with the use of UB_2 MDBAPs shows a greater increase in the first half of the fuel's lifespan compared to that achieved with ZrB_2 MDBAPs.

In conclusion, while MDBAPs suppress reactivity at the beginning of the cycle, they also provide relatively higher reactivity at the end of the cycle compared to the BA-free fuel model and the fuel model using DBAPs. It can be said that it is an important alternative for cycles longer than 24-months as it has a lower ^{10}B content compared to DBAPs and the self-shielding effect continues when a high radius moderator is used.

5.4.6 Boron-10 Depletion Behaviour in IFBAs, DBAPs and MDBAPs

The design differences inherent in IFBAs, DBAPs, and MDBAPs are found to influence the depletion behaviours of ^{10}B atoms within their compositions. This influence is attributed to both the changing surface area and the varying number of ^{10}B atoms. In Figure 42a, the depletion behaviours of ^{10}B in fuel models with IFBAs, ZrB_2 DBAPs, and MDBAPs are presented, whereas Figure 42b compares the fuel models with IFBAs and those with UB_2 DBAPs, and MDBAPs.

As observed in Figure 42, in the fuel model utilising IFBAs, the depletion of ^{10}B atoms occurs more rapidly compared to those models using DBAPs and MDBAPs. This is primarily due to the IFBA being coated as a thin layer on the fuel pellet, resulting in a lower amount of ^{10}B atoms. However, upon examination of the ^{10}B depletion in both 1.00 mm ZrB_2 and 1.00 mm

UB_2 DBAPs, it is noted that the near-complete depletion of ^{10}B atoms occurs beyond 46.00 MWd/kgU. When comparing fuel models with DBAPs to those with MDBAPs, the addition of a 0.50 mm moderator leads to an earlier depletion of ^{10}B atoms as expected. Additionally, it is seen that, in MDBAPs, maintaining a constant moderator radius while increasing the MDBAP radius delays the depletion of ^{10}B atoms, whereas increasing the moderator radius with a constant MDBAP radius accelerates their depletion.

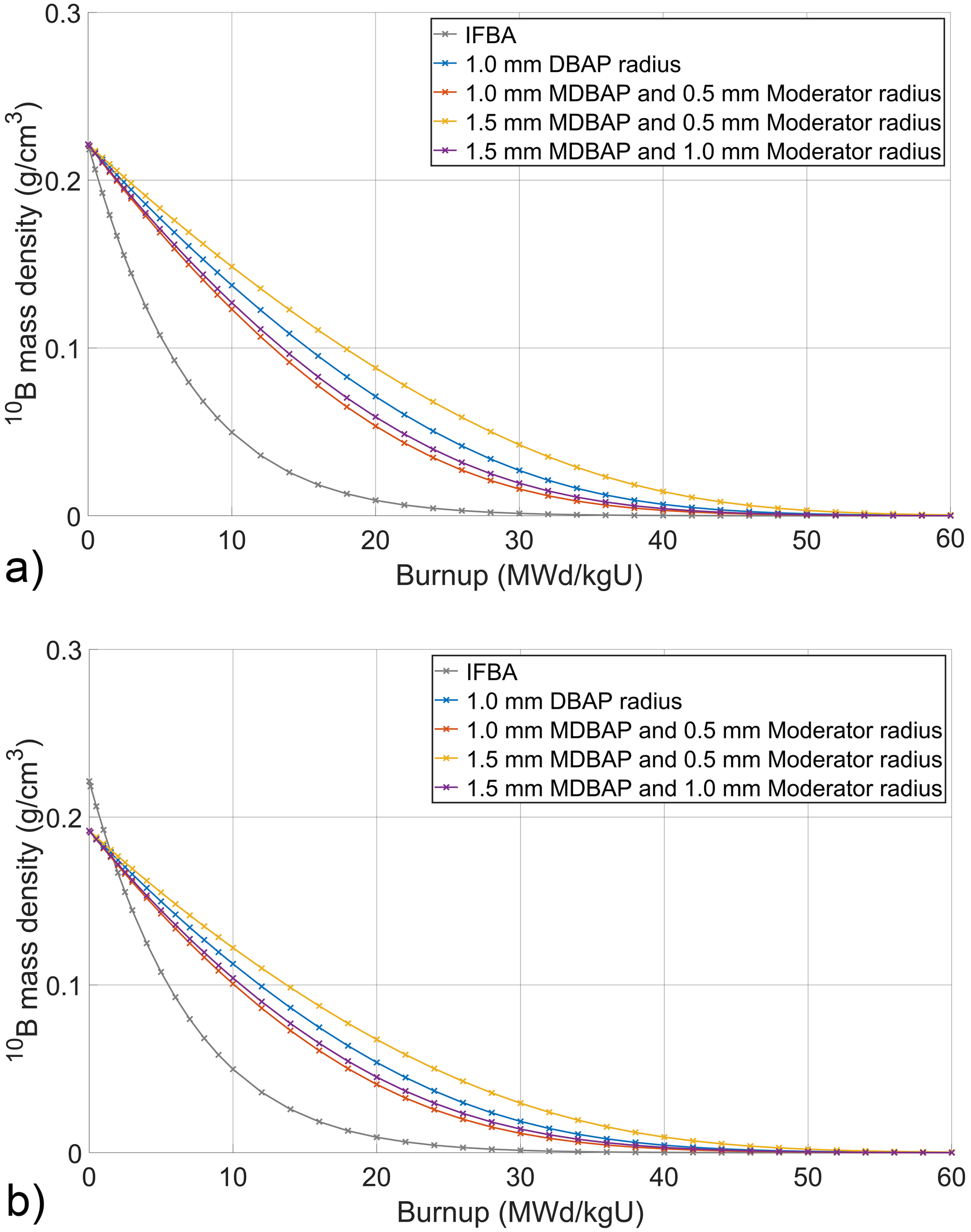

Figure 42 – ^{10}B depletion behaviour of fuel models with ZrB_2 (a) and UB_2 (b) MDBAPs in 112 BA rods.

5.4.7 Serpent and CASMO-4 Comparison for Reactivity Determination

The analyses in this chapter were carried out with the Serpent 2 Monte Carlo reactor physics code using the JEFF-3.1 nuclear data library. However, for the testing of the reactor performances of DBAPs and MDBAPs in 3D fuel cycle analyses, Studsvik's CASMO-4/SIMULATE-3 advanced nuclear design code system, equipped with the ENDF/B-VI neutron data library, will be used. Therefore, examining the infinite multiplication factor values calculated by both codes has importance, as previously discussed in Section 3.3.6. The infinite multiplication factor values for the fuel models enriched with 4.45 wt.% ^{235}U are shown in Figure 43. Specifically, Figure 43a presents the curves of infinite multiplication factors for fuel models using DBAPs and MDBAPs with ZrB_2 content, obtained with Serpent and CASMO-4, while Figure 43b shows the Δk_{inf} curves indicating the differences in values obtained by both codes for the same fuel models. On the other hand, Figures 43c and d respectively illustrate the infinite multiplication factor curves and Δk_{inf} curves for fuel models employing DBAPs and MDBAPs with UB_2 content.

Upon examining Figure 43, it is apparent that differences in k_{inf} values obtained with Serpent and CASMO-4 occur at the beginning of the life of all fuel models, up to 1632 pcm. For all fuel models, after observing the lowest values between 40.00 and 50.00 MWd/kgU, there are observed increases, up to $\sim$250 pcm towards the end of all the fuels' life.

In summary, the results obtained with both codes indicate that all fuel models exhibit similar trends, and the differences between them decrease as burnup progresses towards the end of the fuels' lifespan. The inability to alter the neutron data libraries used in the codes within the scope of the project has prevented the determination of the reasons behind these differences. However, considering the trends and the narrowing gap between obtained k_{inf} values with the two codes as the fuels approach the end of their lifespan, it can be presumed that 3D full core analyses conducted with either code will yield parallel results.

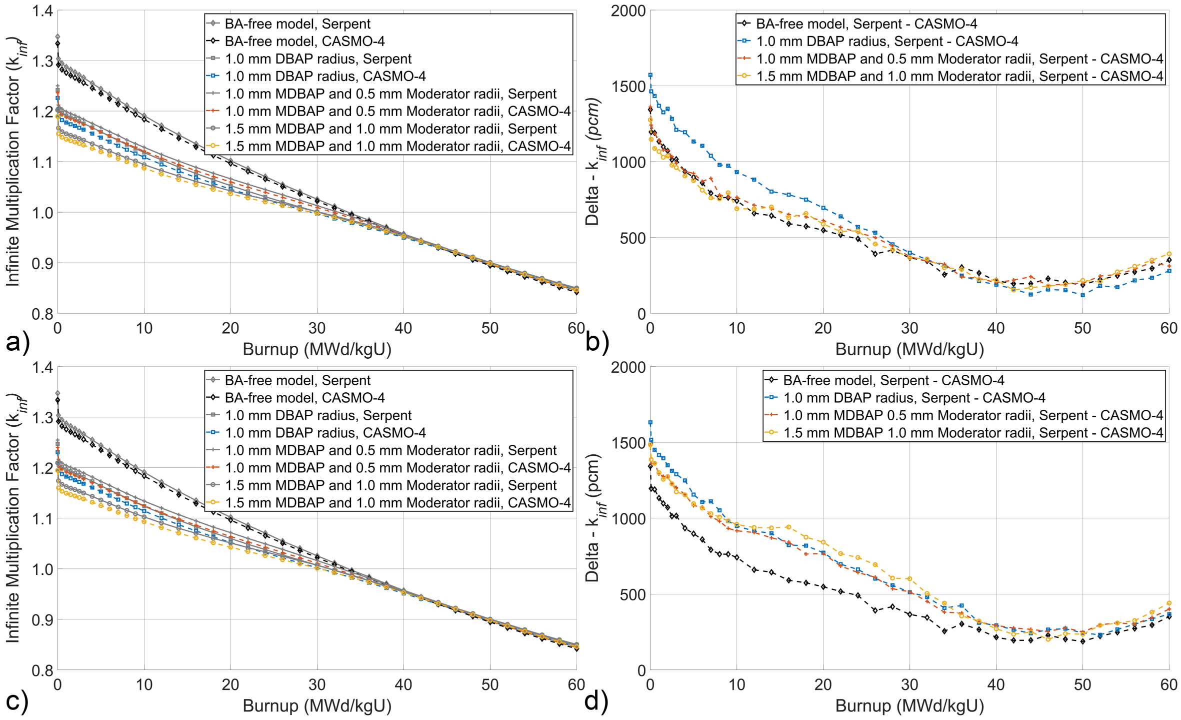

Figure 43 – Comparison of Δk_{inf} curves obtained with Serpent and CASMO-4 for ZrB_2 and UB_2 DBAPs. (a) Comparison of ZrB_2 DBAPs, (b) Δk_{inf} between Serpent and CASMO4 for ZrB_2 DBAPs, (c) Comparison of UB_2 DBAPs, (d) Δk_{inf} between Serpent and CASMO4 for UB_2 DBAPs.

5.5 Chapter Summary

Thorough neutronic analyses were conducted for DBAPs and MDBAPs, with a focus on reactivity behaviour and ^{239}Pu breeding and ^{10}B depletion. The results show that the use of ZrB_2 and UB_2 DBAPs suppresses initial reactivity, with greater suppression as the number of fuel rods with DBAPs or the DBAPs' radius increases. UB_2 suppresses reactivity less than ZrB_2 at the beginning of the fuel's life due to the presence of fissile uranium, although both designs provide similar reactivity values at the end of the fuel's life.

Increasing the distribution of ZrB_2 and UB_2 in the fuel assembly results in higher suppression of reactivity at the beginning of the fuel's life without affecting reactivity at the end. Both types of DBAPs promote faster growth of ^{239}Pu on the outer surface of the BA fuel pellets compared to a non-BA pellet. The depletion rate of ^{10}B atoms is faster on the surface than at the centre for both BA types.

Additionally, the depletion of ^{10}B atoms in the fuel assembly leads to a hardened neutron spectrum, causing a decrease in the depletion rate of ^{235}U atoms and an increase in the breeding rate of ^{239}Pu. The MDBAP design, in comparison, suppresses reactivity at the beginning of the cycle and provides higher reactivity at the end of the cycle, revealing it as an important alternative for longer cycles.

Chapter 6

Fuel Cycle Analysis of DBAPs and MDBAPs in a 36-month Cycle with High Assay Low Enriched Uranium

A research paper titled "Shifting to a 36-month Fuel Cycle with Advanced Moderating Burnable Absorbers Enabling High Assay Low Enriched Uranium (HALEU)" was published in Progress in Nuclear Energy using the methodology and a portion of the data presented in this chapter [121].

6.1 Chapter Overview

In this chapter, an evaluation of the possibility of transitioning from an 18-month fuel cycle, using IFBAs as BA, to a 36-month fuel cycle is discussed. HALEU that contained 5.00 wt.% beyond ^{235}U enrichment was employed as fuel in the 36-month cycle. Furthermore, building upon the neutronic analysis, ZrB_2 and UB_2 DBAPs and MDBAPs, that were previously presented in Section 5.2, were tested as BA with the aim of revealing the potential of this new design and pioneering future studies.

A standard 3-loop PWR designed by Westinghouse Electric Company was preferred as the reference NPP. Peaking factors, including nuclear enthalpy rise hot channel factor and heat flux hot channel factor, were explored, along with the investigation of the change in critical boron concentration. Additionally, the reactivity feedback parameters, such as the moderator temperature coefficient, isothermal temperature coefficient, uniform Doppler coefficient, and boron coefficient, were examined in addition to the average axial 2D relative power distribution and assembly-wise 2D relative power distribution. Finally, the possible economic benefits were discussed.

6.2 Method

Simulations were performed with Studsvik's CASMO-4/SIMULATE-3 code system, utilising the ENDF/B-VI nuclear data library As a reference NPP, a Westinghouse Electric Company designed 3-loop PWR was preferred for these simulations. NPP features, as provided in the Studsvik's CASMO3/SIMULATE4 manual [112], and simulation parameters are given in Table 12 [96], [113].

In the utilisation of IFBAs scenario, the discharge of 35 once-burned fuel assemblies and 29 twice-burned fuel assemblies was considered for the 508 EFPDs, while 64 fresh fuel assemblies were loaded in each fuel cycle. The effect of a decreasing batch number was previously discussed in Section 4.2. However, in order to achieve long cycles such as 36-months, a high number of fresh fuel assemblies must be loaded, which necessitated a reduction in the batch number. In addition, single-batch cores are less flexible in terms of fuel management compared to multi-batch cores, due to the fact that the high reactivity of fresh fuel cannot be effectively offset by the decreased reactivity of fuel assemblies from the previous cycle, as previously noted by Delgado and others [83].

To address this inflexibility, a two-batch loading strategy was employed for the simulations, specifically investigating the DBAPs and MDBAPs usage scenarios with the objective of reaching 1055 EFPDs. Different numbers of fresh fuel assemblies were loaded in each fuel cycle. During initial utilisation, fuel assemblies with the lowest burnup were placed in locations within the reactor core where maximum burning could occur during the subsequent cycle. In addition, it is important to note that the fuel loading patterns used in the simulations are not optimized.

In the case of using UB_2 as a burnable absorber, its uranium enrichment level was kept consistent with the enrichment level of the UO_2 fuel in which it was inserted. Additionally, it was assumed that both ZrB_2 and UB_2 burnable absorbers had a natural boron isotopic composition, with no enrichment of ^{10}B.

Two-group cross-section data for approximately 2,300 fuel assemblies with different enrichment levels and numbers of IFBA rods produced with CASMO-4, applying default azimuthal subdivision. considering dissimilar fuel enrichment levels, varying BA and moderator radii, and different numbers of DBAP and MDBAP rods. The CMS-Link software package was utilised to create the library for SIMULATE-3 simulations. Following that, over 3 million fuel cycle simulations were conducted using SIMULATE-3 to ascertain the required fuel compositions of equilibrium cycles that would achieve the desired EFPDs within the design and operation limits.

Table 12 – Fuel design parameters and operation limits of a standard Westinghouse 3-loop PWR [96], [112], [113].

Parameter	Value
Reactor type	3-loop PWR
Coolant inlet temperature at full power (°C)	286
Power output (MWt/MWe)	2,900/964
System pressure (MPa)	15.5
Control rod material	Ag - In - Cd
Number of fuel assemblies	157
Rod array	17 × 17
Assembly pin pitch (cm)	1.26
Fuel pellet radius (cm)	0.410
Number of control rods/guide tube	24/1
Number of BA rods	28 to 112
Fuel assembly pitch (cm)	21.50
Fuel assembly height (cm)	365.76
Cladding material	Zircaloy-4
UO_2 fuel density (% of TD)	95.5
Nuclear enthalpy rise got channel factor ($F_{\Delta H}$)	≤ 1.66
Heat flux hot channel factor (F_Q)	≤ 2.41
Moderator temperature coefficient (pcm/°F)	$-50 \leq \text{MTC} < 0$
Critical boron concentration (targeted) (ppm)	$\leq$ 1,800
Peak assembly burnup (MWd/kgU)	≤ 62
Shutdown margin (pcm)	≤ -1770
Cycle length (months)	18 - 36
Effective full power days	508 - 1055
Refueling outages (days)	40

In order to achieve 508 days of EFPDs within design and operation limits in the case of IFBA usage, the required enrichment levels were determined by conducting simulations. A constant refueling time was assumed, to determine the required number of fresh fuel assemblies, fuel enrichment levels, necessary properties of DBAP and MDBAP to provide 1055 EFPDs (i.e., a 36-month cycle). The reason behind the selection of EFPDs will be explained later in Section 6.3.6.

The fuel loading pattern, capable of achieving the targeted EFPDs, has been determined to have flexible applicability to all fuel models and to be capable of meeting the power peaking requirements through four different enrichment levels. For this purpose, various fuel loading patterns were established, each consisting of 64, 72, 88, 100, 120, 128, 129, and 130 fresh fuel assemblies.

During the creation of these fuel loading patterns, assemblies with the lowest burnup within each batch were moved to locations where they would burn the most in subsequent cycles, taking into account the symmetry of each quarter of the reactor core. To ensure finding a loading pattern that could provide the required flexibility, all fresh fuel assemblies were tested with equal enrichment levels sequentially at 6.20 wt.%, 6.45 wt.%, 6.70 wt.%, and 6.95 wt.%. It was determined that the fuel loading pattern comprising 129 fresh fuel assemblies could provide the necessary flexibility for 1055 EFPD.

Following this, the fuel loading pattern was divided into four different groups, with attention being paid to the preservation of reactor core symmetry. Subsequently, within these groups, the numbers of fresh fuel assemblies and enrichment levels were set to be inversely proportional (for example, the group with the highest number of fresh fuel assemblies having the lowest level of uranium enrichment). After this, varying the enrichment levels of ^{235}U (from 6.20 wt.% to 6.95 wt.%), DBAP/MDBAP radius (ranging from 0.40 mm to 2.50 mm), and moderator radii for MDBAPs (ranging from 0.40 mm to 2.40 mm), simulations were conducted for each scenario. Finally, the scale of enrichment levels and DBAP/MDBAP properties for each fuel model was narrowed, resulting in 560,000 different simulations being carried out for usage scenarios of each fuel model.

Candidates that satisfied the design and safety limits while demonstrating the lowest critical boron concentration with the minimum possible ^{235}U enrichment level were selected from the simulation results for comparison in the context of MDBAPs usage.

To prevent power peaks, fresh fuel assemblies were divided into four groups based on their enrichment levels in IFBA usage scenario. In the case of IFBA design, a 15.24 cm BA free zone was preferred on both the top and bottom of the fuel assembly, whereas 15.24 cm on the top and 10.24 cm on the bottom BA free zones were preferred for DBAPS and MDBAPs to achieve a more even axial power distribution. For the 18-month and 36-month fuel cycles, the fuel loading schemes displayed in Figure 44 were employed. Additionally, for the distribution of BA within the fuel assemblies, the layout illustrated in Figure 29e was employed.

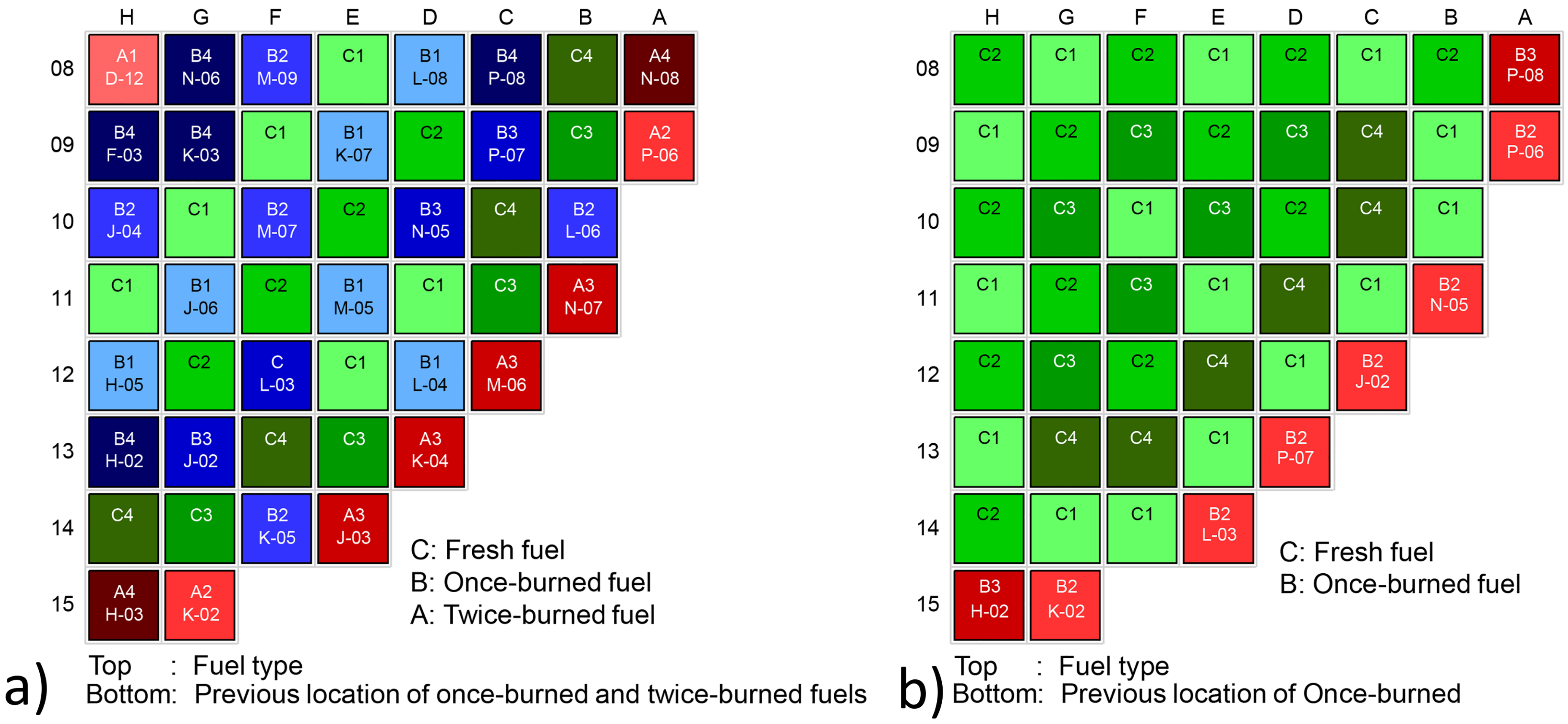

a)

	H	G	F	E	D	C	B	A
08	A1 D-12	B4 N-06	B2 M-09	C1	B1 L-08	B4 P-08	C4	A4 N-08
09	B4 F-03	B4 K-03	C1	B1 K-07	C2	B3 P-07	C3	A2 P-06
10	B2 J-04	C1	B2 M-07	C2	B3 N-05	C4	B2 L-06	
11	C1	B1 J-06	C2	B1 M-05	C1	C3	A3 N-07	
12	B1 H-05	C2	C L-03	C1	B1 L-04	A3 M-06		
13	B4 H-02	B3 J-02	C4	C3	A3 K-04			
14	C4	C3	B2 K-05	A3 J-03				
15	A4 H-03	A2 K-02						

C: Fresh fuel
B: Once-burned fuel
A: Twice-burned fuel

Top : Fuel type
Bottom: Previous location of once-burned and twice-burned fuels

b)

	H	G	F	E	D	C	B	A
08	C2	C1	C2	C1	C2	C1	C2	B3 P-08
09	C1	C2	C3	C2	C3	C4	C1	B2 P-06
10	C2	C3	C1	C3	C2	C4	C1	
11	C1	C2	C3	C1	C4	C1	B2 N-05	
12	C2	C3	C2	C4	C1	B2 J-02		
13	C1	C4	C4	C1	B2 P-07			
14	C2	C1	C1	B2 L-03				
15	B3 H-02	B2 K-02						

C: Fresh fuel
B: Once-burned fuel

Top : Fuel type
Bottom: Previous location of Once-burned

Figure 44 – Fuel loading scheme of the 18-month fuel cycle with IFBAs (a) [115] and 36-month fuel cycles with DBAPs or MDBAPs (b).

A comprehensive analysis of several fuel parameters was conducted, which included the moderator temperature coefficient, nuclear enthalpy rise got channel factor, heat flux hot channel factor, isothermal temperature coefficient, uniform Doppler coefficient, and boron coefficient. Additionally, the average axial 2D relative power fraction profile and assembly-wise 2D relative power fraction of the fuel core were evaluated at 12 axial nodes. Additionally, the fuel loading cost of the 36-month cycle with the use of MDBAPs is discussed using the same methodology as in Section 4.2 ignoring the cost of MDBAP fabrication and utilisation.

6.3 Results and Discussion

6.3.1 Fuel Cycle Analysis of DBAPs

When IFBA is utilised as BA, the necessary fuel compositions for a reactor operating within design and operation limits during an 18-month cycle under the 5.00 wt.% ^{235}U enrichment level, which is the legal limit, were determined.

The information in Table 13 pertains to the required number of fresh fuel assemblies, their ^{235}U enrichment levels, and their corresponding core positions required for an equilibrium cycle using IFBA as BA to achieve 508 EFPDs within the design and operation limits. Based on numerous simulations, it has been determined that an 18-month fuel cycle with 508 EFPDs can be achieved using IFBA by utilising 20 units of fuel enriched with 4.65 wt.% of ^{235}U, 16 units of fuel enriched with 4.70 wt.% of ^{235}U, 16 units of fuel enriched with 4.75 wt.% of ^{235}U, and 12 units of fuel enriched with 4.80 wt.% of ^{235}U, each containing 112 IFBA rods.

Table 13 – Fuel configuration parameters for achieving 508 EFPDs with IFBAs.

Number of fresh FAs	Uranium enrichment (wt.%)	In-core position
20	4.65	C1
16	4.70	C2
16	4.75	C3
12	4.80	C4

Simulations were conducted by targeting 1055 EFPDs with 129 fresh fuel assemblies in each cycle in the case of using DBAP, assuming the planned refueling outage in the 36-month cycle is 40 days, as in the 18-month cycle. As will be explained later, the BOC critical boron concentration is 1,687 ppm in the 18-month cycle with IFBA. Although this value is lower than the design limit of 2,222 ppm for a 3-loop PWR, simulations were designed to keep the critical boron concentration below 1,800 ppm to prevent the moderator temperature coefficient from reaching less (negative) values.

Information regarding the number of fuel assemblies required, their respective locations in the fuel core, and the DBAP radius for scenarios involving separate use of ZrB_2 DBAPs and UB_2 DBAPs is shown in Table 14. The scenarios presented in the table are related to situations where the maximum enrichment level of ^{235}U is below 7.00 wt.%, the critical boron concentration is below 1,800 ppm, and maximum nuclear enthalpy rise hot channel factor and maximum heat flux hot channel factor remain within the design and operation limits during the transition and equilibrium cycles. Additionally, the fuels have been categorized into four groups based on different levels of ^{235}U enrichment and DBAP radius to prevent power peaks. Undoubtedly, employing fixed DBAPs with a constant radius inside the reactor would be simpler and more cost-effective in terms of production engineering. Nonetheless, it is crucial to note that when DBAPs with constant radius were utilised in all BA rods, power peaks were not prevented and a cycle within the design and operation limits could not be obtained.

Table 14 – Fuel configuration parameters for ZrB_2 DBAPs and UB_2 DBAPs.

Number of fresh FAs	Uranium enrichment (wt.%)	ZrB_2 DBAP radius (mm)	UB_2 DBAP radius (mm)	In-core position
48	6.85	0.9	0.9	C1
33	6.90	1.1	1.1	C2
24	6.95	1.0	1.2	C3
24	6.95	0.9	0.9	C4

When Table 14 is examined, it can be seen that under the conditions of maintaining the ^{235}U enrichment level below 7.00 wt% and keeping the critical boron concentration below 1,800 ppm, it is possible to load a maximum of 48 fuel assemblies with 6.85 wt.% ^{235}U enrichment level and 0.90 mm ZrB_2 DBAP radius, 33 fuel assemblies with 6.90 wt.% ^{235}U enrichment level and 1.10 mm ZrB_2 DBAP radius, 24 fuel assemblies with 6.95 wt.% ^{235}U enrichment level and 1.00 mm ZrB_2 DBAP radius, and 24 fuel assemblies with 6.95 wt.% ^{235}U enrichment level and 0.90 mm ZrB_2 DBAP radius, each containing 112 ZrB_2 DBAP rods, within the design and operation limits.

On the other hand, when UB_2 DBAP is used instead of ZrB_2 DBAP, a maximum of 48 assemblies with 6.85 wt.% ^{235}U enrichment level and 0.90 mm UB_2 DBAP radius, 33 assemblies with 6.90 wt.% ^{235}U enrichment level and 1.10 mm UB_2 DBAP radius, 24 assemblies with 6.95 wt.% ^{235}U enrichment level and 1.20 mm UB_2 DBAP radius, and 24 assemblies with 6.95 wt.% ^{235}U enrichment level and 0.90 mm UB_2 DBAP radius can be loaded into the reactor core within the design and operation limits.

Table 15 presents the critical boron concentration, effective multiplication factor at the beginning of the cycle, maximum hot channel factor for nuclear enthalpy rise, maximum hot channel factor for heat flux, cycle burnup, and cycle EFPDs of the 18-month equilibrium cycle using IFBA as BA (hereafter called the IFBA equilibrium cycle). Additionally, the transition and equilibrium cycles targeting 36-month fuel cycle with ZrB_2 DBAP as BA (hereafter called the ZrB_2 DBAP transition or equilibrium cycles) with the fuel compositions reported in Table 14. In Table 15, "cycle 0" is the final 18-month cycle with IFBA, whereas "cycle 1" represents the first feed of ZrB_2 DBAPs.

Table 15 – Equilibrium and transition cycles parameters of 18-month cycle with IFBAs and 36-month targeted cycle with ZrB_2 DBAPs.

Cycle Number	Cycle Definition	CBC - BOC (ppm)	k_{eff} - BOC	Maximum $F_{\Delta H}$	Maximum F_Q	Cycle Burnup (MWd/kgU)	Cycle EFPDs
-1	18-month equilibrium cycle	1,687.4	1.10781	1.616	1.948	19.925	507.8
0	18-month equilibrium cycle	1,687.4	1.10781	1.616	1.948	19.925	507.8
1	36-month targeted transition cycle first feed	1,766.7	1.08101	1.606	1.985	35.877	894.0
2	36-month targeted transition cycle second feed	1,742.1	1.07843	1.640	2.051	36.784	912.4
3*	36-month targeted equilibrium cycle	1,742.3	1.07844	1.639	2.050	36.774	912.2
4	36-month targeted equilibrium cycle	1,742.3	1.07844	1.639	2.050	36.775	912.2

When examining Table 15, it is seen that the IFBA equilibrium cycle requires a critical boron concentration of 1,687.4 ppm at the beginning of the cycle, while the ZrB_2 DBAP equilibrium cycle necessitates an increase of approximately 3.3%, bringing the requirement to 1,742.3 ppm at the beginning of the cycle. While the k_{eff} at BOC of the IFBA equilibrium cycle is 1.10781, the k_{eff} at BOC of the ZrB_2 DBAP equilibrium cycle is 1.07844. Furthermore, the maximum nuclear enthalpy rise hot channel factor, which is 1.616 in the IFBA equilibrium cycle, increases by 1.4% to 1.639 in the ZrB_2 DBAP equilibrium cycle, while the maximum heat flux hot channel factor, which stands at 1.948 in the IFBA equilibrium cycle, increases by 5.2% to 2.050 in the ZrB_2 DBAP equilibrium cycle.

On the other hand, a burnup of 19.93 MWd/kgU is achieved in the IFBA equilibrium cycle, while a burnup of 36.77 MWd/kgU is attained in the ZrB_2 DBAP equilibrium cycle, due to direct impact of increased enrichment and fresh fuel assembly count. However, it is observed that the desired goal of achieving 1055 EFPDs in a 36-month fuel cycle with ZrB_2 DBAPs usage cannot be reached with the loaded fuels reported in Table 14. When ZrB_2 DBAPs are used, the first transition cycle reaches 894 EFPDs after the initial feed. Afterward, approximately 912 EFPDs is obtained in the second transition cycle, and equilibrium is reached in the third cycle, with 912 EFPDs being obtained in all subsequent cycles, that is approximately 13% less than the targeted EFPDs.

In Table 16, the critical boron concentration, effective multiplication factor at the beginning of the cycle, maximum hot channel factor for nuclear enthalpy rise, maximum hot channel factor for heat flux, cycle burnup, and cycle EFPDs are shown for the IFBA equilibrium cycle. Additionally, the transition and equilibrium cycles targeting a 36-month fuel cycle with UB_2 DBAPs as BA (hereafter called the UB_2 transition or equilibrium cycles) are reported with fuel compositions reported in Table 14. In Table 16, "cycle 0" is the final 18-month cycle with IFBA, whereas "cycle 1" represents the first feed of UB_2 DBAPs.

Table 16 – Equilibrium and transition cycles parameters of 18-month cycle with IFBAs and 36-month targeted cycle with UB_2 DBAPs.

Cycle Number	Cycle Definition	CBC - BOC (ppm)	k_{eff} - BOC	Maximum $F_{\Delta H}$	Maximum F_Q	Cycle Burnup (MWd/kgU)	Cycle EFPDs
-1	18-month equilibrium cycle	1,687.4	1.10781	1.616	1.948	19.925	507.8
0	18-month equilibrium cycle	1,687.4	1.10781	1.616	1.948	19.925	507.8
1	36-month targeted transition cycle first feed	1,793.7	1.08175	1.609	1.971	36.699	939.2
2	36-month targeted transition cycle second feed	1,775.5	1.07942	1.633	2.012	37.623	963.5
3*	36-month targeted equilibrium cycle	1,775.0	1.07940	1.634	2.014	37.564	962.0
4	36-month targeted equilibrium cycle	1,775.1	1.07941	1.634	2.013	37.570	962.2

A comparison between the IFBA and the UB_2 DBAP equilibrium cycles reveals that the UB_2 DBAP equilibrium cycle necessitates a 5.2% increase in critical boron concentration, resulting in a requirement of 1,775.0 ppm at the beginning of the cycle. The k_{eff} at BOC of the IFBA equilibrium cycle is 1.10781 while the k_{eff} at BOC of the UB_2 DBAP equilibrium cycle is 1.07940. Moreover, in the UB_2 DBAP equilibrium cycle, the maximum nuclear enthalpy rise hot channel factor is increased by 1.1% to 1.634, while the maximum heat flux hot channel factor is raised by 3.4% to 2.014.

Nonetheless, it is observed that, while a burnup of 37.56 MWd/kgU is reached, the objective of achieving 1055 EFPDs in a 36-month fuel cycle with UB_2 DBAP usage cannot be attained with the loaded fuels reported in Table 14, similar to the ZrB_2 DBAP usage scenario. With the utilisation of UB_2 DBAP, the first transition cycle achieves approximately 939 EFPDs after the initial feed. Subsequently, around 963 EFPDs is obtained in the second cycle, and equilibrium is reached in the third cycle, with approximately 962 EFPDs being acquired in all following cycles, which is nearly 9% less than the targeted EFPDs. Although 50 EFPDs more was achieved with UB_2 DBAP compared to ZrB_2 DBAP, the targeted 1055 EFPDs could not be reached with a maximum of 7.00 wt.% ^{235}U enrichment level and below 1,800 ppm critical boron concentration within the design and operation limits.

6.3.2 Fuel Cycle Analysis of MDBAPs

Given that the DBAP design, which have a relatively high ^{10}B loading, hinders the achievement of the targeted EFPDs at this stage, an alternative design is required. The initial simulations showed that higher burnup and higher EFPDs could be achieved with the moderator addition in the centre of DBAP. Thus, the MDBAP concept emerged, as the design details were explained in detail in Section 5.2. Although there was no noticeable difference between the case where graphite was chosen and where beryllium oxide chosen as the moderator as a result of neutronic analyses, beryllium oxide was preferred for ongoing analyses due to its relatively higher moderation ratio, superior chemical stability, tensile strength and Young's modulus [118], [122].

Within the design and operation limits, an examination was conducted to determine the maximum EFPDs achievable under a 7.00 wt.% ^{235}U enrichment level and a critical boron concentration level below 1,800 ppm. However, since the aim of this study is to reach 1055 EPFD in a 36-month cycle, simulations were carried out reducing the ^{235}U enrichment level in each step while testing the different moderator and MDBAP radii for each ^{235}U enrichment level.

In Table 17, details are provided regarding the necessary fuel quantities, their associated ^{235}U enrichment levels, locations within the fuel core, and dimensions of the BA and moderator radii for the ZrB_2 and UB_2 MDBAPs to achieve 1055 EFPDs during the transition from an 18-month cycle to a 36-month cycle.

The simulation results have shown that for attaining 1055 EFPDs with the lowest initial critical boron concentration using ZrB_2 MDBAPs, each containing 112 MDBAP rods, the following fuel quantities are necessary: 48 units enriched with 6.60 wt.% ^{235}U, 33 units enriched with 6.65 wt.% ^{235}U, 24 units enriched with 6.70 wt.% ^{235}U, and 24 units enriched with 6.75 wt.% ^{235}U. Additionally, the ZrB_2 MDBAPs' dimensions for these groups, labelled as C1, C2, C3, and C4, comprise a 1.00 mm moderator radius and 1.20 mm BA radius, a 0.90 mm moderator radius and 1.30 mm BA radius, a 1.10 mm moderator radius and 1.60 mm BA radius, and a 1.10 mm moderator radius and 1.30 mm BA radius, respectively.

Conversely, employing UB_2 MDBAPs necessitates (each containing 112 MDBAP-loaded fuel rods) 48 units of fresh fuel enriched with 6.50 wt.% ^{235}U, 33 units enriched with 6.55 wt.% ^{235}U, 24 units enriched with 6.60 wt.% ^{235}U, and 24 units enriched with 6.65 wt.% ^{235}U. Moreover, the dimensions of the UB_2 MDBAP for these groups, referred to as C1, C2, C3, and C4, include a 1.00 mm moderator radius and 1.20 mm BA radius, a 1.10 mm moderator radius and 1.50 mm BA radius, a 1.10 mm moderator radius and 1.60 mm BA radius, and a 0.90 mm moderator radius and 1.20 mm BA radius, respectively.

Table 17 – Core configuration parameters for MDBAPs for 36-month cycle.

Number of fresh FAs	ZrB_2 MDBAP			UB_2 MDBAP			In-core position
	^{235}U enrichment (wt.%)	Moderator radius (mm)	BA radius (mm)	^{235}U enrichment (wt.%)	Moderator radius (mm)	BA radius (mm)	
48	6.60	1.0	1.2	6.50	1.0	1.2	C1
33	6.65	0.9	1.3	6.55	1.1	1.5	C2
24	6.70	1.1	1.6	6.60	1.1	1.6	C3
24	6.75	1.1	1.3	6.65	0.9	1.2	C4

In Table 18, critical boron concentration values, effective multiplication factor at beginning of the cycle, maximum nuclear enthalpy rise hot channel factor, maximum heat flux hot channel factor, cycle burnup, and cycle EFPDs are displayed for both the transition and equilibrium cycles, considering scenarios of 18-month cycles with IFBAs and 36-month cycles with ZrB_2 MDBAPs. Similarly, Table 19 presents the values for the same parameters using UB_2 MDBAPs. In both Table 18 and Table 19, the cycles designated as "cycle 0" were identified as the final 18-month cycle with IFBA, whereas "cycle 1" represents the first feed of ZrB_2 or UB_2 MDBAPs.

Table 18 – Equilibrium and transition cycles parameters of 18-month with IFBAs and 36-month with ZrB_2 MDBAPs cycles.

Cycle Number	Cycle Definition	CBC - BOC (ppm)	k_{eff} - BOC	Maximum $F_{\Delta H}$	Maximum F_Q	Cycle Burnup (MWd/kgU)	Cycle EFPDs
-1	18-month equilibrium cycle	1,687.4	1.10781	1.616	1.948	19.925	507.8
0	18-month equilibrium cycle	1,687.4	1.10781	1.616	1.948	19.925	507.8
1	36-month transition cycle first feed	1,242.1	1.05900	1.530	1.983	42.655	1050.2
2	36-month transition cycle second feed	1,224.0	1.05735	1.555	2.009	43.137	1055.3
3*	36-month equilibrium cycle	1,223.2	1.05731	1.556	2.010	43.111	1054.7
4	36-month equilibrium cycle	1,223.3	1.05731	1.556	2.010	43.113	1054.7

As can be seen in Table 18, the first transition cycle reaches approximately 1050 EFPDs upon the initial feed when ZrB_2 MDBAP is employed. It is observed that an equilibrium is attained in the third cycle, with about 1055 EFPDs and a burnup of 43.11 MWd/kgU in all subsequent cycles with a k_{eff} at BOC of 1.05731.

At the beginning of the cycle, the ZrB_2 MDBAP equilibrium cycle necessitates a critical boron concentration of 1,223.2 ppm, which is roughly 28% lower than the critical boron concentration of the IFBA equilibrium cycle. Furthermore, the maximum nuclear enthalpy rise hot channel factor experiences a 3.7% decrease to 1.556 in the ZrB_2 MDBAP equilibrium cycle, while the maximum heat flux hot channel factor increases by 3.2% to 2.010. The utilisation of ZrB_2 MDBAP results in not only the achievement of the desired EFPDs but also the attainment of lower critical boron concentration and peaking factors.

In Table 19, it is evident that when UB_2 MDBAP is utilised, the first transition cycle achieves roughly 1050 EFPDs upon the initial feed. Equilibrium is reached in the third cycle, as observed, with approximately 1055 EFPDs and a burnup of 42.29 MWd/kgU in all following cycles.

At the beginning of the cycle, a critical boron concentration of 1,114.8 ppm is required for the UB_2 MDBAP equilibrium cycle, which is about 34% less than that of the IFBA equilibrium cycle. Additionally, the maximum nuclear enthalpy rise hot channel factor witnesses a 5.7% reduction to 1.524 in the UB_2 MDBAP equilibrium cycle, whereas the maximum heat flux hot channel factor experiences a 3.1% increase to 2.009. The employment of UB_2 MDBAP leads not only to the accomplishment of the desired EFPDs but also to the acquisition of lower critical boron concentration and maximum nuclear enthalpy rise hot channel factor.

Table 19 – Equilibrium and transition cycles parameters of 18-month with IFBAs and 36-month with UB_2 MDBAPs cycles.

Cycle Number	Cycle Definition	CBC - BOC (ppm)	k_{eff} - BOC	Maximum $F_{\Delta H}$	Maximum F_Q	Cycle Burnup (MWd/kgU)	Cycle EFPDs
-1	18-month equilibrium cycle	1,687.4	1.10781	1.616	1.948	19.925	507.8
0	18-month equilibrium cycle	1,687.4	1.10781	1.616	1.948	19.925	507.8
1	36-month targeted transition cycle first feed	1,134.2	1.05422	1.563	2.020	41.923	1050.1
2	36-month targeted transition cycle second feed	1,115.8	1.05260	1.527	2.007	42.318	1055.8
3*	36-month targeted equilibrium cycle	1,114.8	1.05254	1.524	2.009	42.291	1055.1
4	36-month targeted equilibrium cycle	1,115.0	1.05255	1.524	2.009	42.293	1055.2

On the other hand, in comparison to the ZrB_2 MDBAP equilibrium cycle, it is observed that the UB_2 MDBAP equilibrium cycle reaches 1055 EFPDs with a reduced fuel enrichment level and a lower burnup rate (43.11 MWd/kgU for ZrB_2 and 42.29 MWd/kgU for UB_2 MDBAP with a k_{eff} at BOC of 1.05254), which is attributed to the difference in the mass of loaded fissile material. An equal amount of fissile material loading in the reactor core results in an equal amount of discharge burnup. Additionally, it has been observed that the highest burnup in the ZrB_2 MDBAP equilibrium cycle occurs at 61.52 MWd/kgU for a twice-burned fuel assembly, while in the UB_2 MDBAP, the highest burnup occurs at 60.29 MWd/kgU for a twice-burned fuel assembly.

In summary, the desired 1055 EFPDs can be attained with the utilisation of both ZrB_2 and UB_2 MDBAPs. In addition to requiring a lower critical boron concentration compared to the 18-month IFBA equilibrium cycle, it also results in lower peaking factors such as maximum nuclear enthalpy rise hot channel factor and maximum heat flux hot channel factor.

6.3.3 Reactivity Feedback Parameters and Shutdown Margin of MDBAPs

The reactivity feedback parameters for the usage scenarios of ZrB_2 and UB_2 MDBAPs, which reached the targeted 1055 EFPDs, were analysed. Equilibrium cycles were evaluated, and the curves for the moderator temperature coefficient, isothermal temperature coefficient, uniform Doppler coefficient, and boron coefficient are presented in Figures 45 and 46. Specifically, Figure 45 illustrates the curves for an 18-month equilibrium cycle with IFBA, whereas Figures 46a and 46b demonstrate the curves for 36-month equilibrium cycles with ZrB_2 and UB_2 MDBAPs, respectively.

On initial inspection of Figures 45 and 46, it appears that the utilisation of both ZrB_2 and UB_2 MDBAP has not caused any negative impact on the values of the moderator temperature coefficient, isothermal temperature coefficient, uniform Doppler coefficient, and boron coefficient since the changes are within design and operation limits.

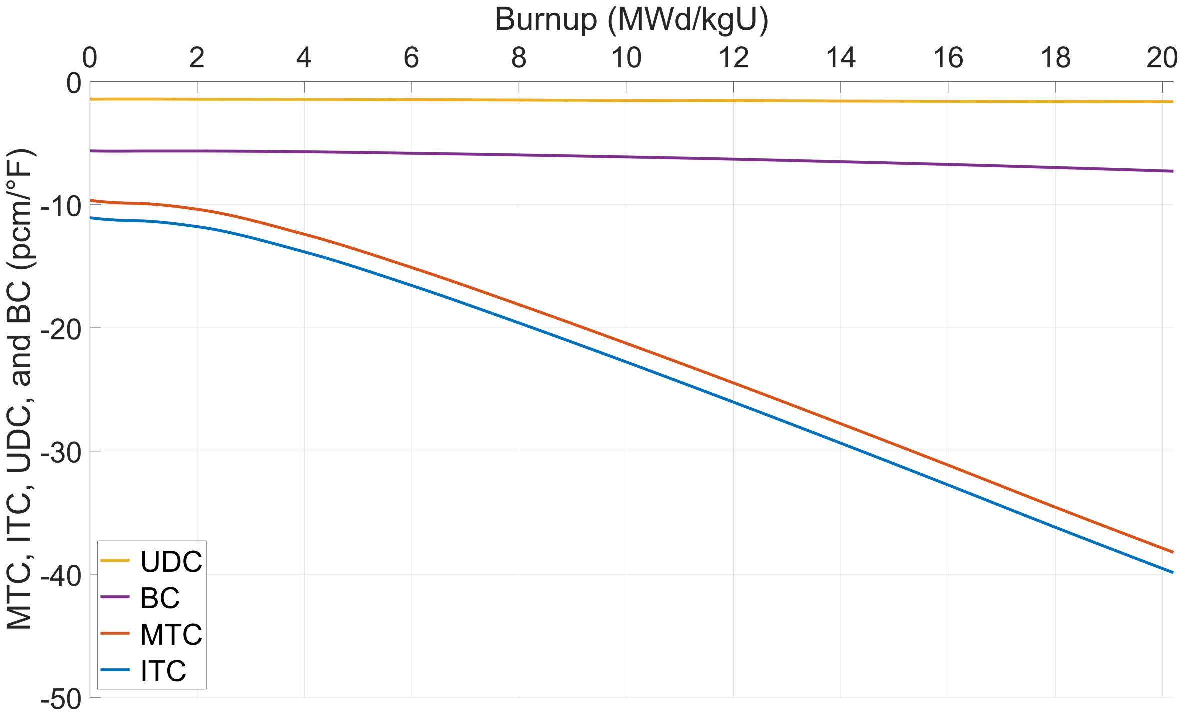

Figure 45 – Moderator temperature coefficient (MTC), isothermal temperature coefficient (ITC), uniform Doppler coefficient (UDC), and boron coefficient (BC) curves of 18-month equilibrium cycle with IFBA.

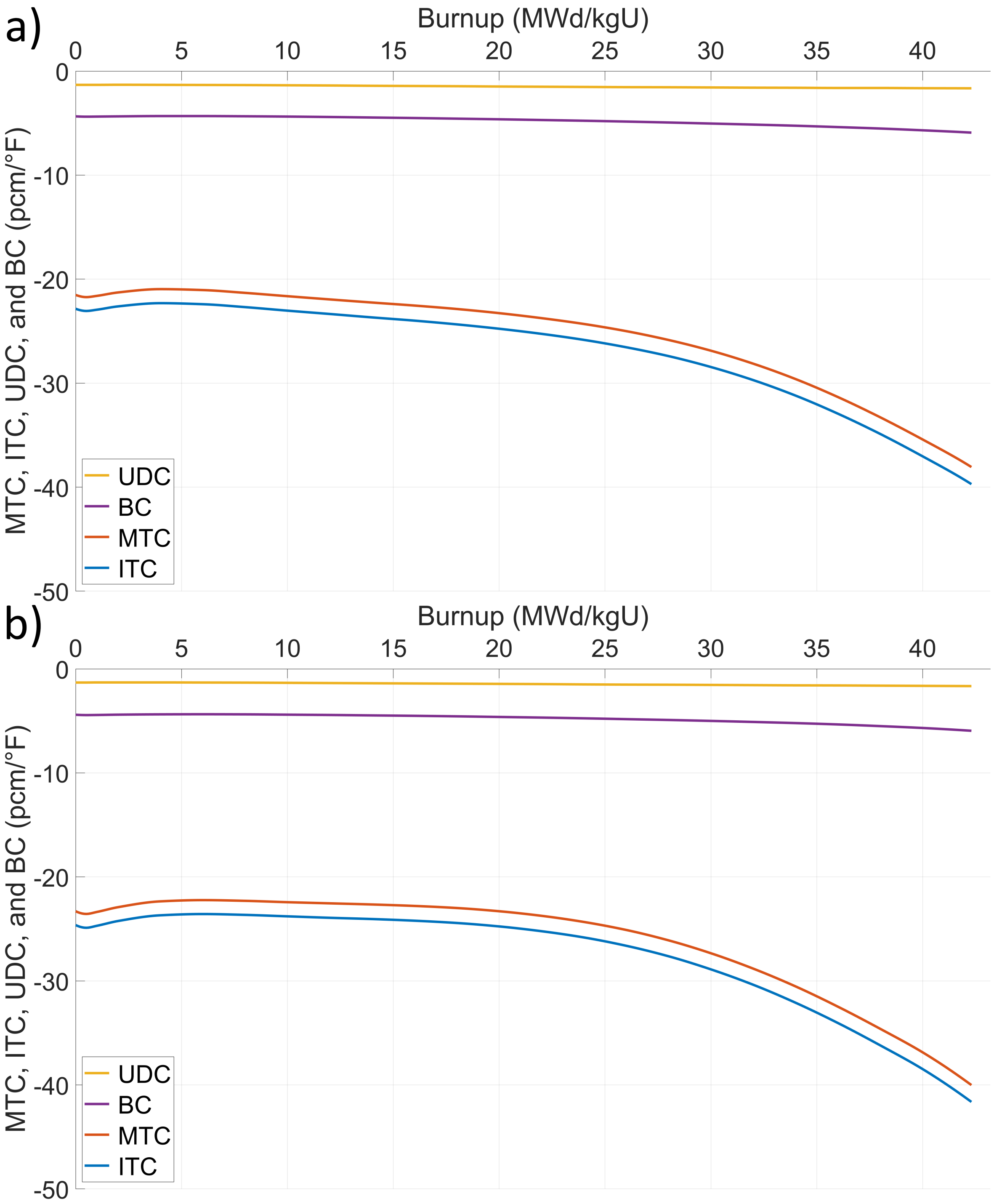

Figure 46 – Moderator temperature coefficient (MTC), isothermal temperature coefficient (ITC), uniform Doppler coefficient (UDC), and boron coefficient (BC) curves of 36-month equilibrium cycles with ZrB_2 MDBAPs (a) and UB_2 MDBAPs (b).

Specifically, the uniform Doppler coefficient, which has an initial value of -1.43 pcm/°F during the IFBA equilibrium cycle, exhibits a less negative value of -1.32 pcm/°F at the beginning of the ZrB_2 MDBAP equilibrium cycle, while the boron coefficient experiences a shift from -5.63 pcm/°F to -4.35 pcm/°F.

The rate of change in the moderator temperature coefficient and isothermal temperature coefficient appears to be comparatively high. At the beginning of the IFBA equilibrium cycle, the moderator temperature coefficient is recorded as -9.65 pcm/°F, whereas for the ZrB_2 MDBAP equilibrium cycle, it is -21.52 pcm/°F, due to reduced amount of boron in the moderator. The isothermal temperature coefficients for IFBA and ZrB_2 MDBAP equilibrium cycles were found to be -11.06 pcm/°F and -22.85 pcm/°F, respectively. Nonetheless, it is noteworthy that the moderator temperature coefficient and isothermal temperature coefficient remained within the prescribed design and operation limits for the entire cycle duration.

Upon analysing the reactivity feedback parameters of the UB_2 MDBAP equilibrium cycle, it is observed that the uniform Doppler coefficient and boron coefficient are measured as -1.31 pcm/°F and -4.41 pcm/°F, respectively. Additionally, the moderator temperature coefficient and isothermal temperature coefficient recorded for the UB_2 equilibrium cycle are -23.30 pcm/°F and -24.63 pcm/°F, respectively. The results obtained in the UB_2 MDBAP equilibrium cycle are parallel to the values obtained in the ZrB_2 MDBAP equilibrium cycle.

Overall, at the beginning of the equilibrium cycles in scenarios utilising ZrB_2 and UB_2 MDBAPs, the moderator temperature coefficient displayed more negativity compared to IFBA equilibrium cycle, as a result of reduced critical boron concentration at the beginning of the cycles.

The beginning and end of cycle shutdown margins of the equilibrium cycles of IFBA, ZrB_2 MDBAP and UB_2 MDBAP were calculated. Shutdown margins of these equilibrium cycles are shown in Table 20.

Upon examination of Table 20, it is noted that the 36-month cycle employing ZrB_2 MDBAPs demonstrates a decrease in shutdown margin value of 1,423 pcm, approximately 42%, at the beginning of the cycle compared to the 18-month cycle using IFBA. Additionally, a reduction of 156 pcm, approximately 7%, is observed at the end of the cycle. Similarly, when the

36-month cycle utilising UB_2 MDBAPs is compared with the 18-month cycle using IFBA, a reduction of 1,552 pcm, approximately 46%, is seen at the beginning of the cycle, along with a reduction of 219 pcm, approximately 10%, at the end of the cycle. Moreover, UB_2 MDBAPs show higher shutdown margin values than ZrB_2 MDBAPs, with differences of approximately 7% and 3%, respectively, at the beginning and end of the cycle. These reductions in shutdown margin within design and operation limits are attributed to the increasing quantity of fissile isotope present in the reactor core and the use of an absorber with a relatively lower initial worth positioned inside the pellet, unlike IFBA, which is unshielded and has a significantly higher worth outside the pellet.

However, to achieve the desired EFPDs design, numerous simulations were conducted with different combinations of ^{235}U enrichment levels, moderator, and BA radii, resulting in up to 1055 EFPDs. In many cases, higher shutdown margin values with UB_2 were also obtained, contrary to the values in Table 17. Therefore, it would be imprudent to determine the superiority of one absorber over the other by comparing ZrB_2 and UB_2 MDBAPs, as the shutdown margin value is significantly impacted by these parameters.

Table 20 – Shutdown margin of IFBAs, ZrB_2 MDBAPs and UB_2 MDBAPs equilibrium cycles.

Fuel Type	BOC (pcm)	EOC (pcm)
18-month cycle with IFBA	-3,368	-2,255
36-month cycle with ZrB_2 MDBAP	-1,945	-2,099
36-month cycle with UB_2 MDBAP	-1,816	-2,036

6.3.4 Relative Power Distributions and Xenon Instability

The impact of the utilisation of MDBAPs on the axial power distribution was evaluated by conducting an examination of the average axial 2D relative power fraction. Figure 47 depicts the average 2D relative power fraction curves for the IFBA, ZrB_2 MDBAP, and UB_2 MDBAP equilibrium cycles at the beginning and end of the cycles in addition to 8.00 MWd/kgU (hereafter called the middle of the cycle) .

When comparing the ZrB_2 MDBAP and UB_2 MDBAP equilibrium cycles' average axial 2D relative power fraction profiles, both at the beginning and end of the cycles, it is observed that at the beginning of the UB_2 MDBAP equilibrium cycle, the average axial 2D relative power fraction is up to 3.2% higher in the lower half of the reactor core compared to the ZrB_2 MDBAP equilibrium cycle, while being up to 2% lower in the upper half. On the other hand, at the end of the cycle, these differences are 1.7% and 1.3%, respectively. Thus, it can be said that fairly similar profiles were obtained in both equilibrium cycles.

However, when comparing the results obtained in the ZrB_2 MDBAP and UB_2 MDBAP equilibrium cycles with the IFBA equilibrium cycle, the differences in the average axial 2D relative power fraction profiles are notable. Considering the maximum and minimum average axial 2D relative power fraction values at the beginning of the cycle, a flatter profile is obtained in the ZrB_2 MDBAP and UB_2 MDBAP equilibrium cycles, while a less flat profile is obtained at the end of the cycle compared to IFBA equilibrium cycle.

Similar to the beginning and end of the cycle, the difference between the ZrB_2 MDBAP equilibrium cycle and UB_2 MDBAP equilibrium cycle in the reactor's upper half reaches up to 1.57%, while in the lower half it is no more than 0.3%, which can be considered negligible. When examining changes at the middle of the cycle, it is observed that high average axial 2D relative power fraction values are reached in the lower half of the reactor compared to the upper half in both the ZrB_2 MDBAP and UB_2 MDBAP equilibrium cycles. The primary reason for this is the choice of a 10.24 cm BA-free area in the lower part of the reactor, while a 15.24 cm BA-free area is preferred in the upper part. Consequently, the presence of more BA in the bottom of the reactor leads to a delayed increase in power, in line with the depletion of BA. The rationale behind this choice is explained in the following section.

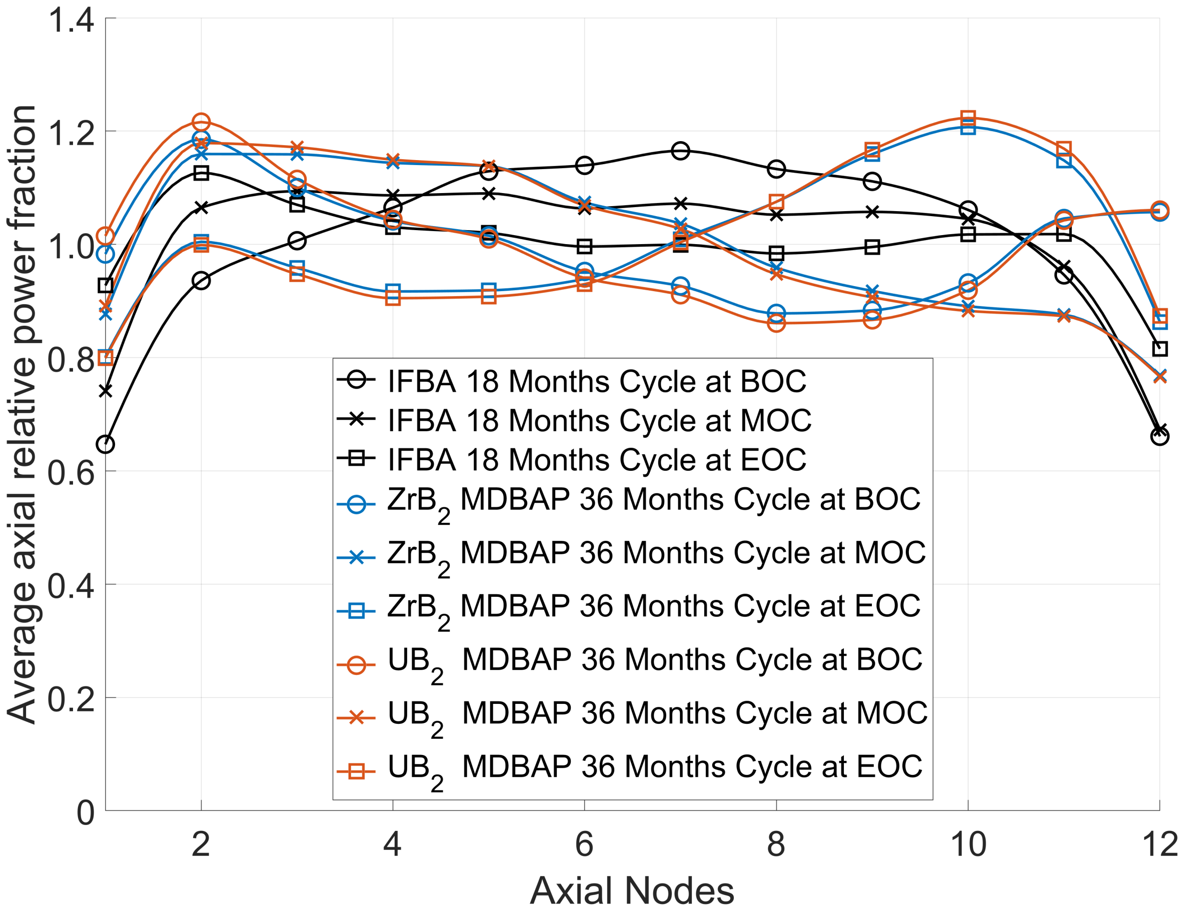

Figure 47 – The average axial relative power fraction curves of equilibrium cycles.

A comparison was made between the assembly-wise 2D relative power fractions of ZrB_2 and UB_2 MDBAPs. In Figure 48, the 2D relative power fraction comparisons are shown for the equilibrium cycles of both ZrB_2 MDBAP and UB_2 MDBAP, at the beginning and end of the cycles.

Upon examination of Figure 48a, it can be observed that the largest negative difference is found at the beginning of the cycle in a fresh fuel assembly located at H-8. At this location, a relative power fraction value is obtained which is 9.81% lower than the value obtained from ZrB_2 MDBAP in the UB_2 MDBAP equilibrium cycle. In contrast, the largest positive difference is observed in two once-burned fuel assemblies situated at C-13 and D-13, where relative power fraction values that are 6.26% higher than those obtained from the ZrB_2 MDBAP equilibrium cycle, in the UB_2 MDBAP equilibrium cycle were obtained.

Furthermore, as depicted in Figure 48b, when comparing the results at the end of the cycle, it is found that the largest negative difference is present in two fresh fuel assemblies at locations G-8 and H-9. At these locations, relative power fraction values are obtained that are 4.89% lower than the value obtained from ZrB_2 MDBAP in the UB_2 MDBAP equilibrium cycle. On the other hand, the largest positive difference is observed in once-burned fuel assemblies at locations A-08 and H-15, where relative power fraction values that are 5.14% higher than those obtained from the ZrB_2 MDBAP equilibrium cycle, in the UB_2 MDBAP equilibrium cycle were obtained.

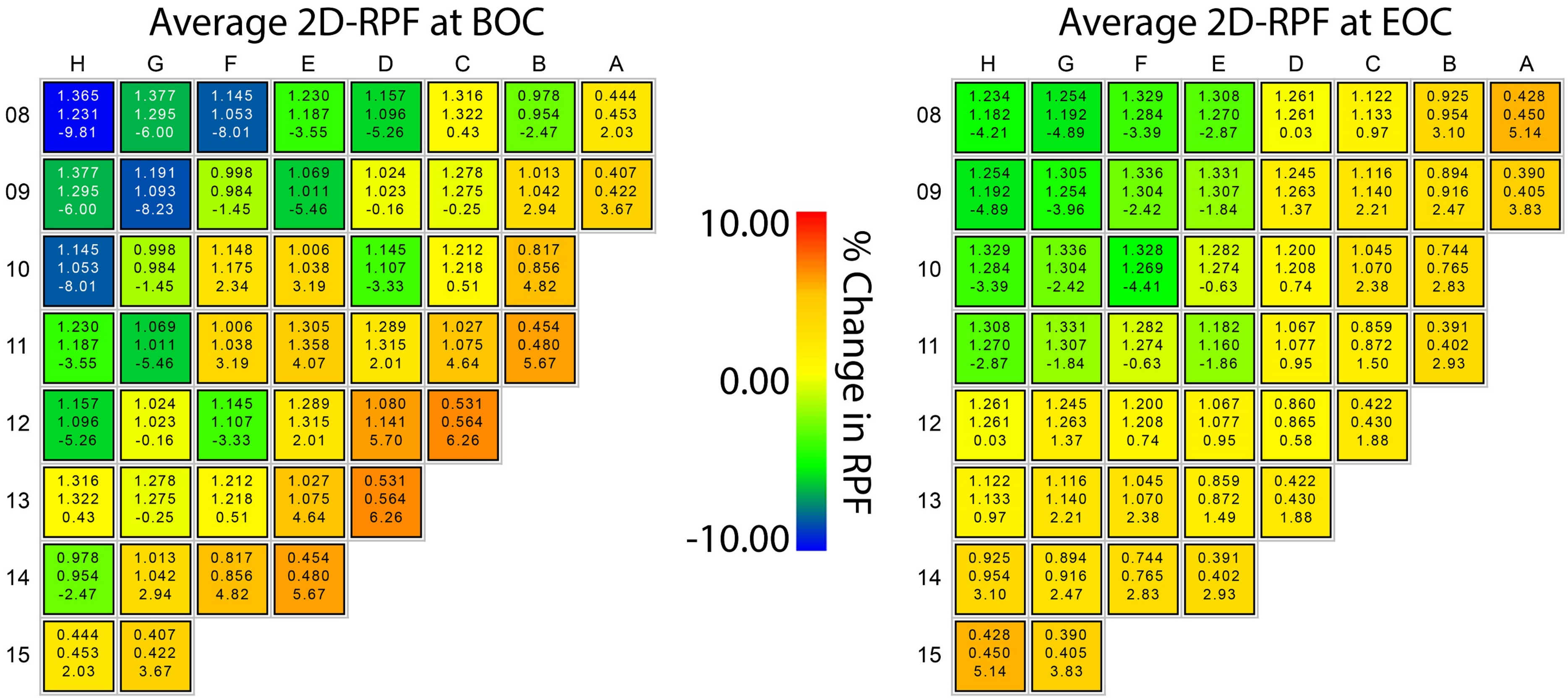

Average 2D-RPF at BOC

	H	G	F	E	D	C	B	A
08	1.365 1.231 -9.81	1.377 1.295 -6.00	1.145 1.053 -8.01	1.230 1.187 -3.55	1.157 1.096 -5.26	1.316 1.322 0.43	0.978 0.954 -2.47	0.444 0.453 2.03
09	1.377 1.295 -6.00	1.191 1.093 -8.23	0.998 0.984 -1.45	1.069 1.011 -5.46	1.024 1.023 -0.16	1.278 1.275 -0.25	1.013 1.042 2.94	0.407 0.422 3.67
10	1.145 1.053 -8.01	0.998 0.984 -1.45	1.148 1.175 2.34	1.006 1.038 3.19	1.145 1.107 -3.33	1.212 1.218 0.51	0.817 0.856 4.82	
11	1.230 1.187 -3.55	1.069 1.011 -5.46	1.006 1.038 3.19	1.305 1.358 4.07	1.289 1.315 2.01	1.027 1.075 4.64	0.454 0.480 5.67	
12	1.157 1.096 -5.26	1.024 1.023 -0.16	1.145 1.107 -3.33	1.289 1.315 2.01	1.080 1.141 5.70	0.531 0.564 6.26		
13	1.316 1.322 0.43	1.278 1.275 -0.25	1.212 1.218 0.51	1.027 1.075 4.64	0.531 0.564 6.26			
14	0.978 0.954 -2.47	1.013 1.042 2.94	0.817 0.856 4.82	0.454 0.480 5.67				
15	0.444 0.453 2.03	0.407 0.422 3.67						

Average 2D-RPF at EOC

	H	G	F	E	D	C	B	A
08	1.234 1.182 -4.21	1.254 1.192 -4.89	1.329 1.284 -3.39	1.308 1.270 -2.87	1.261 1.261 0.03	1.122 1.133 0.97	0.925 0.954 3.10	0.428 0.450 5.14
09	1.254 1.192 -4.89	1.305 1.254 -3.96	1.336 1.304 -2.42	1.331 1.307 -1.84	1.245 1.263 1.37	1.116 1.140 2.21	0.894 0.916 2.47	0.390 0.405 3.83
10	1.329 1.284 -3.39	1.336 1.304 -2.42	1.328 1.269 -4.41	1.282 1.274 -0.63	1.200 1.208 0.74	1.045 1.070 2.38	0.744 0.765 2.83	
11	1.308 1.270 -2.87	1.331 1.307 -1.84	1.282 1.274 -0.63	1.182 1.160 -1.86	1.067 1.077 0.95	0.859 0.872 1.50	0.391 0.402 2.93	
12	1.261 1.261 0.03	1.245 1.263 1.37	1.200 1.208 0.74	1.067 1.077 0.95	0.860 0.865 0.58	0.422 0.430 1.88		
13	1.122 1.133 0.97	1.116 1.140 2.21	1.045 1.070 2.38	0.859 0.872 1.49	0.422 0.430 1.88			
14	0.925 0.954 3.10	0.894 0.916 2.47	0.744 0.765 2.83	0.391 0.402 2.93				
15	0.428 0.450 5.14	0.390 0.405 3.83						

Top : ZrB_2 MDBAP equilibrium cycle's average 2D RPF
Middle : UB_2 MDBAP equilibrium cycle's average 2D RPF
Bottom: % change in average 2D-RPF

Figure 48 – Assembly-wise average 2D relative power fraction profiles for equilibrium cycles of ZrB_2 and UB_2 MDBAPs.

The impact of using MDBAPs on xenon instability was also examined. For this analysis, the power of the reactor operating at 100% was reduced to 90% for a three-hour period, then raised back to 100%. Figure 49 shows the axial offset of xenon instability curves of the IFBA, ZrB_2 and UB_2 equilibrium cycles.

Upon examining Figure 49 it is seen that, in both the ZrB_2 and UB_2 MDBAP equilibrium cycles, the axial offset (AO) of xenon is in the negative region at the beginning and middle of the cycle, stabilizing within the first 50 hours after the power returns to 100%. However, towards the end of the cycles, following the power change, the AO shifts to the positive region, and stability is only achieved about 80 hours after the power returns to 100%. In contrast, when examining the IFBA equilibrium cycle, it is observed that, as the cycle progresses, achieving axial xenon stability takes longer in the later stages, with the AO always in the positive area. In addition, it takes about 50 hours to achieve axial xenon balance after the power is raised to 100% at the beginning of the cycle, approximately 120 hours in the middle of the cycle, and stability is not reached even after 200 hours at the end of the cycle.

In the IFBA equilibrium cycle, the oscillation was monitored for up to 500 hours following the power change at the cycle's end. It was observed that the oscillation persisted even after 500 hours but its frequency significantly decreased. At this point, the difference between MDBAPs and IFBAs becomes apparent. As previously demonstrated in Section 5.4.6, ^{10}B atoms within MDBAPs can sustain their presence for burnup levels ranging from 40.00 to 50.00 MWd/kgU (depending on the MDBAP and the moderator radii). Therefore, in the ZrB_2 and UB_2 MDBAP equilibrium cycles, the existence of ^{10}B atoms in fresh fuel assemblies at the end of the cycles (43.11 MWd/kgU for the ZrB_2 equilibrium cycle and 42.29 MWd/kgU for the UB_2 equilibrium cycle) contributes to xenon stabilization during power changes at the cycle's end. Typically, in standard reactor operation, reducing the power at the end of a cycle can expected as in coastdown action. However, raising the power at the end of the cycle is not a practical scenario, and it should be remembered that the reactor is anticipated to shut down at the end of the cycle.

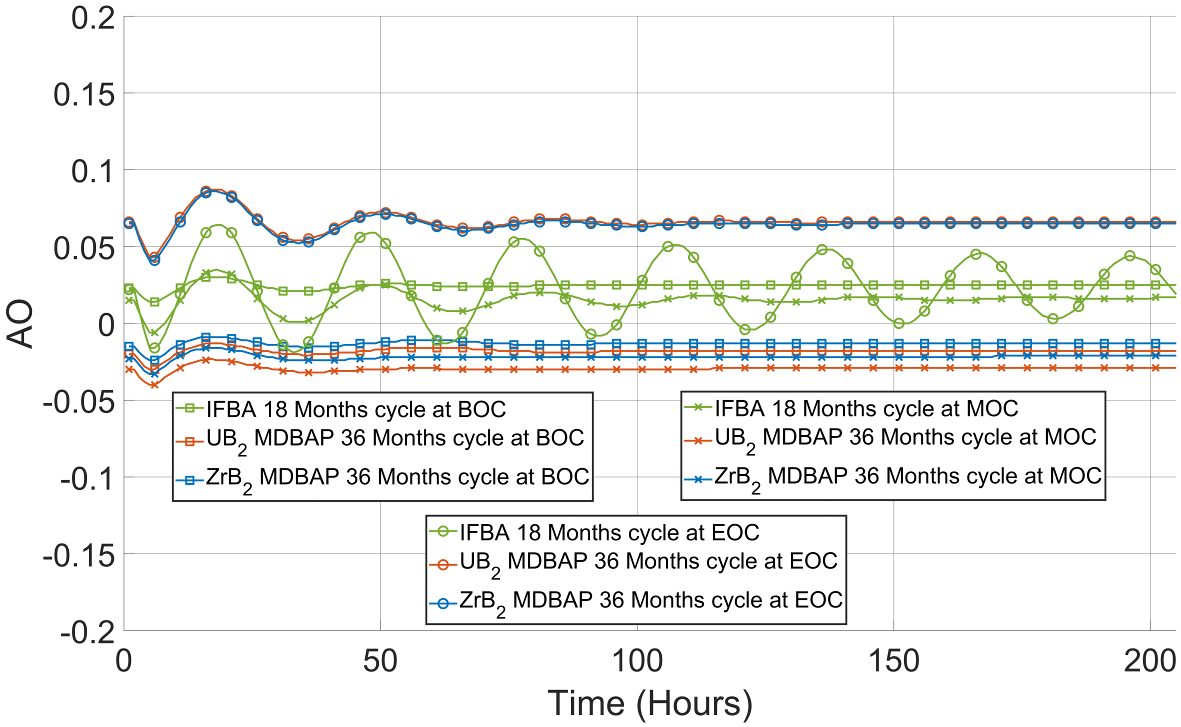

Figure 49 – Xenon instability for equilibrium cycles of IFBA, ZrB_2 and UB_2 MDBAPs.

6.3.5 Impact of BA Loading Length on Axial Relative Power Distribution

Previously, it was mentioned that for obtaining a flatter average axial 2D relative power fraction profile in 18-month IFBA usage, 15.24 cm BA-free zones were preferred at both the top and bottom of the fuel assemblies, as in Figure 50a, whereas in the DBAPs and MDBAPs usage scenarios, 15.24 cm BA-free zones were chosen at the top and 10.24 cm BA-free zones at the bottom of the fuel assemblies, as in Figure 50b.

Simulations demonstrated that the preference for 15.24 cm BA-free zones in both the top and bottom sections of the fuel assemblies resulted in the emergence of undesirable peaks in the average axial 2D relative power fraction profiles. Consequently, to obtain the most suitable profile, the BA-free zone at the bottom section of the fuel assemblies was decreased by 1 cm in each step, and it was concluded that the most suitable profile was achieved by reducing the BA-free zone at the bottom by 5 cm, which is to 10.24 cm.

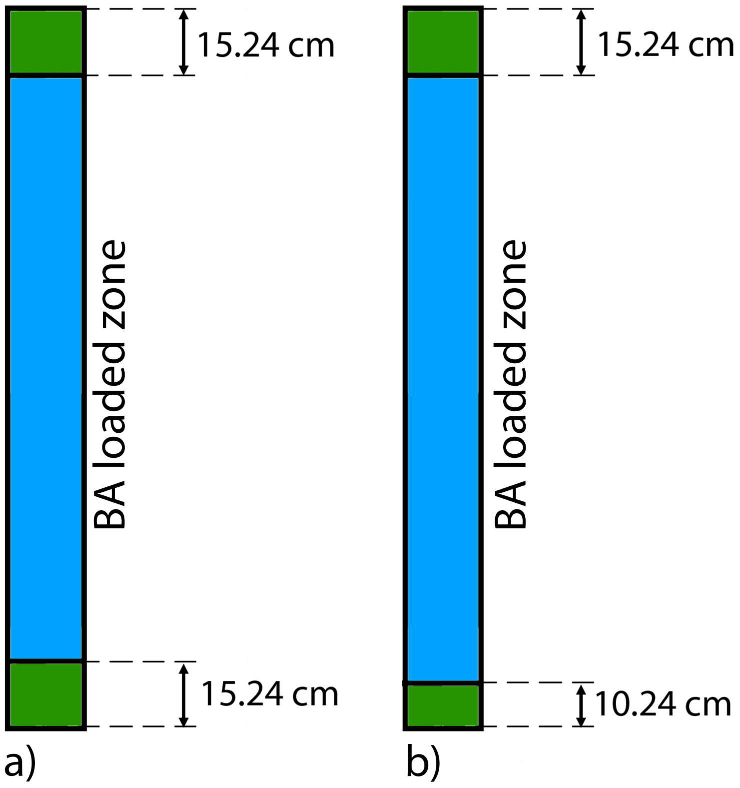

Figure 50 – Various BA loading configurations for fuel rods.

As mentioned earlier, a variety of fuel compositions reaching 1055 EFPDs were identified, but only those results pertaining to fuel compositions with the lowest critical boron concentrations within the design and operation limits were examined in this study. Nevertheless, due to the fuel compositions presented in Table 17 not meeting the design and operation limits when applied with 15.24 cm BA-free zones preferred at the bottom section of the fuel assemblies, the impact of BA loading length on axial relative power distribution will be exemplified using an alternative fuel composition in which ZrB_2 MDBAP satisfies the design and operation limits for both 15.24 cm and 10.24 cm BA-free implementations at the bottom of the fuel assemblies.

Table 21 shows necessary fuel fresh quantities, their associated ^{235}U enrichment levels, locations within the fuel core, and the dimensions of the BA and moderator radii for the ZrB_2 DBAP which can remain within the design and operation limits when both 15.24 cm BA-free and 10.24 cm BA-free areas can be applied separately at the bottom of the fuel assemblies.

Table 22 presents critical boron concentration, maximum nuclear enthalpy rise hot channel factor, maximum heat flux hot channel factor, cycle burnup, and cycle EFPDs for the equilibrium cycles of two distinct scenarios, S1 and S2. The fuel assemblies utilised in these scenarios are loaded with the ZrB_2 MDBAP fuel model shown in Table 21, leaving 10.24 cm and 15.25 cm of BA-free space at the bottom for S1 and S2, respectively, while both scenarios have 15.24 cm of BA-free space at the top of the fuel assemblies.

Table 21 – Core configuration parameters of ZrB_2 MDBAPs cases with varied BA-free areas.

Number of fresh FAs	ZrB_2 MDBAP			In-core position
	^{235}U enrichment (wt.%)	Moderator radius (mm)	BA radius (mm)	
48	6.60	0.9	1.2	C1
33	6.65	0.9	1.3	C2
24	6.70	0.6	1.1	C3
24	6.75	0.6	0.9	C4

Table 22 – The equilibrium cycle parameters for scenarios S1 and S2.

Scenario number	BA-free zone at bottom	CBC-BOC (ppm)	Maximum $F_{\Delta H}$	Maximum F_Q	Cycle Burnup (MWd/kgU)	Cycle EFPDs
S1	10.24	1,634.8	1.539	1.943	42.766	1054.9
S2	15.24	1,693.0	1.532	2.288	42.972	1060.5

As seen in Table 22, in the equilibrium cycle for scenario S2, where fuel assemblies have 15.24 cm of BA-free space at the bottom, the reduced presence of BA in the reactor results in higher burnup and, consequently, higher EFPDs, as expected. Furthermore, reducing the amount of BA results in an increase of approximately 17% in the maximum heat flux hot channel factor, while leading to a decrease of around 0.5% in the maximum nuclear enthalpy rise hot channel factor.

Figure 51 displays the average axial 2D relative power fraction curves for the equilibrium cycles of scenarios S1 and S2 at the beginning of the cycle and end of the cycle. When comparing the average axial 2D relative power fraction values at the beginning of the cycles, S1 exhibits values up to 2% lower compared to S2 at the top of the fuel assembly, while displaying values up to 11% higher at the bottom half of the fuel assembly. It can also be observed that the difference between the highest and lowest average axial 2D relative power fraction values is lower for S1, which indicates that choosing 10.24 cm of BA-free space can result in a flatter profile at the end of the cycle.

On the other hand, significant differences can be observed at the beginning of the cycle. In S1, there are up to 14% lower average axial 2D relative power fraction values in the top half of the fuel assembly compared to S2. However, the peak that occurs in the bottom half of the assembly in S2, which reaches up to 66% higher than in S1, stands out.

At the reactor's bottom, a lower temperature is usually observed as compared to the top, resulting from the coolant's entry at the bottom initially. Consequently, a higher moderator density is present there. An increased moderator density implies that a greater number of thermal neutrons are available for the fission reactions, causing an elevated neutron flux at the core's bottom. This ultimately contributes to a higher number of fissions and, therefore, a power peak in that region where HALEU is utilised with MDBAPs. Consequently, implementing 10.24 cm of BA-free space at the bottom of the fuel assemblies ensures a flatter profile.

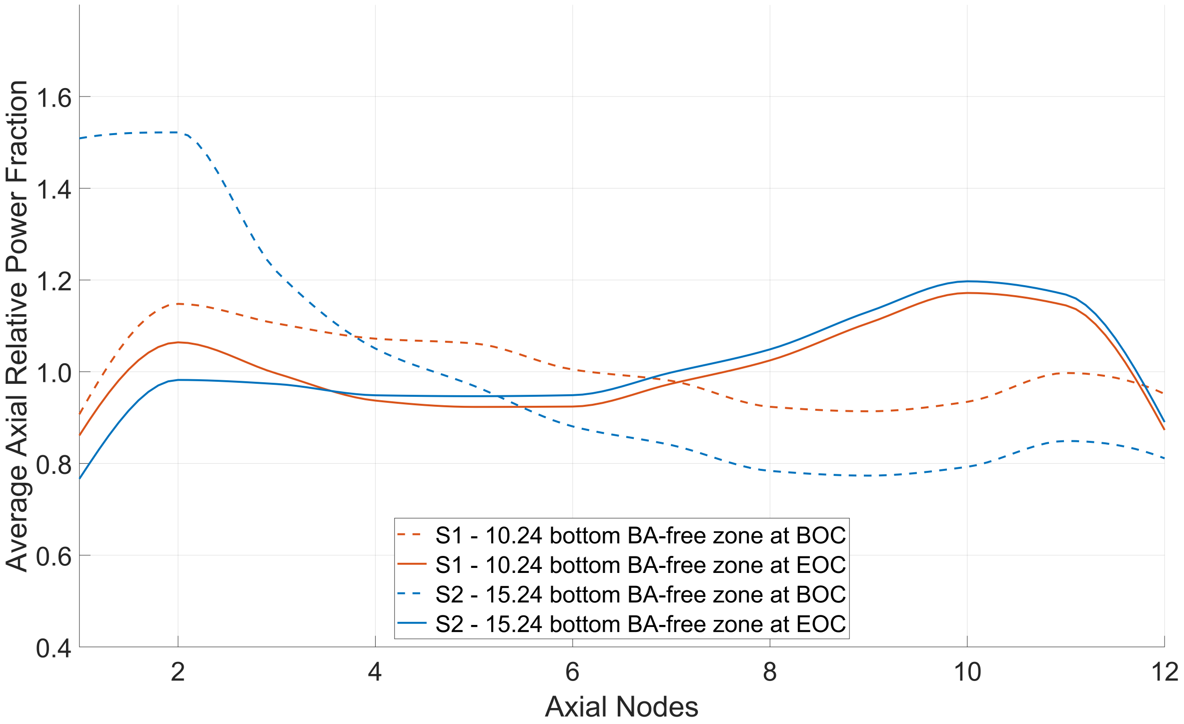

Figure 51 – The average axial relative power fraction curves for the equilibrium cycles of scenarios S1 and S2.

6.3.6 Economic Considerations of MDBAPs

An increase in the cycle length at nuclear power stations is considered to have the potential to enhance the capacity factor, owing to the reduction of refueling outages throughout the lifespan of the reactor [83]. It has been indicated that the use of MDBAPs can achieve a 36-month cycle within design and operation limits, illustrating the potential for MDBAPs to be utilised in extended cycles.

In the context of an 18-month IFBA equilibrium cycle and a 36-month MDBAP cycle equilibrium cycle with HALEU, the fuel loading costs for the equilibrium cycle with the use of ZrB_2 and UB_2 MDBAPs were calculated. However, there is insufficient information in the literature regarding the coating cost of IFBAs for use in calculations. Similarly, a level of uncertainty exists over the cost of implementing MDBAPs. Consequently, the fabrication costs of IFBAs and MDBAPs were neglected in these calculations. Also, it should be noted that variations in the implementation costs of MDBAPs and IFBAs could alter the calculated costs. Therefore, the economic viability of using MDBAPs can only be proven by considering these costs and applying sensitivity analysis.

On the other hand, in the determination of refueling outage duration, not only are used fuel assemblies replaced, but necessary maintenance operations are also considered. While transitioning from an 18-month cycle to a 36-month cycle, the increase in the number of fresh fuel assemblies and the additional processes this entails are not considered in the duration calculation, as they fall outside the scope of this study. However, in both cycle lengths, the refueling outage duration is assumed to be fixed at 40 days, as in a previous study in the literature [76]. However, the choice of a 40-day refueling outage is preferred to mitigate this uncertainty considering it is 25% more than the average refueling outage of operational NPPs in the USA in 2021, 32 days, as mentioned in Section 1.4.

As a result, by maintaining the refueling outage and moving to a 36-month cycle, it was observed that the capacity factor could increase from 92.70% to 96.35%, thus encouraging greater power production. Considering this, the $LCOE_{front-end}$ was calculated for both 18-month and 36-month cycles.

In Table 23, the front-end cost items and LCOE for IFBA, ZrB_2, and UB_2 MDBAP equilibrium cycles are provided. The total fuel loading costs of ZrB_2 and UB_2 DBAPs, as shown in the table, yielded quite similar results. With the use of MDBAP, the cost of fuel loading increases with the increase in the number of fresh fuel assemblies required for the 36-month cycle, as expected. Additionally, $LCOE_{front-end}$ of the IFBA equilibrium cycle is \$7.3/MWe while the ZrB_2 and UB_2 MDBAP equilibrium cycles' $LCOE_{front-end}$ are \$9.340/MWe and \$9.345/MWe respectively.

In nuclear power production, as previously noted in Section 1.4, the cost of fuel is relatively low compared to other items. For this reason, the economic benefit to be obtained can be discovered by revealing changes that will occur in the overall LCOE of the specific NPP. On the other hand, optimization of MDBAPs in reactor operation might result in a decrease in $LCOE_{front-end}$ by reaching the 36-month cycle with lower enrichment levels and/or reduced number of fresh fuels assemblies.

Due to the novelty of the design and its first-time evaluation in the literature, detailed elaboration on the important points for future studies will be provided in Section 7.2.

Table 23 – Component costs for the IFBA, ZrB_2 and UB_2 equilibrium cycles.

	IFBA equilibrium cycle			ZrB_2 MDBAP equilibrium cycle			UB_2 MDBAP equilibrium cycle		
	Low	Nominal	High	Low	Nominal	High	Low	Nominal	High
Cost of uranium ($M)	12.135	30.661	105.6	32.753	82.757	285.025	32.757	82.768	285.061
Cost of conversion ($M)	2.344	4.688	6.852	6.327	12.654	18.494	6.328	12.656	18.497
Cost of enrichment ($M)	26.717	35.255	42.416	78.794	103.976	125.096	78.545	103.647	124.701
Cost of fabrication ($M)	8.739	15.197	21.846	16.434	28.58	41.084	16.696	29.037	41.74
Cost of total fuel loading ($M)	49.935	85.801	176.714	134.308	227.967	469.699	134.326	228.108	469.999
LCOE ($)	4.249	7.3	15.036	5.503	9.340	19.243	5.503	9.345	19.256

6.4 Chapter Summary

In this chapter, potential transition from an 18-month to a 36-month fuel cycle was investigated. Various peaking factors and reactivity feedback parameters were evaluated. Additionally, average axial and 2D assembly-wise relative power distributions were examined and compared as well as the shutdown margin.

The results showed that a relatively high ^{10}B loading into the reactor with DBAPs prevents the reactor from reaching the targeted 1055 EFPDs. The implementation of BeO moderator in DBAPs hardens the neutron spectrum and increases the production of fissile ^{239}Pu [110], [123] which results in a reduction in the consumption of ^{235}U atoms, and thus higher burnup and EFPDs are achieved.

The presence of ^{235}U in UB_2 MDBAPs allows a greater quantity of fissile isotopes to be accommodated in the reactor core, requiring lower enrichment of ^{235}U to achieve the same EFPDs as compared to ZrB_2 MDBAPs. Additionally, the use of MDBAPs contributes to reducing the critical boron concentration required in the reactor, highlighting its potential to be employed in soluble-boron-free reactor designs.

Furthermore, the use of MDBAPs causes no significant negative effects on parameters such as the maximum nuclear enthalpy rise hot channel factor and the heat flux hot channel factor while causing no negative effects on parameters including moderator temperature coefficient, isothermal temperature coefficient, uniform Doppler coefficient, and boron coefficient, ensuring safe and realistic operation.

Despite observing differences in the average axial and 2D assembly-wise relative power distributions resulting from the use of ZrB_2 MDBAPs and UB_2 MDBAPs, compared to IFBAs, both types of MDBAPs exhibited very similar values to each other. Additionally, although the shutdown margin in cases where MDBAPs are used is reduced due to increased ^{235}U enrichment, the values obtained remain within the design and safety limits.

lastly, extending the cycle length from 18-month to 36-month by keeping the refueling outage constant, the capacity factor is increased to 96.35% from 92.70%.

Chapter 7

Summary, Conclusions and Suggestions for Future Work

7.1 Summary and Conclusions

7.1.1 Enriched Gadolinium Oxide

The potential implications of e-Gd_2O_3 in fuel compositions were assessed in this study using 2D neutronic analysis conducted with the Monte Carlo particle transport method. A comparison has been made between the reactivity properties of n-Gd_2O_3 and e-Gd_2O_3. Subsequently, the depletion behaviour of the main neutron absorbing isotopes and the breeding behaviour of ^{239}Pu in the case of e-Gd_2O_3 were examined and compared to n-Gd_2O_3.

Following this, fuel cycle analyses of transition to e-Gd_2O_3 were conducted. After determining the fuel compositions to achieve 508 EFPDs with the use of n-Gd_2O_3 in the 18-month cycle, the impact of transitioning from n-Gd_2O_3 to e-Gd_2O_3 on peaking factors such as the nuclear enthalpy rise hot channel factor and the heat flux hot channel factor as well as critical boron concentration was investigated.

Reactivity feedback parameters, including the moderator temperature coefficient, the isothermal temperature coefficient, the uniform Doppler coefficient, and the boron coefficient, were examined for both e-Gd_2O_3 and n-Gd_2O_3. Furthermore, a comparison was made between the average axial relative power distribution and the assembly-wise 2D relative power fraction for e-Gd_2O_3 and n-Gd_2O_3.

Finally, changes in fuel loading cost and the LCOE resulting from the transition from n-Gd_2O_3 to e-Gd_2O_3 in the fuel cycle were analysed.

The results of 2D neutronic analyses indicated that the time required to reach peak reactivity is delayed by increasing the concentration of n-Gd_2O_3 in the fuel composition due to the longer consumption of Gd isotopes. However, an increase in the amount of n-Gd_2O_3 in the fuel composition also results in a rise in the primary non-neutron absorbing isotopes of Gd in the system, leading to a penalty in residual reactivity.

On the other hand, incorporating e-Gd_2O_3 in the fuel composition can yield similar reactivity behaviour to n-Gd_2O_3 while utilising a smaller volume of BA. This is achieved by implementing a lower proportion of BA in the fuel composition, thus displacing a lower proportion of UO_2 from the fuel and consequently providing higher reactivity. Furthermore, the use of e-Gd_2O_3 reduces the amount of Gd isotopes causing residual reactivity in the fuel matrix, resulting in a cleaner burn of the BA due to lack of Gd isotopes causing residual reactivity penalty.

By correlating the peak point reactivity, it was observed that the use of e-Gd_2O_3 allows for higher reactivity compared to n-Gd_2O_3. The amount of gained reactivity significantly increases with the rise in the n-Gd_2O_3/e-Gd_2O_3 ratio. Similarly, when correlating the equal peak point reactivity, e-Gd_2O_3 can provide a higher total gained reactivity than n-Gd_2O_3 if a high BA addition is present in the fuel composition.

The breeding rate of ^{239}Pu reaches its highest concentration when BA isotopes are depleted, and e-Gd_2O_3 produces a slightly larger amount of ^{239}Pu compared to n-Gd_2O_3. Consequently, the use of e-Gd_2O_3 results in an increase in reactivity in the late life of the fuel.

The benefits of e-Gd_2O_3 in fuel cycle analyses were confirmed as anticipated due to the lower BA requirement in the fuel composition, leading to an increased amount of uranium fuel loading. The ^{235}U enrichment level needed to reach a cycle length of 508 EFPDs using n-Gd_2O_3 allows a cycle length of 527 EFDPs to be reached when e-Gd_2O_3 is utilised as BA. Furthermore, the use of e-Gd_2O_3 enabled the attainment of a cycle length of 508 EFPDs with a lower enrichment level.

As a BA, e-Gd_2O_3 has no adverse effects on peak factor parameters such as heat flux hot channel factor and nuclear enthalpy rise hot channel factor. Similarly, e-Gd_2O_3 does not cause any negative effects on reactivity feedback parameters such as moderator temperature coefficient, isothermal temperature coefficient, uniform Doppler coefficient, and boron coefficient, ensuring safe and reliable operation. The use of e-Gd_2O_3 does not result in a detectable negative effect on the shutdown margin either. Additionally, the utilisation e-Gd_2O_3 does not significantly impact the assembly-wise average 2D relative power fraction and average axial relative power distribution.

Preferring e-Gd_2O_3 as BA provides significant economic advantages compared to n-Gd_2O_3, despite the cost of enriching ^{157}Gd. Depending on future prices, potential savings range from \$1.06 million to \$3.98 million, demonstrating the economic benefits of choosing e-Gd_2O_3 in the equilibrium cycle.

7.1.2 HALEU with DBAPs and MDBAPs

A comprehensive investigation was conducted to explore promising designs for new BA designs. Two designs, utilising zirconium diboride or uranium diboride as the BA, DBAPs and MDBAPs, which features a BeO moderator at the centre of the DBAP, were investigated. These designs offer significant advantages for fuel cycles longer than 24-month. Extensive neutronic analyses were performed on the DBAPs and MDBAPs, focusing on reactivity behaviour, ^{239}Pu breeding, and ^{10}B depletion.

Subsequently, an investigation was carried out to test the viability of ZrB_2 and UB_2 DBAPs transitioning from a fuel cycle utilising IFBA with a duration of 18-month and 508 EFPDs to a 36-month cycle employing HALEU fuel. Additionally, various peaking factors, such as the nuclear enthalpy rise hot channel factor and heat flux hot channel factor, were examined, along with changes in critical boron concentration.

Furthermore, the investigation included an examination of reactivity feedback parameters, such as the moderator temperature coefficient, isothermal temperature coefficient, uniform Doppler coefficient, and boron coefficient. Additionally, average axial 2D relative power distribution and assembly-wise 2D relative power distribution were analysed. Finally, the potential economic benefits were discussed.

The 2D neutronic analyses demonstrated that the utilisation of ZrB_2 and UB_2 DBAPs leads to the suppression of initial reactivity. Greater suppression is observed as the number of fuel rods containing DBAP or the DBAP radius increases. At the beginning of the fuel's life, UB_2

DBAPs exhibit less reactivity suppression than ZrB_2 DBAPs due to the presence of fissile uranium. However, both designs yield similar reactivity values at the end of the fuel's life.

Increasing the distribution of ZrB_2 and UB_2 DBAPs in the fuel assembly results in greater and flatter suppression of reactivity at the beginning of the fuel's life, while not affecting reactivity at the end. The depletion rate of ^{10}B atoms is faster on the surface than at the centre for both types of BA. Furthermore, the depletion of ^{10}B atoms in the fuel assembly leads to a hardened neutron spectrum, causing a delay in the depletion rate of ^{235}U atoms and an increase in the breeding rate of ^{239}Pu.

On the other hand, the MDBAP design also suppresses reactivity at the beginning of the cycle and provides higher reactivity at the end of the cycle. The utilisation of graphite or BeO as moderators did not result in any significant differences in reactivity.

Fuel cycle analyses revealed that the introduction of a relatively high amount of ^{10}B into the reactor through DBAPs prevents the reactor from achieving the targeted 1055 EFPD. However, implementing a BeO moderator in DBAPs leads to a hardened neutron spectrum, consequently higher burnup and EFPDs due to increased ^{239}Pu density in the fuel composition.

The presence of ^{235}U in UB_2 MDBAPs allows a greater quantity of fissile isotopes to be accommodated in the reactor core, necessitating lower enrichment of ^{235}U to achieve the same EFPDs compared to ZrB_2 MDBAPs. Furthermore, the use of MDBAPs contributes to reducing the critical boron concentration required in the reactor, highlighting its potential in soluble-boron-free reactor designs.

Moreover, the use of MDBAPs does not have any significant negative effects on parameters such as the maximum nuclear enthalpy rise hot channel factor and the heat flux hot channel factor. It also does not negatively impact parameters like the moderator temperature coefficient, isothermal temperature coefficient, uniform Doppler coefficient, and boron coefficient, ensuring safe and realistic operation.

Despite observing differences in the average axial and 2D assembly-wise relative power distributions resulting from the use of ZrB_2 and UB_2 MDBAPs, both types of MDBAPs exhibit very similar profiles compared to IFBAs. Additionally, although the shutdown margin is reduced when MDBAP is used due to increased ^{235}U enrichment, the obtained values remain within the design and safety limits.

Finally, extending the cycle length from 18-month to 36-month while keeping the refueling outage constant increases the capacity factor from 92.70% to 96.35%.

7.2 Suggestions for Future Work

Considering the potential of e-Gd_2O_3, the target EFPDs can be achieved in an 18-month period with lower ^{235}U enrichment by different reactor core designs. Therefore, higher economic benefits can be obtained by optimizing the reactor core based on this observation.

Further research is needed to examine the impact of e-Gd_2O_3 on the thermal profile, taking into account the aforementioned potential positive effects on reduced BA ratio and improved thermal conductivity, as well as any unforeseen negative effects. Additionally, e-Gd_2O_3 could serve as a significant candidate for reactivity control within 24 and 36-month cycles. Therefore, an investigation into the in-core performance and economic benefits of e-Gd_2O_3 for cycles longer than 18-month is necessary.

As mentioned earlier, the MDBAP design is relatively new, lacking sufficient studies in the literature. It is essential to address this gap by conducting extensive research to explore its potential as a burnable absorber for HALEU fuel, as well as to examine all possible negative and positive effects associated with its implementation.

Based on these considerations, it is crucial to determine the production costs of fuel pellets containing MDBAP and compare them with IFBA. Moreover, the impact of the design on the levelized electricity cost during the front-end of the cycle needs to be investigated. Another important aspect is to analyse the differences that may arise in the back-end of the cycle when transitioning from an 18-month to a 36-month cycle, which will provide valuable insights into the economic benefits of the MDBAP design.

To ensure the effective use of MDBAPs, the material interactions between MDBAPs and annular UO_2 pellets, as well as the possible swelling that ^4He can cause, need to be evaluated to determine if a barrier is required. Additionally, the thermal properties of the design should be investigated using the finite element method. Understanding the behaviour of MDBAP during accidents or anticipated operational events requires considering factors such as the melting point, thermal expansion, and changes in the specific heat capacity of the fuel.

Furthermore, a research study should be conducted to explore the possibility of positioning burnable absorbers at different lengths on the fuel rods to achieve a flatter axial 2D relative power fraction profile, which aligns well with the design's capabilities.

Incorporating IFBA on some of the outer pellets in a hybrid IFBA/MDBAP design can effectively enhance the shutdown margin. This approach has the potential to improve the overall performance of shutdown margin. Testing different sizes of MDBAPs with the objective of achieving a lower critical boron concentration is also important while ensuring that the shutdown margin remains within safety limits. In such cases, optimization of control rods will be necessary.

The thermal neutron flux distribution within a pellet should be study to compare UB_2 and ZrB_2 DBAPs since the presence of fissile material in UB_2.

Maximizing the economic benefit of the MDBAP design can be achieved by reducing the number of fresh fuel pellets loaded into the reactor in each cycle. Therefore, optimizing the reactor core arrangement can help in reducing the number of fresh fuel pellets required.

To evaluate the advantages of ZrB_2 and UB_2 MDBAPs over each other, it is recommended to test an equal amount of fissile material loading in each cycle, within operational and design limits.

The impact of the transition to a 36-month fuel cycle on the duration of the refueling outage should be investigated. This will facilitate a comprehensive understanding of how the use of MDBAPs affects the capacity factor.

Lastly, burnup uncertainty is not just a consequence of input parameters, such as the enrichment level of ^{235}U and fuel density, but is also influenced by the presence of generated fission products. The CASMO-4 nuclear data library includes combined total scattering and capture reactions, rather than having individual capture and scattering reactions discretely, as mentioned in Section 2.1.2, which also requires adjustments to the cross-sections in the nuclear data to accurately assess sensitivity. This approach enables the use of uncertainties in modified cross-section data to determine uncertainties in calculations [124]. However the CASMO-4 nuclear data library used within this project is not user-modifiable, which limited the ability to perform sensitivity analyses. For this reason, it is essential to conduct sensitivity analyses for the usage scenarios of ZrB_2 and UB_2 MDBAPs which may reveal their potential economic advantages in a 36-month fuel cycle. Similarly, conducting sensitivity analyses to thoroughly assess the economic advantages of e-Gd_2O_3 is necessary, ensuring a comprehensive understanding of its financial benefits.

Bibliography

[1] IAEA, ‘Nuclear Energy for a Net Zero World,’ 2021 (p. 1).

[2] L. Carlson, Z. Wu, J. Olson and L. Liu, ‘An Economic Cost Assessment on HALEU Fuels for Small Modular Reactors,’ *Science and Technology of Nuclear Installations*, vol. 2020, 2020, ISSN: 16876083. DOI: `10.1155/2020/8815715` (p. 1, 26).

[3] M. Durazzo, A. C. Freitas, A. E. Sansone *et al.*, ‘Sintering behavior of UO_2–Er_2O_3 mixed fuel,’ *Journal of Nuclear Materials*, vol. 510, pp. 603–612, 2018, ISSN: 00223115. DOI: `10.1016/j.jnucmat.2018.08.051`. [Online]. Available: `https://doi.org/10.1016/j.jnucmat.2018.08.051` (p. 1).

[4] M. S. Dias, J. R. de Mattos and E. P. de Andrade, ‘Very high burnup fuel for Angra 2 NPP within the 5 w/o limit of the ^{235}U-enrichment,’ *Nuclear Engineering and Design*, vol. 346, no. February, pp. 17–23, 2019, ISSN: 00295493. DOI: `10.1016/j.nucengdes.2019.02.023`. [Online]. Available: `https://doi.org/10.1016/j.nucengdes.2019.02.023` (p. 1).

[5] R. B. Rebak, ‘Chapter 2 - Current materials in light water reactors. Why do we need a materials renewal?’ In *Accident Tolerant Materials for Light Water Reactor Fuels*, R. B. Rebak, Ed., Elsevier, 2020, pp. 15–41, ISBN: 978-0-12-817503-3. DOI: `https://doi.org/10.1016/B978-0-12-817503-3.00002-X`. [Online]. Available: `https://www.sciencedirect.com/science/article/pii/B978012817503300002X` (p. 2).

[6] W. Martin, *Nuclear Power*, 2023. [Online]. Available: `https://www.britannica.com/technology/nuclear-power` (visited on 14th May 2023) (p. 2).

[7] IAEA, *In Operation and Suspended Operation Reactors*, 2023. [Online]. Available: `pris.iaea.org/PRIS/WorldStatistics/OperationalReactorsByType.aspx` (visited on 14th May 2023) (p. 2, 3, 6).

[8] NEA, ‘Small Modular Reactors: Challenges and Opportunities,’ 2021. DOI: `10.4324/9781003400196-4` (p. 2, 8).

[9] M. D. Carelli and D. T. Ingersoll, *Handbook of Small Modular Nuclear Reactors*. Woodhead Publishing, 2014, pp. 1–516, ISBN: 9780857098535. DOI: `10.1016/C2013-0-16379-9` (p. 2).

[10] P. Breeze, 'Chapter 4 - Water-Cooled Reactors,' in *Nuclear Power*, P. Breeze, Ed., Academic Press, 2017, pp. 33–44, ISBN: 978-0-08-101043-3. DOI: `https://doi.org/10.1016/B978-0-08-101043-3.00004-3`. [Online]. Available: `https://www.sciencedirect.com/science/article/pii/B9780081010433000043` (p. 4).

[11] D. K. Vogt, 'Nuclear Fission Reactors: Boiling Water and Pressurized Water Reactors,' in *Encyclopedia of Energy*, C. J. Cleveland, Ed., New York: Elsevier, 2004, pp. 333–340, ISBN: 978-0-12-176480-7. DOI: `https://doi.org/10.1016/B0-12-176480-X/00302-8`. [Online]. Available: `https://www.sciencedirect.com/science/article/pii/B012176480X003028` (p. 4).

[12] G. J. Suppes and T. S. Storvick, 'Chapter 8 - The Future in Nuclear Power,' in *Sustainable Power Technologies and Infrastructure*, G. J. Suppes and T. S. Storvick, Eds., Boston: Academic Press, 2016, pp. 247–343, ISBN: 978-0-12-803909-0. DOI: `https://doi.org/10.1016/B978-0-12-803909-0.00008-7`. [Online]. Available: `https://www.sciencedirect.com/science/article/pii/B9780128039090000087` (p. 4).

[13] J. Knott, '11 - design and material issues in improving fracture/fatigue resistance and structural integrity in power plants,' in *Structural Alloys for Power Plants*, ser. Woodhead Publishing Series in Energy, A. Shirzadi and S. Jackson, Eds., Woodhead Publishing, 2014, pp. 319–354, ISBN: 978-0-85709-238-0. DOI: `https://doi.org/10.1533/9780857097552.2.319`. [Online]. Available: `https://www.sciencedirect.com/science/article/pii/B9780857092380500115` (p. 4).

[14] Energy Encyclopedia, *Pressurized Water Reactor (PWR)*, 2023. [Online]. Available: `https://www.energyencyclopedia.com/en/nuclear-energy/the-nuclear-reactors/pressurized-water-reactor-pwr` (visited on 11th May 2023) (p. 5, 7).

[15] A. Prieto-Guerrero and G. Espinosa-Paredes, 'Description of boiling water reactors,' in *Linear and Non-Linear Stability Analysis in Boiling Water Reactors*, ser. Woodhead Publishing Series in Energy, A. Prieto-Guerrero and G. Espinosa-Paredes, Eds.,

Woodhead Publishing, 2019, pp. 25–55, ISBN: 978-0-08-102445-4. DOI: https://doi.org/10.1016/B978-0-08-102445-4.00002-3. [Online]. Available: https://www.sciencedirect.com/science/article/pii/B9780081024454000023 (p. 6).

[16] P. Breeze, 'Chapter 17 - Nuclear Power,' in *Power Generation Technologies (Third Edition)*, P. Breeze, Ed., Third Edit, Newnes, 2019, pp. 399–429, ISBN: 978-0-08-102631-1. DOI: https://doi.org/10.1016/B978-0-08-102631-1.00017-1. [Online]. Available: https://www.sciencedirect.com/science/article/pii/B9780081026311000171 (p. 6, 8).

[17] US-NRC, 'Reactor Concepts Manual: Pressurized Water Reactor (PWR) Systems,' vol. 603, p. 28, 2007. [Online]. Available: https://www.nrc.gov/reading-rm/basic-ref/students/for-educators/04.pdf (p. 6).

[18] UK-NNL, 'Boiling Water Reactor Technology - International Status and UK Experience Position Paper,' 2012 (p. 6).

[19] T. W. Kerlin and B. R. Upadhyaya, 'Chapter 13 - Boiling water reactors,' in *Dynamics and Control of Nuclear Reactors*, T. W. Kerlin and B. R. Upadhyaya, Eds., Academic Press, 2019, pp. 167–189, ISBN: 978-0-12-815261-4. DOI: https://doi.org/10.1016/B978-0-12-815261-4.00013-5. [Online]. Available: https://www.sciencedirect.com/science/article/pii/B9780128152614000135 (p. 6).

[20] R. Winterton, 'CHAPTER 2 - Reactor Systems,' in *Thermal Design of Nuclear Reactors*, 1981. DOI: https://doi.org/10.1016/B978-0-08-024215-6.50006-1 (p. 8).

[21] World Nuclear Association, *Small Nuclear Power Reactors*, 2023. [Online]. Available: https://www.world-nuclear.org/information-library/nuclear-fuel-cycle/nuclear-power-reactors/small-nuclear-power-reactors.aspx (visited on 15th May 2023) (p. 8).

[22] F. Aydogan, 'Chapter 20 - Systems of Advanced Small Modular Reactors (ASMRs),' in *Handbook of Generation IV Nuclear Reactors (Second Edition)*, ser. Woodhead Publishing Series in Energy, I. L. Pioro, Ed., Second Ed, Woodhead Publishing, 2023, pp. 681–711, ISBN: 978-0-12-820588-4. DOI: https://doi.org/10.1016/B978-0-12-820588-4.00026-8. [Online]. Available: https://www.sciencedirect.com/science/article/pii/B9780128205884000268 (p. 8).

[23] J. Liou, *What are Small Modular Reactors?* 2021. [Online]. Available: `https://www.iaea.org/newscenter/news/what-are-small-modular-reactors-smrs` (visited on 15th May 2023) (p. 8).

[24] M. E. Ricotti and R. V. Fomin, '5 - Small modular reactors,' in *Nuclear Reactor Technology Development and Utilization*, ser. Woodhead Publishing Series in Energy, S. U.-D. Khan and A. Nakhabov, Eds., Woodhead Publishing, 2020, pp. 187–211, ISBN: 978-0-12-818483-7. DOI: `https://doi.org/10.1016/B978-0-12-818483-7.00005-6`. [Online]. Available: `https://www.sciencedirect.com/science/article/pii/B9780128184837000056` (p. 8).

[25] L. Rodríguez-Penalonga and B. Yolanda Moratilla Soria, 'A review of the nuclear fuel cycle strategies and the spent nuclear fuel management technologies,' *Energies*, vol. 10, no. 8, 2017, ISSN: 19961073. DOI: `10.3390/en10081235` (p. 8, 13–15).

[26] US-NRC, 'Overview of the Nuclear Fuel Cycle,' Tech. Rep., 2012. [Online]. Available: `https://www.nrc.gov/docs/ML1204/ML12045A003.pdf` (p. 9, 11–14).

[27] Massachusetts Institute of Technology, 'The Future of the Nuclear Fuel Cycle: An Interdisciplinary MIT Study,' MIT, Tech. Rep., 2011. [Online]. Available: `http://large.stanford.edu/courses/2017/ph241/steffens1/docs/mit-apr11.pdf` (p. 9, 207).

[28] B. M. T. C. Peluzo and E. Kraka, 'Uranium: The Nuclear Fuel Cycle and Beyond,' *International Journal of Molecular Sciences*, vol. 23, no. 9, 2022, ISSN: 14220067. DOI: `10.3390/ijms23094655` (p. 10).

[29] CRS, 'The front end of the nuclear fuel cycle: Current issues,' *Key Congressional Reports for July 2019: Part IV*, pp. 35–76, 2019 (p. 11, 12).

[30] World Nuclear Association, *Nuclear Fuel Cycle Overview*, 2021. [Online]. Available: `https://world-nuclear.org/information-library/nuclear-fuel-cycle/introduction/nuclear-fuel-cycle-overview.aspx` (p. 11–15).

[31] US EIA, *Nuclear explained: The nuclear fuel cycle*, 2022. [Online]. Available: `https://www.eia.gov/energyexplained/nuclear/the-nuclear-fuel-cycle.php` (visited on 15th May 2023) (p. 11–13).

[32] IAEA, 'Getting to the Core of the Nuclear Fuel Cycle,' 2014 (p. 11–14).

[33] N. Power, *Interim Storage of Spent Nuclear Fuel*, 2023. [Online]. Available: `https://www.nuclear-power.com/nuclear-power-plant/nuclear-fuel/spent-`

fuel/interim-storage-of-spent-nuclear-fuel/ (visited on 15th May 2023) (p. 14).

[34] P. Högselius, ‘Spent nuclear fuel policies in historical perspective: An international comparison,’ *Energy Policy*, vol. 37, no. 1, pp. 254–263, 2009, ISSN: 03014215. DOI: 10.1016/j.enpol.2008.09.043 (p. 14, 15).

[35] J. A. Evans, M. D. DeHart, K. D. Weaver and D. D. Keiser, ‘Burnable absorbers in nuclear reactors – A review,’ *Nuclear Engineering and Design*, vol. 391, p. 111 726, 2022, ISSN: 0029-5493. DOI: 10.1016/J.NUCENGDES.2022.111726 (p. 15, 16).

[36] E. H. Uguru, S. F. Sani, M. U. Khandaker, M. H. Rabir and J. A. Karim, ‘A comparative study on the impact of Gd_2O_3 burnable neutron absorber in UO_2 and (U, Th)O_2 fuels,’ *Nuclear Engineering and Technology*, vol. 52, no. 6, pp. 1099–1109, 2020, ISSN: 2234358X. DOI: 10.1016/j.net.2019.11.010. [Online]. Available: https://doi.org/10.1016/j.net.2019.11.010 (p. 15, 16, 39).

[37] A. Galahom, ‘Simulate the effect of integral burnable absorber on the neutronic characteristics of a PWR assembly,’ *Nuclear Energy and Technology*, vol. 4, no. 4, pp. 287–293, 2018, ISSN: 2452-3038. DOI: 10.3897/nucet.4.30379 (p. 15).

[38] M. I. Santala, A. S. Daavittila, H. M. Lauranto and R. R. Salomaa, ‘Odd-isotope enrichment studies of Gd by double resonance laser-ionization for the production of burnable nuclear reactor poison,’ *Applied Physics B: Lasers and Optics*, vol. 64, no. 3, pp. 339–347, 1997, ISSN: 09462171. DOI: 10.1007/s003400050182 (p. 15, 17).

[39] E. K. Papynov, O. O. Shichalin, A. A. Belov *et al.*, ‘Spark plasma sintering of UO_2 fuel composite with Gd_2O_3 integral fuel burnable absorber,’ *Nuclear Engineering and Technology*, vol. 52, no. 8, pp. 1756–1763, 2020, ISSN: 2234358X. DOI: 10.1016/j.net.2020.01.032. [Online]. Available: https://doi.org/10.1016/j.net.2020.01.032 (p. 15, 16).

[40] A. Galahom, ‘Investigation of different burnable absorbers effects on the neutronic characteristics of PWR assembly,’ *Annals of Nuclear Energy*, vol. 94, pp. 22–31, 2016, ISSN: 18732100. DOI: 10.1016/j.anucene.2016.02.025. [Online]. Available: http://dx.doi.org/10.1016/j.anucene.2016.02.025 (p. 16).

[41] H. N. Tran, H. T. Hoang and P. H. Liem, ‘Feasibility of using Gd_2O_3 particles in VVER-1000 fuel assembly for controlling excess reactivity,’ *Energy Procedia*,

vol. 131, pp. 29–36, 2017, ISSN: 18766102. DOI: `10.1016/j.egypro.2017.09.442`. [Online]. Available: `https://doi.org/10.1016/j.egypro.2017.09.442` (p. 16).

[42] A. Galahom, M. Y. Mohsen and N. Amrani, 'Explore the possible advantages of using thorium-based fuel in a pressurized water reactor (PWR) Part 1: Neutronic analysis,' *Nuclear Engineering and Technology*, vol. 54, no. 1, pp. 1–10, 2022, ISSN: 1738-5733. DOI: `10.1016/J.NET.2021.07.019` (p. 16, 19).

[43] E. Walker, P. Miller and J. Clarity, 'Insert Modeling in UNF ST&NDARDS,' US Department of Energy Spent Fuel, Waste Science and Technology, Tech. Rep., 2022 (p. 16).

[44] F. Franceschini and B. Petrović, 'Fuel with advanced burnable absorbers design for the IRIS reactor core: Combined Erbia and IFBA,' *Annals of Nuclear Energy*, vol. 36, no. 8, pp. 1201–1207, 2009, ISSN: 03064549. DOI: `10.1016/j.anucene.2009.04.005` (p. 16).

[45] P. Čudrnák and V. Nečas, 'Optimized Gadolinium Fuel Assemblies for Light Water Reactors,' *10th International Conference ENERGY – ECOLOGY – ECONOMY*, pp. 7–11, 2011 (p. 16).

[46] M. Schlieck, H. D. Berger and A. Neufert, 'Optimized gadolinia concepts for advanced in-core fuel management in PWRs,' *Nuclear Engineering and Design*, vol. 205, no. 1-2, pp. 191–198, 2001, ISSN: 00295493. DOI: `10.1016/S0029-5493(00)00355-1` (p. 16).

[47] H. N. Tran, V. K. Hoang, P. H. Liem and H. T. Hoang, 'Neutronics design of VVER-1000 fuel assembly with burnable poison particles,' *Nuclear Engineering and Technology*, vol. 51, no. 7, pp. 1729–1737, 2019, ISSN: 1738-5733. DOI: `10.1016/J.NET.2019.05.026` (p. 16).

[48] C. Oprea and A. Oprea, 'Cross sections of gadolinium isotopes in neutron transmission simulated experiments with low energy neutrons up to 100 eV,' February 2015, Dubna, Russia: 22nd International Seminar on Interaction of Neutrons with Nuclei: Fundamental Interactions and Neutrons, Nuclear Structure, Ultracold Neutrons, Related Topics, 2014. DOI: `10.13140/RG.2.1.4373.5122` (p. 17).

[49] U. M. Nabila, M. H. Sahadath, M. T. Hossain and F. Reza, 'An approach to minimize reactivity penalty of Gd_2O_3 burnable absorber at the early stage of fuel burnup in Pressurized Water Reactor,' *Nuclear Engineering and Technology*, vol. 54, no. 9,

pp. 3516–3525, 2022, ISSN: 1738-5733. DOI: `https://doi.org/10.1016/j.net.2022.04.015`. [Online]. Available: `https://www.sciencedirect.com/science/article/pii/S1738573322002182` (p. 17).

[50] S. Fukushima, T. Ohmichi, A. Maeda and H. Watanabe, 'The effect of gadolinium content on the thermal conductivity of near-stoichiometric (U,Gd)O_2 solid solutions,' *Journal of Nuclear Materials*, vol. 105, no. 2-3, pp. 201–210, 1982, ISSN: 0022-3115. DOI: `10.1016/0022-3115(82)90375-0` (p. 17).

[51] H. M. Dalle, J. R. L. de Mattos and M. S. Dias, 'Enriched Gadolinium Burnable Poison for PWR Fuel – Monte Carlo Burnup Simulations of Reactivity,' in *Current Research in Nuclear Reactor Technology in Brazil and Worldwide*, October 2017, 2013. DOI: `10.5772/53381` (p. 17, 18, 43).

[52] M. J. Qin, S. C. Middleburgh, M. W. Cooper *et al.*, 'Thermal conductivity variation in uranium dioxide with gadolinia additions,' *Journal of Nuclear Materials*, vol. 540, p. 152 258, 2020, ISSN: 00223115. DOI: `10.1016/j.jnucmat.2020.152258`. [Online]. Available: `https://doi.org/10.1016/j.jnucmat.2020.152258` (p. 17).

[53] S. Yilmaz, 'Multi Level Optimization of Burnable Poison Utilization for Advanced PWR Fuel Management,' Doctor of Philosophy Thesis, The Pennsylvania State University, 2005, ISBN: 9788578110796 (p. 17, 204).

[54] J.-P. A. Renier and M. Grossbeck, 'Development of Improved Burnable Poisons for Commercial Nuclear Power Reactors,' Tech. Rep. October, 2001, p. 207 (p. 17, 19, 43).

[55] K. H. Bejmer and O. Seveborn, 'Enriched Gadolinium as Burnable Absorber for PWR,' *Proceedings of the PHYSOR The Physics of Fuel Cycles and Advanced Nuclear Systems - Global Developments*, 2004, ISSN: 1098-6596. arXiv: `arXiv:1011.1669v3` (p. 18).

[56] D. Campolina, E. F. Faria, A. A. C. Santos *et al.*, 'Parametric study of enriched gadolinium in burnable neutron poison fuel rods for Angra-2,' *Annals of Nuclear Energy*, vol. 118, pp. 375–380, 2018, ISSN: 0306-4549. DOI: `https://doi.org/10.1016/j.anucene.2018.04.025`. [Online]. Available: `https://www.sciencedirect.com/science/article/pii/S030645491830210X` (p. 18).

[57] F. Khoshahval, ‘The effect of enriched gadolinia and its concentrations on the neutronic parameters of AP-1000 fuel assembly,’ *Radiation Physics and Chemistry*, vol. 195, p. 110 086, 2022, ISSN: 0969-806X. DOI: `10.1016/J.RADPHYSCHEM.2022.110086` (p. 18).

[58] S. Yilmaz, K. Ivanov, S. Levine and M. Mahgerefteh, ‘Development of enriched Gd-155 and Gd-157 burnable poison designs for a PWR core,’ *Annals of Nuclear Energy*, vol. 33, no. 5, pp. 439–445, 2006, ISSN: 03064549. DOI: `10.1016/j.anucene.2005.11.011` (p. 18).

[59] M. Berglund and M. E. Wieser, ‘Isotopic compositions of the elements 2009 (IUPAC Technical Report),’ *Pure and Applied Chemistry*, vol. 83, no. 2, 2011. DOI: `doi:10.1351/PAC-REP-10-06-02`. [Online]. Available: `https://doi.org/10.1351/PAC-REP-10-06-02` (p. 19).

[60] W. Lee, K. W. Kim, J. E. Lim *et al.*, ‘In vivo evaluation of the effects of combined boron and gadolinium neutron capture therapy in mouse models.,’ *National Library of Medicine*, 2022. DOI: `doi:10.1038/s41598-022-17610-4`. [Online]. Available: `https://doi.org/10.1351/PAC-REP-10-06-02` (p. 19).

[61] N. Gupta and B. Basu, ‘10 - Hot pressing and spark plasma sintering techniques of intermetallic matrix composites,’ in *Intermetallic Matrix Composites*, R. Mitra, Ed., Woodhead Publishing, 2018, pp. 243–302, ISBN: 978-0-85709-346-2. DOI: `https://doi.org/10.1016/B978-0-85709-346-2.00010-8`. [Online]. Available: `https://www.sciencedirect.com/science/article/pii/B9780857093462000108` (p. 19).

[62] P. Makurunje, G. Woodhouse, D. T. Goddard and S. C. Middleburgh, ‘Self-contained dual-scale composite architectures in spray dried zirconium diboride,’ *Ceramics International*, vol. 48, no. 12, pp. 17 529–17 538, 2022, ISSN: 0272-8842. DOI: `https://doi.org/10.1016/j.ceramint.2022.03.018`. [Online]. Available: `https://www.sciencedirect.com/science/article/pii/S0272884222007556` (p. 19).

[63] K. Hesketh, G. Rossiter, R. Largenton and M. Puide, ‘2.04 - Burnable Poison-Doped Fuel,’ in *Comprehensive Nuclear Materials (Second Edition)*, R. J. M. Konings and R. E. Stoller, Eds., Second Edi, Oxford: Elsevier, 2020, pp. 106–124, ISBN: 978-0-08-102866-7. DOI: `https://doi.org/10.1016/B978-0-12-803581-8.11699-6`.

[Online]. Available: `https://www.sciencedirect.com/science/article/pii/B9780128035818116996` (p. 19).

[64] J. Choe, H. C. Shin and D. Lee, 'New burnable absorber for long-cycle low boron operation of PWRs,' *Annals of Nuclear Energy*, vol. 88, pp. 272–279, 2016, ISSN: 18732100. DOI: `10.1016/j.anucene.2015.11.011`. [Online]. Available: `http://dx.doi.org/10.1016/j.anucene.2015.11.011` (p. 19).

[65] P. A. Burr, E. Kardoulaki, R. Holmes and S. C. Middleburgh, 'Defect evolution in burnable absorber candidate material: Uranium diboride, UB_2,' *Journal of Nuclear Materials*, vol. 513, pp. 45–55, 2019, ISSN: 00223115. DOI: `10.1016/j.jnucmat.2018.10.039`. [Online]. Available: `https://doi.org/10.1016/j.jnucmat.2018.10.039` (p. 19, 20).

[66] A. Dandi, M. J. Lee and M. H. Kim, 'Feasibility of combinational burnable poison pins for 24-month cycle PWR reload core,' *Nuclear Engineering and Technology*, vol. 52, no. 2, pp. 238–247, 2020, ISSN: 1738-5733. DOI: `10.1016/J.NET.2019.07.026` (p. 19).

[67] Westinghouse Electric Company, *Nuclear Fuel - Integral Fuel Burnable Absorber (IFBA) Fuel Cycles and IFBA/Gad Hybrid Fuel Cycles*, 2018. [Online]. Available: `https://www.westinghousenuclear.com/Portals/0/operating%20plant%20services/fuel/fuel%20products/NFCM-0015%20IFBA.pdf` (p. 19, 96).

[68] E. Kardoulaki, J. T. White, D. D. Byler *et al.*, 'Thermophysical and mechanical property assessment of UB_2 and UB_4 sintered via spark plasma sintering,' *Journal of Alloys and Compounds*, vol. 818, p. 153 216, 2020, ISSN: 09258388. DOI: `10.1016/j.jallcom.2019.153216`. [Online]. Available: `https://doi.org/10.1016/j.jallcom.2019.153216` (p. 19).

[69] J. Turner, F. Martini, J. Buckley, G. Phillips, S. C. Middleburgh and T. J. Abram, 'Synthesis of candidate advanced technology fuel: Uranium diboride (UB_2) via carbo/borothermic reduction of UO_2,' *Journal of Nuclear Materials*, vol. 540, p. 152 388, 2020, ISSN: 0022-3115. DOI: `10.1016/J.JNUCMAT.2020.152388` (p. 20).

[70] IEA, *Monthly Electricity Statistics*, 2023. [Online]. Available: `https://www.iea.org/data-and-statistics/data-tools/monthly-electricity-statistics` (visited on 19th May 2023) (p. 20, 23).

[71] World Nuclear Association, *Economics of Nuclear Power*, 2022. [Online]. Available: `https://world-nuclear.org/information-library/economic-aspects/economics-of-nuclear-power.aspx` (visited on 15th May 2023) (p. 20, 21).

[72] OECD/NEA, 'The Economics of the Nuclear Fuel Cycle,' Nuclear Energy Agency, Organisation for Economic Co-Operation and Development, Tech. Rep., 1994 (p. 21, 72, 204, 207).

[73] OECD/NEA, *The Economics of the Back End of the Nuclear Fuel Cycle*, 2013 (p. 21, 22).

[74] R. I. Smith, G. J. Konzek and J. W. E. Kennedy, 'Technology , Safety and Costs of Decommissioning a Reference Pressurized Water Reactor Power Station,' *NUREG/CR-0130*, vol. 2, 1978 (p. 21).

[75] C. S. Handwerk, 'Economic and Fuel Performance Analysis of Extended Operating Cycles in Existing Light Water Reactors (LWRs),' Ph.D. dissertation, Massachusetts Institute of Technology, 1998 (p. 24, 25).

[76] G. Rothwell and J. Rust, 'A Dynamic Programming Model of U.S. Nuclear Power Plant Operations,' *Microeconomics*, no. September 2014, 1995. [Online]. Available: `http://ideas.repec.org/p/wpa/wuwpmi/9502001.html` (p. 24, 175).

[77] M. Kovac, 'Evaluation of the Middle Part of the Nuclear Fuel Cycle,' *Nuclear Engineering and Technology*, vol. 48, no. 1, pp. 169–174, 2016, ISSN: 2234358X. DOI: `10.1016/j.net.2015.08.010`. [Online]. Available: `http://dx.doi.org/10.1016/j.net.2015.08.010` (p. 24).

[78] US EIA, 'Capacity outages at U.S. nuclear power plants,' (p. 24).

[79] IAEA, 'Nuclear power plant outage optimisation strategy,' Tech. Rep. October, 2002 (p. 24).

[80] P. A. David, R. Maude-Griffin and G. Rothwell, 'Learning by accident? Reductions in the risk of unplanned outages in U.S. nuclear power plants after Three Mile Island,' *Journal of Risk and Uncertainty*, vol. 13, no. 2, pp. 175–198, 1996, ISSN: 08955646. DOI: `10.1007/BF00057867` (p. 24).

[81] J. R. Secker, B. J. Johansen, D. L. Stucker *et al.*, 'Optimum discharge burnup and cycle length for PWRs,' *Nuclear Technology*, vol. 151, no. 2, pp. 109–119, 2005, ISSN: 00295450. DOI: `10.13182/NT05-A3636` (p. 25).

[82] G. J. Youinou and R. S. Sen, 'Impact of accident-tolerant fuels and claddings on the overall fuel cycle: A preliminary systems analysis,' *Nuclear Technology*, vol. 188, no. 2, pp. 123–138, 2014. DOI: `10.13182/NT14-22`. [Online]. Available: `https://doi.org/10.13182/NT14-22` (p. 25).

[83] L. Garcia-Delgado, M. J. Driscoll, J. E. Meyer and N. E. Todreas, 'An economically optimum PWR reload core for a 36-month cycle,' *Annals of Nuclear Energy*, vol. 26, 1999 (p. 25, 135, 175).

[84] IAEA, *Reload Design and Core Management in Operating Nuclear Power Plants Experiences and Lessons Learned*, 2020 (p. 25).

[85] S. Middleburgh, M. Bolukbasi and D. Goddard, 'Enhancing economics with ATF,' *Nuclear Engineering International Magazine*, pp. 24–27, 2020 (p. 26).

[86] S. Gallier, *Looking high and low for HALEU*, 2019. [Online]. Available: `https://www.ans.org/news/article-3509/looking-high-and-low-for-haleu/` (visited on 16th May 2023) (p. 26).

[87] J. Leppänen, *Serpent - a Continuous-energy Monte Carlo neutron and photon transport code*, 2023. [Online]. Available: `https://serpent.vtt.fi/serpent/` (visited on 16th May 2023) (p. 28, 29).

[88] J. Leppänen, M. Pusa, T. Viitanen, V. Valtavirta and T. Kaltiaisenaho, 'The Serpent Monte Carlo code: Status, development and applications in 2013,' *Annals of Nuclear Energy*, vol. 82, pp. 142–150, 2015, ISSN: 18732100. DOI: `10.1016/j.anucene.2014.08.024` (p. 28, 29).

[89] Studsvik Scandpower, 'CASMO4 user's manual,' Tech. Rep., 2009 (p. 29).

[90] M. Pusa, 'Incorporating sensitivity and uncertainty analysis to a lattice physics code with application to Casmo-4,' *Annals of Nuclear Energy*, vol. 40, no. 1, pp. 153–162, 2012, ISSN: 0306-4549. DOI: `https://doi.org/10.1016/j.anucene.2011.10.013`. [Online]. Available: `https://www.sciencedirect.com/science/article/pii/S0306454911004117` (p. 29).

[91] Studsvik Scandpower, 'SIMULATE3 user's manual,' 2009 (p. 30).

[92] R. L. Murray and K. E. Holbert, 'Chapter 16 - neutron chain reactions,' in *Nuclear Energy (Eighth Edition)*, R. L. Murray and K. E. Holbert, Eds., Eighth Edition, Butterworth-Heinemann, 2020, pp. 291–305, ISBN: 978-0-12-812881-7. DOI: `https://doi.org/10.1016/B978-0-12-812881-7.00016-2`. [Online]. Available:

`https://www.sciencedirect.com/science/article/pii/B9780128128817000162` (p. 30).

[93] IAEA, *Physics and Kinetics of TRIGA Reactors*, 2004. [Online]. Available: `https://ansn.iaea.org/Common/documents/Training/TRIGA%20Reactors%20(Safety%20and%20Technology)/chapter2/physics113.htm` (visited on 12th May 2023) (p. 30).

[94] B. Hiscox, ‘Analysis and Optimization of a New Accident Tolerant Fuel Called Fuel-in-Fibers,’ Ph.D. dissertation, Massachusetts Institute of Technology, 2018 (p. 31, 32).

[95] D. A. Bloore, ‘Reactor Physics Assessment of Thick Silicon Carbide Clad PWR Fuels,’ M.Sc. dissertation, Massachusetts Institute of Technology, 2013 (p. 31).

[96] US-NRC, ‘Technical Specifications, Virgil C. Summer Nuclear Station,’ no. 1, 1982 (p. 31, 67, 68, 135, 137).

[97] N. Power, *Boron Coefficient*, 2023. [Online]. Available: `nuclear-power.com/nuclearpower/reactor-physics/nuclear-fission-chain-reaction/reactivity-coefficient-sreactivity-feedbacks/boron-coefficient` (visited on 17th May 2023) (p. 31).

[98] C. Castagna and E. Gilad, ‘Study of radionuclide inventory in nuclear fuel under uncertainties in boron concentration using high-fidelity models,’ *International Journal of Energy Research*, vol. 46, no. 6, 2022. DOI: `10.1002/er.7702` (p. 31).

[99] US-NRC, *Moderator temperature coefficient of reactivity*, 2021. [Online]. Available: `Moderator%20temperature%20coefficient%20of%20reactivity` (visited on 15th May 2023) (p. 31).

[100] N. Power, *Shutdown Margin*, 2023. [Online]. Available: `https://www.nuclear-power.com/reactor-physics/reactor-operation/shutdown-margin-sdm/` (visited on 15th May 2023) (p. 32).

[101] M. J. Bolukbasi, S. C. Middleburgh, M. Dahlfors and W. E. Lee, ‘Performance and economic assessment of enriched gadolinia burnable absorbers,’ *Progress in Nuclear Energy*, vol. 137, no. March, p. 103 752, 2021, ISSN: 01491970. DOI: `10.1016/j.pnucene.2021.103752` (p. 33).

[102] J. P. Gorton, B. S. Collins, A. T. Nelson and N. R. Brown, ‘Reactor performance and safety characteristics of ThN-UN fuel concepts in a PWR,’ *Nuclear Engineering*

and Design, vol. 355, no. July, p. 110 317, 2019, ISSN: 00295493. DOI: `10.1016/j.nucengdes.2019.110317`. [Online]. Available: `https://doi.org/10.1016/j.nucengdes.2019.110317` (p. 34, 98).

[103] S. Pinem, T. M. Sembiring, Tukiran, Deswandri, G. Rina and Sunaryo, 'Reactivity Coefficient Calculation for AP1000 Reactor Using the NODAL3 Code,' in *J. Phys.: Conf. Ser. 962 012057*, 2018. [Online]. Available: `https://iopscience.iop.org/article/10.1088/1742-6596/962/1/012057/pdf` (p. 34, 98).

[104] IAEA, 'Characteristics and Use of Urania-Gadolinia Fuels,' 1995 (p. 34, 67).

[105] Westinghouse Electric Company, 'Chapter 4.1 Reactor Summary Description AP1000 DCD,' pp. 1–12, 2011 (p. 35, 100).

[106] L. Pagano, G. P. Valença, S. L. Silva *et al.*, 'Mössbauer study and structural characterization of UO_2-Gd_2O_3 sintered compounds,' *Journal of Nuclear Materials*, vol. 378, no. 1, pp. 25–29, 2008, ISSN: 00223115. DOI: `10.1016/j.jnucmat.2008.03.024` (p. 36).

[107] S. M. Reda, S. S. Mustafa and N. A. Elkhawas, 'Investigating the Performance and safety features of Pressurized water reactors using the burnable poisons,' *Annals of Nuclear Energy*, vol. 141, p. 107 354, 2020, ISSN: 18732100. DOI: `10.1016/j.anucene.2020.107354`. [Online]. Available: `https://doi.org/10.1016/j.anucene.2020.107354` (p. 38).

[108] A. M. Attom, J. Wang, C. Yan and M. Ding, 'Neutronic analysis of thorium MOX fuel blocks with different driver fuels in advanced block-type HTRs,' *Annals of Nuclear Energy*, vol. 129, pp. 101–109, 2019, ISSN: 0306-4549. DOI: `https://doi.org/10.1016/j.anucene.2019.01.049`. [Online]. Available: `https://www.sciencedirect.com/science/article/pii/S0306454919300374` (p. 40).

[109] C. E. Sanders and J. C. Wagner, *Study of the Effect of Integral Burnable Absorbers for PWR Burnup Credit*. Oak Ridge National Laboratory, 2002, ISBN: 1800553684 (p. 40, 104).

[110] C. E. Sanders and J. C. Wagner, 'Impact of Integral Burnable Absorbers on PWR Burnup Credit Criticality Safety Analyses,' 10, Oak Ridge National Laboratory, NCSD Conference Paper, 2001 (p. 51, 178).

[111] M. Bolukbasi, S. Middleburgh and W. Lee, 'In-reactor behaviour and economic assessment of enriched gadolinia burnable absorbers,' *Progress in Nuclear Energy*, vol. 164, p. 104 873, 2023, ISSN: 0149-1970. DOI: `https://doi.org/10.1016/j.pnucene.2023.104873`. [Online]. Available: `https://www.sciencedirect.com/science/article/pii/S0149197023003086` (p. 66).

[112] A. S. DiGiovine and H.-N. M. Gheorghiu, 'Generic CMS PWR Equilibrium Model Revision 3,' Studsvik Scandpower, Tech. Rep., 1999 (p. 67, 68, 135, 137).

[113] Duke Energy, 'Harris Nuclear Power Plant Core Operating Limits Report,' Tech. Rep., 2018 (p. 67, 68, 135, 137).

[114] B. D. Hanson, S. C. Marschman, M. C. Billone, J. Scaglione, K. B. Sorenson and S. J. Saltzstein, 'High Burnup Spent Fuel Data Project Sister Rod Test Plan Overview,' 2016. [Online]. Available: `https://www.energy.gov/sites/prod/files/2017/02/f34/2HBUSNFSisterRodTestPlanOverview.pdf` (p. 69).

[115] N. Amjad, Y. Hidekazu and Y. Ming, 'Burnup study of 18 months and 16 / 20 months cycle AP1000 cores using CASMO4E and SIMULATE-3 codes,' *Nuclear Safety and Simulation*, vol. 5, no. 2, 2014 (p. 71, 140).

[116] M. J. Bolukbasi, S. C. Middleburgh, S. Vrtiska and W. E. Lee, 'Effect of ZrB_2 and UB_2 Discrete Burnable Absorber Pins on fuel reactivity,' *Progress in Nuclear Energy*, vol. 150, no. October 2021, p. 104 295, 2022, ISSN: 01491970. DOI: `10.1016/j.pnucene.2022.104295`. [Online]. Available: `https://doi.org/10.1016/j.pnucene.2022.104295` (p. 96).

[117] A. Enica, S. C. Middleburgh and S. J. Vrtiska, 'Annular Nuclear Fuel Pellets with Discrete Burnable Absorber Pins,' *U.S. Patent 2018/0330832 A1*, 2018 (p. 97).

[118] W. P. Wallace and M. T. Simnat, 'Comparison of BeO versus Graphite as a Moderator for MGCR,' *General Atomics Tech. Rep. GAMD-974*, 1959 (p. 97, 149).

[119] D. E. Ames II, P. V. Tsvetkov, G. E. Rochau and S. Rodriguez, 'High Fidelity Nuclear Energy System Optimization Towards an Environmentally Benign, Sustainable, and Secure Energy Source,' Sandia National Laboratories, Tech. Rep., 2010. DOI: `10.2172/992769` (p. 100, 101, 103).

[120] G. Rossiter and M. Mignanelli, 'The characteristics of LWR fuel at high burnup and their relevance to AGR spent fuel,' *National Nuclear Laboratory*, vol. (10) 10930, no. 1, pp. 1–60, 2010 (p. 115).

[121] M. J. Bolukbasi, S. C. Middleburgh, S. Vrtiska and W. E. Lee, ‘Shifting to a 36-month fuel cycle with advanced moderating burnable absorbers enabling high assay low enriched uranium (HALEU),’ *Progress in Nuclear Energy*, vol. 168, no. December 2023, p. 105 011, 2024, ISSN: 01491970. DOI: `10.1016/j.pnucene.2023.105011`. [Online]. Available: `https://doi.org/10.1016/j.pnucene.2023.105011` (p. 134).

[122] S. Atkinson, T. J. Abram, D. Litskevich and B. Merk, ‘Small modular high temperature reactor optimisation – Part 1: A comparison between beryllium oxide and nuclear graphite in a small scale high temperature reactor,’ *Progress in Nuclear Energy*, vol. 111, pp. 223–232, 2019, ISSN: 0149-1970. DOI: `https://doi.org/10.1016/j.pnucene.2018.10.017`. [Online]. Available: `https://www.sciencedirect.com/science/article/pii/S0149197018302695` (p. 149).

[123] S. Chen and C. Yuan, ‘Neutronic study of UO_2-BeO fuel with various claddings,’ *Nuclear Materials and Energy*, vol. 22, p. 100728, 2020. [Online]. Available: `https://doi.org/10.1016/j.nme.2020.100728` (p. 178).

[124] C. De Saint-Jean, E. Dupont, M. Ishikawa, G. Palmiotti and M. Salvatores, ‘Assessment of Existing Nuclear Data Adjustment Methodologies,’ *A report by the Working Party on International Evaluation Co-operation of the NEA Nuclear Science Committee*, no. NEA/NSC/WPEC/DOC(2010)429, 2011 (p. 185).

[125] B. Dixon, F. Ganda, K. Williams, E. Hoffman and J. Hanson, ‘Advanced Fuel Cycle Cost Basis – 2017 Edition,’ Advanced Fuel Cycle Initiative Tech. Rep., 2017. [Online]. Available: `https://www. osti.gov/servlets/purl/1423891` (p. 204).

[126] World Nuclear Association, *HARRIS 1 operating details*, 2021. [Online]. Available: `https://www.world-nuclear.org/reactor/default.aspx/HARRIS-1` (p. 207).

Appendix

Figure 52 presents the initial core loading utilised for the SIMULATE simulations and Figure 53 shows the Pyrex burnable poison rod cross-section. In addition, the distribution of Pyrex bunable poison rods in the fuel assembly is shown in Figure 54.

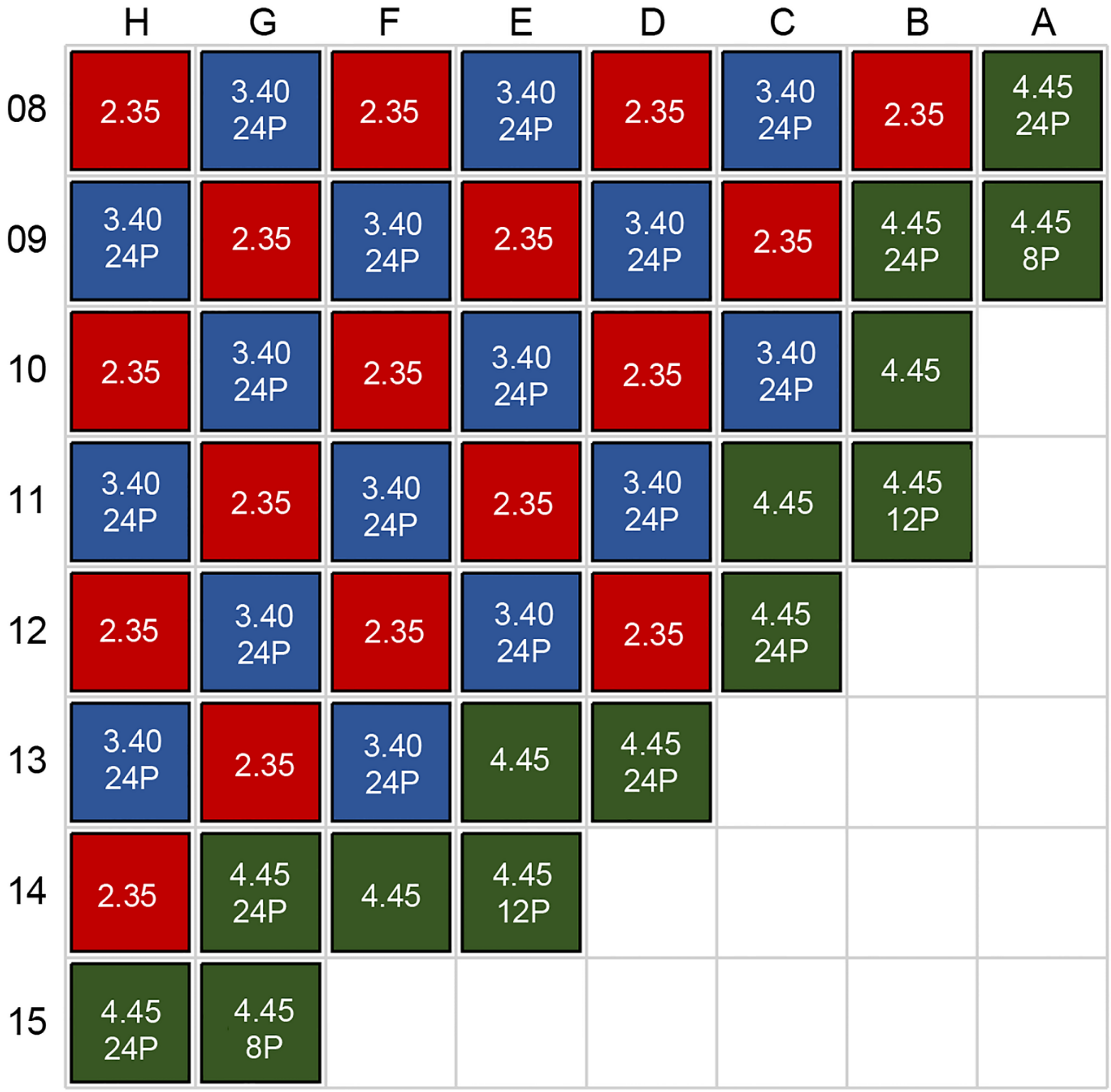

	H	G	F	E	D	C	B	A
08	2.35	3.40 24P	2.35	3.40 24P	2.35	3.40 24P	2.35	4.45 24P
09	3.40 24P	2.35	3.40 24P	2.35	3.40 24P	2.35	4.45 24P	4.45 8P
10	2.35	3.40 24P	2.35	3.40 24P	2.35	3.40 24P	4.45	
11	3.40 24P	2.35	3.40 24P	2.35	3.40 24P	4.45	4.45 12P	
12	2.35	3.40 24P	2.35	3.40 24P	2.35	4.45 24P		
13	3.40 24P	2.35	3.40 24P	4.45	4.45 24P			
14	2.35	4.45 24P	4.45	4.45 12P				
15	4.45 24P	4.45 8P						

Top : Uranium-235 enrichment level
Bottom: Number of Pyrex rods

Figure 52 – Initial core loading pattern.

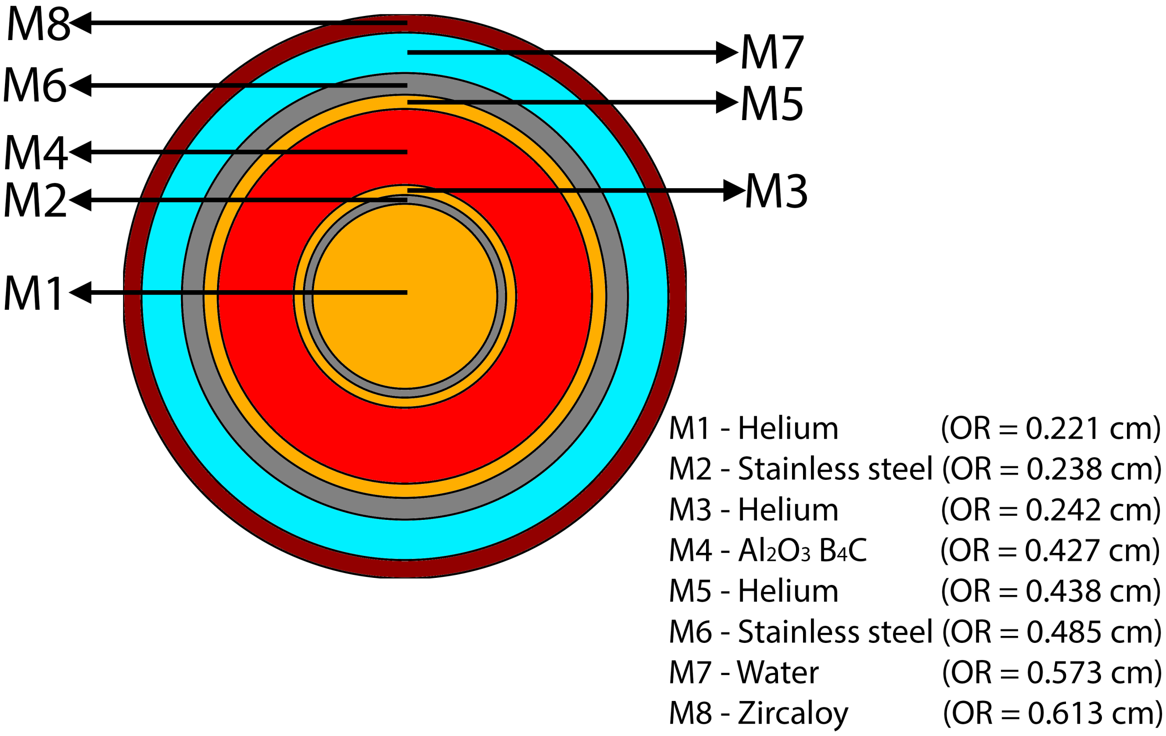

Figure 53 – Pyrex burnable poison rod cross-section.

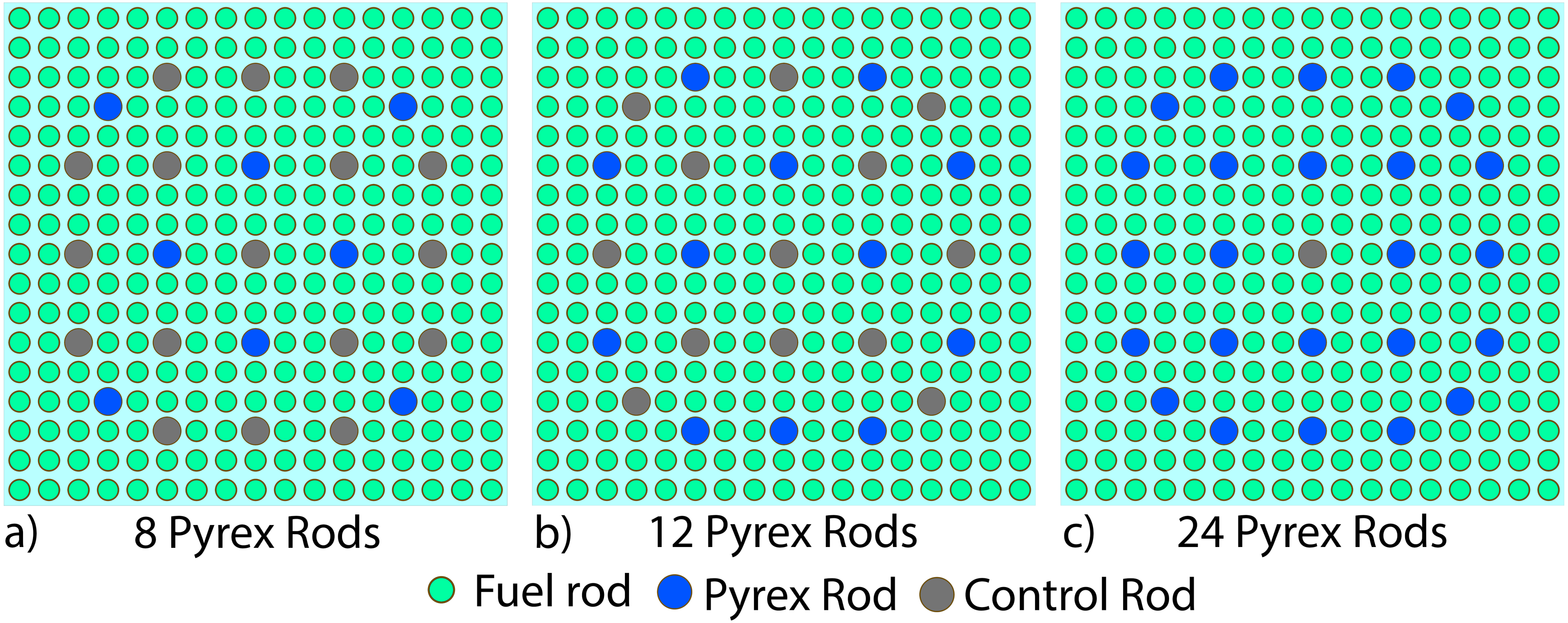

Figure 54 – Pyrex burnable poison rod distribution.

In the Figure 53, M1 corresponds to helium with an outer radius of 0.221 cm. M2 represents stainless steel with an outer radius of 0.238 cm. M3 is helium with an outer radius of 0.242 cm. M4 corresponds to Al_2O_3-B_4C with an outer radius of 0.427 cm. M5 is helium with an outer radius of 0.438 cm. M6 represents stainless steel again with an outer radius of 0.485 cm. M7 corresponds to water with an outer radius of 0.573 cm. Lastly, M8 represents Zircaloy with an outer radius of 0.613 cm.

Table 24 displays the costs of the high, nominal, and low costs of front-end components utilised for calculating the fuel loading cost in the study.

In the table, the high and low costs of the ^{157}Gd enrichment process were determined by assuming that the nominal cost consistently rose and fell according to the average USA escalation rate during the period from which it was documented in the literature [53] to 2022.

In addition, the front-end costs were calculated using the formulas shown between Equations 5 and 20 [72]. The parameter notation for these formulas can be conveniently referenced in Table 25 while the fuel cycle data is given in Table 26.

Table 24 – Unit prices for front-end components [53], [125].

Type of component	Unit Prices		
	Low	Nominal	High
Uranium \$/lb U_3O_8	13.1	33.1	114
Conversion \$/kg	6.5	13	19
Uranium enrichment \$/SWU	97	128	154
Fabrication \$/kg	230	400	575
^{157}Gd enrichment \$/g	6.48	10	15.25

Table 25 – Parameter notation for fuel cost calculations.

Time	t
Base date of monetary unit	t_b
Date of fuel loading	t_c
Mass of uranium feed (kg)	M_f
Mass of uranium charged in reactor (kg)	M_p
Mass of uranium in the tails (kg)	M_t
Fraction of ^{235}U in the uranium feed	e_f (0.711%)
Fraction of ^{235}U charged in reactor	e_p
Fraction of ^{235}U in the tails	e_t
Conversion factor from kg U to lb U_3O_8 (lb U_3O_8 per kg U)	a (2.6)
Total component cost	F_i
Unit cost	P_i
Escalation rate	S_i
Material losses	l_i
Total loss factor	f_i
Lead or lag time	t_i
Power output (MWe)	P_e

where:

$i = 1$ Uranium purchase	P_1 = Monetary units per lb U_3O_8
$i = 2$ Conversion	P_2 = Monetary units per kg U
$i = 3$ Enrichment	P_3 = Monetary units per SWU
$i = 4$ Fabrication	P_4 = Monetary units per kgU

Cost of uranium

$$F_1 = M_f \times a \times f_1 \times P_1 \times (1+S_1)^{t-t_b} \tag{5}$$

where:

$$M_f = \frac{e_p - e_t}{e_f - e_t} \times M_p \tag{6}$$

$$f_1 = (1+l_2) \times (1+l_3) \times (1+l_4) \tag{7}$$

From all front-end components:

$$t = t_c - t_i \tag{8}$$

Cost of conversion

$$F_2 = M_F \times f_2 \times P_2 \times (1+S_2)^{t-t_b} \tag{9}$$

where:

$$f_2 = (1+l_2) \times (1+l_3) \times (1+l_4) \tag{10}$$

Cost of enrichment

$$F_3 = SWU \times f_3 \times P_3 \times (1+S_3)^{t-t_b} \tag{11}$$

where:

$$SWU = M_p \times V_p + M_t \times V_t - M_f \times V_f \tag{12}$$

$$M_t = M_f - M_p \tag{13}$$

$$V_x = (2e_x - 1) \ln \left[\frac{e_x}{(1-e_x)} \right] \tag{14}$$

where x is a subscript for f, p or t

$$f_3 = (1+l_3) \times (1+l_4) \tag{15}$$

Cost of fabrication

$$F_4 = M_F \times f_4 \times P_4 \times (1+S_4)^{t-t_b} \tag{16}$$

where:

$$f_4 = (1+l_4) \tag{17}$$

Cost of ^{157}Gd enrichment

$$F_5 = M_{Gd} \times P_5 \times 1000 \tag{18}$$

Total cost of fuel

$$\text{Total fuel cost} = \sum_i F_i \tag{19}$$

LCOE$_{front-end}$

$$\text{LCOE}_{\text{front-end}} = \frac{\sum_i F_i}{EFPD \times 24 \times P_e} \tag{20}$$

Table 26 – Fuel cycle data [27], [72], [126].

Lead time of uranium purchase	24 months
Lead time of conversion	18 months
Lead time of uranium enrichment	12 months
Lead time of fabrication	6 months
Material loss during conversion (%)	0.2
Material loss during enrichment (%)	0.2
Material loss during fabrication (%)	0.2
Tails assay (%)	0.25
Escalation rate	2.46
P_e (MWe)	964